Nanometric Characterisation of III-Nitride Semiconductors

A Thesis Submitted to
The Department of Physics
University of Strathclyde
For the Degree of
Doctor of Philosophy

By
Lay-Theng Tan
February 2009

Declaration of Author's Rights

Abstract

An investigation on the optical, composition and surface properties of the III-nitride ternary alloys $In_xGa_{1-x}N$ and $Al_{1-x}In_xN$ is presented. The structures studied are single quantum wells (SQWs) and epilayers. The effects of various GaN cap thicknesses, well widths, Si doping concentrations in the barriers, InN compositions, epilayer thicknesses and substrates are examined. The techniques used are photoluminescence (PL) and PL excitation (PLE) spectroscopy for investigating the optical properties, wavelength dispersive x-ray (WDX) and Rutherford backscattering spectrometry (RBS) for measuring InN composition. RBS is also used to study the crystalline quality of the samples; and secondary electron microscopy (SEM) and atomic force microscopy (AFM) for examining the surface quality.

$In_xGa_{1-x}N$/GaN SQWs with a variety of GaN cap thicknesses and different barrier doping levels were studied using PL spectroscopy. It was demonstrated that the $In_xGa_{1-x}N$/GaN SQWs with thin caps give reduced PL intensity and larger PL linewidths, indicating degradation due to the increasing effects of the surface. As the doping level in the GaN barrier layers increases the luminescence intensity decreases, the linewidth increases and the SQW transition energy red-shifts. The latter is attributed to band-gap renormalisation. The properties of GaN/$Al_{1-x}In_xN$ SQWs were investigated for varying quantum well width and for different substrates. The GaN/$Al_{1-x}In_xN$ SQW luminescence peak energy decreases as the well-width increases, mainly due to the intense spontaneous polarisation fields, and its dependence on excitation power reveals the effects of carrier screening. $Al_{1-x}In_xN$ epilayers were also characterised and here the PL peak emission energies decrease with increasing InN composition. The energy bandgap bowing parameter is found to be linearly decreasing with increasing InN composition in the limited composition range studied. Cracks are observed in highly tensile strained epilayers with $x < 0.10$. For variations in layer thickness the surface quality and crystal quality worsens with increasing thickness. Finally, the samples on FS-GaN substrates have 3 to 4 atomic % more InN than those grown on sapphire. Surface quality degradation is observed in samples grown on non-polished sapphire substrates and $Al_yGa_{1-y}N$ templates with high Al content.

Acknowledgements

I would like to express my gratitude to all people who have provided help, support and encouragement for the completion of this thesis and the work contained within. Here I will mention the one closest to this work.

First of all I would like to thank my supervisor Prof Robert Martin for his constant guidance, patience and kindness throughout the course of my PhD. He has been enthusiastic towards my work and always provides much appreciated input. I would also like to thank my second-supervisor Prof Kelvin O'Donnell for sharing his extensive knowledge of semiconductor physics and generous support and guidance. Without them, it would not have been possible for me to fulfil my childhood ambition and complete this thesis. I am grateful forever for this.

I also like to extend my thanks to all the internal and external collaborators that have provided invaluable access to advance experimental techniques and data which provided valuable feedback. Many thanks go to Dr. Ian Watson of the Institute of Photonics at University of Strathclyde; Thomas Sadler, Dr. Menno Kappers and Dr. Rachel Oliver at the Department of Materials Science and Metallurgy from University of Cambridge; and Dr. David Schenk at CRHEA-CNRS, Valbonne, France for supplying the samples. I would also like to thank Dr. Katharina Lorenz and her PhD student Sérgio Magalhães from the Instituto Tecnologico e Nuclea (ITN, Sacavém, Portugal for their excellent RBS measurements; Dr. Stephanie Hodgen from Strathclyde Pure and Applied Chemistry Department for AFM measurement; Kean-Boon Lee and Dr. Peter Parbrook in Sheffield University, and Prof. D. Wolverson in Bath University for use of 244nm Ar^+ laser; Dr. Zhi-Hao Wu and Prof. Fernando Ponce in Arizona State University for TEM measurement; Prof. Mark Fox from Sheffield University for his fruitable discussions on the built-in electric field and band gap renormalisation as well as Dr. Ruediger Goldhahn from Technische Universität Ilmenau for sharing generously his extensive knowledge of bandgap renormalisation and band filling with me.

I would also like to warmly thank everyone in the Semiconductor Devices Group for making the laboratory a stimulating environment to work in. Special thanks to Paul for his gracious assistance and advices in the equipments; to Dave for his excellent technical support in the laboratory; to Carol for her great company during our conference trips and her enthusiasm in physics; to Frank for making my stay filled with laughters; to Ben for his kind explanation on some theories; and to Iman and Kasia for the ladies-talks and making delicious food to satisfy my greediness.

Last but not least, I dedicate this work to my beloved family especially my mother for their non-conditional love, support and encouragement. To my good friends Wenyi, Diana, Feeldy, Kelly, Guanzhen and Yanmei thanks for always having their yahoo messenger on to talk to in their late nights. Most importantly, to my boyfriend, Dr. Chee-Leong Lee, without whose love, understanding and encouragement I could not have survived and completed this PhD. He has been endlessly patient, sweet and supportive despite having his own thesis to worry over. I also want to dedicate this work to my father who would have been very proud and happier than anybody else if he had been alive. In addition, I would like to share the joy with my nephew Kangwei for waiting patiently for his best friend to complete the study and come home to play with him.

Lay-Theng Tan
Glasgow, February 2009.

TABLE OF CONTENTS

CHAPTER 4 Optical Properties and Surface Morphology of $In_xGa_{1-x}N$/GaN Single Quantum Wells with Various GaN Cap Thicknesses

CHAPTER 5 Optical Properties of $In_xGa_{1-x}N$/GaN Single Quantum Wells with Various Si-doping Concentrations in GaN Barriers

CHAPTER 6 Photoluminescence of Near-Lattice-Matched GaN/$Al_{1-x}In_xN$ Single Quantum Wells with Various Well widths

CHAPTER 7 Optical Properties and Surface Morphology of $Al_{1-x}In_xN$ Epilayers with Various InN Compositions, Epilayer Thickness and Substrates

CHAPTER 8 Conclusions

CHAPTER 1

Introduction

1.1 Introduction to III-Nitride Semiconductors

Wide band gap semiconductor materials extend the field of semiconductor applications to the regions where conventional semiconductors such as silicon (Si) and gallium arsenide (GaAs) fail. They can emit light at shorter wavelength (blue and ultraviolet), and can operate at higher temperatures due to their larger band gaps, high thermal conductivity and chemical inertness.

In the past decade, one of the most studied families of wide band gap semiconductors is the Group III-nitrides. The Group III-nitrides comprise GaN, InN, AlN and their alloys ($In_xGa_{1-x}N$, $Al_yGa_{1-y}N$, $Al_{1-x}In_xN$ and $Al_{1-x-y}Ga_yIn_xN$) which are produced by mixing binary nitride compounds. They possess direct energy band gaps from around 0.7 eV for InN [1] to 6.2 eV for AlN [2], covering the entire spectral range from the infrared red to the deep ultraviolet (UV). Since 1993, when Shuji Nakamura produced the first high brightness InGaN-based blue light-emitting diodes (LEDs) [3], III-nitrides have become particularly significant materials for semiconductor optoelectronic technologies [4]. This, combined with the fact that they are non-toxic, robust, thermally stable and have high thermal conductivities, makes them excellent candidates for the use in LEDs and laser diodes (LDs) [5-7]. The energy band gaps of $In_xGa_{1-x}N$, $Al_yGa_{1-y}N$ and $Al_{1-x}In_xN$ alloys as a function of the lattice constant (a) are shown in Figure 1.1.

Much attention has been paid to $In_xGa_{1-x}N$ due to its highly efficient emission with the possibility to cover the entire visible spectral region by changing the InN composition. It is already widely used in blue, green and white LEDs which are beginning to replace light bulbs due to their reliability, robustness and most importantly, low power consumption. For example, in a comparative study of a 70 W incandescent light bulb and 120 Nichia LEDs, the array of LEDs consumed only 8.6 W [8].

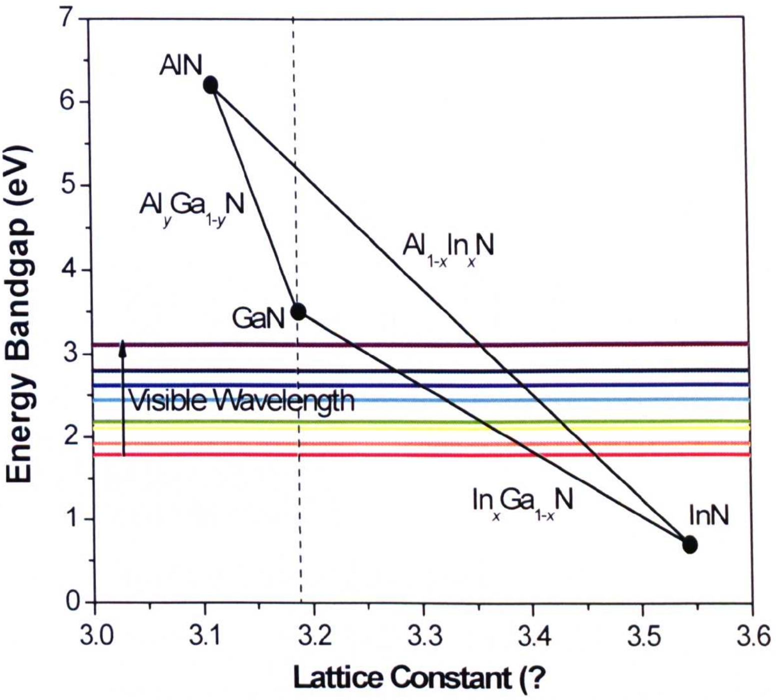

Figure 1.1 Energy band gaps of InGaN, AlGaN and AlInN alloys as a function of the *a* lattice constant [4, 6, 8]. Straight lines are an approximation, ignoring band bowing.

Blue laser diodes (LDs) based on $In_xGa_{1-x}N$ are found in a number of applications including high density data storage, high resolution colour printing and laser displays. Digital versatile disks (DVDs), which entered production in 1996, reply on red $Al_{1-x-y}In_xGa_yP$ semiconductor lasers, emitting at around 650 nm. By moving to violet wavelength through the use of $In_xGa_{1-x}N$-based semiconductors, the storage capacity can be increased by more than 5 times as compared to traditional DVDs using 405 nm blue-violet lasers [9]. There are two competing new generation DVD formats at the present time: Blu-ray DVD and high definition DVD (HD-DVD), both of which employs LDs emitting at 405 nm. The first Blu-ray DVD players, produced by Samsung, hit the market in June 2006 with other companies to follow suit later in the year [9]. Sony's PlayStation 3 games launched in 2007 uses Blu-ray technology whereas Microsoft uses an external HD-DVD drive for its X-box 360 games console [9]. HD-DVD players produced by Toshiba were launched in April 2006. Figure 1.2 shows some of the applications of III-nitrides [9-12].

Figure 1.2 Some applications of III-nitrides. Clockwise from top left-hand side: Traffic signal lights, digital camera backlighting, cellular phone backlighting, giant outdoor screens [10], a bridge across the river Clyde in Glasgow [11], Sony Playstation 3 Blu-ray player [9], and Hydro-Photon SteriPEN™ for water purification [12].

$Al_yGa_{1-y}N$ alloys with band gaps covering a substantial range of the UV spectral region, from 200 to 360 nm, are very promising as active media for UV LEDs and solar-blind UV detectors. UV LEDs can be used in chemical and biological agent detection systems, air sterilisation and water purification. As for solar-blind detectors, they can be applied in missile guidance systems, flame detection and secure space-to-space communication. However the most exceptional range for the band gap tunability from infra-red to UV could be achieved by using $Al_{1-x}In_xN$; it possibly will find a broader range of applications than both $In_xGa_{1-x}N$ and $Al_yGa_{1-y}N$ simply because it covers a much broader range of wavelengths. Furthermore, $Al_{1-x}In_xN$ can be lattice-matched to GaN with an InN fraction of approximately 17 % [13-15]. With free-standing GaN (FS-GaN) substrates now commercially available, lattice-matched $Al_{1-x}In_xN$ can be deployed to reduce defect densities in strain free GaN-based devices, such as laser diodes and transistors.

Technological advances have, to a certain extent, over-taken scientific understanding in the development of III-nitrides. Devices have been commercially produced and applied in a wide range of fields but we lack a complete understanding of the relationships between optical, surface and compositional properties of these materials. In this work, the optical, surface and compositional properties of the ternary alloys $In_xGa_{1-x}N$ and $Al_{1-x}In_xN$ have been investigated in order to contribute to the understanding of the workings of the nitride system.

1.2 Objectives of Thesis

This work presents the studies of $In_xGa_{1-x}N$ and $Al_{1-x}In_xN$ materials by means of photoluminescence (PL) spectroscopy, photoluminescence excitation (PLE) spectroscopy, scanning electron microscopy (SEM), atomic force microscopy (AFM), electron-probe microanalysis (EPMA), Rutherford backscattering spectrometry (RBS) and Hall Effect.

This thesis consists of eight chapters. The present chapter has given a brief introduction to III-nitrides, their applications and stated the objectives of this work. **Chapter 2** present some background to nitride semiconductors including the growth technique, the crystal and electronic band structure, and the luminescence properties of III–nitrides. **Chapter 3** describes the basic principles and experimental setups for the various characterisation techniques, in this case, PL, PLE, SEM, AFM, EPMA, RBS and Hall Effect.

The experimental results are presented and discussed in **Chapters 4, 5, 6** and **7**. **Chapter 4** presents the optical properties; in particular, the phonon replicas in luminescence and temperature-dependent PL spectra, and surface morphology of $In_xGa_{1-x}N$/GaN single quantum wells (SQWs) as a function of GaN cap thickness. **Chapter 5** describes the effect of various Si-doping concentrations in GaN barrier layers on the band gap energy of $In_xGa_{1-x}N$/GaN SQWs. **Chapter 6** analyses the optical properties of near-lattice-matched GaN/$Al_{1-x}In_xN$ SQWs as a function of well width and discusses a quantitative model to characterise the built-in electric field. The influence of different substrates, in this case *c*-plane sapphire and free-standing (FS)-GaN, on the optical properties of the SQWs is also considered. In **Chapter 7**, the optical, compositional and surface properties of $Al_{1-x}In_xN$ epilayers with a range of InN molar fractions, epilayer thickness and substrates are presented. Finally, the main results of the thesis are summarised and some suggestions for future work are given in **Chapter 8**.

1.3 References

[1] B. Monemar, P.P. Paskov, and A. Kasic, Superlattices and Microstructures **38**, 38 (2005).

[2] J. H. Edgar, S. Strite, I. Akasaki, H. Amano, and C. Wetzel, *Properties, Processing and Applications for GaN and Related Semiconductors*, EMIS Datareview No. 23, INSPEC London (1999).

[3] S. Nakamura, M. Senoh and T. Mukai, Japanese J. Appl. Phy. **32**, L8 (1993).

[4] Bernard Gil, *Low-dimensional Nitride Semiconductors*, 1st Edition, Oxford University Press (2002).

[5] J. H. Edgar, *Properties of Group III Nitrides*, EMIS Datareview No. 11, INSPEC London (1994).

[6] O. Ambacher, J. Phys. D: Appl. Phys. **31**, 2653 (1998).

[7] S. Nakamura, S. Pearton and G. Fasol, *The Blue Laser Diode*, 2nd Edition, Spring-Verlag (2000).

[8] Stephen J. Matthews, Laser Focus World, *Back to Basics; III-V Light Emitting Diodes, New Light from Old Sources* (April 2001).

[9] Blu-ray Disk Website: http://www.blu-ray.com/

[10] Nichia Corporation Website: http://www.nichia.co.jp

[11] Lumileds Website: http://www.lumileds.com/pdfs/glasgow_case_study.PDF

[12] Hydro-Photon Inc: http://www.hydro-photon.com/steripen_products.html

[13] J-F. Carlin, C. Zellweger, J. Dorsaz, S. Nicolay, G. Christmann, E. Feltin, R. Butté, and N. Grandjean, Phys. Stat. Solidi (b) **242**, 2326 (2005).

[14] K. Lorenz, N. Franco, E. Alves, I. M. Watson, R. W. Martin, and K.P. O'Donnell, Phys. Rev Lett. **97**, 085501 (2006).

[15] I. M. Watson, C. Liu, E. Gu, M. D. Dawson, P. R. Edwards, and R. W. Martin, Appl. Phys. Lett. **87**, 151901 (2005).

CHAPTER 2

III-Nitrides: Growth, Structures and Properties

2.1 Introduction

This chapter introduces the relevant background for the III-nitride materials, $In_xGa_{1-x}N$ and $Al_{1-x}In_xN$, which are the subject of this thesis. The fundamental material, optical and electrical properties of III-nitride semiconductors determine their utility and applications in optoelectronics. $In_xGa_{1-x}N$ and $Al_{1-x}In_xN$ samples investigated in this work are grown by metalorganic chemical vapour deposition (MOCVD). This chapter begins with an outline of the growth technique. Challenges associated with growth of the different III-nitride compounds will be highlighted, and the structure of the samples studied, including their crystal and energy band structure are discussed. Finally, the optical properties of III-nitrides will be presented and important issues in the areas will be addressed.

2.2 Growth of III-Nitrides

Due to the extremely high melting temperatures and equilibrium pressures of the binary compounds, it is very difficult to grow III-nitrides from their stoichiometric melts using techniques such as the Czochralski method [1-2]. The melting temperatures [2] of GaN, InN and AlN are shown in Table 2.1, along with the approximate temperatures for the onset of decomposition [3]. Hence, growth techniques involving low pressure and temperature are employed. As mentioned above, the technique used in this work is MOCVD.

Table 2.1 Melting temperatures [2] and decomposition temperatures [3] of GaN, InN and AlN.

Binary Compound	Melting Temperature (°C)	Decomposition Temperature (°C)
GaN	2500	850
InN	1900	630
AlN	3200	1040

2.2.1 Metalorganic Chemical Vapour Deposition (MOCVD)

Metalorganic chemical vapour deposition, also known as metalorganic vapour phase epitaxy (MOVPE), has developed over the past years as the most commonly used method for the epitaxial growth of commercial III-nitride materials [4-5]. It is chosen over other methods such as molecular beam epitaxy (MBE) because of its ability to be scaled up to industrial-scale production with relative ease. In contrast to MBE, the growth of crystals takes place not in a vacuum, but from the gas phase at moderate pressures (0.02 to 1 bar).

The reactive elements required for the MOCVD growth are produced by the thermal decomposition of source gases which are heated above a substrate and chemically react producing the nitride compound. This process requires organo-metallic source materials (precursors) of high purity. Typically (and in all cases in this thesis) for GaN, $In_xGa_{1-x}N$ and $Al_{1-x}In_xN$ production, the precursors used are trimethylgallium (TMGa or $Ga(CH_3)_3$), trimethlyaluminum (TMAl or $Al(CH_3)_3$) and trimethylindium (TMIn or $In(CH_3)_3$) to provide gallium, aluminium and indium respectively. Ammonia (NH_3) is used as the source material for nitrogen. The stoichiometric expressions describing GaN, $In_xGa_{1-x}N$ and $Al_{1-x}In_xN$ growth are as follows:

$$Ga(CH_3)_3 + NH_3 \rightarrow GaN + 3CH_4 \qquad (2.1)$$

$$x.In(CH_3)_3 + (1-x).Ga(CH_3)_3 + NH_3 \rightarrow In_xGa_{1-x}N + 3CH_4 \qquad (2.2)$$

$$x.In(CH_3)_3 + (1-x).Al(CH_3)_3 + NH_3 \rightarrow Al_{1-x}In_xN + 3CH_4 \qquad (2.3)$$

A typical MOCVD growth reactor system is represented in Figure 2.1. The TMGa, TMIn and TMAl are stored in separate containers called bubblers. Here a carrier gas (usually hydrogen (H_2), nitrogen (N_2) or an H_2/N_2 mixture) is bubbled through these precursors, which picks up some metalorganic vapour and transports it to the heated reactor chamber. Ammonia is also introduced directly into the chamber from a separate gas cylinder. It is important to keep the group III precursors and the ammonia separate as long as possible in order to avoid pre-reactions. Any prior interactions (also known as parasitic reactions), particularly between Al and ammonia, would lead to adduct formation in the gas phase and prevent efficient and high quality crystal growth. The reagent separation plate in the inlet end of the reactor is used to prevent pre-reaction of the group III sources and ammonia. The growth rate of the epilayers can be estimated through *in situ* reflectometry [6]. This involves reflecting laser light off the surface of the growing layer. Oscillations occur in the reflected intensity due to constructive and destructive interference of the light reflecting from surfaces at different depths and these are used to determine layer thickness [6]. This technique can only be used for structures in which there is refractive index contrast between differing layers.

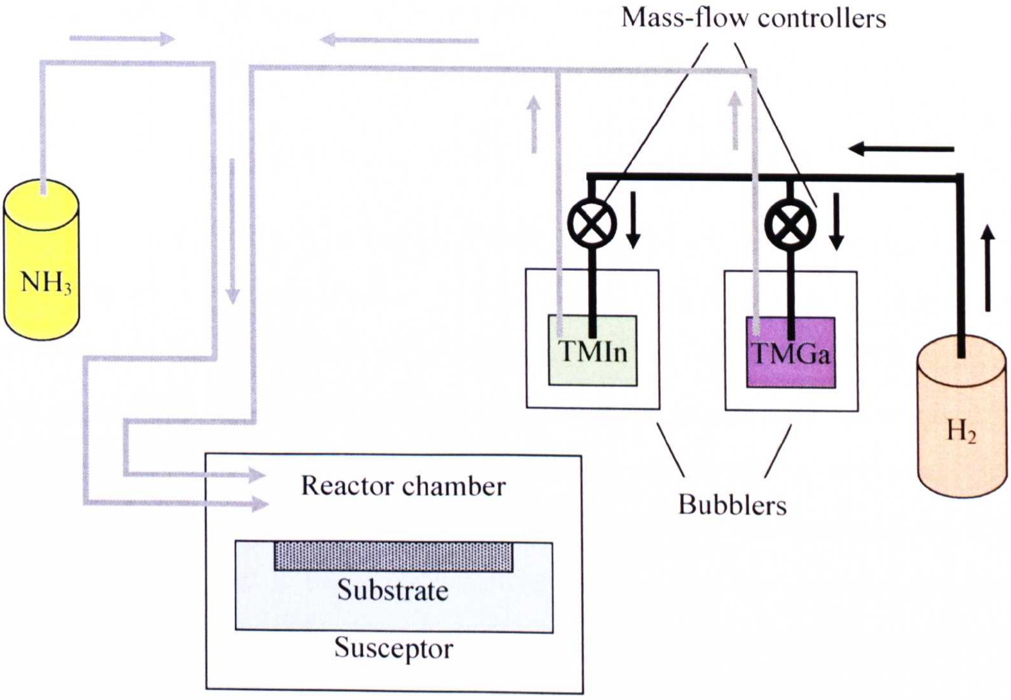

Figure 2.1 Schematic view of a MOCVD growth reactor system for $In_xGa_{1-x}N$.

The samples studied in this thesis were grown by several collaborators. The majority of the samples were from Dr. Ian Watson of the Institute of Photonics at Strathclyde University as well as samples grown at the Department of Materials Science and Metallurgy from University of Cambridge by Thomas Sadler, Dr. Menno Kappers and Dr. Rachel Oliver, at CRHEA-CNRS, Valbonne, France by Dr. H. P. David Schenk and commercially from a LED wafer supplier. N_2 was used as the carrier gas for $In_xGa_{1-x}N$ growth, $Al_{1-x}In_xN$ growth, and for thin GaN layers grown in heterostructures (in this case, for GaN quantum wells (QWs) with $Al_{1-x}In_xN$ barriers, plus barrier and cap layers in $In_xGa_{1-x}N$-based QWs structures). This is because the presence of H_2 inhibits indium incorporation. H_2 was used as the carrier gas for growth of GaN buffer layers, which allows faster growth rate.

2.2.2 Challenges Associated with Growth of III-Nitrides

Despite the fact that commercial nitride based optoelectronic devices are readily available, growth of high quality nitride structures is complicated. The main problems associated with III-nitrides growth are (i) the extreme differences in physics and chemical properties between the binaries GaN, InN and AlN; and (ii) the lack of suitable substrates for homoepitaxial growth, which will be further discussed in **Section 2.5.3**.

For $In_xGa_{1-x}N$, it is difficult to incorporate indium and nitrogen into the material at the same time. As shown earlier in Table 2.1, InN has a low decomposition temperature and the equilibrium vapour pressure of N_2 over InN is high. Hence, this puts an upper limit on the temperature that can be used. However, due to the high stability of the ammonia molecule, its cracking efficiency is very poor at low temperatures. Thus, a high V/III ratio is required to avoid the formation of nitrogen vacancies. Furthermore if the growth temperature is too low, indium droplets can form on the film surface [7]. These act as sinks for additional indium and severely degrade the film quality. Droplet formation can be suppressed by using nitrogen as a carrier gas instead of hydrogen [2]. The typical MOCVD growth temperature for $In_xGa_{1-x}N$ is ~ 800 °C compared to over 1000 °C for GaN.

As for $Al_{1-x}In_xN$ structures, the difficulties in growing layers of sufficient quality include the large immiscibility gap and difference in the thermal stability between AlN and InN. As discussed above, In-containing layers are grown at low temperatures and high V/III ratio, in contrast to Al-containing layers which are grown at high temperatures and reduced V/III ratios [8]. There is a need to balance the low temperature demands for In incorporation with the higher temperature needed for sufficient surface mobility of the Al adatoms. Moreover, the large difference in bond lengths in $Al_{1-x}In_xN$ leads to the prediction of a miscibility gap in these alloys [9] which may lead to phase separation and compositional inhomogeneities [8-9]. The best $Al_{1-x}In_xN$ quality is obtained close to lattice match to GaN [10-11].

2.2.3 Dopants

Usually, GaN material without any intentional doping (or non-intentional-doped) is lightly *n*-type with a carrier background of 10^{15} to 10^{16} cm^{-3}. However, devices require intentional doping for highly doped *n*-type and *p*-type layers in order to raise or control the density of carriers that are involved in current flow. Silicon (Si) is commonly used as *n*-type dopant in GaN since it effectively incorporates on the gallium site and forms a single shallow donor level, with a low activation energy of around 20 meV. Thus, this allows almost complete donor activation at room temperature. Magnesium (Mg) is widely used as *p*-type dopant. However, post-growth activation is required to dissociate Mg-H complexes incorporated in as-grown material and has a high activation energy of approximately 200 meV. Hence, in order to get hole concentrations in the mid-10^{17} cm^{-3} range, Mg atom concentrations must approach the solid solubility limit (~ 10^{20} cm^{-3} in GaN [12]).

2.3 Crystal Structure

The III-nitride semiconductors can occur in two common crystal structures: the wurtzite (hexagonal) and zincblende (cubic) structures as shown in Figure 2.2. The wurtzite structure is more common as it is easier to grow and is thermodynamically stable [2, 5, 8] hence giving better results in optoelectronic devices [13]. In this thesis, all the samples under investigation have the wurtzite structure.

Crystallographically, the wurtzite and zincblende structures are very similar with tetrahedral bonding to the next nearest neighbours. The wurtzite structure can be thought of as a sequence of layers of atoms of the same elements built up from regular hexagons where the Bravais lattice is hexagonal. The hexagonal unit cell has two lattice constants, *c* and *a*. The *c*-axis is the principal axis of rotational symmetry and is usually the growth axis of III-nitride materials in most cases. There is also an internal cell parameter u which is defined as the ratio of the length of the III-nitride chemical bond parallel to the c-axis to the c lattice constant. The ideal values for u and c/a for the wurtzite structure are $3/8 = 0.375$ and $\sqrt{8/3} = 1.633$, respectively. The lattice parameters obtained experimentally for GaN [14], InN [15] and AlN [16] are listed in Table 2.2. The deviations of experimental values of the lattice parameters from ideal values are due to the asymmetry in atomic charge distribution which is induced by the lack of a centre of symmetry [17].

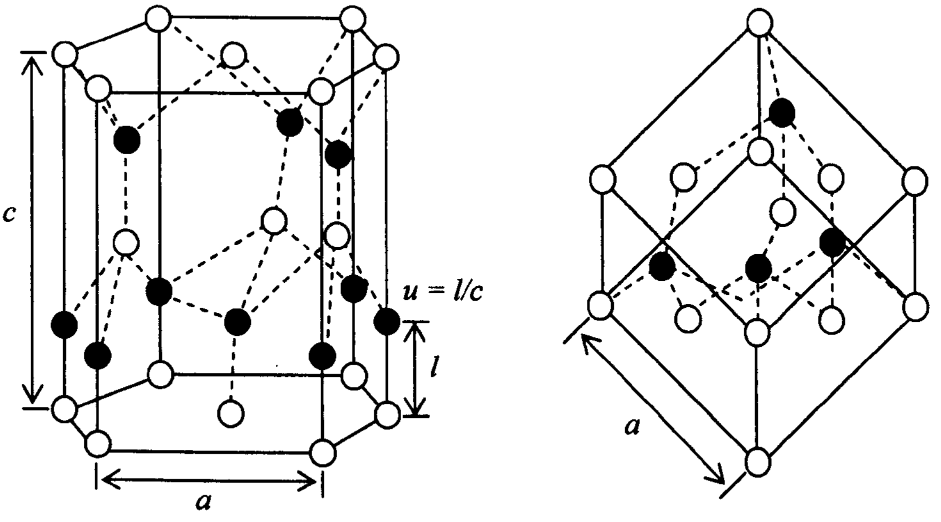

Figure 2.2 Crystal structures of III-Nitrides: Wurtzite (left) and Zincblende (right). The white circles represent group III atoms and the black are nitrogen [2, 13].

Table 2.2 Lattice parameters of GaN [14], InN [15] and AlN [16].

Material	a (Å)	c (Å)	c/a	u
GaN	3.189	5.185	1.626	0.3768
InN	3.538	5.704	1.612	0.3790
AlN	3.111	4.98	1.601	0.3819

The random ternary alloys of binary semiconductors, $A_xB_{1-x}C$ alloys, are expected to follow Vegard's law [18] whereby the lattice constant varies linearly with composition between the binary constituents AB and AC:

$$a(x) = x.a(AC) + (1-x).a(BC) \tag{2.4}$$

$$c(x) = x.c(AC) + (1-x).c(BC) \tag{2.5}$$

However, a deviation from Vegard's law for the lattice constant has recently been reported in some of the III-nitride alloys by K. Lorenz *et. al.* [19] and V. Darakchieva *et. al.* [20]. K. Lorenz *et. al.* observed that the measurement of strain by Rutherford Backscattering/Channeling (RBS/C) in combination with Monte Carlo (MC) simulations give excellent agreement with x-ray diffraction (XRD) data but significant differences are revealed in the measured $Al_{1-x}In_xN$ compositions. This discrepancy can be eliminated by introducing a correction to Vegard's law. Also, V. Darakchieva *et. al.* have studied the lattice parameters and strain evolution in $Al_{1-x}In_xN$ films with $0.07 \leq x \leq 0.22$ grown on GaN-buffered sapphire substrates by MOCVD using reciprocal space mapping. Strain in the Al-rich $Al_{1-x}In_xN$ films is found to affect the differences between the In contents determined by XRD and Rutherford backscattering spectrometry (RBS) for highly strained pseudomorphic films, suggesting a strain-driven deviation of the lattice parameters from Vegard's rule in this case. On the other hand, a good agreement between the In contents determined by XRD and RBS is found for $Al_{1-x}In_xN$ films with low degree of strain or partially relaxed, suggesting applicability of Vegard's rule in the narrow compositional range around the lattice matching to GaN. These findings suggest that the experimentally observed deviations from Vegard's rule may depend on the growth technique and conditions, material properties, strain and composition range.

2.4 Energy Band Structure

When atoms condense to form a solid, their discrete atomic energy levels transform into energy bands due to Pauli's Exclusion Principle. The energy band structure determines the optical and electrical properties of semiconductors. All wurtzite nitrides are direct band gap semiconductors, meaning the minimum conduction band energy and the maximum valence band energy occur at the same value of crystal momentum k [21]. Hence, the fundamental optical transitions of lowest energy occur at the same point of the Brillouin zone, namely Γ-point ($k = 0$).

2.4.1 GaN

The valence band in GaN is split into three bands due to the crystal field interaction and spin-orbit interactions [22-23]. They are denoted as $A(\Gamma^v_9)$, $B(\Gamma^v_7)$ and $C(\Gamma^v_7)$.

Figure 2.3 shows the calculated band structure of GaN [22]. The holes (and excitons) associated with $A(\Gamma^{v}{}_{9})$, $B(\Gamma^{v}{}_{7})$ and $C(\Gamma^{v}{}_{7})$ bands are called A-, B- and C-type holes (or excitons).

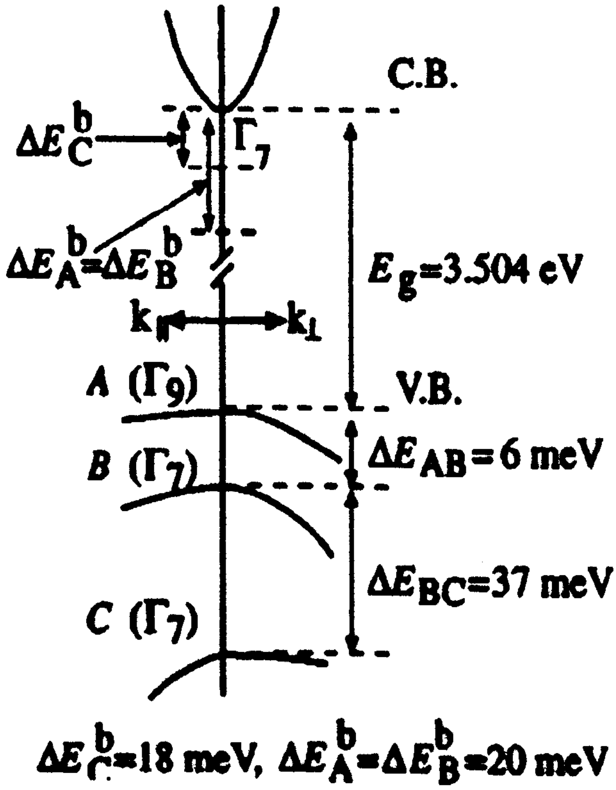

Figure 2.3 Calculated band structure of wurtzite GaN at 10 K [22]. The symbols 'C.B.' and 'V.B.' stand for conduction band and valence band, respectively.

2.4.2 InN

Early research had yielded a band gap of about 1.89 eV [24] in polycrystalline InN samples. With the improvement in the growth techniques, good quality InN films can now be produced. Recent measurements suggest that the band gap of wurtzite InN is below 1 eV, i.e. around 0.68 to 0.80 eV [25-27] much smaller than the earlier accepted value. The discrepancy between 0.68 to 0.8 eV is attributed to the use of different approaches for modelling the spectral response around the absorption edge and to shifts due to band gap renormalisation (BGR) and/ or Burstein–Moss (BM) type conduction band filling [27-28]. Figure 2.4 shows the calculated band gap structure of InN. The valence band ordering in InN is the same as GaN [26].

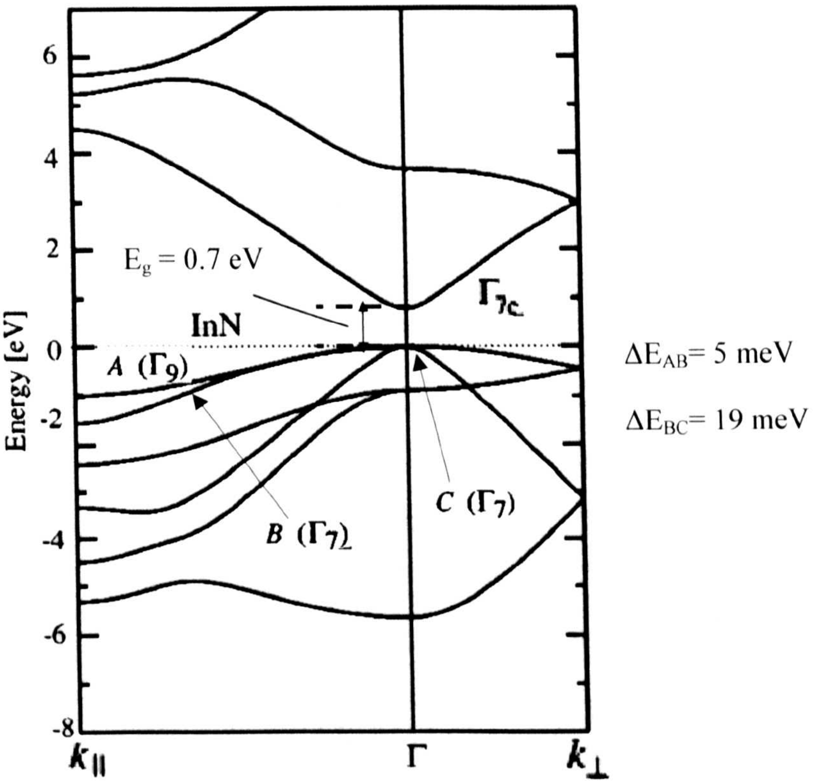

Figure 2.4 Calculated band structure of wurtzite InN [26]. The sign ⊥ (||) denotes the direction perpendicular (parallel) to the *c* axis of the InN epilayer.

2.4.3 AlN

AlN is the only wurtzite semiconductor compound that has been predicted to have a negative crystal field splitting at the top of valence band [29-31], and this is confirmed through experiments [32]. Figure 2.5 shows the calculated band structure of AlN. By comparing with the band structure of GaN, the most significant difference is the negative crystal-field splitting in AlN (-217 meV) instead of a positive value (42 meV) in GaN [31]. It is because the order of the valence bands in AlN is different from that of GaN. The valence bands, given in increasing order of their transition energies, are $A(\Gamma^{v}_{7})$, $B(\Gamma^{v}_{9})$ and $C(\Gamma^{v}_{7})$ for AlN, whereas in GaN the order is $A(\Gamma^{v}_{9})$, $B(\Gamma^{v}_{7})$ and $C(\Gamma^{v}_{7})$.

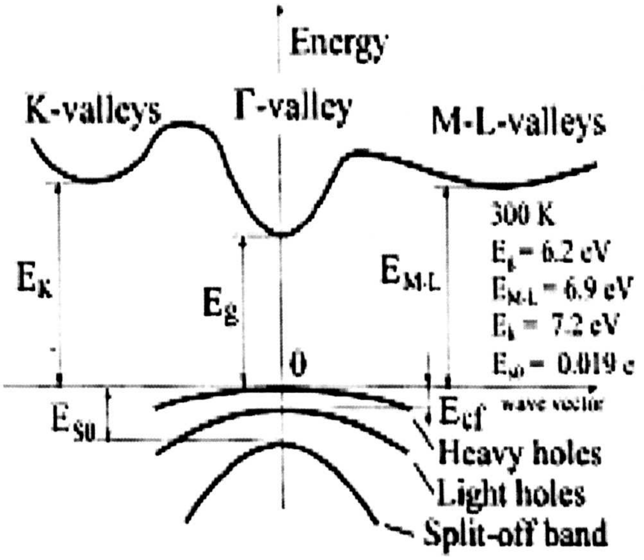

Figure 2.5 Calculated band structure of wurtzite AlN at 300 K [29].

The band gap energies of $A_xB_{1-x}C$ alloys can be expressed as follows:

$$E_g(A_xB_{1-x}C) = x.E_g(AC) + (1-x).E_g(BC) - b.x.(1-x) \tag{2.6}$$

where b denotes the bowing parameter accounting for the deviation from a linear interpolation between the two binaries AB and BC. The bowing parameter is always positive for the ternary alloys $In_xGa_{1-x}N$, $Al_{1-x}In_xN$ and $Al_yGa_{1-y}N$, which reflects a reduction of the alloy energy gaps. For $In_xGa_{1-x}N$, recent band gap data give a relatively small bowing parameter of 1.43 eV [25, 33]. A bowing parameter as large as 2.6 eV was needed when the band gap of InN was determined as 1.9 eV earlier [34]. For $Al_{1-x}In_xN$ alloys, the bowing parameter is reported to be 6.2 eV [35].

2.5 Sample Structures

The $In_xGa_{1-x}N$ and $Al_{1-x}In_xN$ structures investigated in this thesis are epilayers and single quantum wells (SQWs). The substrates used are *c*-plane (0001) sapphire, free-standing (FS)-GaN and $Al_yGa_{1-y}N$ templates with AlN molar fraction y ranging up to 23.4 %. The latter were purchased commercially from TDI Inc. [36].

2.5.1 Epilayers

An epilayer is a single crystal layer of material grown on the surface of another single crystal material (called the substrate) [21]. When such a layer is grown on a substrate of the same material, the process is known as homoepitaxy [37]. This is the best way to obtain high quality epilayers. However, this is not always possible, as is the case with the nitrides due to high melting temperatures and corresponding high nitrogen equilibrium pressures. Hence, the growth is usually carried out on substrates of a different material. This process is known as heteroepitaxy [37]. In order to obtain a good quality epilayer, nucleation and buffer layers are grown before the epilayer as illustrated in Figure 2.6. A discussion about the nucleation and buffer layers is presented in the next section **2.5.2**.

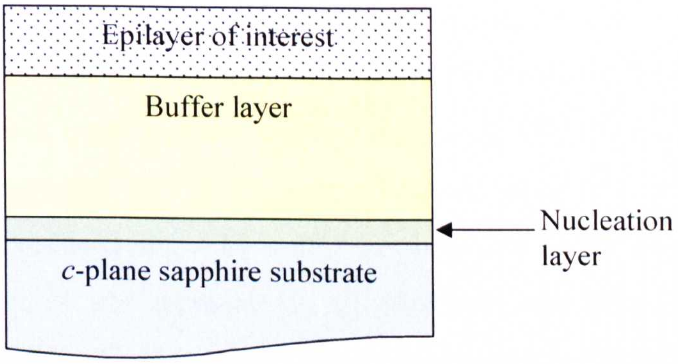

Figure 2.6 **Schematic diagram of an epilayer structure on *c*-plane sapphire substrate.**

The state of strain in the material has been shown to be dependent on the thickness of the epilayer [38]. It can be grown either pseudomorphically strained, relaxed or a mix of both. Pseudomorphic growth is where the in-plane lattice constant of one epilayer matches that of the material it is grown on. In the case of $In_xGa_{1-x}N$, the material undergoes compressive strain to match the smaller lattice constant of its GaN buffer layer. It has been reported that beyond a certain layer thickness, called the critical thickness (h_c), no more strain can be accommodated in the lattice [38]. At this point, defects and dislocations form and the $In_xGa_{1-x}N$ layer begins to relax. An estimated value for the critical thickness in $In_xGa_{1-x}N$, with InN content of 15 % is $\approx$ 65 nm [39].

It has been found that the polarity of the GaN buffer layer can affect the luminescence efficiency of $In_xGa_{1-x}N$ [40]. The polarity is dependent on the growth technique used. In MOCVD samples Ga-faced polarity films are generally obtained, while in MBE material N-faced polarity is predominant. The $In_xGa_{1-x}N$ on Ga-faced polarity film was found to have better crystalline quality and more efficient luminescence than that grown on the N-faced polarity films [40].

2.5.2 Substrates

As mentioned earlier, III-nitrides are mainly obtained by epitaxial growth on various substrates. Sapphire is most commonly used as it is readily available, low cost, transparent, thermally stable, good crystalline quality and has high thermal conductivity [3, 6]. Other possible substrates include silicon carbide (SiC) and silicon (Si). However, there are major drawbacks in the form of high degree of lattice and thermal mismatch between them and the nitride compounds. For example, the in-plane lattice mismatch between GaN and *c*-plane (0001) sapphire is ~ 16.1 %. This lattice mismatch can be reduced slight by a 30 ° in plane rotation of the III-nitride lattice compared to that of the sapphire [3, 6]. However the degree of lattice mismatch remains high. When GaN is grown directly on sapphire, the strain induced by the lattice mismatch is partially relaxed by the formation of 3D islands resulting in low quality material with rough surfaces.

In order to produce good quality film, a two-step growth process was introduced by Yoshida *et al.* [41] in 1983 and perfected by Akasaki, Amano and co-workers in later years [42-43]. Nucleation layers of either AlN or GaN are grown at low temperatures (500-600 °C) to reduce the strain between the substrate and film and to promote lateral growth. The optimum thickness of the AlN nucleation layer at 500 °C is ~ 20-50 nm [44]. This is followed by the growth of a buffer layer (GaN or AlN) at high temperature to reduce further the strain and defect density and provide an effective substrate for the final epilayer growth. GaN buffer layers generally consist of many hexagonal columns with similar orientations and the resulting epilayer shows a similar form [1]. The nucleation layer is originally grown as 3D islands but as the growth temperature is increased for the main growth, it recrystallises allowing high quality layers to be formed [6, 44]. Although the two-step growth process leads to GaN layers with smooth crack free surfaces, the different coefficients of thermal expansion between substrate and nitride layer introduce residual stress upon cooling. These induced stresses lead to the formation of threading dislocations which are detrimental to the lifetimes of the laser diodes and the performance of UV devices. One way to reduce such defect density is to grow a thick buffer to further reduce the strain and defect density and provide an effective substrate for the final epilayer growth. Table 2.3 summarises the basic parameters of GaN, InN, AlN, sapphire, SiC and Si.

Table 2.3 Lattice mismatch and thermal expansion coefficients of GaN, InN, AlN, SiC and Si with respect to (w.r.t.) sapphire [13-16, 45].

Material	Lattice constant	In-plane mismatch (w.r.t. sapphire) (%)	Thermal expansion coefficient (x 10^{-6} K^{-1})	Thermal expansion mismatch (w.r.t. sapphire) (%)
GaN	$a = 3.189$ $c = 5.185$	+ 16.1 -	5.59 7.75	-25.5 -8.8
InN	$a = 3.538$ $c = 5.704$	+ 25.9 -	3.90 2.80	-48.0 -67.1
AlN	$a = 3.111$ $c = 4.978$	+ 13.2 -	5.30 4.20	-29.3 -50.6
Sapphire	$a = 4.758$ $c = 12.991$	- -	7.50 8.50	- -
6H- SiC	$a = 3.08$ $c = 15.12$		5.0374	
Si	$a = 5.4301$		3.59	

2.5.3 Quantum Wells

A quantum well (QW) consists of a thin layer of material whose typical thickness is of a few nanometres, being sandwiched between two layers of another wider-gap semiconductor material. Figure 2.7 shows a representation of Type I $In_xGa_{1-x}N$/GaN QW where the electrons and holes are confined in the same layer ($In_xGa_{1-x}N$). The sandwiched material with a smaller band gap is called 'well', and the material at both sides with larger band gap is called 'barrier'. This structure creates a two-dimensional quantum confinement of the excited carriers giving a series of discrete energy levels in the well. The width and depth of the well determines the energy of these levels. In **Chapter 6**, the optical properties of GaN/$Al_{1-x}In_xN$ QWs as a function of well width will be presented.

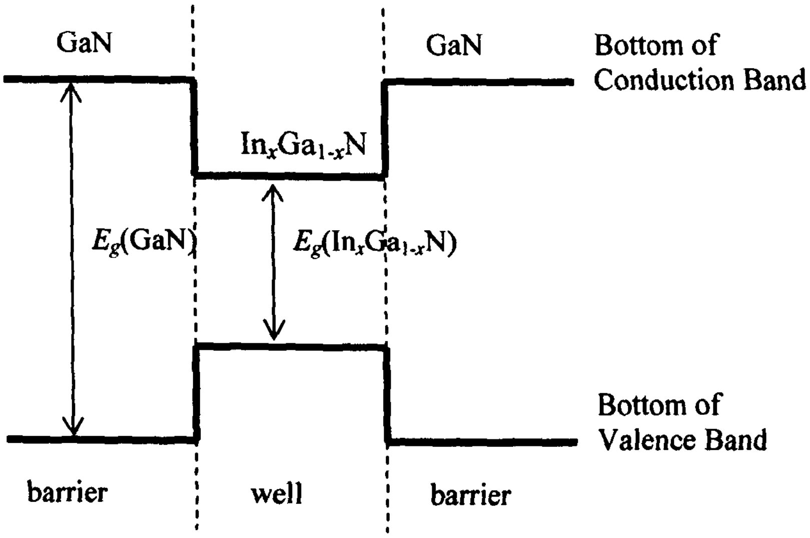

Figure 2.7 **A representation of $In_xGa_{1-x}N$/GaN QW structure. E_g denotes energy gap.**

QW structures with one well are referred to as single quantum wells (SQWs). For a sample with a number of wells where each is separated by a barrier layer, the structure is termed a multiple quantum well (MQW). In a MQW, the barrier has to be sufficiently thick to prevent coupling of carriers between layers, leading the wells to act independently. This effectively amplifies the optical properties of the structure while maintaining the original confinement conditions of a SQW. Typical thicknesses of the well are of the order of a few nm, suggesting that the well layers are grown pseudomorphically with the barrier layer. In this work, SQW structures were employed with well widths varying from 1.5 to 4 nm.

2.6 Luminescence Properties of III-Nitrides

The III-nitrides (AlN, GaN and InN) are a family of semiconductors that crystallise predominantly in the wurtzite (hexagonal) system. They have direct optical band gaps: AlN of 6.2 eV at 300 K [29]; GaN of 3.5 eV at 10 K [21]; InN of 0.68 eV at 4.2 K [27].

2.6.1 Phonons

Phonons are quanta of the collective lattice vibrations. They play an important role in the luminescence spectrum because in the exciton recombination process, the energy delivered is not only given to the photon but also to the lattice, leading to the so-called phonon sidebands (PSBs). This energy is that of the phonon and its value corresponds to the difference in energy from the main PL peak [zero-phonon line (ZPL)] and the satellite peaks at lower energy in the spectra. The interaction of carriers with phonons is known to strongly affect the optical properties of semiconductors. Among all types of electron-phonon interactions, the Fröhlich interaction which arises from the Coulomb interaction between the carriers and the electric field produced by the longitude optical (LO) phonons, is the dominant one in III-nitride semiconductors due to the strong ionic nature of the chemical bonds [45]. As the LO-phonon Fröhlich interaction is the strongest, usually only the LO phonon replicas are observed. The strong exciton-LO-phonon coupling is manifested by the appearance of phonon-assisted emissions in the photoluminescence (PL) spectrum, as illustrated in Figure 2.8, which show the occurrence of a series of equally spaced emission peaks [i.e. ZPL and LO-PSBs (1LO, 2LO, etc.)] whose intensity decreases as the emission energy decreases.

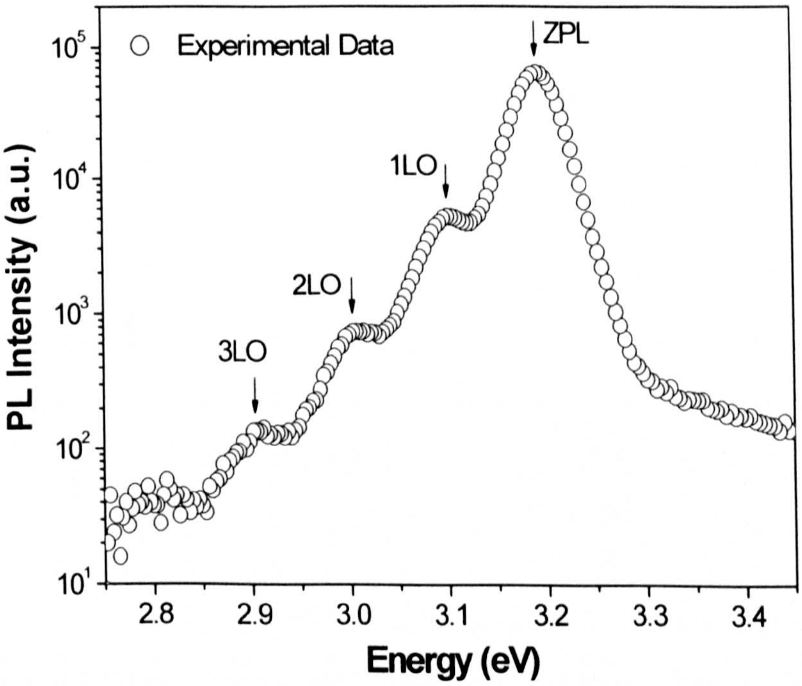

Figure 2.8 **Low temperature (T ≈ 25 K) PL spectrum of the 2.5 nm thick cap $In_xGa_{1-x}N/GaN$ SQW (well width of 2.5 nm) with zero-phonon line (ZPL) and its phonon sidebands (1LO, 2LO, 3LO).**

The distribution of the emission intensities between the main peak and the phonon replicas has been found to depend strongly on the exciton–phonon coupling strength. Within the Franck–Condon approximation, this coupling is expressed by the Huang–Rhys factor S [46-48]. At low temperature, the relationship between the intensity of the n^{th} phonon replica I_n and the main emission I_0 is given by:

$$I_n = I_0 . \frac{S^n}{n!} \qquad n = 0, 1, 2, \ldots \tag{2.7}$$

where the S factor is defined as [45-47]:

$$S = \frac{1}{2h\omega^3 LO} \sum_q | D_q |^2 \tag{2.8}$$

where ω is the frequency associated to the phonon energy and D_q has a magnitude proportional to the q^{th} Fourier transform coefficient of the particle charge distribution, which is related to the degree of localisation. Thus, localised excitons show strong PSBs because their wave function contains large q components which allow them to couple to a wide range of LO phonons.

There are several important aspects to take into account for LO-PSBs, namely, the degree of exciton localisation and the spatial separation of the electron and hole wave functions, enhanced by the intense in-built electric fields (spontaneous and piezoelectric polarisation fields). These factors will be discussed in the following subsections.

2.6.2 Exciton Localisation

An exciton is defined as the bound state of an electron and a hole. Exciton formation can be explained as follows: a photon enters a semiconductor, exciting an electron from the valence band into the conduction band. The missing electron in the valence band leaves a hole behind, of opposite electric charge, to which it is attracted to the electron by the Coulomb force. The exciton results from the binding of the electron with its hole. When an exciton gets trapped in a confined area, it is considered as localised. This is caused mainly by potential fluctuations due to alloy fluctuations, well thickness variations, phase separation, strain inhomogeneities, or localised defect states. For example, due to fluctuation of indium composition within the

$In_xGa_{1-x}N$ layer, excitons can transfer to localised potential minima in real space; local tensile strain reduces the effective band gap, and compressive strain increases it, hence a juxtaposition of these different strains would lead to potential inhomogeneities holding localised states; and for localised defect states, they could be caused by deep donor or deep acceptor-like states [49-50]. Some of these mechanisms are illustrated in Figure 2.9.

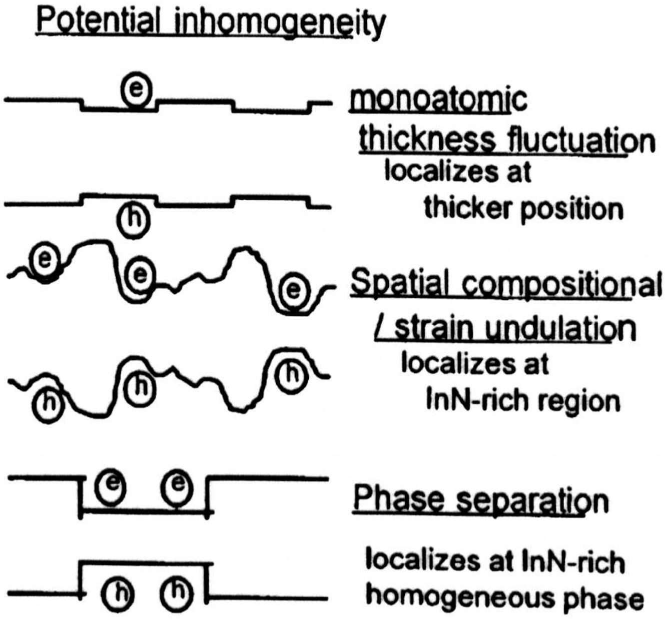

Figure 2.9 Schematic illustrations of some of the origins of the carrier localisation in $In_xGa_{1-x}N$ [50].

Hopfield [51] has shown that in a direct gap semiconductor, an optical transition involving excitons with a well-defined *k* has a vanishing small LO-PSB intensity relative to that of its zero-phonon line (ZPL). This is a direct result of momentum conservation. However, if the recombination of excitons takes place in the field of an imperfection (i.e. localised excitons), the *k* conservation rule can be relaxed. Thus stronger PSBs are expected to be observed in the case of increasingly localised excitons. In other words, the transitions involving weakly localised excitons are expected to show relatively smaller LO-PSBs. Thus, the degree of exciton localisation is related to the strength of the PSBs. Luminescence of PSBs has been used to extract information regarding the degree of exciton localisation in alloys such as GaAs [47], GaInP [52] and $In_xGa_{1-x}N$ [53].

The form of LO-PSBs in the PL spectra of $In_xGa_{1-x}N$/GaN quantum wells with variations in InN fraction, PL peak energy, and number of wells were described in Ref. 54. The Huang-Rhys factors were shown to decrease linearly with PL peak energy. At the same time the difference between the S factor for transitions involving the ZPL and those for higher satellites was shown to decrease. These observations were related to increasing localisation with InN content in the wells. The temperature dependence of these differences between successive S factors for an $In_xGa_{1-x}N$/GaN multiple quantum well has also been discussed in terms of exciton localisation [53]. Modelling of the PSBs in $In_xGa_{1-x}N$ QW and quantum dots of different dimensions led to discussions of the offsets between the electron and hole wave functions [55-56]. Later work fitted the PSBs in a series of $In_xGa_{1-x}N$/GaN QWs to a single S factor and used theoretical modelling in combination with TEM observation to argue that well-width fluctuations were the primary source of exciton localisation on a length scale of approximately 2 nm [57].

2.6.3 Spontaneous and Piezoelectric Polarisation Fields

In the following the influence of spontaneous and piezoelectric polarisation on the physical properties of III-nitrides will be discussed. This class of polarisation related properties is important for devices because the electric fields influence the shape of the band edges and the carrier distribution inside nitride-based heterostructures. Therefore spontaneous and piezoelectric polarisation can influence the radiative recombination in light-emitting devices [3]. In the absence of external electric fields, the total macroscopic polarisation P of a material is the sum of the spontaneous polarisation P^{SP} in the equilibrium lattice and the strain-induced or piezoelectric polarisation P^{PE}.

Ambacher *et. al.* [58] explained a large spontaneous polarisation (P^{sp}) is present due to the lack of inversion symmetry of the wurtzite structure and the ionic nature of the covalent-nitrogen bond. The orientation of P^{sp} depends on the polarity of the material

[59-60]. This is in turn determined by the substrate- and preparation-dependent growth face [N-face, i.e. (000-1) surface up and Ga-face, i.e. (0001) surface up] [61], and growth techniques as mentioned in **Section 2.5.2.**

Lattice and thermal mismatch in epitaxial materials is commonly present, especially in wurtzite III-V materials. For instance, $Al_yGa_{1-y}N$/GaN QWs are usually epitaxially grown on GaN buffer layers along the crystal axis (0001), using sapphire as the substrate. The $Al_yGa_{1-y}N$ layers, which have smaller lattice parameters than GaN, are under tensile strain while the GaN layers remain unstrained. Thus, piezoelectric fields P^{PE} are introduced into the barrier layers. Following Bernardini *et. al.* [59], P^{PE} can be calculated by using the piezoelectric coefficients e_{33} and e_{31} as:

$$P^{PE} = e_{33}.\epsilon_z + e_{31}.(\epsilon_x + \epsilon_y) \tag{2.9}$$

where a_0 and c_0 are the equilibrium values of the lattice parameters, $\epsilon_z = (c - c_0)/ c_0$ is the strain along the *c*-axis (0001), and the in-plane strain $\epsilon_x = \epsilon_y = (a - a_0)/ a_0$. Table 2.4 lists the calculated spontaneous polarisation and piezoelectric constants for III-V wurtzite nitrides [62].

Table 2.4 Calculated spontaneous polarisation fields (P^{sp}) and piezoelectric constants (e_{33} and e_{31}) for III-nitrides [62].

Material	**P^{sp} (C/m^2)**	**e_{33} (C/m^2)**	**e_{31} (C/m^2)**
GaN	-0.034	0.67	-0.37
InN	-0.042	0.81	-0.45
AlN	-0.09	1.5	-0.62

The strain acting on the material determines the direction of the piezoelectric polarisation. For compressively strained $In_xGa_{1-x}N$, both spontaneous and piezoelectric polarisations are orientated along the hexagonal *c*-axis. For a layer under tensile strain (e.g. $Al_yGa_{1-y}N$ on GaN), the piezoelectric polarisation points along $(000\bar{1})$. Hence, it is clear that the two components (P^{SP} and P^{PE}) can add or cancel each other depending on the strain and polarity. Hence, the total electric field (E) is:

$$E = \frac{(P^{sp} \pm P^{z})}{\varepsilon_0 . \varepsilon_r} \tag{2.10}$$

where ε_0 is the permittivity of free space (8.85×10^{-12} F/m) and ε_r is the dielectric constant of the material.

These fields significantly influence the distribution and lifetime of excess carriers in $In_xGa_{1-x}N$ and GaN QWs and can have an important impact on the performance of the devices. The influence of the electric field on the recombination process can be described using the quantum-confined Stark effect (QCSE) as illustrated in Figure 2.10.

(a) **quantum confinement in SQWs**

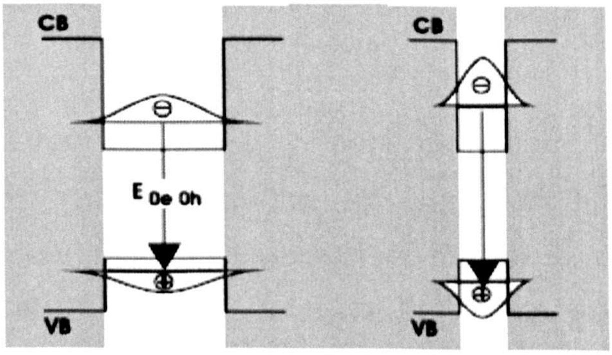

(b) **Stark effect**

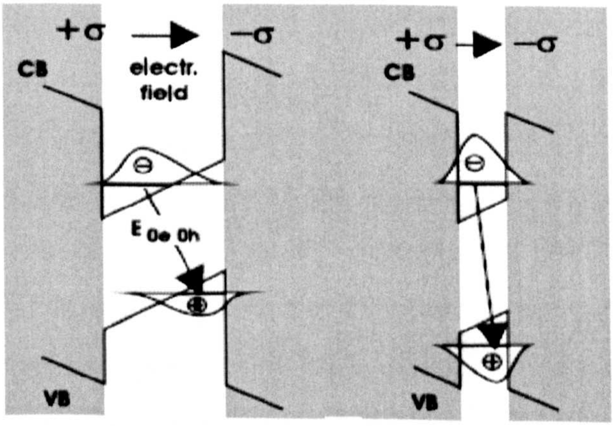

Figure 2.10 Schematic drawing of the band edge profiles of two QWs with different thicknesses under (a) quantum confinement and (b) quantum confined stark effect (QSCE) [60].

The radiative recombination between the hole and electron ground levels inside the rectangular QW is increasing in energy with decreasing well width due to quantum confinement (Figure 2.10(a)). The optical transition is blue shifted in energy. In the presence of a polarisation-induced electric field, the shape of the rectangular well has to be replaced by a triangular QW in which the recombination of the photogenerated electron–hole pairs is red shifted in energy due to the QCSE effect (Figure 2.10(b)). With increasing well width, the transition energy decreases as a result of QCSE. The PL lifetime also shows large well width dependence, varying from sub-ns to more than μs if the well-width increases from 2 to 7 nm [63]. This is because the QCSE results in the separation of wavefunctions between electron and hole, resulting in a reduction of the oscillator strength as the well width increases. It is also important to note that the transition energy tends to blue-shift as the injected carrier density increases, which is a result of screening effect of the internal electric field by charged carriers.

There has been controversy on the emission mechanism in $In_xGa_{1-x}N$-based semiconductors. Some reports claim that the large Stokes-like shift between absorption and emission is due to the effect of exciton localisation caused by inhomogeneous distribution of indium in $In_xGa_{1-x}N$ [64]. On the other hand, some groups have reported it is due to the quantum confined Stark effects [65], which are induced by the large internal electric fields whose origins are piezoelectric effects. The ideas of exciton localisation and piezoelectric fields are not in contradiction and may be thought of as influencing each other. The presence of a localisation site, such as a QD, could affect the strain acting on the material and subsequently affect the piezoelectric field induced. Similarly, the piezoelectric field could affect the recombination process in the localisation site by means of the QCSE. The degree of exciton localisation and the contribution from internal electric fields differs from samples because of the difference in growth conditions. Their relative contributions are hard to separate but the SQW samples with varying cap thickness are shown to provide some details as discussed in **Chapter 5.**

2.6.4 Band Gap Tailoring of Heavily Doped III-Nitrides

As previously mentioned, III-nitrides can be doped with various impurities such as Si or Mg to obtain the required doping concentration and resistivity. Usually Si is used as the *n*-dopant due to its relative ease of doping and availability. Doping can influence the band gap measured optically from QWs in a number of ways by making it larger or smaller in comparison to the original host crystal as shown in Figure 2.11. In a heavily doped *n*-type semiconductor, the donor electrons partly fill the conduction band resulting in widening of band gap as shown in Figure 2.11(b). The band gap widening is counteracted by a narrowing associated with different many-body effects on the conduction and valence bands as shown in Figure 2.11(c).

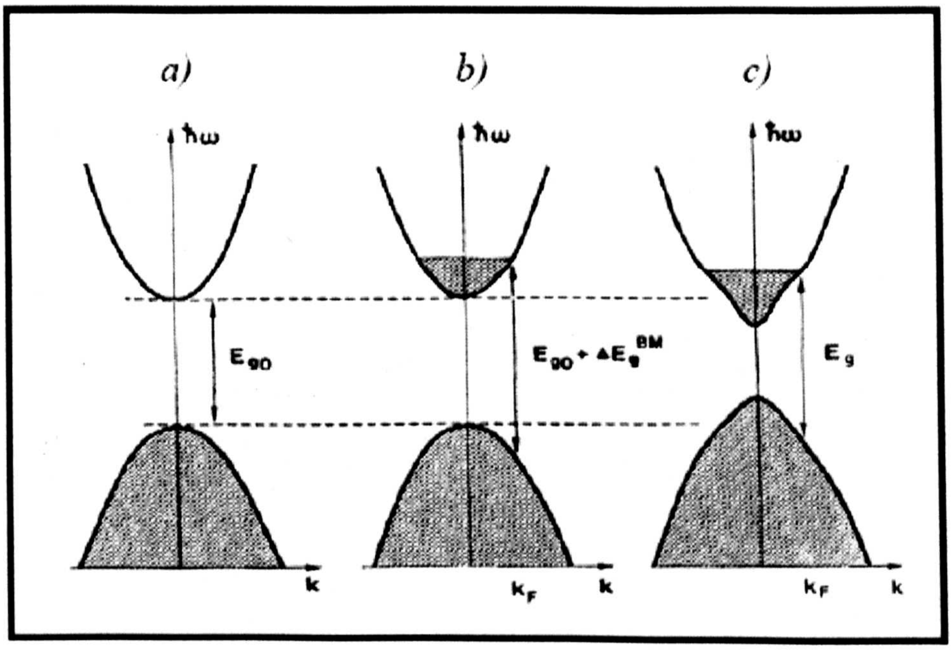

Figure 2.11 (a) Schematic band structure with parabolic conduction and valence band separation defined by E_{go}, (b) optical gap widening due to the Burstein-Moss (BM) shift and, (c) representation of a perturbed band structure and ensuing optical gap E_g in the case of many body interactions. The shaded areas denote the occupied states. The Fermi wave vector k_F is indicated [66].

A more detailed discussion will now focus on the band gap widening and narrowing. Band-filling describes the occupation of electron bands by carriers (or hole bands depending on the type of dopants). If the absorption properties are studied then band-filling has, of course, an influence on the observed absorption edge. Due to the Pauli-exclusion principle for electrons, the absorption into the occupied states is not possible. Therefore, the absorption edge is blue-shifted to higher energies due to the lack of empty states in the conduction band. This observation of such a shift in absorption edge is known as the Burstein-Moss (BM) shift [67-68]. Also, due to the band-filling, there are now a lot of electrons in the conduction band with different *k*-vectors. If the valence band has a small curvature (high hole mass), the photo-excited holes are found over a larger *k*-range. This means that the electrons with a certain *k*-vector can recombine with these holes, under *k*-conservation rule. Hence, a blue-shift in energy can also be observed from the emission spectrum [69].

Band gap narrowing occurs when the carrier density is above the critical Mott density. The critical Mott density [70] is defined as the carrier density at which the semiconductor–metal transition occurs. It is known to be inversely proportional to the cube of the effective Bohr radius of the donor [71-72]. A modification of electronic states begins to appear in the crystal where the exchange and correlation energies renormalise the band gap energy, resulting in an energy downshift of the conduction band edge and an energy upward shift of the valence band edge [72-75]. Such band gap narrowing due to many-body effects arising from the presence of free carriers is known as band gap renormalisation (BGR). The BGR effect has to be treated by many-body theory, since the energy seen by a carrier depends upon the presence of other electrons and holes. Electrons and holes are charged particles with Coulomb forces acting between them. At low densities, this interaction does not play any role. At high densities however it becomes more and more important. Jain and Roulston [75] reported general equations for BGR for *n*- and *p*-type Si, Ge and GaAs layers. The equations are derived by identifying the exchange energy shift of the majority band edge (*A*), correlation energy shift of the minority band edge (*B*), and impurity interaction shifts (*C*) of the two band edges:

$$\Delta E_g(BGR) = A.n^{1/3} + B.n^{1/4} + C.n^{1/2} \tag{2.11}$$

where n is the carrier concentration.

This BGR effect is competitive with the band-filling effect. These effects are of great importance in determining optical properties and device performances since they play significant roles in affecting the energy gap in intentionally doped semiconductors. Their relative contributions on the energy gap will be discussed further in **Chapter 6**.

2.7 Summary

In this chapter, a brief description of the growth technique used, the crystal structure, energy band gap, and an outline of the structures of the samples investigated were presented. Furthermore, the main theories currently proposed to explain the exciton recombination process and subsequently the luminescent properties of III-Nitrides were discussed. The discussion was split into three main parts: localisation of the exciton, the effects of spontaneous and strain-induced piezoelectric fields, and band gap tailoring due heavy doping.

2.8 References

[1] B. Gil, *Low-Dimensional Nitride Semiconductors*, Oxford University Press, New York (2002).

[2] J. H. Edgar, S. Strite, I. Akasaki, H. Amano, and C. Wetzel, *Properties, Processing and Applications of GaN and Related Semiconductors*, EMIS Datareview No. 23, INSPEC London (1999).

[3] O. Ambacher, J. Phys. D: Appl. Phys. **31**, 2653 (1998).

[4] J. H. Edgar, *Gallium Nitride and Related Semiconductors*, No 23, EMIS Datareview, INSPEC, London (1998).

[5] I. M. Watson, Lecture Notes, *Semiconductor Thin Film Growth Techniques*, Class 12-902, University of Strathclyde (2003).

[6] S. C. Jain, M. Willander, J. Narayan, R. van Overstraeten, J. Appl. Phys. **87** 965 (2000).

[7] E. L. Piner, F. G. McIntosh, J. C. Roberts, M. E. Aumer, V. A. Joshkin, S. M. Bedair, and N. A. El-Masry, MRS Internet J. Nitride Semicond. **Res. 1**, 43 (1996).

[8] S. Keller, and S. P. DenBaars, J. Crystal Growth **248**, 479 (2003).

[9] T. Matsuoka, Appl. Phys. Lett. **71**, 105 (1997).

[10] J.-F. Carlin, C. Zellweger, J. Dorsaz, S. Nicolay, G. Chritmann, E. Feltin, R. Butte, and N. Grandjean, Phys. Stat. Sol. (B) **242**, 2326 (2005).

[11] J. Li, K. B. Nam, K. H. Kim, J. Y. Lin, and H. X. Jiang, Appl. Phys. Lett. **78**, 61 (2001).

[12] C. J. Deatcher, K Bejtka, R W Martin, S Romani, H Kheyrandish, L M Smith, S A Rushworth, C Liu, M G Cheong, and I M Watson, Semicond. Sci. Technol. **21** 1287 (2006).

[13] S. Nakamura, S. Pearton and G. Fasol, *The Blue Laser Diode: The Complete Story*, 2nd Ed., Springer, Berlin (2000).

[14] Michael S. Shur and M. Asif Khan, MRS. Bull. **22** (2), 44 (1997).

[15] W. Paszkowicz, R. Cerny, and S. Krukowski, Powder Diffr. **18**, 114 (2003).

[16] M. Tanaka, S. Nakahata, K. Sogabe, H. Nakata, and M. Tabioka, Jpn. J. Appl. Phys., Part 2 **36**, L1062 (1997).

[17] J. D. Joannopoulos, and M. L. Cohent, J. Phys C: Solid State Physics **6**, 1572 (1973).

[18] L. Vegard, Z. Phys. **5**, 17 (1921).

[19] K. Lorenz, N. Franco, E. Alves, I. M. Watson, R. W. Martin, and K. P. O'Donnell, Phys. Rev. Lett. **97**, 085501 (2006).

[20] V. Darakchieva, M. Beckers, M.-Y. Xie, L. Hultman, B. Monemar, J.-F. Carlin, E. Feltin, M. Gonschorek, and N. Grandjean, J. Appl. Phys. **103**, 103513 (2008).

[21] D. A. Neaman, *Semiconductor Physics and Devices Basic Principles*, McGraw-Hill (1997).

[22] G. D. Chen, M. Smith, J. Y. Lin, H. X. Jiang, S.-H. Wei, M. A. Khan and C. J. Sun, Appl. Phys. Lett. **68**, 2784 (1996).

[23] A. K. Viswanath, J. I. Lee, S. K. Yu, D. H. Kim, Y. H. Choi, and C-H. Hong, J. Appl. Phys. 84, 3848 (1998).

[24] H. Morkoc, *Nitride Semiconductors and Devices*, Springer, Heidelberg, (1999).

[25] J. Wu, and W. Walukiewicz, Superlatt. Microstruct. **34**, 63 (2003).

[26] P. Carrier, and S.-H. Wei, J. Appl. Phys **97**, 033707 (2005).

[27] M. Feneberg, J. Däubler, K. Thonke, R. Sauer, P. Schley, and R. Goldhahn, Phys. Rev. B **77**, 245207 (2008).

[28] J. Wu, W. Walukiewicz, K. M. Yu, J. W. Ager III, E. E. Haller, Hai Lu, and W. J. Schaff, Phys. Rev. B **66**, 201403(R) (2002).

[29] N. E. Christensen,and I. Gorczyca, Phys. Rev. B **50**, 4397 (1994).

[30] M. Suzuki, T. Uenoyama, and A. Yanase, Phys. Rev. B **52**, 8132 (1995).

[31] S.-H. Wei, and A. Zunger, Appl. Phys. Lett. **69**, 2719 (1996).

[32] J. Li, K. B. Nam, M. L. Nkarmi, J. Y. Lin, H. X. Jiang, P. Carrier, and S.-H. Wei, Appl. Phys. Lett. **83**, 5163 (2003).

[33] J. Wu, W. Walukiewicz, K. M. Yu, J. W. Ager, S. X. Li, E. E. Haller, and H. Lu Solid State Communication **127**, 411 (2003).

[34] S. Pereira, M. R. Correia, T. Monteiro, E. Pereira, E. Alves, A. D. Sequeira, and N. Franco, Appl. Phys. Lett. **78**, 2137 (2001).

[35] K. Wang, R. W. Martin, S. Herbabdez, K. P. O'Donnell, I. M. Waston, D. Wolverson, K. Lorenz, E. Alves, V. Matias, and A. Vantomme, J. Appl. Phys. **103**, 073510 (2008).

[36] $Al_yGa_{1-y}N$ Template Website: http://www.tdii.com/products/AlGaN_sap.html

[37] P. F. Yu, M. Cardona, *Fundamentals of Semiconductors,* Springer-Verlag, Berlin, Heidelberg (1996).

[38] S. Pereia, M. R. Correia, E. Pereia, K. P. O'Donnell, R. W. Martin, M. E. White, E. Alves, A. D. Sequeira, and N. Franco, Mat. Sci. Eng. B **93**, 163 (2002).

[39] C. A. Parker, J. C. Bedair, S. M. Bedair, M. J. Reed, S. X. Liu, and N. A. El-Masry, Appl. Phys. Lett. **75**, 2776 (1999).

[40] X. Q. Shen, T. Ide, M. Shimizu, and H. Okumura, J. Appl. Phys **89**, 5731 (2001).

[41] S. Yoshida, S. Misawa, and S. Gonda, Appl. Phys. Lett. **42**, 427 (1983).

[42] H. Amano, I. Akasaki, T. Kozawa, K. Hiramatsu, N. Sawak, K. Ikeda, and Y. Ishi, J. Lumin. **40**, 121 (1988).

[43] H. Amano, N. Sawaki, I. Akasaki, and Y. Toyoda, Appl. Phys. Lett. **48**, 353 (1986).

[44] H. Amano, and I. Akasaki, J. Phys.: Condens. Matter **13**, 6935 (2001).

[45] Q. X. Guo, T. Yamamura, A. Yoshida, and N. Itoh. J. Appl. Phys. **75**, 4927 (1994).

[46] X. B. Zhang, T. Taliercio, S. Kalliakos, and P Lefebvre, J. Phys.: Condens. Matter **13**, 7053 (2001).

[47] I. Brener, M. Olszakier, E. Cohen, E. Ehrenfreund, A. Ron, and L. Pfeiffer, Phys. Rev B **46**, 7927 (1992).

[48] Huang K, and Rhys A, Proc. R. Soc. A **204**, 406 (1950).

[49] V. Yu. Davydov, A. A. Klochikhin, R. P. Seisyan, V. V. Emtsev, S. V. Ivanov, F. Bechstedt, J. Furthmuller, H. Harima, A. V. Mudryi, J. Aderhold, O. Semchinova, and J. Graul, Phys. Stat. Sol. (B) **R1**, 229 (2002).

[50] T. Sota, K. Wada, S. Nakamura, J. Vac. Sci. Technol. B **16**, 2004 (1998)].

[51] J. J. Hopfield, J. Phys. Chem. Solids **10**, 110 (1959).

[52] D. J. Mowbray, O. P. Kowalski, M. S. Skolnick, M. Hopkinson, and J. P. R. David, Superlatt. Microstruct. **15**, 313 (1994).

[53] P. P. Paskov, P. O. Holtz, B. Monemar, S. Kamiyama, M. Iwaya, H. Amano, and I. Akasaki, Phys. Stat. Sol. (B) **234**, 755 (2002).

[54] R. Pecharromán-Gallego, P. R. Edwards, R. W. Martin, and I. M. Watson, Mater. Sci. Eng., B **93**, 94 (2002).

[55] S. Kalliakos, X. B. Zhang, T. Taliercio, P. Lefebvre, B. Gil, N. Grandjean, B. Damilano, and J. Massies, Appl. Phys. Lett. **80**, 428 (2002).

[56] S. Kalliakos, P. Lefebvre, X. B. Zhang, T. Taliercio, B. Gil, N. Grandjean, B. Damilano, and J. Massies, Phys. Stat. Sol. (A) **190**, 149 (2002).

[57] D. M. Graham, A. Soltani-Vala, P. Dawson, M. J. Godfrey, T. M. Smeeton, J. S. Barnard, M. J. Kappers, C. J. Humphreys, and E. J. Thrush, J. Appl. Phys. **97**, 103508 (2005).

[58] O. Ambacher, R. Dimitrov, M. Stutzmann, B. E. Foutz, M. J. Murphy, J. A. Smart, J. R. Shealy, N. G. Weimann, K. Chu, M. Chumbes, B. Green, A. J. Sierakowski, W. J. Schaff, and L. F. Eastman, Phys. Stat. Sol. (B) **216**, 381 (1999).

[59] F. Bernardini, V. Fiorentini, and D. Vanderbilt. Phys. Rev. B. **56**, R10024 (1997).

[60] O. Ambacher, J. Majewski, C. Miskys, A. Link, M. Hermann, M. Eickhoff, M. Stutzmann, F. Bernardini, V. Fiorentini, V. Tilank, B. Schaff, and L. F. Eastman, J. Phys.: Condens. Matter **14**, 3399 (2002).

[61] F. Bernardini, and V. Fiorentini, Appl. Surface Science **166**, 23 (2000).

[62] F. Bernardini, V. Fiorentini, and D. Vanderbilt, Phys. Rev. B **63**, 193201 (2001).

[63] A. Hangleiter, J. S. Im, H. Kollmer, S. Heppel, J. Off, and F. Scholz, MRS Internet J. Nitride Semicond. **Res. 3**, 15 (1998).

[64] R. W. Martin, P. G. Middleton, K. P. O'Donnell, and W. Van der Stricht, Appl. Phys. Lett. **74**, 263, (1999).

[65] T. Takeuchi, S. Sota, M. Katsuragawa, M. Komori, H. Takeuchi, H. Amano, and I. Akasaki, Jpn J. Appl. Phys. **36**, L382 (1997).

[66] B. E. Sernelius, K.-F. Berggren, Z.-C. Jin, I. Hamberg, and C. G. Granqvist, Phys. Rev. B **37**, 10244 (1988).

[67] E. Burstein, Phys. Rev. **93**, 632 (1954)

[68] T. S. Moss, Proc. Phys. Soc. London, Section B **67**, 775 (1954).

[69] Private Communications with Dr. R. Goldhahn.

[70] N. F. Mott, *Metal-Insulator Transitions* Taylor and Francis, London (1974).

[71] A. P. Roth, J. B. Webb, and D. F. Williams, Phys. Rev. B **25**, 7836 (1982).

[72] K.-F. Berggren and B. E. Sernelius, Phys. Rev. B **24**, 1971 (1981).

[73] H. C. Casey and F. Stern, J. Appl. Phys. **47**, 631 (1976).

[74] G. D. Mahan, J. Appl. Phys. **51**, 2634 (1980).

[75] S. C. Jain, J. M. McGregor, and D. J. Roulston, J. Appl. Phys. **68**, 3747 (1990).

CHAPTER 3

Experimental Techniques

3.1 Introduction

As is the case in much semiconductor research, this work has relied on the application of a range of characterisation techniques for optical, surface and compositional properties. These techniques have been accessed either at Strathclyde University or through collaborations. This chapter provides a comprehensive survey of the characterisation techniques used in this thesis. The techniques used are photoluminescence (PL) and PL excitation (PLE) spectroscopy for investigating the luminescence properties; secondary electron microscopy (SEM) and atomic force microscopy (AFM) for visualisation of the surface morphology; electron probe micro-analysis (EPMA) and Rutherford backscattering spectrometry (RBS) to study the compositional properties; and Hall Effect for the carrier concentration and mobility.

3.2 Optical Characterisation

The luminescence properties and excitation mechanisms of III-nitrides are the main topics described in this thesis. Luminescence is defined as the emission of light, usually as a result of some input of energy into a material. It is classified according to the way in which the material is excited: photoluminescence (PL) for light excitation, cathodoluminescence (CL) for electron-beam excitation, electroluminescence (EL) for electric field as excitation source, etc. By analysing the luminescence spectra, important properties such as the band gap energy, peak emission energy, peak widths, relative intensities and thermal quenching could be determined and compared with compositional and surface information to give a fuller picture of the materials under investigation.

Various setups, excitation sources and detection methods have been used to characterise the optical properties of the samples. There are two setups used to measure PL and PL excitation (PLE) spectra. One PL setup uses either a 325 nm Helium Cadmium (He-Cd) laser or 244 nm line of an Ar ion laser as the excitation sources. The other PL/PLE setup uses a 1000 W xenon lamp as excitation source. Details of these setups will be presented in this section.

3.2.1 Photoluminescence (PL) Spectroscopy

Photoluminescence (PL) is a non-destructive technique that provides information about the radiative process [1-2]. It relies on the creation of electron-hole pairs by exciting the sample with an optical source, typically a laser with photon energy larger than the energy gap of the sample material. These generated electron-hole pairs will subsequently undergo radiative recombination with photon emission.

PL spectra plot the variation of luminescence intensity as a function of emission wavelength and can provide information about the energy levels in the sample. For example, PL spectra and their intensity dependences can determine:

- Impurity levels- Radiative transitions in semiconductors sometimes involve localised defect levels. The PL energy associated with these levels can be used to identify the specific defects, for example, donor-acceptor pair (DAP) at about 3.27 eV or yellow luminescence at 2.5 eV. DAP emission is due to optical transitions from a shallow donor to a shallow Mg acceptor and the latter is attributed to transitions from the conduction band to a deep acceptor level or an Mg complex [3-7].

3.2.1.1 PL Setup

A schematic representation of the PL set-up using the 325 nm He-Cd laser [8] is shown in Figure 3.1. A narrow band-pass interference filter near 325 nm is used to remove plasma lines. The detection side is a combination of a spectrograph (Oriel Instruments MS125^{TM}, Model no. 77400, with an f-number of 3.7) and a 1024 x 255 pixel silicon charge-coupled detector (CCD; Andor front illuminated Model DV420 OE). The luminescence from the sample is focused on the 25 μm entrance slit of the spectrograph and reflected by two mirrors inside onto the surface of a diffraction grating which disperses the collected luminescence onto the CCD detector. A Schott WG345 long-pass filter is placed in front of the entrance slit of the spectrograph in order to block any remaining 325 nm laser. The detector is cooled using a thermoelectric cooler to about -55 °C. During measurements, the signal from pixels in the same column is integrated as the PL intensity at a particular wavelength. Therefore, each column acts as an output slit and detects the light dispersed at a particular angle. The width of each column is 26 μm, which matches the entrance slit.

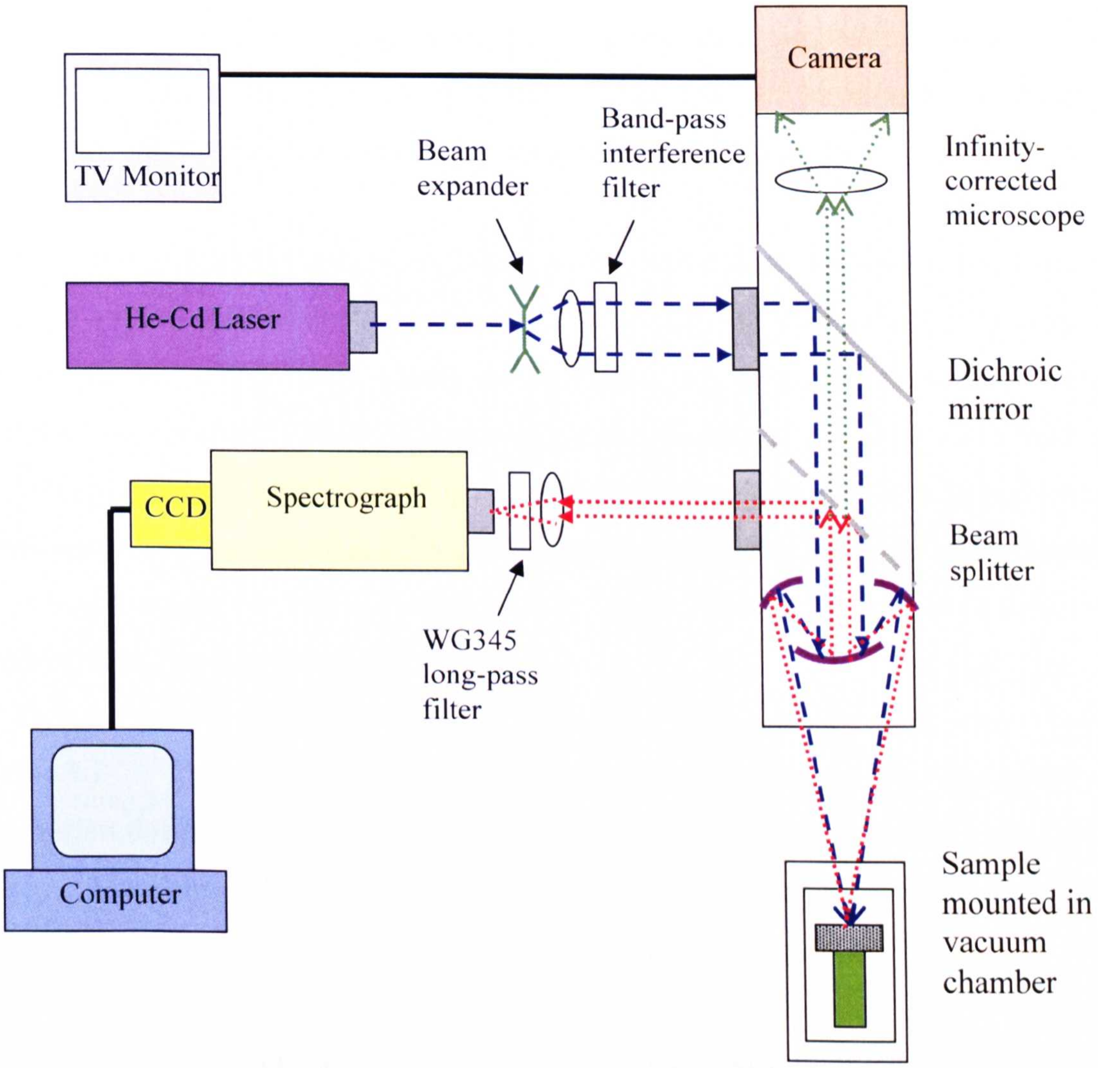

Figure 3.1 **325 nm He-Cd laser PL spectroscopy setup. The blue lines are the excitation light path, the red lines represent the luminescence from the sample, and the green lines represent a part of the luminescence monitored by an accessory camera to check the position of the luminescence spot.**

All samples were mounted on an aluminium sample holder inside a closed cycle helium cryostat. A rotary pump and an oil based diffusion pump have been used to produce the vacuum required in the cryostat. A Cryogenics CT1 helium compressor allows the cryostat to be cooled down to around 15 K. The temperature around the sample is controlled via combination of the helium cryogenerator and a film heater, which is connected to a temperature controller (Oxford Instruments ITC-4). A temperature sensor is used to monitor the temperature in the cryostat and gives feedback to the temperature controller. In this way, the temperature of the samples can be controlled in the range from 15 K up to room temperature. During the experiment, the position of the PL spot was fixed on a certain location on the sample as the temperature was increased in several steps up to room temperature.

The spectral resolution depends on the slit width, wavelength and diffraction grating selected [9]. In this work, the spectral resolution of the measured PL spectra is determined by the diffraction grating inside the spectrograph, since the widths of the slits are kept constant. Table 3.1 summarises some parameters of each grating used in this thesis. If a wide spectral range is desired, a low resolution grating will be chosen otherwise a finer grating is used for higher spectral resolution but with only a limited wavelength range. For 400 lines/mm grating, the PL spectrum covers more than the entire visible wavelength range.

Table 3.1 Parameters of the gratings used in the spectrograph. The spectral resolution data are obtained using a 25 μm entrance slit and 1024 element CCD array. The blaze wavelength and the primary wavelength region is the wavelength at which the grating efficiency is the maximum and ≥ 20 %, respectively [10-11].

Line Density (lines/mm)	Blaze Wavelength (nm)	Type	Spectral Resolution (nm)	Primary Wavelength (nm)
400	350	Ruled	1.2	200-800
1200	350	Ruled	0.4	200-1000
2400	400	Holographic	0.2	230-650

3.2.2 Photoluminescence Excitation (PLE) Spectroscopy

In photoluminescence excitation (PLE) spectroscopy, an optical excitation is used to excite electrons across the band gap of a semiconductor [12]. In such a measurement the detection system is set to record at a specific emission energy, commonly the PL peak energy or energies close to it, and the energy of the excitation source is varied. The emission intensity is plotted as a function of excitation energy in the PLE spectrum. Figure 3.2 illustrates an example of PL and PLE spectra of $Al_{0.83}In_{0.17}N$ epilayer sample. The arrow at the sharp emission line at 330 nm indicates the wavelength at which the PLE spectrum is detected.

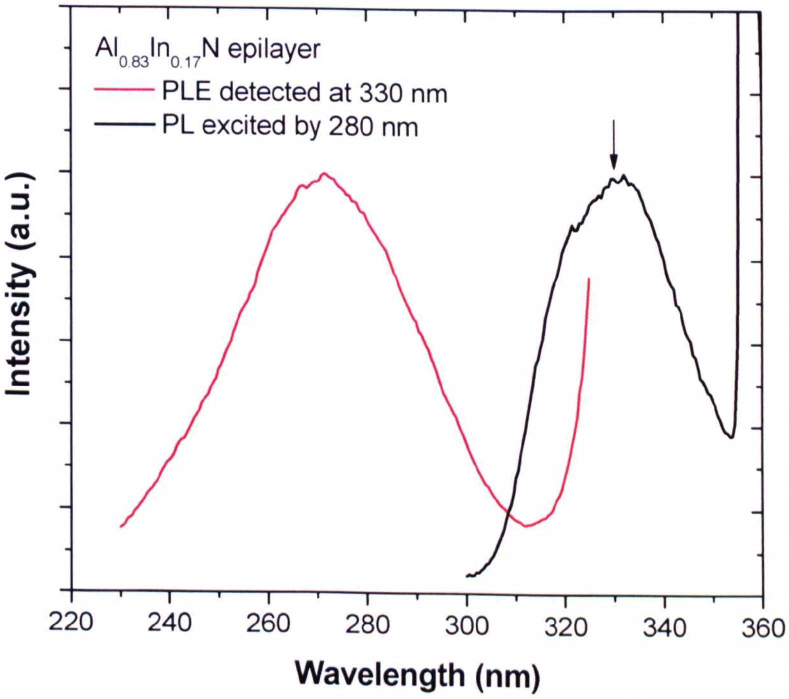

Figure 3.2 PL (black) and PLE (red) spectra of $Al_{0.83}In_{0.17}N$ epilayer. The PLE spectrum was detected at 330 nm (as indicated by arrow) and PL spectrum was excited by the light at 280 nm.

The PLE spectrum gives similar information to the absorption spectrum: for example, it can be used to determine a value for the optical band gap of a luminescent material. PLE spectroscopy has advantages over optical absorption technique as it does not require the sample substrate to be transparent at the excitation energy and is not dependent on the thickness of the material. Thus, this can be used to investigate samples with thin active layers.

3.2.2.1 PLE Setup

To measure the PLE spectra and selectively excited PL spectra, a wavelength-adjustable excitation source is necessary. The variation of excitation wavelength is achieved by rotating the excitation monochromator whereas the detection monochromator remains fixed at the desired position. A short arc 1000 W xenon (Xe) lamp with a quartz envelope has been chosen as the excitation source. The output of the Xe lamp covers the deep ultraviolet (UV) of 220 nm to the visible wavelength range. The quartz envelope totally blocks the emission shorter than 220 nm, giving a short wavelength limit. Although 220 nm (5.64 eV) is not short enough to reach the band gap of AlN, it is more than sufficient to excite all the samples studied in this thesis.

A schematic representation of the PLE set-up using Xe-lamp is shown in Figure 3.3. The Xe-lamp emits continuous wide band light, which is focused by a quartz lens onto the slit of a Jobin Yvon 0.25 m monochromator, referred to as the excitation monochromator and contains UV grating of 1200 lines/mm. The light wavelength is selected and changed continually from 220 to 700 nm using this monochromator. The band-pass of the quasi-monochromatic light is determined by the width of the slit. The narrower the slit is, the narrower the band-pass is, and the higher the excitation spectral resolution is but the intensity of the output light is lower. Thus, in order to balance the resolution and the excitation intensity, a slit width of 2 mm is chosen in this study, giving a band-pass of approximately 3 nm at 300 nm. The output from the excitation monochromator passes through a chopper (set to around 36.5 Hz) and is focused on the sample surface in a spot size of approximately 2 x 5 mm^2. The sample is mounted on the cold head of a closed-cycle helium refrigerator on a moveable stage. An Oxford Instruments ITC-4 Temperature Controller in conjunction with a heater and sensor inside the cryostat is used to measure and change the temperature in the same manner as described for the PL system in **subsection 3.2.1.1.**

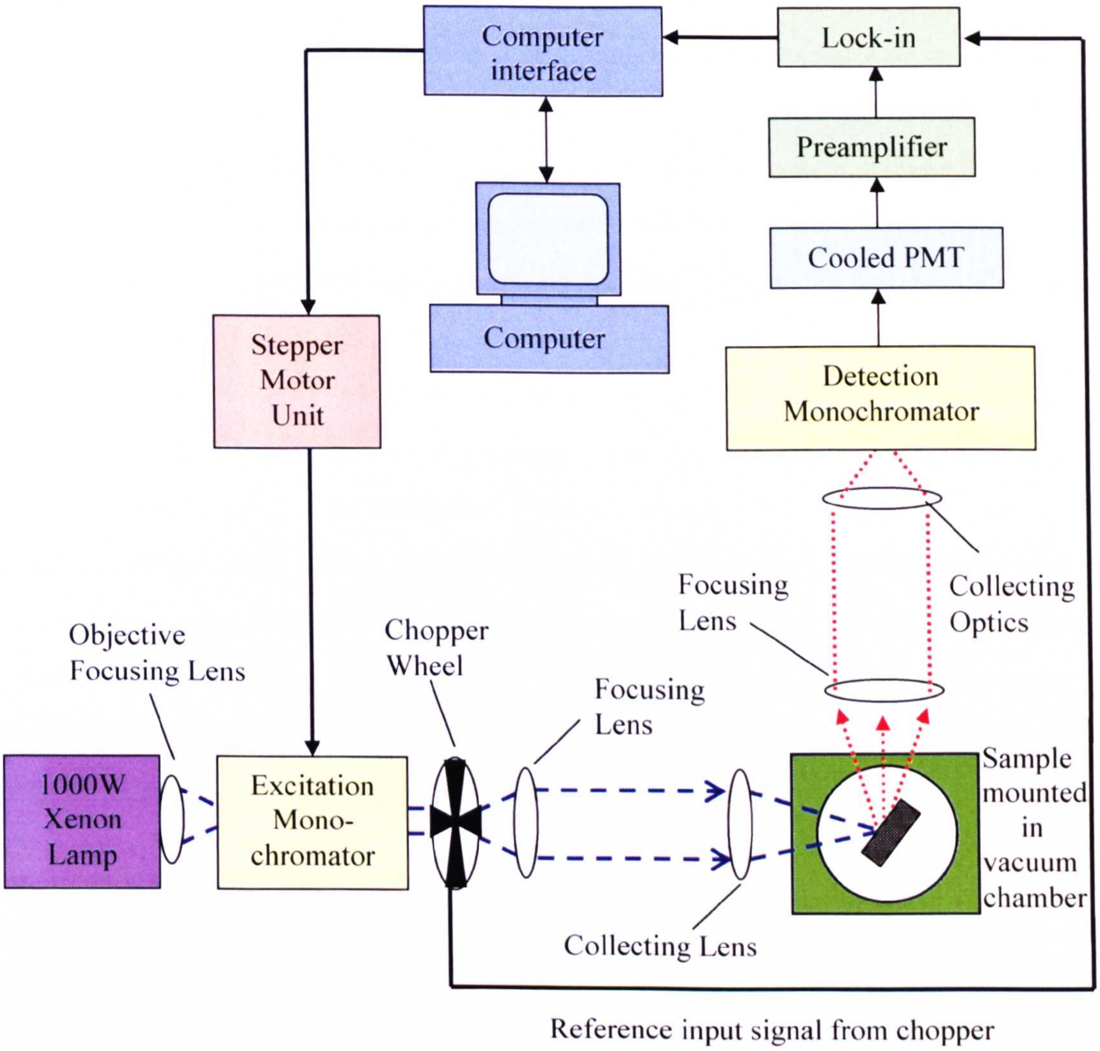

Figure 3.3 Schematic diagram of PLE/PL spectroscopy set-up using Xe-lamp. The blue lines are the excitation light path and the red lines represent the luminescence from the sample.

Two lenses are arranged in series to collect and collimate the luminescence from the sample and focus it onto the entrance slits of a McPherson 0.67 m detection monochromator. The sample is mounted at an angle of 60° to the excitation beam to reduce reflected excitation light entering the detection monochromator. The lenses are adjusted to maximise the amount of light collected into the slit. An 1800 lines/mm UV/visible grating is installed in the detection monochromator (for 350 nm wavelength and 0.5 mm entrance slit width, the spectral resolution is 0.4 nm). The output from the detection monochromator is detected using a Thorn EMI Gencom Inc 3365 cooled photomultiplier tube (PMT). The PMT is connected via a Stanford

SR570 current preamplifier to a Stanford SR810 DSP lock-in amplifier, which uses a reference signal from the chopper to distinguish the luminescence from background noise. The resultant DC signal from the lock-in is then sent via a built in RS232 interface to a computer. A train of pulses is provided from the computer via another RS232 interface to control the steeper motor unit driving the monochromator. The measurements are recorded using in-house software written by Dr. Paul Edwards, a colleague from my research group.

All PLE spectra presented in this thesis have been corrected for the combined throughput of lamp and the excitation monochromator. This is done by using an UV sensitive photodiode which was installed at the sample position. Scanning the excitation monochromator, the photodiode recorded the intensity as a function of excitation wavelength. The sensitivity of the photodiode was available from the supplier. Dividing the measured intensity by the sensitivity function, one could obtain the excitation intensity as a function of wavelength.

This Xe-lamp set-up can also be used to perform PL measurements. In a PL measurement the set-up is the same, the only difference being that the stepper motor is now used to drive the detection monochromator whilst the excitation wavelength remains unchanged. Prior to acquisition of a PLE spectrum, a PL spectrum is acquired in order to determine the detection energy at which the emission monochromator should be set. As already mentioned, in the PL mode, the He-Cd laser or Ar ion laser can also be used as excitation sources instead of using the Xe lamp. Table 3.2 shows the excitation sources that have been used in this thesis and their powers.

Table 3.2 Excitation sources and powers applied in PL and/ or PLE system.

Type	Output Wavelength (nm)	Output Power (mW)	Power on samples (mW)
Xe lamp	e.g. 356±1.5 (2 mm slit)	1	0.6
He-Cd Laser (Melles Griot 3056-S-A2)	325	5.0	0.5
Ar ion laser	244	0.095 to 150	0.06 to 90

3.3 Surface Characterisation

In this section, secondary electron microscopy (SEM) and atomic force microscopy (AFM) are employed to investigate the surface morphology of the materials will be discussed in detail.

3.3.1 Secondary Electron Microscopy (SEM)

Scanning electron microscope (SEM) is a microscope that uses electrons rather than light to form an image. Figure 3.4 shows a schematic FEI SEM employed in this project. Four main components combine to produce the images from the sample are: an electron gun, a demagnification unit, a scan unit and a detection unit. The electron gun, which is the source emitter, produces electrons within a small spatial volume with a small angular spread and a selectable energy. This electron beam enters the demagnification unit which consists of several electromagnetic lenses. The beam is condensed by a condenser lens and focused on a small point using the objective lens. The electron beam exits to arrive at the sample surface with a smaller dimension than that produced by the gun.

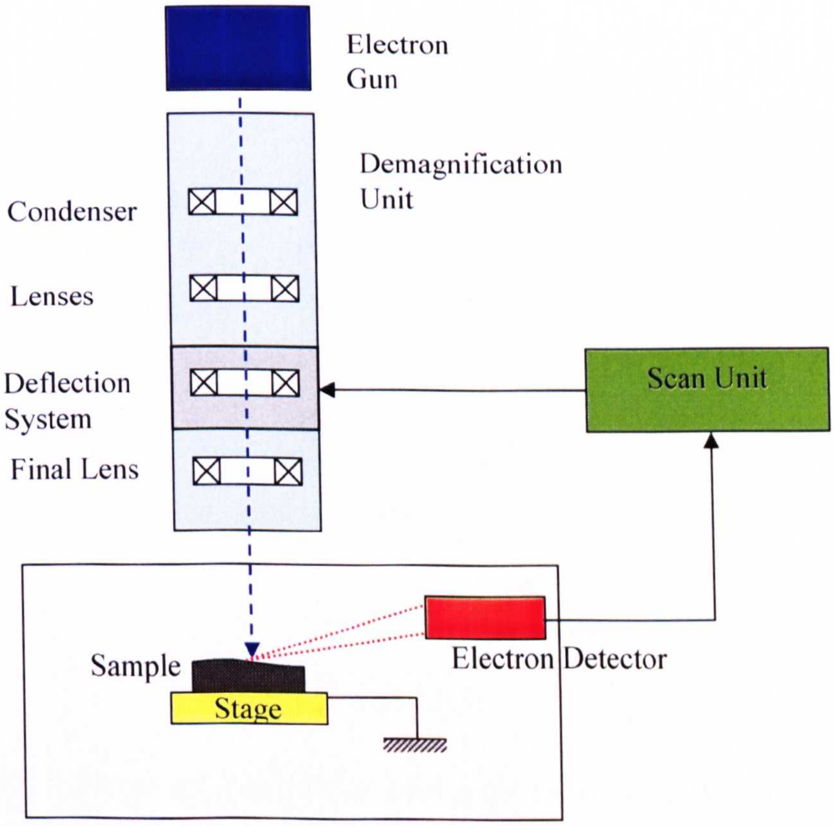

Figure 3.4 SEM schematic overview.

When an electron beam hits a material, lots of interactions between the electrons and the material occur. Some of the incident electrons are scattered elastically by the atoms (called backscattered electrons) whilst a large part of the incident electrons penetrate into the material [13-15]. The penetrating electrons lose their energy by inelastic collisions with the lattice ions along the electron trajectories, generating secondary electrons, Auger electrons, cathodoluminescence, characteristic X-rays and etc., as summarised in Figure 3.5. The detector system picks up the secondary electrons, amplifies them and converts them into electrical voltage. The scan generator signal (in scan unit), fed to the deflection system of the column, moves the beam in a raster pattern over the sample area. At approximately the same time the monitor for viewing the image is also scanned. The electrical voltage changes as it rasters, which provides serial information of the specimen surface. This signal, modulated by the one from the detection system, produces the onscreen image that corresponds to the topography of the sample [16]. The data are recorded using an intermediate software layer which acting on instructions from the application layer controls the column, detectors, stage and vacuum functions. In this work, the beam voltage of 5 kV was selected.

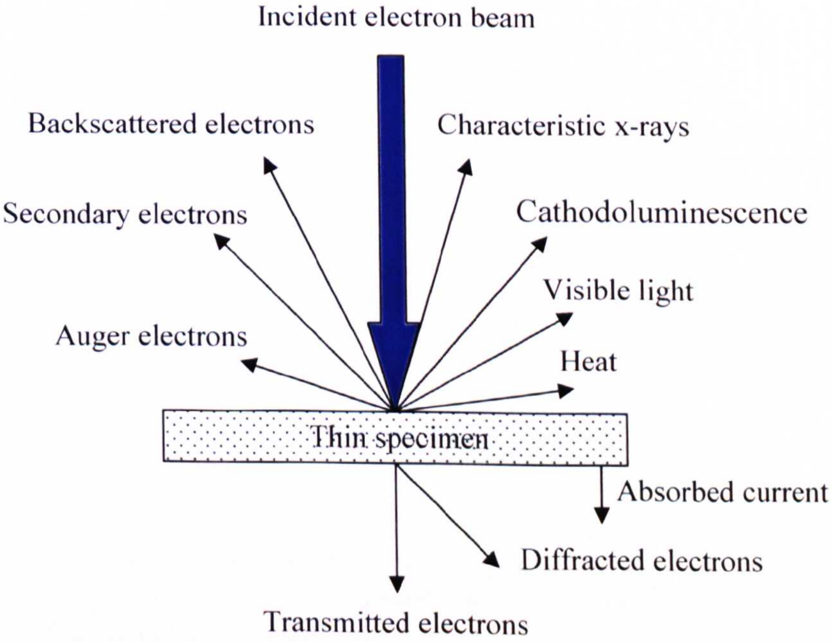

Figure 3.5 **Electron interactions with a thin specimen [13-15].**

3.3.2 Atomic Force Microscopy (AFM)

An AFM consists of four primary components: a probe, laser, detector and piezoelectric scanner. The probe consists of three parts: a cantilever block that supports a very fine cantilever, which in turn has the delicate tip situated underneath (Figure 3.6). The probe tip traces the surface of the sample and provides a three-dimensional topography of the sample surface.

A Digital Instruments Multimode Nanoscope IIIa AFM instrument was used in this work. Figure 3.6 shows a schematic of the AFM hardware used. Etched silicon tips were used to image the sample surface in tapping mode. The nominal radius of curvature of the tips is 5 to 10 nm. The height resolution is approximately 0.1 nm, while lateral resolution is determined by the convolution of the tip sharp and the feature shape under optimised imaging conditions, and is normally 5 nm. These characteristics make AFM very suitable for the observation of surface morphological features such as growth steps, nanoscale islands and pits.

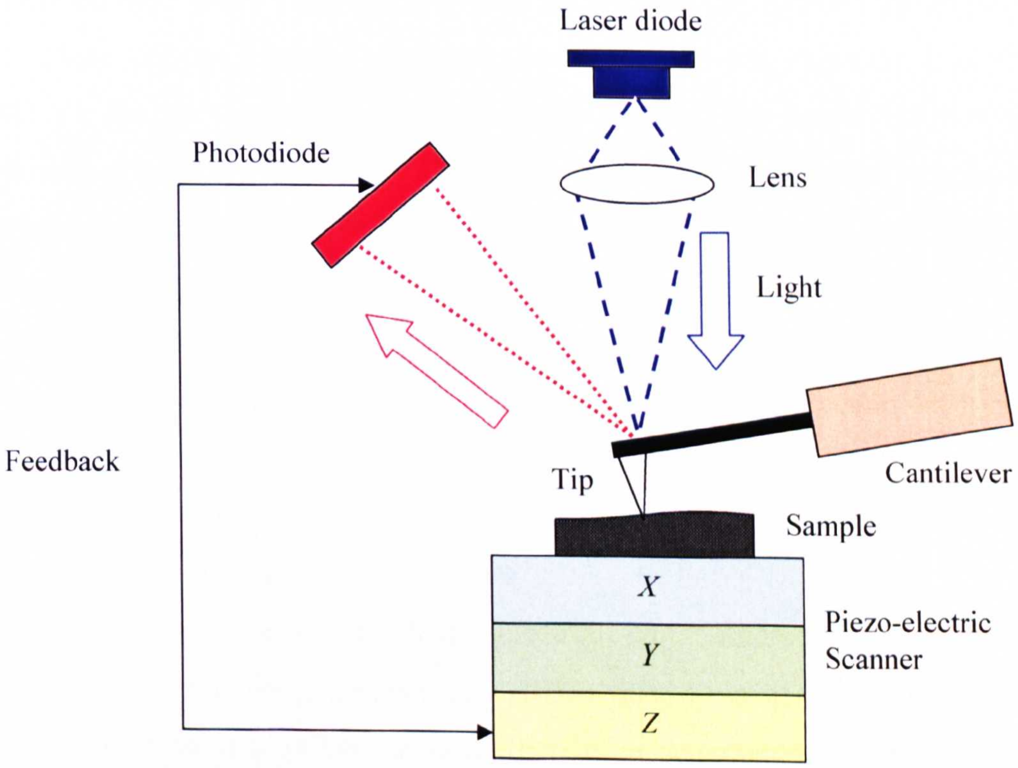

Figure 3.6 Schematic of an AFM hardware.

The instrument detects the *z*-displacement of the cantilever using the reflection of a laser beam focused on the top surface of the cantilever. Feedback from the scanner maintains the probe at a constant force under tapping mode. The image datasets thus obtained contain a height co-ordinate *z* for a large set of different *x*-*y* positions on the sample. They can be processed in different formats to serve different purposes, normally using the software suite WSxM [17].

In this thesis, the data were presented in the following ways:

- Plan-view or 3-D images: In these images, the height of the surface features is scaled using a brightness code so that intrusions look bright, and depressions look dark. Sizes and areal densities of topographic features in film surfaces can thus quantify from plan view images.
- Datasets can be used to produce line-scans, showing the height variation along a straight-line traverse over the sample surface.

In this Nanoscope IIIa AFM system, the scanners have a large motion range of up to 120 μm on the *x* and *y* axes, and a *z*-range up to 6 μm. By lightly tapping the tip on the surface during scanning, tapping-mode measurements eliminate lateral shear forces on the tip that would degrade image quality. The instrument has a fully automatic proprietary method of controlling the tip approach to the sample, which prevents hard collisions. Such collisions may damage soft samples, although this is not an issue for hard III-nitride materials. However, sample sizes are limited to below 15 mm in lateral dimensions, and 5 mm in thickness. In this thesis, the AFM measurements were carried out in association with Dr. Stephanie Hodgen from Strathclyde Pure and Applied Chemistry Department.

3.4 Compositional Characterisation

This section focus on the methods, electron probe microanalysis (EPMA) and Rutherford backscattering spectrometry (RBS), used to investigate the composition. The composition will affect the band gap of a semiconductor alloy as well as properties such as the strain in the system and the magnitude of the built-in electric fields present.

3.4.1 Electron Probe Micro-Analysis (EPMA)

Electron probe microanalysis (EPMA) is both a quantitative and qualitative non-destructive method to determine the elemental composition of the materials [15]. As mentioned in earlier section, when a target material is bombarded with a beam of electrons, lots of interactions between the electrons and the material occur leading to characteristic X-rays of the atoms, secondary electrons, cathodoluminescence and etc. Many of these signals can be measured simultaneously, depending on the available facilities and experimental aims. The EPMA system used in this thesis is able to collect the characteristics X-rays, cathodoluminescence, secondary electrons and backscattered electrons at the same time.

3.4.1.1 EPMA Setup

Figure 3.7 shows a schematic overview of Cameca SX100 EPMA system employed in this thesis. The EPMA is configured with a tungsten electron gun. The accelerating voltage of the EPMA electron probe beam can be adjusted in steps from 1 to 50 kV. During the experimental set-up, the sample is placed on an automated stage with 100 nm step-size to allow images to be acquired by scanning the sample. The sample is viewed optically in reflected light by a cooled silicon CCD camera with the magnification to observe the material surface quality and to select an area for measurement. CL of the material can also simultaneously be observed in this set-up and monitored as the stage moved. The acquisition and processing of CL spectral maps was done using an in-house computer program CHIMP written by Dr. Paul Edwards. The EPMA can also operate like an SEM, providing SE imaging. By combining the simultaneous composition mapping and SE imaging, CL spectral mapping allows one to correlate spectral features with compositional and topographical ones [19].

The characteristic X-ray emission is excited using a stationary focused electron probe beam. It is produced when an electron with sufficient energy (typically > few keV) strikes an atom and a tightly-bound electron (K-, L-, M-shell electrons). An electron from a higher shell drops to fill the vacancy. If an electron from the K-shell is ejected and an electrons from the L-shell to fill the vacancy, a K_α X-ray emerges; whereas if an electron from the M-shell fills the K-shell vacancy, K_β radiation results [20]. In qualitative chemical analysis, the energy of a given K, L or M line is measured, the atomic number of the element producing that line can be determined. As the intensity of a characteristics X-ray line of a particular element is proportional to the amount of atoms present in the excited region, its composition can be measured but a correction procedure is needed to calculate the composition accurately (see next section).

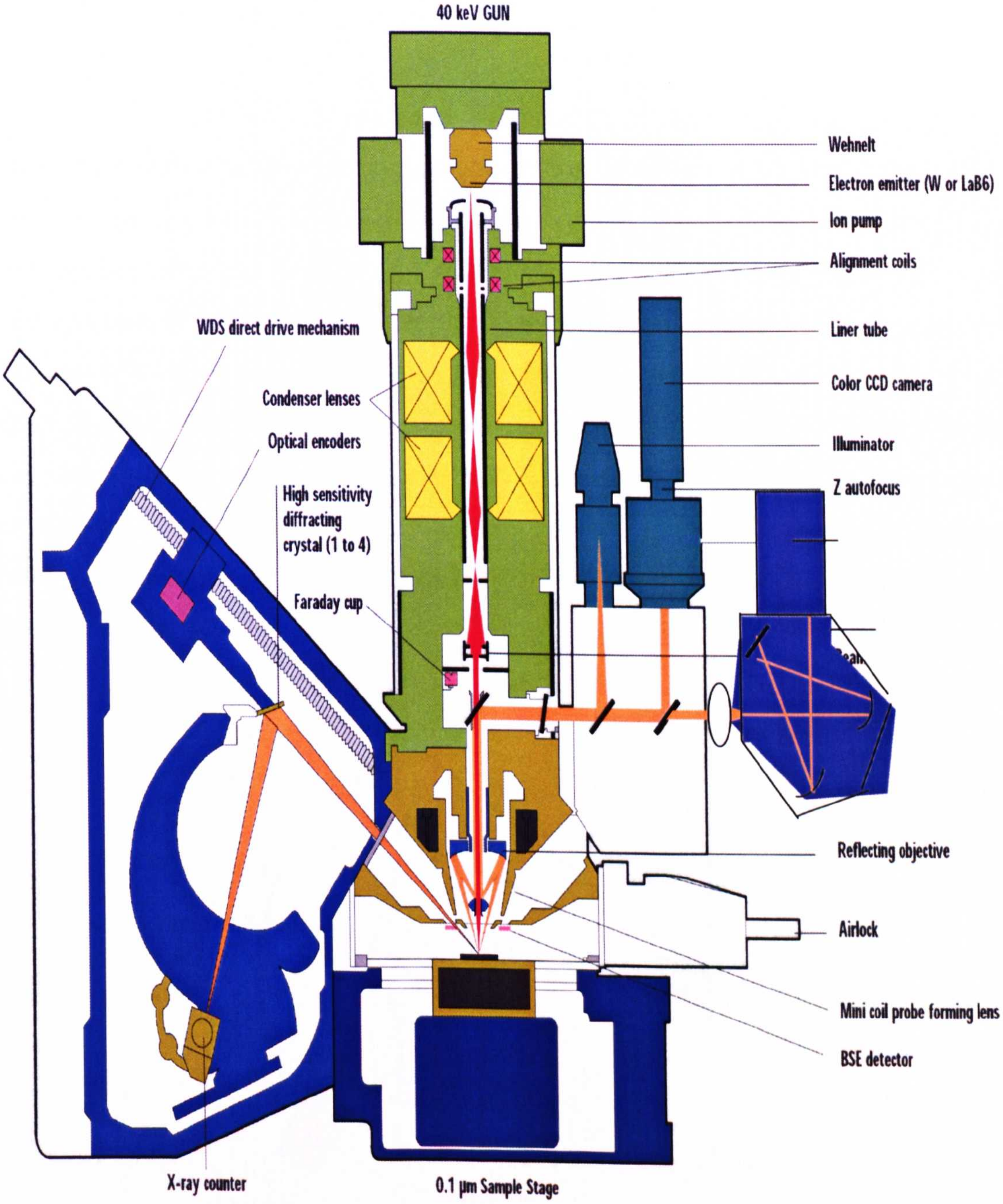

Figure 3.7 Schematic overview of Cameca SX100 EPMA System [18].

3.4.1.2 Wavelength Dispersive X-ray (WDX) Spectroscopy

There are two methods for detecting characteristics X-ray emission: Energy Dispersive X-ray (EDX) analysis and Wavelength Dispersive X-ray (WDX) analysis. WDX analysis is chosen as it has several advantages over EDX analysis: a much better resolution and lower background noise, which results in narrower peak widths and, consequently, a much more quantitative and sensitive analytical tool. Typical resolution of a WDX spectrometer is approximately 5 eV, contrasting to 100-200 eV for an EDX spectrometer.

In our EPMA system, it is provided by three WDX spectrometers, whose high spectral resolution and peak-background ratios result in excellent composition detection limits (< 0.05 atomic % demonstrated for rare-earth ions in GaN [21]). Each spectrometer has two or four interchangeable diffraction crystals which are used as monochromators to measure the X-ray emission spectrum from the sample. They cover a wide range of elements from Be to Rb. The WDX spectrometers can detect X-ray emission in the range from approximately 100 eV to 14 keV. Four analysing crystals are standard for a WDX spectrometer. To obtain even higher sensitivities, so-called large area crystals can be used. In this case there is only space for two crystals due to their increased size. The layout of a WDX spectrometer is shown in Figure 3.8.

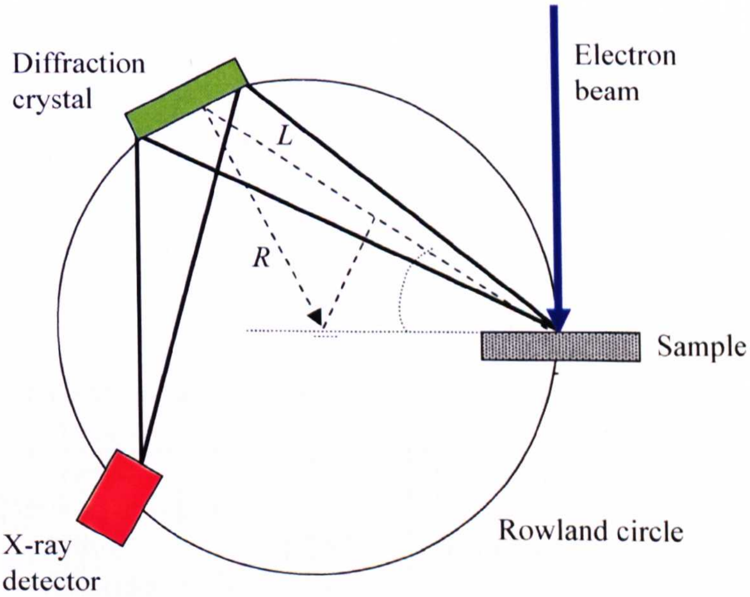

Figure 3.8 Rowland circle geometry for WDX spectrograph.

The operation of WDX spectrometer is based on Bragg's law. X-rays that are incident on the analysing crystal are diffracted and consequently detected if they satisfy the Bragg's condition. If the sample, diffraction crystal and X-ray detector all lie in a circular path with radius R, the distance L between sample and crystal is given by:

$$\frac{L}{2} = R \sin \theta \tag{3.1}$$

Combining (3.1) with Bragg's diffraction condition, $n\lambda = 2d\,sin\theta$, gives:

$$n\lambda = \frac{d}{R} L \tag{3.2}$$

The geometry described above is called the Rowland circle. In this geometry, the wavelength detected is proportional to the distance between the sample and crystal. By simultaneously scanning and rotating both the crystal and detector, wavelength selection is achieved. To retain the same conditions of characteristic X-ray detector, it is important to ensure the angle between detected X-rays and the sample surface, i.e. the take-off angle φ is unchanged by moving the analysing crystal in a straight line away from the same as the Bragg angle is increased [22].

The diffraction crystal is curved to focus the diverging beam of emitted X-rays and only diffracts those X-rays that satisfy the Bragg condition [22-24]. An appropriate diffraction crystal must therefore be selected to diffract the required X-ray emission from the sample as listed in Table 3.3. For example, the X-ray emission of gallium (Ga: 1.098 keV) and indium (In: 3.287 keV) are measured using thallium acid phthalate (TAP) and large pentaerythritol (LPET) diffraction crystals, respectively.

Table 3.3 SX 100 Crystals and their wavelength coverage [24-25].

Crystal Designation	Crystal Type	2d Spacing (Å)	Element Range		
			Kα	Lα	Mα
TAP	Thallium acid phthalate	25.76	F to P	Mn to Nb	La to Hg
LPET	Large Pentaerythritol	8.742	Si to Mn	Sr to Tb	Ta to U
LIF	Lithium Fluoride	4.207	Sc to Rb	Te to Np	
PC1	Pseudocrystal 1	60	C to F		

The EPMA system is also designed for quantitative element analysis. This is achieved by using standard samples (known elements and compositions) as the reference. The concentration of a particular element in a sample is measured by comparing its intensity of the emission from the characteristic X-ray with that from a standard sample with a known composition. This gives the experimental *k*-ratio:

$$k - ratio = \frac{Sample\ Intensity}{Standard\ Intensity} \tag{3.3}$$

When the measurements are carried out at a single beam energy, this *k*-ratio will be converted into a weight percentage value (wt. %) using a corrective-iterative procedure which calculates the so-called *ZAF* correction factors in order to obtain accurate concentration. This is because the primary generated X-rays may be absorbed or may generate secondary X-rays by fluorescence in the material. Furthermore, some of the primary electrons may be backscattered out of the material and consequently, the number of inner-shell ionisations will be lesser than expected. The three constituents of the correction are the atomic number correction, *Z* (related to electron backscattering which affects the efficiency of characteristics X-ray emission), the absorption correction, *A* which may reduce the count rate), and the fluorescence correction, *F*. This is done using the instrument's own software. The correction procedure takes into account the differences in backscattered electron yield, rate of energy loss, absorption and secondary fluorescence between the sample and the standard.

The selection of an appropriate standard is extremely important so as to achieve accurate quantitative measurements. Several criteria must be met: (i) the composition must be homogeneous, (ii) the material must be chemically and thermally stable, and (iii) it is preferable if the standard is of a similar composition to the material under investigation so as to minimise the error arising from inaccurate correction procedures [22]. Dr. Debbie Amabile, a colleague in my research group, performed a comprehensive investigation on the compositional measurements of $Al_{1-x}In_xN$ epilayers. Details of the compositional measurements and structural characterisation have been included in her thesis [8]. The most challenging aspect of the WDX composition measurements was the accurate determination of Al concentration in the $Al_{1-x}In_xN$ layer because of the difficulties to obtain a reliable Al standard. For Al metal standard, there are two problems, namely, the carbon contamination, and a surface oxidation layer due to the high affinity of Al for oxygen. For AlN standard, it is notoriously difficult to dope AlN to achieve good conductivity [25]. Fortunately, Ive *et. al.* have managed to grow thick (0.8 μm) and conducting AlN:Si layers with electron concentration, n_e, up to 7.4 x 10^{17} cm^{-3} by plasma assisted molecular beam epitaxy (MBE) on 6H-SiC substrates [26]. One of their samples with n_e = 1.4 x 10^{17} cm^{-3} was supplied for us as standard to measure Al content. Si concentration was measured as low as 0.1 at%. Thus, we treat the sample as pure AlN standard. Testing in the EPMA revealed that the sample did not charge when the electron beam was either focused or scanned across its surface. Thus AlN:Si was deemed suitable for use as a standard for measuring Al. Table 3.4 shows the analysing crystals, X-ray lines and standards used for quantitative analysis in this thesis.

Table 3.4 X-ray lines, standards and analysis crystals used in WDX quantative analysis [25].

Element	X-Ray Line	X-Ray Energy (keV)	Standard	WDX Crystal
Aluminium	K_α	1.487	AlN	TAP
Indium	L_α	3.287	InP	PET
Gallium	L_α	1.098	GaN	TAP
Nitrogen	K_α	0.392	GaN	PC1

It is also very important to select a suitable accelerating voltage when determining the quantative measurements. The interaction volume (or penetration depth) depends on the acceleration voltage and the atomic number of the material [14, 27], and can be estimated using Monte Carlo electron trajectory simulation [28] as illustrated in Figure 3.9. The effect of increasing the voltage can be clearly seen: the electrons penetrate further into the sample and the size of the interaction volume- the volume in which the electrons interact with the atoms of the samples- increases. Penetration into the underlying buffer layer will result in inaccuracies in the measurement of the composition of the material. Thus it is desirable to contain the interaction volume entirely within the layer that is of interest. The threshold for In L_α emission is 3.29 keV. The minimum practical accelerating voltage for quantitative analysis is ~ 1.3 times the threshold for X-ray excitation [29]. Hence for In composition measurement, the beam energy should be above 4.3 keV in order to obtain reasonable X-ray counts. The penetration depth of an $Al_{0.83}In_{0.17}N$ material is estimated to be around 120 nm at 5 keV using Monte Carlo simulation.

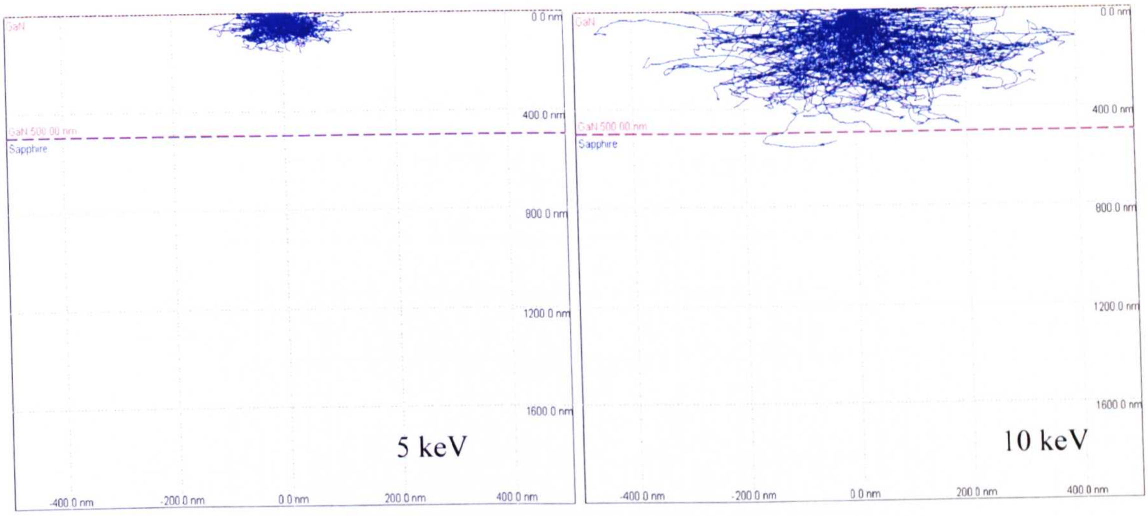

Figure 3.9 Monte Carlo electron trajectory simulations of GaN epilayer on sapphire substrate using beam energies of 5 and 10 keV [28].

Experiments were carried out on $Al_{1-x}In_xN$ epilayers to study the effect of accelerating voltages on the In compositions measured by EPMA system where the In values obtained from Rutherford backscattering spectrometry (RBS) act as the reference, as shown in Figure 3.10. Various $Al_{1-x}In_xN$ epilayers with different In compositions and epilayer thicknesses were used. It is observed that as the accelerating voltage increases, the In composition measured by EPMA system decreases. There is a levelling at around 4.5 to 5 kV for $Al_{1-x}In_xN$ epilayers with thick layers (< 150 nm) whereas no levelling is present for thin $Al_{1-x}In_xN$ epilayers. In addition, the decrease in the In composition is the steepest for the thinnest epilayer (in this case 75 nm). This is because as the accelerating voltage increases, more electrons will penetrate into the GaN buffer layer especially true for thin epilayers. The WDX correction assumes the whole measured volume has the same composition and as a result the extra Ga will impact on the measured In and Al. Hence, the In composition measured by EPMA system will be underestimated at high voltages, indicating that the measured In composition is lesser than the actual In composition. According to Figure 3.10, the measured In composition using EPMA system at an acceleration voltage of 5 kV is close to the RBS value. Therefore in this thesis, 5kV is selected when performing quantative measurement.

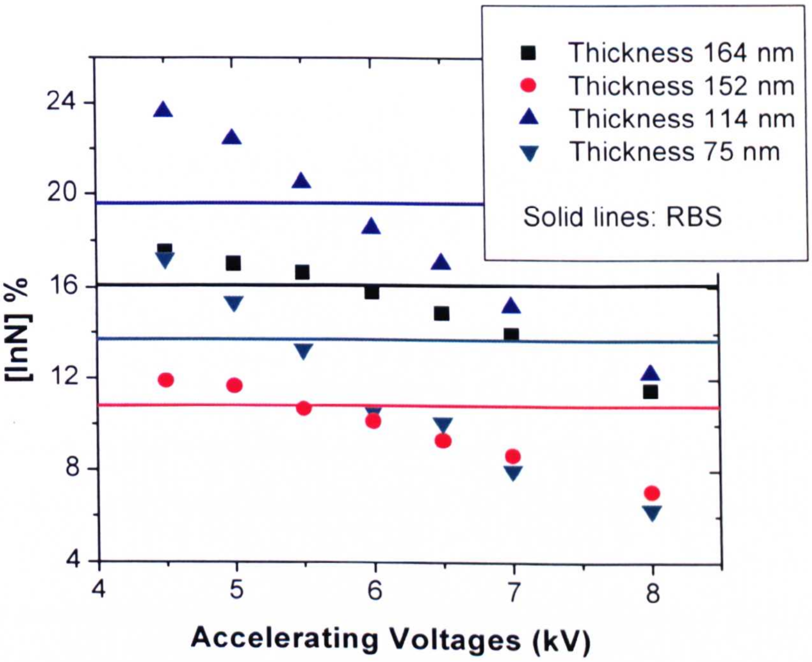

Figure 3.10 In composition measured by EPMA system as a function of accelerating voltages on $Al_{1-x}In_xN$ epilayers of different In composition and epilayer thickness. Solid lines are In compositions obtained using RBS.

3.4.2 Rutherford Backscattering Spectrometry (RBS)

Rutherford backscattering spectrometry (RBS) uses backscattering of charged particles by nuclei in a solid to obtain information such as the type of atoms, the amount of atoms, the thickness of a thin film and the crystalline quality. It involves bombarding a target sample with a high energy ion beam, typically consisting of He^+ ions with energies of a few MeV. Those which are scattered through large angles, i.e. backscattered, are detected using a detector which is sensitive to both their energy and number. Usually an annular detector is used and arranged with large scattering angles (a maximum angle of 170° can be attained).

The atoms in a sample can be identified by RBS because the highest energy of the scattered He^+ ions depends on the mass of the target atoms. The elemental composition and the layer thickness can be determined from a RBS spectrum, i.e. yield as a function of the energy of the backscattered particles [30-32]. As the energy spectrum is quite complicated, a computer program is used to fit the data to obtain both compositional and thickness information. RBS has the advantage of being a direct and standardless technique.

The crystalline quality of a target sample can be determined by the RBS/Channelling technique. Target ions which are incident on the sample at an angle which corresponds to a particular crystal plane travel along the channel between the atomic rows and penetrate much further before backscattering. This effect is known as channelling [30-32] and the corresponding spectrum is known as the channelling or aligned spectrum. This is then compared with the spectrum obtained when the ions are incident at an angle which does not correspond to any of the crystal planes, the so-called random spectrum, as used above to obtain composition and thickness information. If the atoms within the target are displaced from their crystalline lattice site this will result in a higher backscattering yield in relation to a perfect crystal. The ratio of the backscattered yields from the two spectra gives a value for the crystalline quality denoted as χ_{min} and is usually quoted as a percentage. The lower the χ_{min} value, the better the crystalline quality. State of the art values of χ_{min} for GaN are around 2 % [33].

One disadvantage of RBS is that it alters the sample under investigation. Bombardment of the lattice with high energy ions results in the formation of vacancies and interstitials which can join together to form extended defects resulting in degradation of the luminescence obtained from a sample. A black spot is usually seen in PL maps corresponding to the area where the RBS beam was incident [34]. To this end, the RBS measurements described in this thesis were either carried out after luminescence characterisation or were performed on another piece of the same wafer but efforts were made to ensure these were from adjacent regions.

All RBS measurements presented in this thesis were carried out at the Instituto Tecnologico e Nuclea (ITN), Sacavém, Portugal by Dr. Katharina Lorenz together with her PhD student Sérgio Magalhães.

3.5 Electrical Characterisation

The Hall Effect provides a simple method for determining the charge carrier concentration, resistivity and mobility in a semiconductor sample of suitable geometry, and is widely used in research and industrial quality control. Van der Pauw configuration was used in this work.

As originally devised by van der Pauw [35], one uses an arbitrarily shaped (but simply connected, i.e., no holes or non-conducting islands or inclusions), thin-plate sample containing four very small ohmic contacts placed on the periphery (preferably in the corners) of the plate. By measuring the Hall voltage V_H and from the known values of the current I, magnetic field B, sample thickness d, electronic charge q, one can determine the sheet density n_s of charge carriers in semiconductors:

$$n_s = \frac{I.B}{q.V_H} \tag{3.4}$$

The sheet resistance R_S of the semiconductor can be conveniently determined by use of the van der Pauw resistivity measurement technique. The sheet resistivity R_s of an irregular shaped sample is given by [12, 35]:

$$R_s = \frac{\pi}{In2}.(R_{12-34} + \frac{R_{13-24}}{2}).f(\frac{R_{12-34}}{R_{13-24}}) \tag{3.5}$$

where $R_{12\text{-}34} = V_{34}/I$. The current I enters the sample through contact *1* and leaves through contact *2* and $V_{34} = V_4 - V_3$ is the voltage between contacts *4* and *3*. $R_{13\text{-}24}$ is similarly defined. f is correction factor which is a function of the ratio of $R_{12\text{-}34}$ to $R_{13\text{-}24}$. Usually a large value for this ratio is undesirable and suggests that either the contacts are bad or that the sample is inhomogeneously doped.

The mean carrier mobility μ can be calculated simply from the resistivity and sheet density as follows:

$$\mu = \frac{1}{n_s . q . R_s} \tag{3.6}$$

In this work, low temperature (≈ 77K) Hall measurements were conducted using a custom-built system consisting of a Keithley 236 *I-V* source-measure unit, and movable permanent magnets producing a variable magnetic field up to 0.3 T. The *I-V* system can source currents from 100 fA to 100 mA, and measure voltage from 10 μV to 110 V. The magnetic field used in this work was 0.18 T and the intentionally doped samples were cleaved into approximately 5 mm squares. Ohmic contacts on these samples were achieved by annealing the indium dots at the corners.

3.6 Summary

This chapter has summarised the main experimental instrumentation relevant to the studies of the III-nitrides discussed in later chapters. They are photoluminescence (PL) and PL excitation (PLE) spectroscopy for investigating the optical properties, scanning electron microscopy (SEM) and atomic force microscopy (AFM) for the surface measurement, electron probe microanalysis (EPMA) and rutherford backscattering spectrometry (RBS) for the compositional analysis, and Hall Effect for the carrier concentration and mobility.

3.7 References

[1] Donald A. Neamen, *Semiconductor Physics and Devices: Basic Principles*, 3rd Edition, McGraw Hill (2002).

[2] M. Fox, *Optical Properties of Solids*, Oxford University Press (2001).

[3] S. C. Jain, M. Willander, J. Narayan, and R. Van Overstraeten, J. Appl. Phys. **87**, 965 (2000).

[4] A.K. Viswanath, E. Shin, J.I. Lee, S. Yu, D. Kim, B. Kim, Y. Choi, and C.H. Hong, J. Appl. Phys. **83**, 2272 (1998).

[5] M. Smith, G.D. Chen, J.Y. Lin, H.X. Jiang, A. Salvador, B.N. Sverdlov, A. Sverdlov, A. Botchkarev, H. Morko, and B. Goldenberg, Appl. Phys. Lett. **68**, 1883 (1996).

[6] U. Kaufmann, M. Kunzer, M. Maier, H. Obloh, A. Ramakrishnan, B. Santic, and P. Schlotter, Appl. Phys. Lett. **72**, 1326 (1998).

[7] W. G. Otz, N.M. Johnson, J. Walker, D.P. Bour, and R.A. Street, Appl. Phys. Lett. **68** ,667 (1996).

[8] Debbie Amabile, PhD Thesis, University of Strathclyde, *Investigation of the Relationship between Composition and Luminescence Properties of Novel Nitride-based Semiconductors* (2006).

[9] Spectral Resolution Website:
http://www.jobinyvon.co.uk/ukdivisions/OOS/oos1.htm#11

[10] R. Pecharromán-Gallego, PhD Thesis, University of Strathclyde, *Investigations of the Luminescence of GaN and InGaN/GaN Quantum Wells* (2004).

[11] Catalogue: *Oriel Instruments, The Book of Photon Tools*, USA (1999).

[12] Peter Y. Yu and Manuel Cardona, *Fundamentals of Semiconductors: Physics and Materials Properties*, 3rd Ed., Springer-Verlag Berlin, Heidelberg (1996).

[13] Lyuji Ozawa, *Cathodoluminescence: Theory and Applications*, Kodansah VCH (1990).

[14] B. G. Yacobi and D. B. Holt, *Cathodoluminescence Microscopy of Inorganic Solids*, Plenum, New York (1990).

[15] North Arizona State University EPMA Course Notes:
http://www4.nau.edu/microanalysis/Microprobe/Interact-Effects.html

[16] National Renewable Energy Laboratory (NREL) Website on SEM:
http://www.nrel.gov/measurements/scanning.html

[17] AFM Website: http://www.nanotec.es/

[18] CAMECA SX1000 EPMA Website:
http://www.cameca.fr/doc_en_pdf/sx_100_synoptic_poster.pdf with some modifications by Dr. Paul R. Edwards, Department of Physics, University of Strathclyde

[19] R. W. Martin, P. R. Edwards, K. P. O'Donnell, M. D. Dawson, C.-W. Jeon, C. Liu, G. R. Rice, and I. M. Watson, Phys. Stat. Sol. (A) **201**, 665 (2004).

[20] J. J. Friel, *X-ray and Image Analysis in Electron Microscopy*, 2nd Edition, Princeton Gamma-Tech, Inc. Princeton (1998).

[21] R. W. Martin, S. Dalmasso, K. P. O'Donnell, Y. Nakanishi, and A. Wakahara, *A. Yoshida & the RENiBEl Network*, Mat. Res. Soc. Symp. Proc. **743**, 411 (2003).

[22] V. D. Scott, G. Love, S. J. B. Reed, *Quantitative Electron-Probe Microanalysis.* 2nd Edition, Ellis Howard Series in Physics and Its Applications, Ellis Howard Ltd Hemel Hempsted, New York (1995).

[23] University of Calgary, Laboratory for Electron Microbeam Analysis website: http://wwww.geo.ucalgary.ca/UCLEMA/EPMA1.html

[24] North Arizona State University EPMA Course Notes: http://www4.nau.edu/microanalysis/Microprobe/Probe.html

[25] CAMECA SX1000 Website: http://www.cameca.fr/doc_en_pdf/sx100_crystals_and_their_wavelength_sept2003.pdf

[26] T. Ive, O. Brandt, H. Kostial, K. J. Friedland, L. Daweritz, and K. H. Ploog, Appl. Phys. Lett. **86**, 024106 (2005).

[27] K. Kanaya and S. Okayama, J. Phys. D: Appl. Phys. **5**, 43 (1972).

[28] CASINO Software: P. Hovington, D. Drouin, and R. Gauvin, Scanning **19**, 1 (1997).

[29] D. E. Newbury, Nanotechology **1** 103 (1990).

[30] M. V. Yakushev, Lecture Notes, *Ion Beam Techniques*, Class 12-902, University of Strathclyde (2003).

[31] K. Lorenz, N. Franco, E. Alves, I. M. Watson, R. W. Martin and K. P. O'Donnell, Phys. Rev Lett. **97**, 085501 (2006).

[32] L. C. Feldman, J. W. Mayer and S. T. Picraux, *Materials Analysis by Ion Channeling*, Academic Press(1982).

[33] K. Lorenz to R. W. Martin, Private Communication.

[34] M. E. White, PhD Thesis, University of Strathclyde, *Investigation of the Optical Properties, Composition and Local Structure of InGaN* (2002).

[35] L. J. van der Pauw, Philips Research Reports, **13** (1) (1958).

CHAPTER 4

Optical Properties and Surface Morphology of $In_xGa_{1-x}N$/GaN Single Quantum Wells with Various GaN Cap Thicknesses

4.1 Introduction

$In_xGa_{1-x}N$/GaN semiconductor structures have found applications as efficient, robust, short-wavelength-visible- and ultraviolet (UV)-light sources. The ternary alloy $In_xGa_{1-x}N$ has a direct band gap which can be varied from that of GaN (3.5 eV) to that of InN (0.7 eV) by changing the InN composition (x), leading to emission covering the UV to infrared regions of the spectrum. However the difficulty in growing $In_xGa_{1-x}N$ (as mentioned in **Section 2.2.2**) with high InN content and the consequent degradation of the luminescence properties with increasing InN presently limits commercial devices to emission from the UV to amber region of the spectrum with violet, blue and green devices being the most efficient and commonly used [1-2]. On the other hand, organic semiconductors offer excellent luminescence properties, with a greater variety of emission wavelengths and significantly higher photoluminescence efficiencies, but exhibit poor electrical behaviour. Hence, combination of the best attributes of $In_xGa_{1-x}N$-based and organic semiconductors would clearly be an attractive proposition. This could be achieved by transferring the excitations from $In_xGa_{1-x}N$ quantum wells (QWs) into the luminescent organic media.

Previous works specifically relevant to the current investigation involve non-radiative energy transfer from near-surface $In_xGa_{1-x}N$ QWs to either colloidal semiconductor quantum dots [3] or light emitting polymers [4]. Ref. 4 reported a hybrid inorganic/organic semiconductor structure by placing a polyfluorene thin film in sufficiently close proximity to an underlaying $In_xGa_{1-x}N$ QW that the prospect of highly efficient non-radiative Förster resonant energy transfer (FRET) occurs [5-6], as illustrated in Figure 4.1(a). FRET is mediated by dipole-dipole interactions, the magnitude of which depends on the spectral overlap between donor emission and acceptor absorption, and the dipole separation distance [5-6]. Energetic alignment (as shown in the energy level diagram of Figure 4.1(b)) is thus needed in order to maximise the resonant coupling between the inorganic and organic excitation [7]. Thus, in this work, two sets of $In_xGa_{1-x}N$ QWs with different PL peak wavelengths of 390 and 415 nm were studied, which had been designed to match the absorption bands in the organics, in this case polyfluorene copolymer F8DP. The 390 nm single quantum wells (SQWs) have emission matched to the maximum absorption of the polymer whilst the 415 nm samples are intended to be matched to the point where the absorbance of the polymer is 50 % of the maximum.

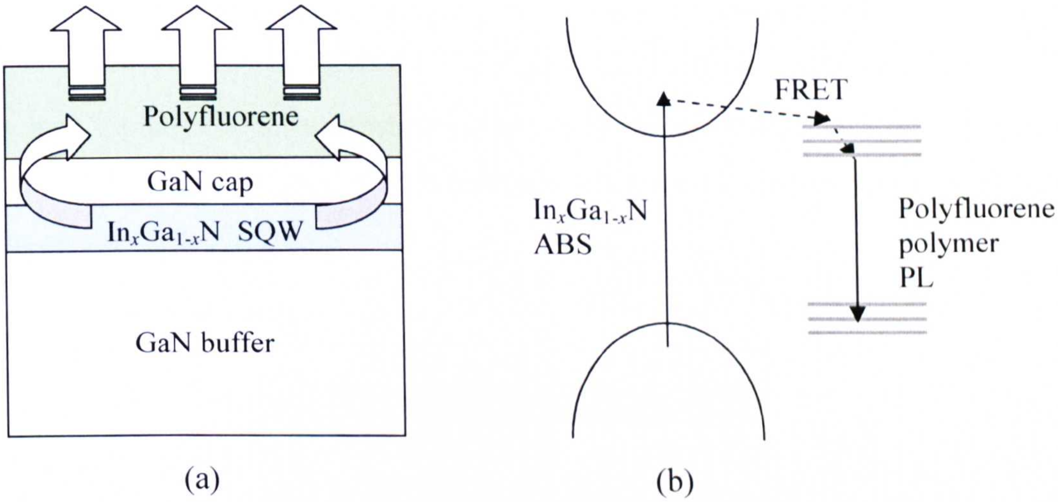

Figure 4.1 (a) Schematic of the hybrid inorganic/organic semiconductor heterostructures and (b) a simplified energy-level diagram illustrating the proposed energy-transfer scheme: excitations initially generated by absorption (ABS) in the $In_xGa_{1-x}N$ QW layer may resonantly Förster transfer (FRET) to the polyfluorene polymer layer following radiatively decay and emit luminescence [4].

Adjusting the separation between the $In_xGa_{1-x}N$ QWs and polymer layers determines the strength of the Förster transfer between them. This is achieved experimentally by varying the GaN cap layer thickness. Typically for light-emitting devices, GaN cap layers are a few tens to hundreds of nanometres thickness. They are often used for a wide variety of reasons ranging from controlling doping, to form a suitable layer for contacts and to prevent the loss of indium during growth. In this chapter, the study of the optical properties and surface morphology of near-surface $In_xGa_{1-x}N/GaN$ SQWs as a function of the thickness of the thin GaN caps from 2.5 to 15 nm will be discussed. The effects of the types of GaN cap on the optical properties and the surface depletion field will also be considered.

4.2 Specific Samples and Experimental Details

The sample structures used in this work were grown at the Institute of Photonics in University of Strathclyde by Dr. Ian M. Watson. The growth method used was metal organic chemical vapour deposition (MOCVD), as explained in **Chapter 2**, in an Aixtron 200-series reactor. Trimethylindium (TMIn), trimethylgallium (TMGa) and ammonia (NH_3) were used as precursors for In, Ga and N respectively.

Two inch *c*-plane sapphire substrates were used. Single $In_xGa_{1-x}N$ QWs, nominally 2.5 nm thick, were deposited on standard non-intentionally-doped (n-i-d) GaN buffer layers as shown in Figure 4.2.

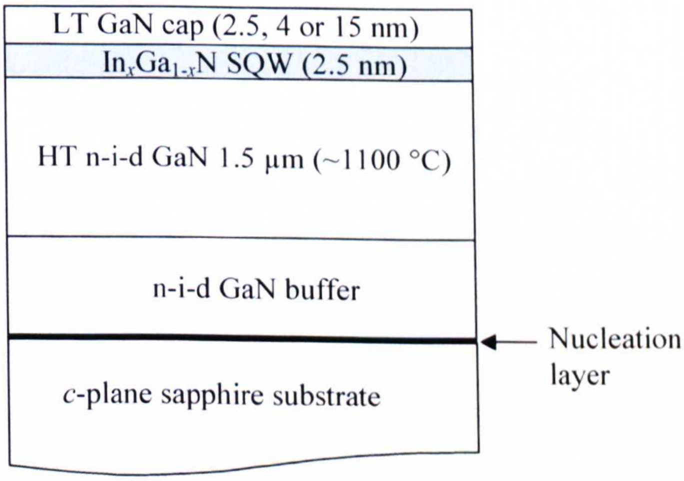

Figure 4.2 Schematic diagram of $In_xGa_{1-x}N/GaN$ single quantum well (SQW) sample (not to scale).

Two series of SQWs with peak emission wavelengths near 390 and 415 nm were deposited at set point temperatures of 860 and 825 °C respectively. Finally n-i-d GaN cap layers with thicknesses of 2.5, 4 and 15 nm were grown at the same temperature as the $In_xGa_{1-x}N$ QWs. The purpose of this is to avoid any temperature ramps and associated growth interruptions. The 2.5 nm QW growth period was 90 s and the longest cap growth period was 540 s. A structure with a 2.5 nm Si-doped GaN cap with doping concentration of approximately 5 x 10^{18} cm^{-3} was grown for comparison with an otherwise equivalent undoped structure. In this study, SQW structures were advantageous because their PL peaks are not broadened by interwell variations. Table 4.1 summarises the growth conditions of $In_xGa_{1-x}N$/GaN SQW samples used in this work.

Table 4.1 Growth conditions of $In_xGa_{1-x}N$/GaN single quantum well samples.

Sample ID	Cap Thickness, Tcap (nm)	Growth Temp (°C)	Cap Type
A) "415 nm series"			
STR424	2.5	825	GaN
STR423	4	825	GaN
STR425	15	825	GaN
B) "390 nm series"			
STR408	2.5	860	GaN
STR410	4	860	GaN
STR409	15	860	GaN
STR426	2.5	845	GaN: Si
STR428	2.5	845	GaN

The "390 nm series" and "415 nm series" each contain samples whose growth conditions differ only in the thickness of the cap. Study of each series provides information on the influence of the cap thickness on the optical properties. Comparison of the two series shows how this effect changes with the peak emission wavelength. In addition, similar structures with the same cap thickness but different doping were compared to evaluate the effect of surface depletion fields.

The photoluminescence (PL) data were measured as described in **Chapter 4**, excited by a 325 nm He-Cd laser. The PL spectra were detected using a cooled CCD spectrograph. The samples were cooled using a closed cycle helium refrigerator. The temperature was varied from around 15 to 300 K using a temperature controller and heater. The surface morphology of the samples with various cap thicknesses were characterised using scanning electron microscopy (SEM) and atomic force microscopy (AFM) techniques.

4.3 Experimental Results and Discussion

4.3.1 Low Temperature PL Spectra

The low temperature PL spectra of "415 nm series" and "390 nm series" samples in log-scale are shown in Figure 4.3 and Figure 4.4, respectively. All spectra exhibit broad, asymmetrical peaks due to emission from the QWs. The $In_xGa_{1-x}N$ quantum well transition energy (or zero-phonon line (0LO)) and its phonon satellites (1LO, 2LO etc.) at the low energy side of the PL spectra are clearly observed as marked by arrows. The appearance of LO-phonon sidebands (LO-PSBs) to the low energy side of the zero-phonon line results from the coupling of excitons to phonons and their relative strength can be expressed by Huang-Rhys parameters as explained previously in **Section 2.6.1**.

In order to obtain accurate information of the integrated emission intensity, peak emission energy, and full-width-half-maximum (FWHM) of the zero-phonon line and its phonon satellites for each of the samples, multi-Gaussian peak fittings following subtraction of a linear background are used as illustrated in Figure 4.5. The zero-phonon line and its phonon satellites are fitted by Gaussians which have the same FWHM while their emission energies and intensities are varied as fit parameters. For each sample the energy separation of successive phonon satellites remains constant at approximately 90 meV, the LO-phonon energy of GaN as observed in the literatures [8-13]. A third phonon satellite (3LO) is clearly seen only in STR408 ("390 nm series" sample with the thinnest cap thickness of 2.5 nm).

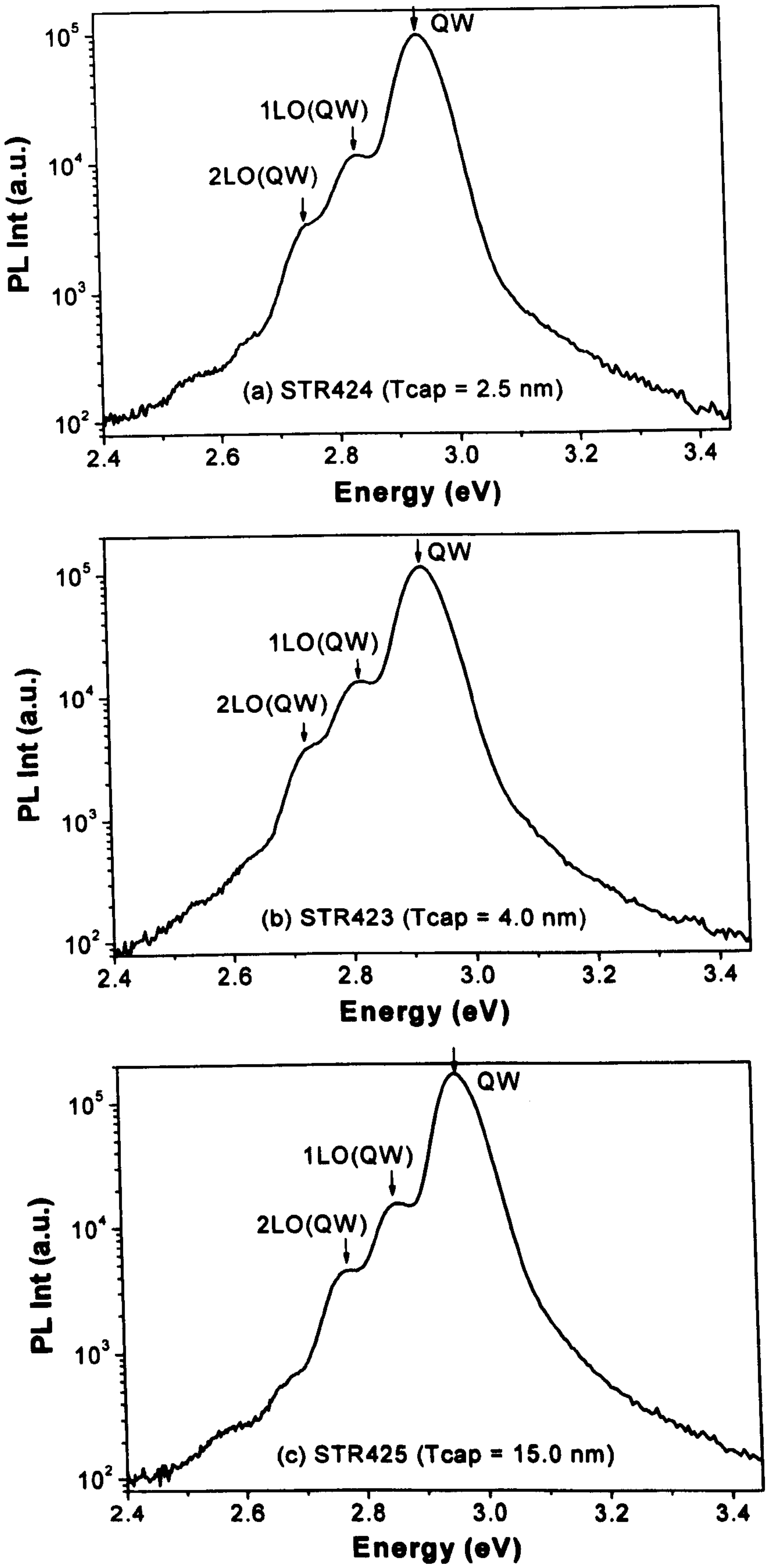

Figure 4.3 Low-temperature (≈ 25 K) PL spectra of "415 nm series samples" (a) STR424, (b) STR423 and (c) STR425.

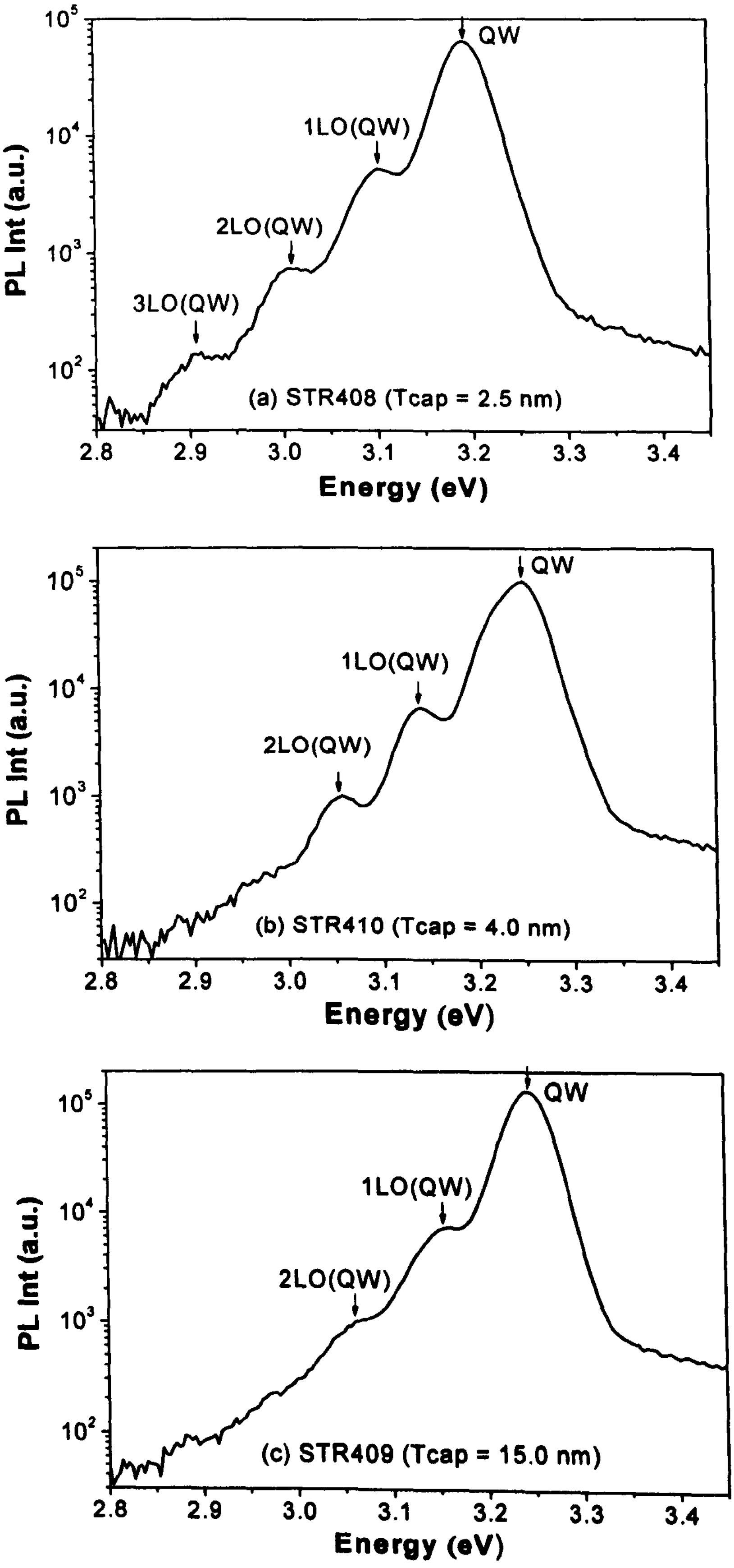

Figure 4.4 Low-temperature (≈ 25 K) PL spectra of "390 nm series samples" (a) STR408, (b) STR410 and (c) STR409.

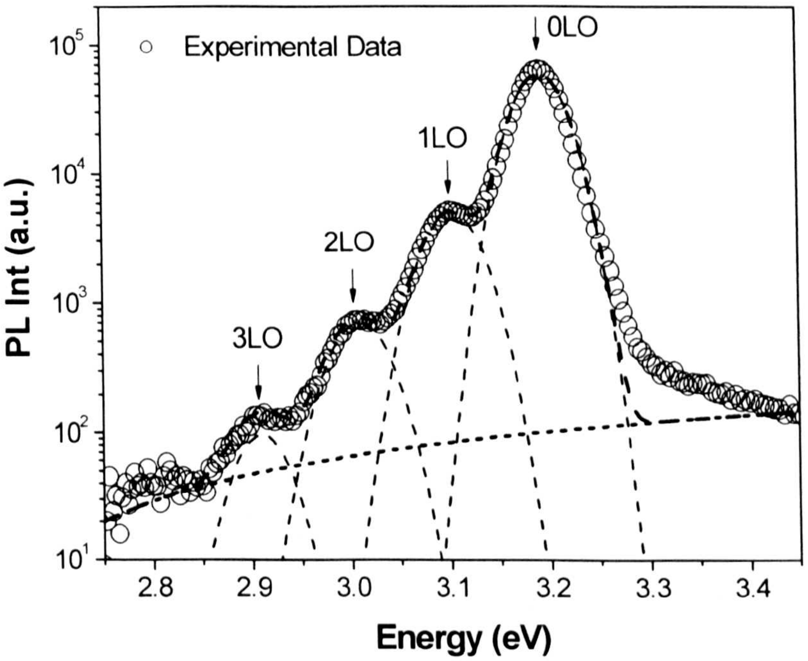

Figure 4.5 Low temperature (≈ 25 K) PL spectrum of STR408 with 2.5 nm thick cap $In_xGa_{1-x}N/GaN$ SQW from the "390 nm series". The dashed and dotted lines show the multi-Gaussian peak fitting and linear background subtraction respectively.

4.3.1.1 Zero-Phonon Line vs. Cap Thickness

The intensity, peak energy and FWHM of the zero-phonon line for all samples are plotted against the thickness of the GaN cap as shown in Figure 4.6. Similar trends are seen for both series. The PL intensity increases by almost 2 times as the cap thickness increases from 2.5 to 15 nm. Larger values of FWHM are seen for the thinner cap (2.5 and 4 nm) samples compared to those with a thick cap of 15 nm. The PL is thus seen to be degraded for the thinner cap samples, as evidenced by the decrease in PL intensity accompanied by an increase in FWHM.

In addition, a more pronounced decrease in the line-width for the shorter wavelength series is observed. These degradation behaviours may be related to the increasing effects of the surface, for example surface losses. The surface loss is generally classified into three different mechanisms: absorption, scattering and radiation. If the surface imperfections and surface roughness increase, the surface scattering losses increase. Such scattering effect is more pronounced at shorter wavelengths.

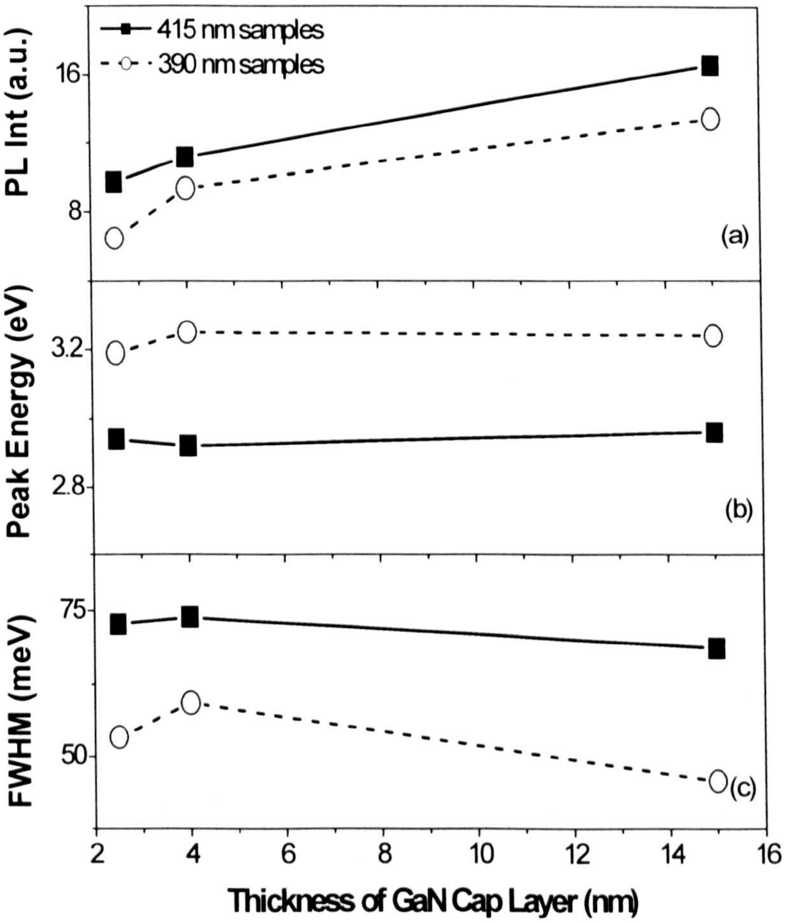

Figure 4.6 **(a) Integrated intensity, (b) peak emission energy and (c) FWHM of the zero-phonon line peak for the two series of $In_xGa_{1-x}N/GaN$ SQWs as a function of GaN cap thickness.**

It is seen in Figure 4.6(b) that there is no significant change in the peak emission energy as the cap thickness is varied for both long (415 nm) and short (390 nm) wavelength series samples. As discussed in **Section 2.6.3**, the electric fields that appear in III-nitride materials are the consequence of strong spontaneous and piezoelectric (strain-induced) polarisation effects. The influence of the electric field on the recombination process can be described using the quantum-confined Stark effect (QCSE) which will result in a red shift in the wavelength. Thus, the absence of significant change in the peak emission energy suggests that the electric field is not changing regardless of the variation of the cap thickness.

4.3.1.2 LO-Phonons and Huang-Rhys Parameters vs. Emission Energy

Let us compare the intensities of the phonons of the $In_xGa_{1-x}N$ SQW samples at low temperature. Figure 4.7(a) shows the ratio of the intensity (I_0/I_1) of zero-phonon line (0LO) to that of the first phonon satellite (1LO), as a function of the emission energy of main peak (0LO), for current samples with thick cap layers (≥ 10 nm) including an earlier 390 nm sample with cap thickness of 10 nm and data from the literature carried out by Graham *et. al.* [8], Pecharromán-Gallego *et. al.* [9] and Kalliakos *et. al.* [11]. Based on the literature data, the ratio increases with increasing peak energy of the main peak, and approaches 14 at the highest energies while for lower energies is around 2. The new samples used in this work fit the trend and, in fact, extend the plot to higher values, in excess of 19 for an emission energy of approximately 3.2eV.

Using Equation (2.7) in **Section 2.6.1**, one can easily work out a theoretical expression for the intensity ratio of successive phonon satellites (*n* and *n* + 1), and hence by comparing these relative intensities the Huang–Rhys parameters (*S*) can be obtained as follows [8-16]:

$$S_n = (n+1)\left(\frac{I_{n+1}}{I_n}\right) \tag{4.1}$$

where I_n is the integrated intensity of the n^{th} phonon satellite and 1LO/0LO will be referred to as S_0, 2*2LO/1LO as S_1, etc.

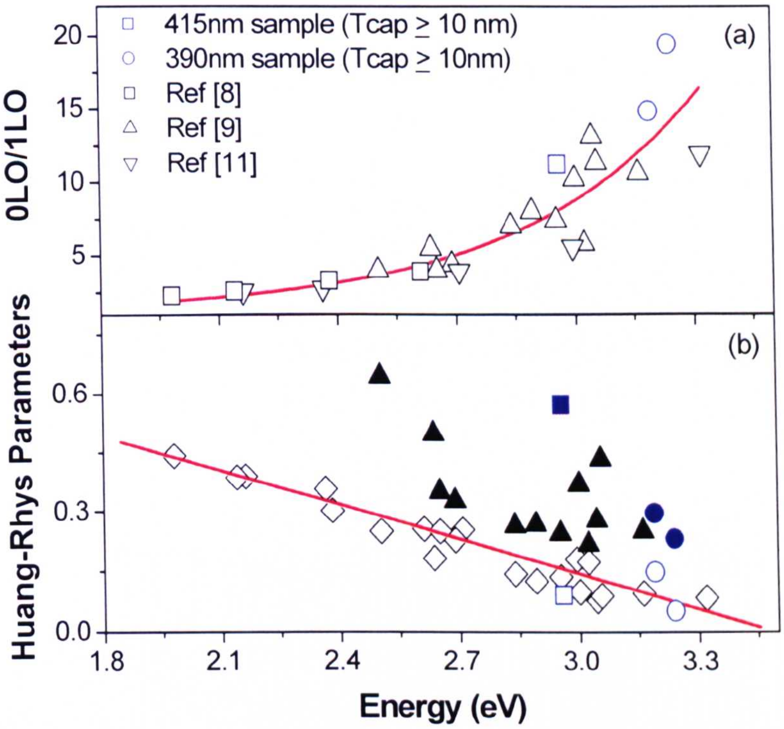

Figure 4.7 **(a) Ratio of the intensity of the zero-phonon line (0LO) to 1st phonon satellite (1LO) for thick cap samples (b) Huang-Rhys parameters, S_0 (open symbols) and S_1 (closed symbols) as a function of zero-phonon line peak emission energy. The solid triangles are from Ref. 9 and the open diamonds are all the data from Ref. 8, 9 and 11. Symbols in blue are from the current work.**

Figure 4.7(b) plots the Huang-Rhys parameters S_0 and S_1 as a function of emission energy. It is observed that S_0 shows a linear dependence on emission energy whilst S_1 has a higher degree of scatter. In addition, the values of S_1 are larger than S_0. The reason that accounts for the fact that the ratio of S_0 is smaller than S_1 is that only strongly localised excitons contribute to the intensity of the phonon satellites whereas all recombining excitons contribute to the zero-phonon line [9-10, 14-18]. Therefore the value of S determined from the ratio of the first satellite to the zero-phonon line will be smaller than the values determined from the ratios of successive satellites. Furthermore, comparison of the magnitudes of S_1 and S_0 can thus lead to an estimation of the fraction of the more strongly localised excitons.

4.3.1.3 Huang-Rhys Parameters vs. Cap Thickness

For the present samples the form of the LO-phonon sidebands (PSBs) can also be analysed as a function of GaN cap thickness. Clear variations are observed, as shown in Figure 4.8, with similar behaviour in both series of samples. The intensity ratio of the first phonon satellite and the zero-phonon line (given by S_0) decreases as the cap thickness increases from 2.5 to 15 nm. At the same time S_1 shows an insignificant change and remains at all times larger than S_0. Therefore the thinner cap (2.5 and 4 nm) samples have smaller values for S_1/S_0 than those with thicker (15 nm) caps.

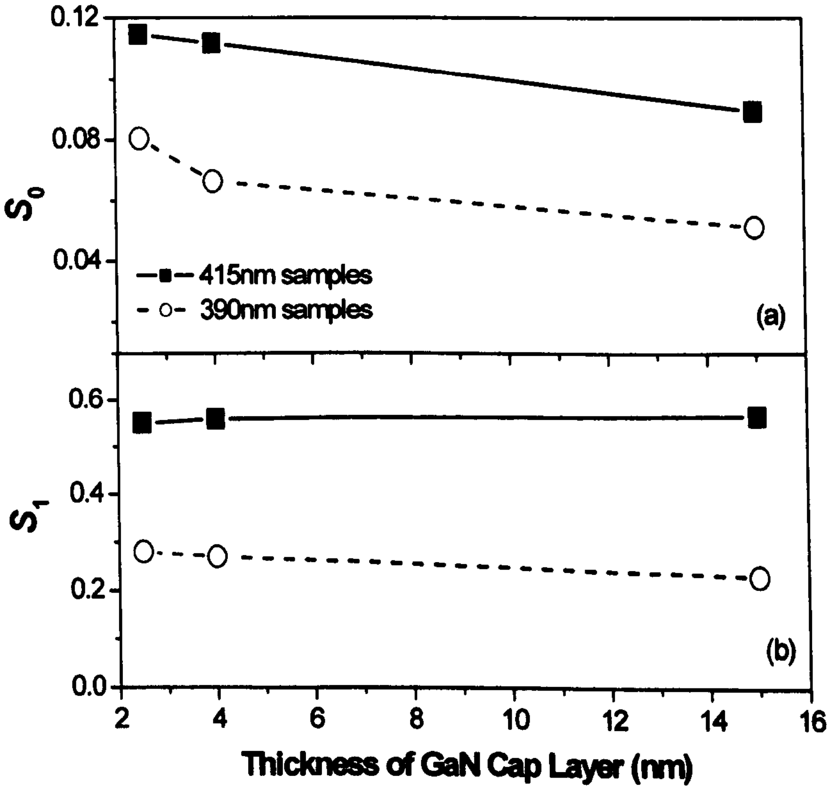

Figure 4.8 Huang-Rhys parameters S_0 and S_1 as a function of GaN cap thickness.

4.3.1.4 Analysis

A factor that needs to be considered here is any change in density of excess carriers excited within the wells. The optical absorption length for the 325 nm excitation wavelength in the GaN cap layer is 80 nm [19], much larger than the thickest cap layer of 15 nm used in this work. Therefore the excitation light is absorbed everywhere throughout the GaN cap layer, generating electron-hole pairs. The literature value [19] for the GaN absorption coefficient (1.2 x 10^7 m^{-1} at 3.8 eV) indicates that the rate of generation of excess carriers in the well decreases by less than a factor of 1.2 when the depth increases from 2.5 to 15 nm. Furthermore the carrier density within the wells will be determined mainly by diffusion within the GaN below the well. There is some scatter in the published values of the minority carrier diffusion lengths for *n*-GaN but all values are considerably greater than our cap thicknesses, for example 200 nm as stated in Ref. 20. As a result, the number of carriers reaching the wells will not vary strongly with the cap thickness. However, the movement of the carriers to the surface could be an issue but there are reports of work on surface quantum wells point to very low values for the surface recombination velocity for GaN [21-22]. As reported in Boroditsky *et. al.* [22], the fraction of carriers reaching the well approaches 100 % if the cap layer is thinner than the diffusion length and the surface recombination velocity is small which are applicable in this work. Furthermore, it is thought to be unlikely that there is significant alteration to the SQWs occurred during cap layer growth, in view of the use of identical growth temperature for the SQW and cap, and the similar timescales for the two growth steps. Therefore there is no significant change in density of excess carriers excited within the wells as the cap thickness varies.

As discussed in **Chapter 2**, III-nitride materials have strong polarisation charges. Both spontaneous and piezoelectric polarisations are, in general, important, but for the $In_xGa_{1-x}N$/GaN QW system, the piezoelectric field is expected to dominate due to the strong coherent strain built in these systems [23-24]. At an outer surface, such polarisation charges are expected to have a strong influence on the pinning of the Fermi level. In the common case of Ga face surfaces a pinning at the valence band edge or possibly in the lower part of the band gap is expected [25]. Since the Fermi level further inside the grown structure is typically close to the conduction band edge, a depletion region is formed close to the surface [24-26]. Since the QW structures used in this work are very near to the surface, it is important to consider the influence of the surface depletion field on the luminescence properties. This can be done by comparing the PL spectra of samples that differ only in the doping concentration within the caps.

The low temperature (25 K) PL spectra from the present SQW samples with n-i-d of doping concentration of approximately 5 x 10^{16} cm^{-3} and Si-doped of 5 x 10^{18} cm^{-3} caps are compared and presented in Figure 4.9. The GaN cap thickness is 2.5 nm.

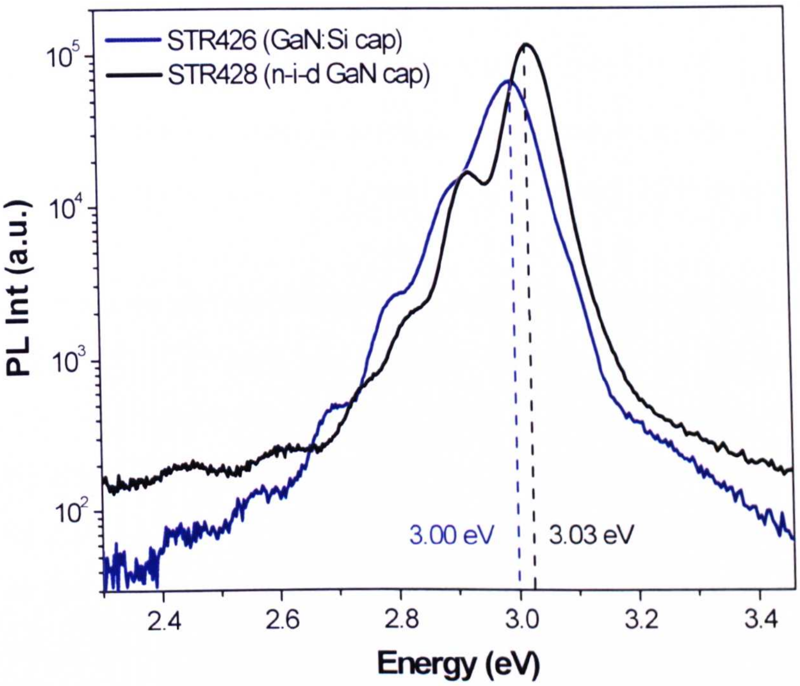

Figure 4.9 **Low-temperature (≈ 25 K) PL spectra of the Si-doped 2.5 nm cap sample (STR426) and otherwise identical n-i-d cap sample (STR428).**

It is observed that there is no significant change (a small change of 30 meV) in the peak emission energy although the doping has resulting in some peak broadening due to the impurity scattering. The maximum strength and the width of the surface depletion fields for the n-i-d and Si-doped layers are estimated using Poisson's equations and Gauss's law as follows:

$$\frac{d^2\phi}{dx^2} = \frac{-\rho}{\varepsilon_0\varepsilon_r} = \frac{-q}{\varepsilon_0\varepsilon_r}(p - n + N_D^+ - N_A^-) \qquad (4.2)$$

$$x_d = \sqrt{\frac{2\varepsilon_0\varepsilon_r[\phi(x)]}{qN_D^+}} \qquad (4.3)$$

$$E_{\max} = \frac{-qN_D^+}{\varepsilon_0\varepsilon_r}(x_d) \qquad (4.4)$$

where ϕ is the potential, ρ is the charge density, ε_0 is the free permittivity, ε_r is the dielectric constant, q is the electron charge, p (n) is the hole (electron) concentration, N_D^+ (N_A^-) is the charged donor (acceptor) concentration, x_d is the depletion width and E_{max} is the maximum depletion field. In this calculation, the parameters and assumptions used are:

- Surface potential $\phi(x = 0)$ of 1.7 eV is obtained from Ref. 27;
- Hole (p) and electron (n) concentration in the depletion region is equal to zero;
- No acceptor concentration ($N_A^- = 0$) and the donors are fully ionised ($N_D^+ = N_D$)

The maximum strength and the width of the surface depletion fields are calculated to be 0.17 MV/cm (0.72 MV/cm) and 200 nm (8 nm) for the n-i-d (Si-doped) cap samples. In the n-i-d sample the depletion field is much smaller than the internal field (> 1 MV/cm), therefore it is not surprising that variations in the depletion field have no significant effect. Although there is a large increase in the surface depletion field by 5 times as the cap doping increases by two orders of magnitude, it is still smaller than the internal field and the PL peak energy remains almost unchanged. Thus the influence of surface depletion field on the optical properties is not significant. Hence, it is suggested that the degradation of PL as the cap thickness reduces is related to the increasing detrimental effects of the surface.

The changes in the strength of $In_xGa_{1-x}N$ QW LO-phonon satellites, manifested by variations in the Huang-Rhys parameters S_0 and S_1, can be associated to the changes in the localisation of the excitons and/or the effects of the intense internal electric fields, as explained in **Chapter 2**. For these samples, the earlier figure (Figure 4.6) shows that the PL peak emission energies do not change with GaN cap thickness. This indicates that the electric field is not changing. Therefore the variations in the Huang-Rhys parameters are thought to be dominated by the additional localisation of the excitons. In fact, similar behaviour has been observed for thick $Al_yGa_{1-y}N$ epilayers where the intensity of the LO-phonon satellite relative to that of the zero-phonon line increases with AlN content up to $Al_{0.7}Ga_{0.3}N$ [28]. Since the macroscopic electric fields are known to be very small in $Al_{0.7}Ga_{0.3}N$ samples, the increasing strength of the phonon satellites is most likely related to increasing alloy disorder induced localisation. The increase of S_0 and the reduction of S_1/S_0 for the thinner cap samples both point to a greater amount of localisation for the excitons present in these samples. Following the approach of Ref. 16 one can estimate that the fraction of strongly localised excitons increases from 16 % (23 %) to 21 % (29 %) for the 415 nm (390 nm) series samples as the cap thickness decreases from 15 to 2.5 nm. The cause of this could be surface roughness or defects, which would go some way to explain the overall degradation of PL described earlier.

In order to verify the surface roughness hypothesis, scanning electron (SEM) and atomic force (AFM) microscopies were performed on the "415 nm series" samples. The SEM and AFM images of these samples are presented in Figure 4.10. SEM images reveal pits on the sample surfaces which can be seen more clearly at higher magnifications using AFM. These nanometre scale pits appear as dark contrast. It is observed that the pit density increases as the cap thickness decreases. Also, clear atomic step patterns are observed. The pit density was evaluated for a 2 × 2 μm area of each sample examined by AFM by dividing it into 16 squares, in a 4 × 4 grid, and first counting the numbers of pits in each individual square. The pit density is estimated to increase from 2.4 to 3.3×10^9 cm^{-2} as the cap thickness decreases from 15 to 2.5 nm. These pits are observed to be located at the end of the atomic steps, and are believed to be the termination sites on the surface of threading dislocations with mixed and pure screw character [29]. Threading dislocations are undesirable in the electroluminescent devices as they provide current leakage paths and non-radiative recombination sites.

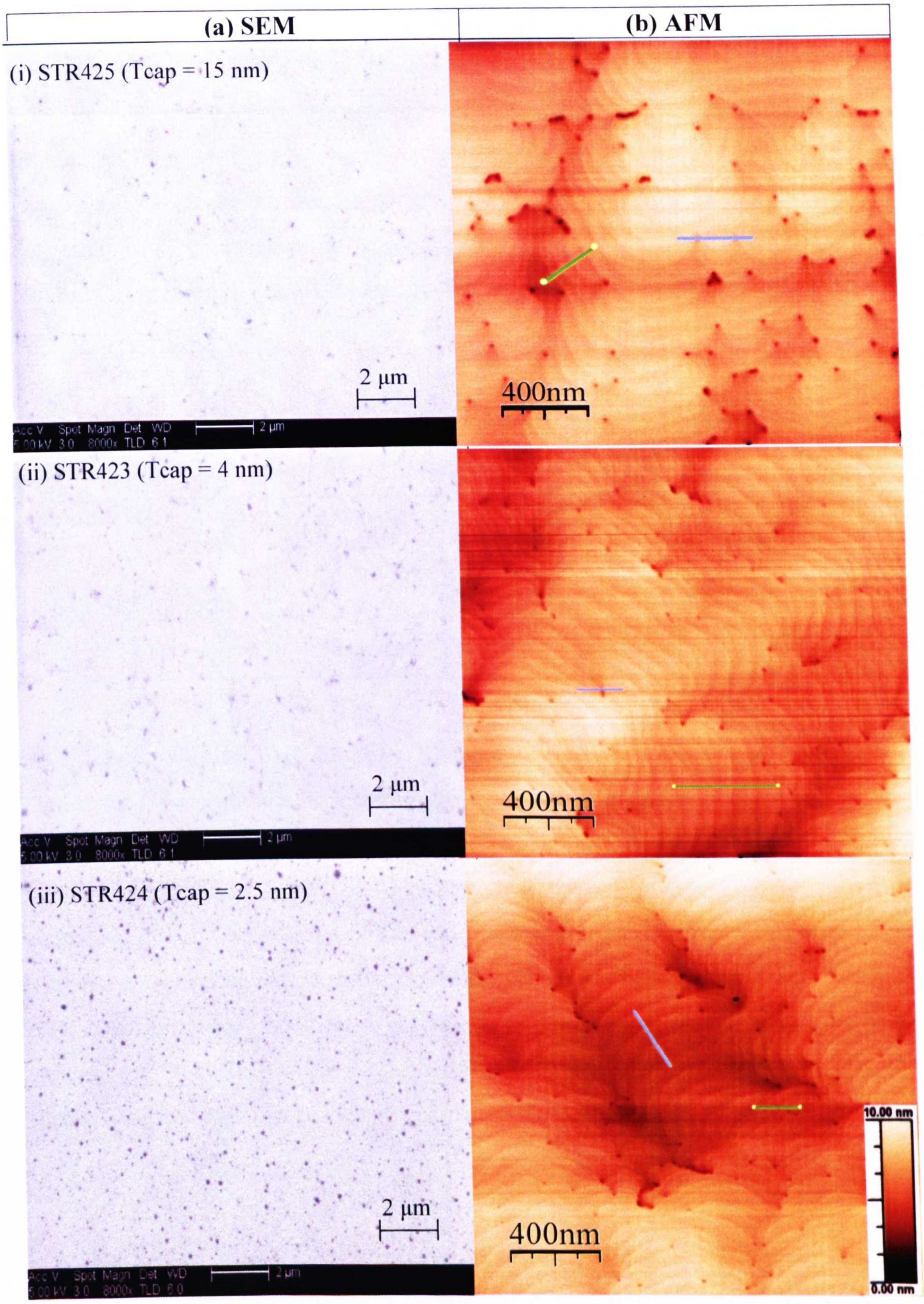

Figure 4.10 (a) SEM and (b) AFM images of "415 nm series" samples (i) STR425, (ii) STR423 and (iii) STR424. Straight lines (green and blue) are those used to determine the pit diameter (profiles not shown).

The pit density, pit diameter and root-mean-square (RMS) surface roughness are summarised in Table 4.2. The RMS surface roughness increases from 0.96 to 1.58 nm as the cap thickness decreases. At the same time the pit diameter is observed to increase from 34 to 54 nm as the cap thickness increases from 2.5 to 15 nm, as expected for the opening out of V-pits. SEM and AFM images confirm that the degradation of PL intensity and larger PL linewidth, and greater amount of exciton localisation present in structures with thinner caps than those with thick cap is due to the increase in the surface roughness.

Table 4.2 Pit density, pit diameter and RMS surface roughness of "415 nm series" samples determined by AFM technique.

Sample ID	Tcap (nm)	Pit density (cm^{-2})	Mean pit diameter (nm)	RMS surface roughness (nm)
STR425	15	2.4×10^9	54	0.96
STR423	4	2.8×10^9	47	0.95
STR424	2.5	3.3×10^9	34	1.58

4.3.2 Temperature-Dependent PL Spectra

Figure 4.11 presents the temperature-dependent PL spectra of "415 nm series" samples. The LO-phonon sidebands and PL peak intensity decreases as the temperature increases from ≈ 15 K to room temperature. This is due to thermal quenching effect. The position of the peak emission energy is observed to shift as the temperature varies as indicated by the dotted line in the figure. Figure 4.12 plots the peak emission energy position as a function of temperature for these samples with various cap thickness where a decrease-increase-decrease pattern (or called 'S-shaped') dependence can be clearly visible in all cases.

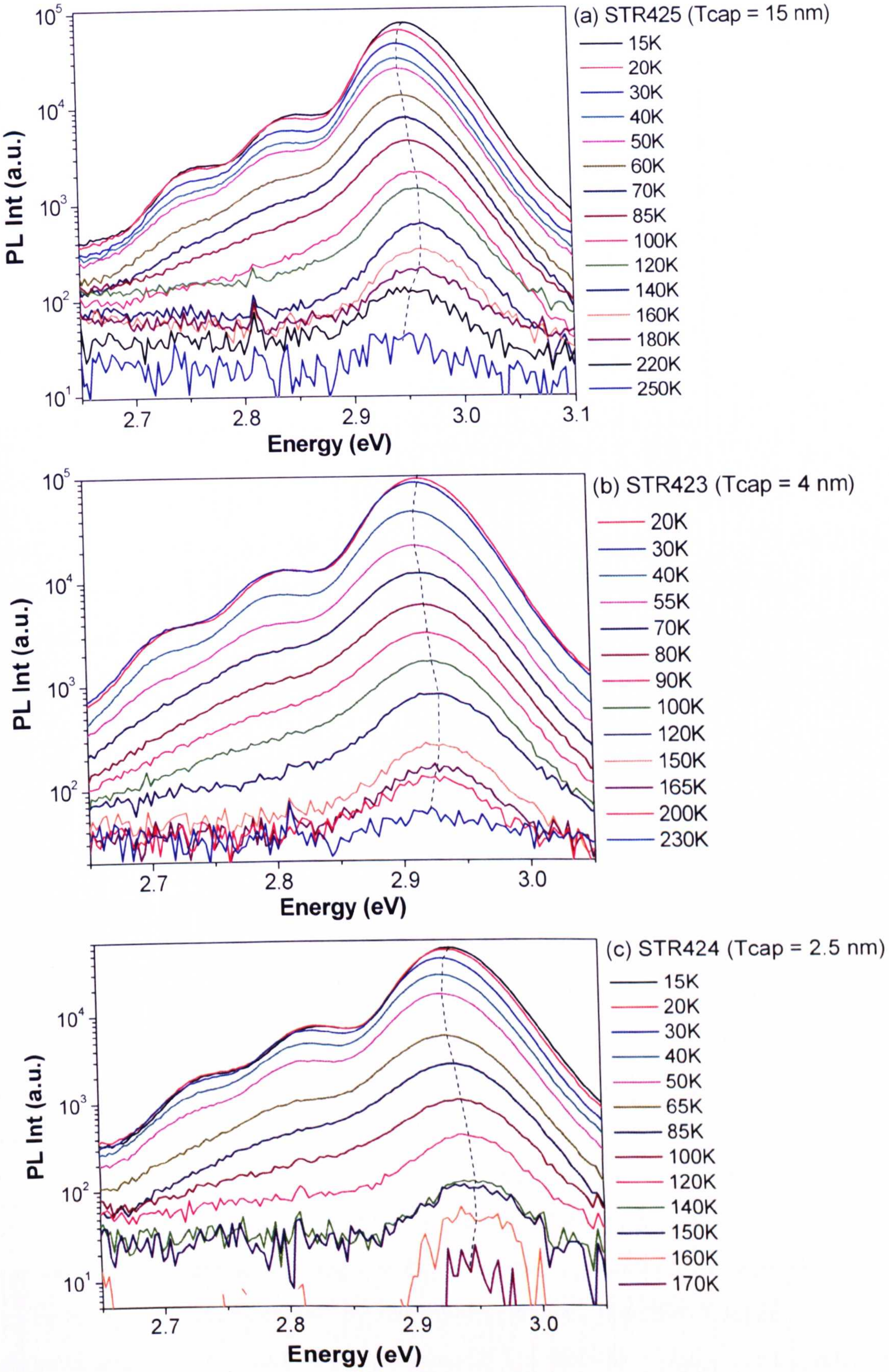

Figure 4.11 **Temperature-dependent PL spectra of "415 nm series" samples (a) STR425, (b) STR423 and (c) STR424. Dashed lines act as guide to the eye.**

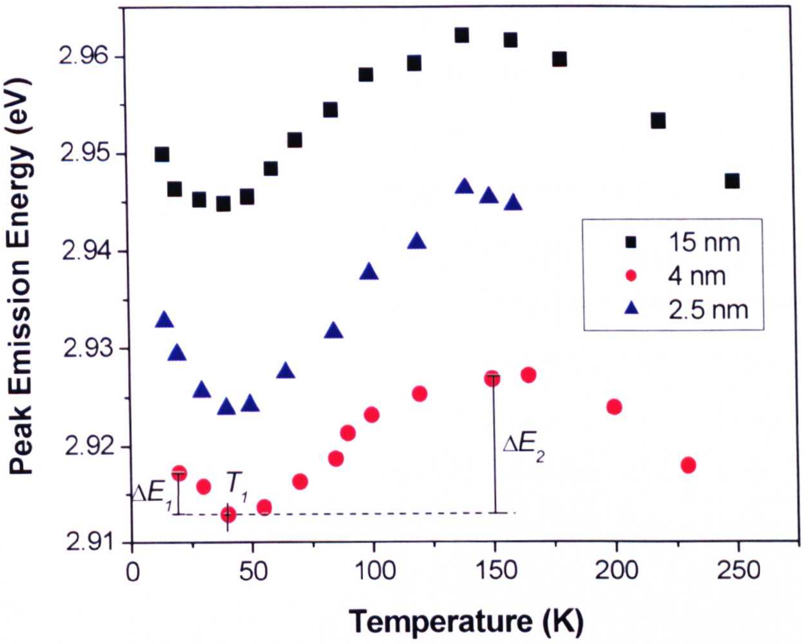

Figure 4.12 Position of the main peak emission energy as a function of temperature for "415 nm series" samples with cap thickness of 2.5, 4 and 15 nm. T_1 is defined as the temperature at which the blue-shift starts; ΔE_1 as the initial red-shift at low temperature; and ΔE_2 as the subsequent blue-shift.

'S-shaped' behaviour has been reported in several papers describing a number of material systems including $In_xGa_{1-x}N/GaN$ [30-33], $GaAs_xN_{1-x}/GaAs$ [34], $GaIn_xP_{1-x}/GaAs$ [35] and $Al_xGa_{1-x}N/GaN$ [36-37]. Several explanations for this behaviour have been given earlier. It has been proposed by Cho *et. al.* [30] that the cause of the temperature-induced 'S-shaped' PL shift is a change in the carrier recombination dynamics due to inhomogeneity of the potential energy states and carrier localisation in the quantum wells as well as the decreasing carrier lifetimes in the blueshift region. The inhomogeneity of the potential energy is attributed to various factors such as composition fluctuations, layer thickness variations and possibly defects in the quantum wells. The initial red-shift (ΔE_1) in the peak energy at low temperature occurs as the radiative recombination process is dominant and the carrier lifetime increases, giving the carriers more opportunity to relax down into lower energy tail states caused by the inhomogeneous potential fluctuations before recombining. Above a certain temperature (T_1), a blue-shift (ΔE_2) occurs since the dissociation rate is increased and other non-radiative processes become dominant.

The carrier lifetime decreases greatly and these carriers recombine before reaching the lower energy tail states. As the temperature increases further, since non-radiative recombination processes are dominant and the lifetimes are almost constant, the carriers are less affected by the change in carrier lifetime so that the blue-shift behaviour becomes smaller. Temperature induced bandgap shrinkage in the material therefore results in an overall red-shift in the peak emission energy. The definitions of T_1, ΔE_1 and ΔE_2 can be found in Figure 4.12. The 'S-shaped' behaviour is conventionally interpreted as a sign of localisation due to inhomogeneities of the potential and the carrier localisation in its band-tail states. It is thus of interest to consider how the behaviour and the T_1, ΔE_1 and ΔE_2 vary with emission energy and cap thickness.

Figure 4.13 plots the temperature at which the blue-shift starts (T_1) and the energy ranges for the initial red-shift at low temperature (ΔE_1) and the subsequent blue-shift (ΔE_2) as a function of the emission peak energy, for current samples including the data from the earlier publications $In_xGa_{1-x}N$ SQWs [33], 12-period $In_xGa_{1-x}N$ MQW [30] and a 5-period $In_xGa_{1-x}N$ MQW [38]. Based on the literature data, the start of the blue-shift (T_1), and both ΔE_1 and ΔE_2 show a general decrease as the emission peak energy increases which corresponds to higher In content. The new samples used in this work are similar in size and lie in the trend.

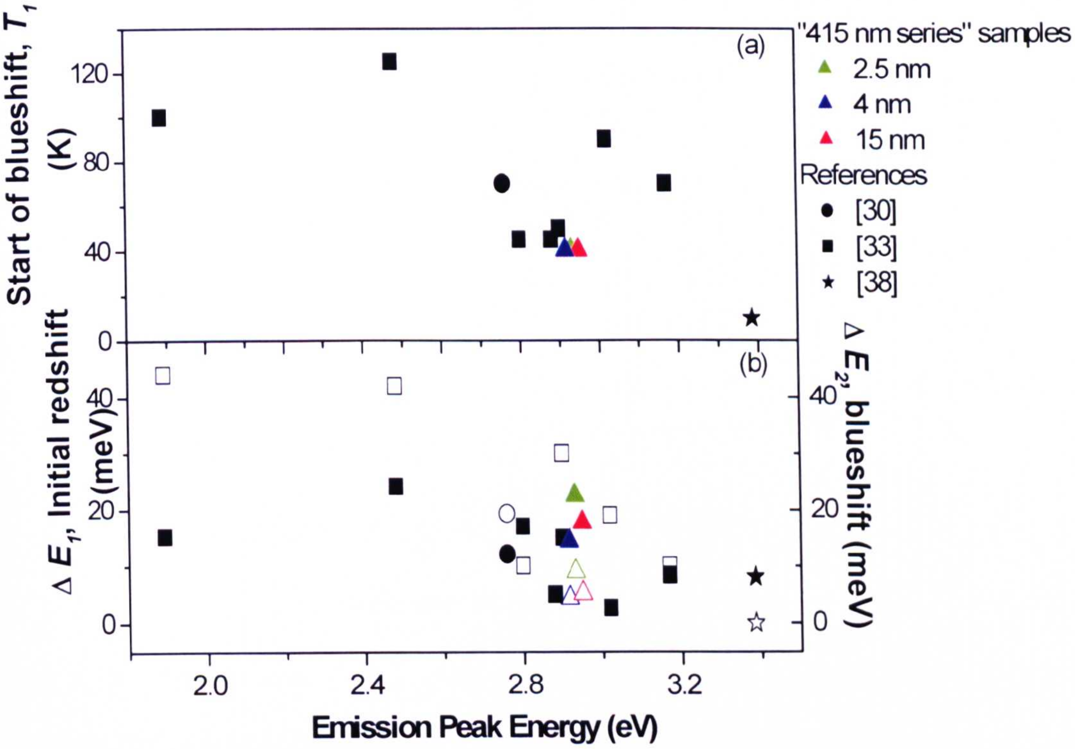

Figure 4.13 (a) Start of the blue-shift section, T_1 as a function of the emission peak energy; (b) magnitude of the blue-shift (ΔE_2, filled symbols) and the initial red-shift at low temperature (ΔE_1, open symbols) as a function of the emission peak energy. Triangles are from this work, and the squares, circles and stars from Ref. 30, 33 and 38 respectively.

For the present samples, the form of the change in energies ΔE_1 and ΔE_2 can also be analysed as a function of GaN cap thickness. Clear variations are observed as shown in Figure 4.14, with similar behaviour in both series of energies. The initial red-shift, ΔE_1, and subsequent blue-shift, ΔE_2, are the largest for the thinnest cap sample. This indicates that the thinnest cap (2.5 nm) sample has the largest degree of carrier localisation. This is in agreement with the calculated localisation as explained above in **subsection 4.3.1.4**. It is believed that the increase in the carrier localisation is likely to be related to the increase in the interface roughness as supported by SEM and AFM results in Figure 4.9.

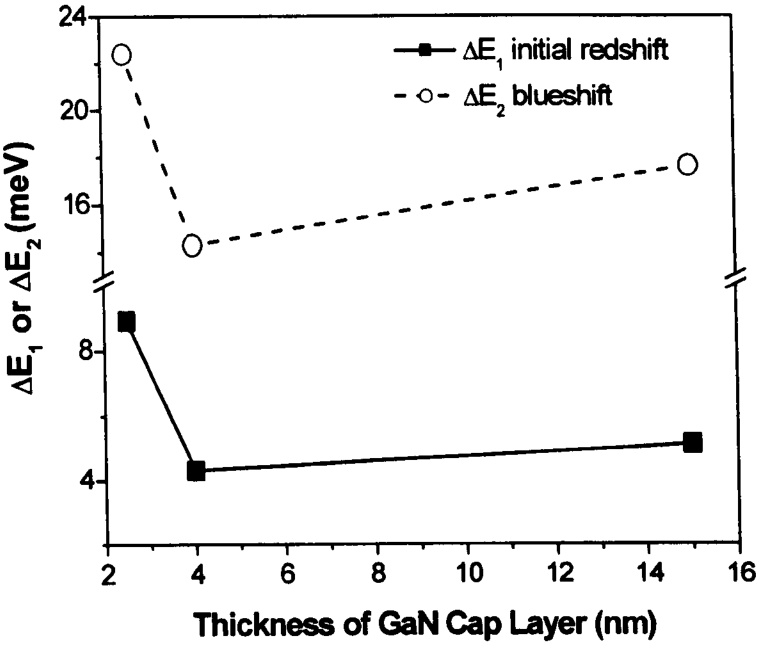

Figure 4.14 **Magnitude of the blue-shift (ΔE_2) and the initial red-shift (ΔE_1) as a function of GaN cap thickness for "415 nm series" samples.**

4.4 Summary

Low temperature photoluminescence (PL) spectra from two series of $In_xGa_{1-x}N$/GaN single quantum well structures have been studied as a function of GaN cap thickness (ranging from 2.5 to 15 nm). The motivation of using thin cap layer is to strengthen the non-radative Förster resonant energy transfer (FRET) from the underlaying $In_xGa_{1-x}N$ quantum well to the polyfluorence thin film [4]. The structures with thinner caps are found to give reduced PL intensity and larger PL linewidth indicating degradation due to the increasing effects of the surface. The relative strength of the LO-phonon satellites is found to have a clear dependence on the cap thickness. SEM and AFM images show that the RMS surface roughness and pit density increase as the cap thickness decreases. Temperature-dependent PL spectra display the anomalous 'S-shaped' emission behaviour of the quantum well energy peak, indicating the presence of carrier localisation. The thinner sample exhibits a larger rate of change in the energy (initial redshift ΔE_1 and blueshift ΔE_2) at low temperature range than thicker samples. Analysis of the Huang-Rhys parameters, peak energies, surface morphology and temperature-dependent PL spectra suggests that the amount of localisation excitons increases as the cap thickness is reduced and is related to the increase in the surface roughness.

4.5 References

[1] B. Gil, *Low-Dimensional Nitride Semiconductors*, Oxford University Press, New York (2002).

[2] R. W. Martin, *In Search of the Blue Light*, Chemistry & Industry (March 1999).

[3] M. Achermann, M. A. Petruska, S. Kos, D. L. Smith, and V. I. Klimov, Nature (London) **429**, 642 (2004).

[4] G. Heliotis, G. Itskos, R. Murray, M. D. Dawson, I. M. Watson, and D. D. C. Bradley, Adv. Mater. (Weinheim, Ger.) **18**, 334 (2006).

[5] T. Förster, Discuss. Faraday Soc. 27, 7 (1959).

[6] T. Virgili, D. G. Lidzey, D. D. C. Bradley, Adv. Mater. 12, 58 (2000).

[7] D. Basko, G. C. La Rocca, F. Bassani, V. M. Agranovich, Eur. Phys. J. B. **8**, 353 (1999).

[8] D. M. Graham, A. Soltani-Vala, P. Dawson, M. J. Godfrey, T. M. Smeeton, J. S. Barnard, M. J. Kappers, C. J. Humphreys, and E. J. Thrush, J. Appl. Phys. **97**, 103508 (2005).

[9] R. Pecharromán-Gallego, P.R. Edwards, R.W. Martin, and I.M. Watson, Mater. Sci. & Eng **B93**, 94 (2002).

[10] P. P. Paskov, P. O. Holtz, B. Monemar, S. Kamiyama, M. Iwaya, H. Amano, and I. Akasaki, Phys. Stat. Sol. (B) **234**, 755 (2002).

[11] S. Kalliakos, X.B. Zhang, T. Taliercio, P. Lefebvre, B. Gil, N. Grandjean, B. Damilano, and J. Massies, Appl. Phys. Lett. **80**, 428 (2002).

[12] S. Kalliakos, P. Lefebvre, X.B. Zhang, T. Taliercio, B. Gil, N. Grandjean, B. Damilano, and J. Massies, Phys. Stat. Sol. (A) **190**, 149 (2002).

[13] L. T. Tan, R. W. Martin, I. M. Watson, and K. P. O'Donnell, Appl. Phys. Lett. **89**, 101910 (2006).

[14] I. Brener, M. Olszakier, E. Cohen, and E. Ehrenfreund, Phys. Rev B **46**, 7927 (1992).

[15] J. J. Hopfield, J. Phys. Chem. Solids **10**, 110 (1959).

[16] D. J. Mowbray, O. P. Kowalski, M. S. Skolnick, M. Hopkinson, and J. P. R. David, Superlattices Microstruct. **15**, 313 (1994).

[17] K. J. Nash, M. S. Skolnick, P. A. Claxton, and J. S. Roberts, Phys. Rev. B **39**, 5558 (1989).

[18] K. J. Nash and D. J. Mowbray, J. Lumin **44**, 315 (1989).

[19] J. F. Muth, J. H. Lee, I. K. Shmagin, R. M. Kollbas, H. C. Casey, B. P. Keller, U. K. Mishra, and S. B. DenBaars, Appl. Phys. Lett. **71**, 2572 (1997).

[20] Z. Z. Bandic, P. M. Bridger, E. C. Piquette, and T. C. McGill, Appl. Phys. Lett. **72**, 3166 (1998).

[21] J. F. Muth, X. Zhang, A. Cai, D. Fothergill, J. C. Roberts, P. Rajagopal, J. W. Cook, E. L. Piner, and K. J. Linthicum, Appl. Phys. Lett. **87**, 192117 (2005).

[22] M. Boroditsky, I. Gontijo, M. Jackson, R. Vrijen, E. Yablonovitch, T. Krauss, C. C. Cheng, A. Scherer, R. Bhat, and M. Krames, J. Appl. Phys. **87**, 3497 (2000).

[23] T. Takeuchi, H. Takeuchi, S. Sota, H. Sakai, H. Amano, and I. Akasaki, Jpn. J. Appl. Phys. **36**, L177 (1997).

[24] B. Monemar and G. Pozina, Progress in Quantum Electronics **24**, 239 (2000).

[25] O. Mayrock, H. J. Wünsche, and F. Henneberger, Phys. Rev. B **62**, 16870 (2000).

[26] B. Monemar, P.P. Paskov, G. Ponzina, J.P. Bergman, S. Kamiyama, M. Iwaya, H. Amano, and I. Akasaki, Phys. Stat. Sol. (A) **192**, 21 (2002).

[27] K. Köhler, J. Wiegert, H. P. Menner, M. Maier, and L. Kirste, J. Appl. Phys. **103**, 023706 (2008).

[28] M. Leroux to R. Martin, Private Communication.

[29] B. Heying, E. J. Tarsa, C. R. Elsass, P. Fini, S. P. DenBaars, and J. S. Speck, J. Appl. Phys. **85**, 6470 (1999).

[30] Y. H. Cho, G. H. Gainer, A. J. Fischer, J. J. Song, S. Keller, U. K. Mishra, and S. P. DenBaars, Appl. Phys. Lett. **73**, 1370 (1998).

[31] H. P. D. Schenk, M. Leroux and P. de Mierry, J. Appl. Phys. **88**, 1525 (2000).

[32] M. G. Cheong, H. S. Yoon, R. J. Choi, C. S. Kim, S. W. Yu, C. –H. Hong, E. –K. Suh, and H. J. Lee, J. Appl. Phys. **90**, 5642 (2001).

[33] R Pecharrom´an-Gallego, R W Martin and I M Watson, J. Phys. D: Appl. Phys. **37**, 2954 (2004).

[34] R. J. Potter, N. Balkan, H. Carrère, A. Arnoult, E. Bedel, and X. Marie, Appl. Phys. Lett. **82**, 3400 (2003).

[35] M. Kondow, S. Minagawa, Y. Inoue, T. Nishino, and Y. Hamakawa, Appl. Phys. Lett. **54**, 1760 (1989).

[36] G. Steude, B. K. Meyer, A. Goldner, A. Hoffmann, F. Bertram, J. Christen, H. Amano, and I. Akasaki. Appl. Phys. Lett. **74**, 2456 (1999).

[37] Y. –H. Cho, G. H. Gainer, J. B. Lam, J. J. Song, W. Yang, and W. Jhe, MRS Internet J. Nitride Semicond. Res. **5S1**, W11.57 (2000).

[38] K. L. Teo, J. S. Colton, P. Y. Yu, E. R. Weber, M. F. Li, W. Liu, K. Uchida, H. Tokunaga, N. Akatsu and K. Matsumoto Appl. Phys. Lett. **73**, 1697 (1998).

CHAPTER 5

Optical Properties of $In_xGa_{1-x}N$/GaN Single Quantum Wells with Various Si-doping Concentrations in GaN Barriers

5.1 Introduction

The dependence of the optical properties of $In_xGa_{1-x}N$/GaN quantum wells on characteristics, such as cap thickness (as discussed in **Chapter 4**) and well thickness, has been widely investigated. There is also strong interest in the structural, optical and electronic effects of silicon doping in the barrier layers of $In_xGa_{1-x}N$/GaN quantum wells, as used to fabricate high-performance LEDs. Silicon doping has been shown to affect such properties of $In_xGa_{1-x}N$/GaN quantum wells as the crystal and interfacial quality [1] and the photoluminescence intensity [2-3]. Doping can influence the band gap measured optically from quantum wells in a number of ways. As mentioned in **Chapter 2**, the optical band gap can be larger or smaller than the undoped crystal host due to band filling or band gap renormalisation (BGR), respectively. BGR competes with band filling at high carrier density. The relative importances of these effects are significant in determining optical properties and device performance.

Many research groups have investigated the effects of BGR and band filling on the energy gap of group IV (for example Si [4-5]) and conventional III-V (for example GaAs [4], InP [4] and InN [5]). Jain and Roulston [4] reported a general equation for BGR for *n*- and *p*-type Si, Ge and GaAs layers. They fitted the narrowing of the gap (ΔE_g) by BGR using an expression with $n^{1/3}$, $n^{1/4}$ and $n^{1/2}$ terms [4]:

$$\Delta E_g(BGR) = A.n^{1/3} + B.n^{1/4} + Cn^{1/2} \qquad (5.1)$$

where n is the free carrier concentration (electrons or holes depending on the type of dopants) and A, B, and C are constants. The three terms are (i) exchange energy of majority carriers, (ii) correlation energy of minority carriers, and (iii) carrier-ion interaction energy, respectively. They observed that BGR fits quite successfully to a $n^{1/3}$ dependence, in agreement with Casey *et. al.* [6]:

$$\Delta E_g(BGR) \sim a.n^{1/3} \qquad (5.2)$$

where a is known as BGR coefficient (a is not simply related to exchange energy). The magnitude of the renormalised band gap in semiconductors with gaps in the infrared, such as GaAs, has been shown to have a $n^{1/3}$ dependence [4]. It was not clear whether this dependence would also be true for materials with higher gaps.

Recent studies have extended the investigation of BGR to wide-gap III-nitrides including Si-doped GaN [7-11], AlN [12], $Al_{0.7}Ga_{0.3}N$ [13] and ZnO [14-16] films. As explained previously, there is a competition between band filling and BGR at high carrier density. Lu *et al.* [16] observed that as the electron concentration (n) increased the optical gap first increased as $n^{2/3}$, due to a Burstein-Moss (BM) shift caused by band filling, followed by a sudden decrease for $n > 4.2 \times 10^{19}$ cm^{-3} due to the BGR effect, and then increased again but at a slower rate controlled by competition between BM and BGR. In many cases the BGR-induced shifts in energy gap can be accounted for by a $n^{1/3}$ dependence. Table 5.1 lists the reported BGR coefficients for various materials. It is noteworthy that the BGR coefficients for GaN vary by almost an order of magnitude. There is limited information on BGR in highly doped $In_xGa_{1-x}N$/GaN structures, with minimal data [17] or no explanation [3].

Table 5.1 BGR coefficients of III-V and II-VI materials.

Material	**BGR coefficient (x 10^{-5} meVcm)**	**Reference**
p-GaAs	- 2.60	4
p -GaSb	- 2.22	4
p -InP	- 2.69	4
p -$In_{0.53}Ga_{0.47}As$	- 2.43	4
n-InN	- 1.70	5
n -GaN	- 0.57	11
	- 1.30	9
	- 2.10	7, 9
	- 2.40	8
	- 4.70	10
n -AlN	- 2.99	12
n -$Al_{0.7}Ga_{0.3}N$	- 1.20	13
n -ZnO	- 1.33	15

In this work, the effects of various Si dopant concentrations on the emission peak energies of $In_xGa_{1-x}N$/GaN single quantum wells (SQWs) using photoluminescence

(PL) as a function of temperature including comparison with relevant published data from doped $In_xGa_{1-x}N$ wells are presented. In addition, since the presence of excess free carriers may cause Coulomb screening of the piezoelectric field [18-20], therefore it is necessary to study the effect of excitation power density on the optical properties. As the excitation power is increasing, more photo-generated carriers are produced, which may lead to the screening the internal electric field and results in a blue-shift in the transition energy. Other factors including surface recombination, surface depletion field and strain will also be considered.

5.2 Specific Samples and Experimental Details

The samples were grown in consecutive runs on *c*-plane double-polished sapphire substrates, by a commercial LED wafer supplier, using metal organic chemical vapour deposition (MOCVD). Trimethylindium (TMIn), trimethylgallium (TMGa) and ammonia (NH_3) were used as precursors for In, Ga and N respectively.

Each sample comprises of a single $In_xGa_{1-x}N$ quantum well, nominally 2 nm thick, with an 8 nm GaN cap layer, a lower GaN barrier of 20 nm, and 3 μm GaN buffer layer. The barrier, cap and buffer layers were intentionally doped with nominal Si dopant concentrations (N_{Si}) varied from 5 x 10^{17} to 1 x 10^{19} cm^{-3}. The $In_xGa_{1-x}N$ wells were undoped and have a nominal InN molar fraction (x) of 0.09. A schematic diagram of Si-doped GaN barriers of $In_{0.09}Ga_{0.91}N$/GaN SQW sample is shown in Figure 5.1.

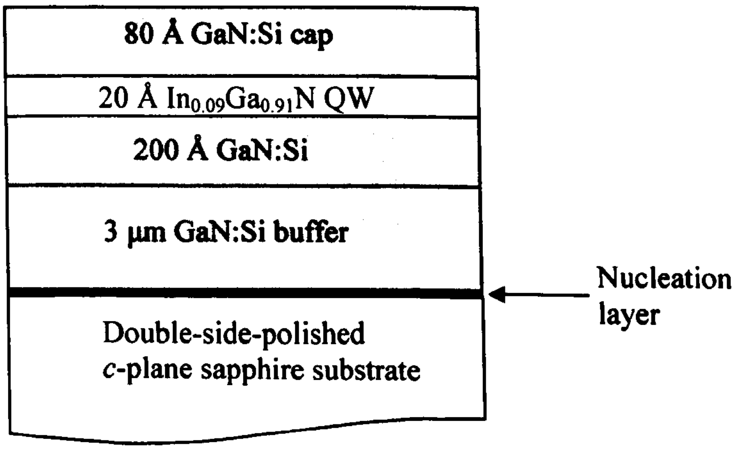

Figure 5.1 Schematic structure of Si-doped GaN barriers of $In_xGa_{1-x}N$/GaN SQW with nominal InN molar fraction (x) of 0.09 (not to scale).

PL spectra were measured using excitation by 325 nm radiation from a low-power He-Cd laser and detected using a cooled CCD spectrograph. The laser power was varied from 0.05 to 5 mW in a 0.3 mm diameter spot. The sample temperature was controlled in the range ≈ 16 to 300 K. The electron concentration and mobility in the Si-doped samples were measured at ≈ 77 K using conventional Hall-effect method (van der Pauw configuration). The measured free carrier concentrations are around 70 to 80 % of the nominal dopant concentrations, with the measured mobility decreasing from approximately 210 to 120 cm^2/Vs as the doping increases.

5.3 Experimental Results and Discussion

5.3.1 Low Temperature PL Spectra

Figure 5.2 presents the low temperature (≈ 16 K) PL spectra of $In_{0.09}Ga_{0.91}N$/GaN SQW samples with various dopant concentrations (N_{Si}) ranging from 0.05 to 1 x 10^{19} cm^{-3}. Several emission peaks are observed. The quantum well transition energies (or zero-phonon line) as marked by solid arrows and their phonon satellites (1LO, 2LO) at the low energy side of the PL spectra are clearly observed. The appearance of LO-phonon sidebands (LO-PSBs) to the low energy side of the zero-phonon line results from the coupling of excitons to phonons and their relative strength can be expressed by Huang-Rhys parameters as explained previously in **Section 2.6.1**. Also, there are a few PL features appearing at the higher energy side of the spectra. The sharp emission lines at around 3.28, 3.19 and 3.10 eV are assigned to the donor-acceptor pair (DAP) of GaN and its LO-phonons (LO-DAP) satellites, respectively. In order to obtain accurate information, the QW peak intensity, emission energy and FWHM are estimated using multi-Gaussian peak fitting following subtraction of a linear background, as shown in green dotted line in the figure.

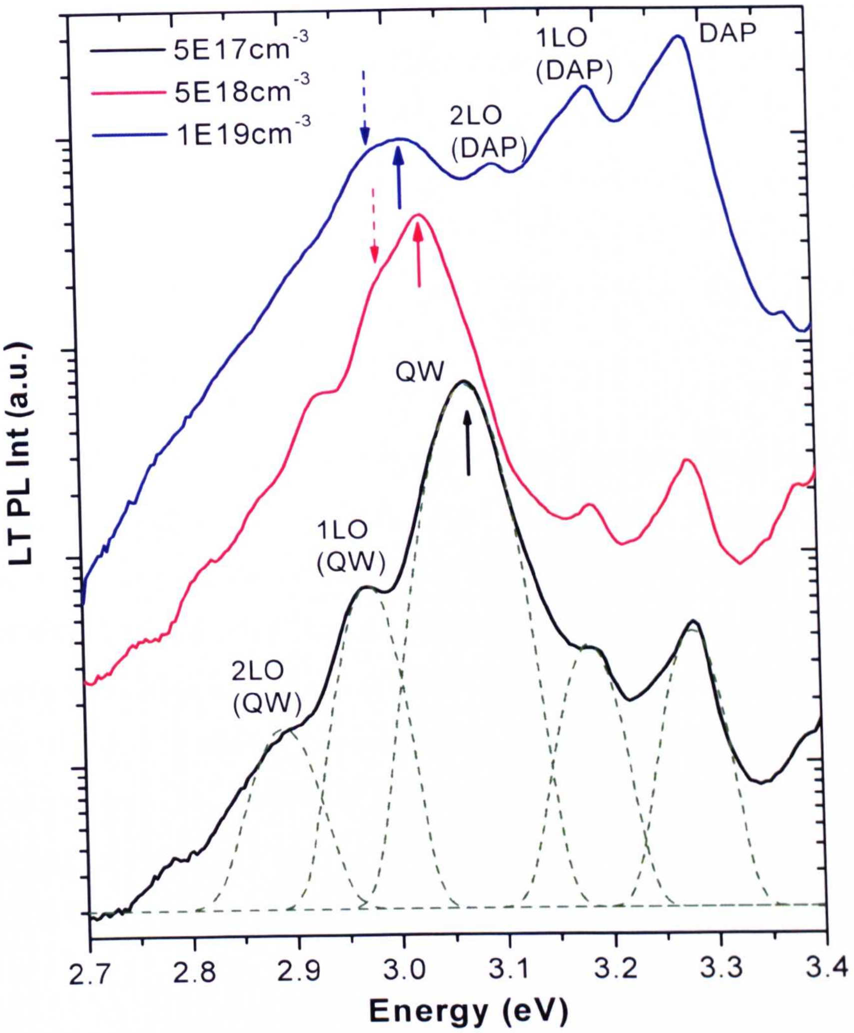

Figure 5.2 Low temperature PL (≈ 16 K) spectra of barrier-doped In$_{0.09}$Ga$_{0.91}$N/GaN SQW with various dopant concentrations. The solid arrows indicate the QW transitions, and the dashed arrow points to the lower energy shoulder. The green dotted lines show the multi-Gaussian peak fitting and linear background subtraction.

A red-shift in the QW transition energy from around 3.07 to 3.01 eV is observed as the doping concentration increases from 0.05 to 1 x 10^{19} cm^{-3}. Clear QW LO-phonon satellites are seen in the most lightly doped sample of 5 x 10^{17} cm^{-3} with Huang-Rhys parameters for the first and second satellites of 0.11 and 0.1, respectively. For each sample the energy separation of successive phonon satellites remains constant at approximately 90 meV, as observed previously [21]. A shoulder on the low-energy side of the QW emission peak as indicated by dashed arrow is observed. It is present in highly doped samples and become stronger in samples with higher doping levels. It is also seen to strengthen at higher temperatures which will be discussed and presented in **subsection 5.3.4**. Furthermore, it is noted that the LO-phonon satellites for the more heavily doped samples are not very noticeable. On the other hand, the peak emission intensities of the DAP and its LO-DAP satellites in these heavily doped samples become stronger. This is possibly due to more defects being introduced as the doping increases.

The intensity and FWHM of the QW transition for all samples are plotted against the dopant concentration as shown in Figure 5.3. The PL peak intensity decreases by almost 5 times as the dopant concentration increases from 0.05 to 1 x 10^{19} cm^{-3} whilst the FWHM almost doubles. The FWHM of the lowest doped sample is near 64 meV with an emission energy of 3.07 eV. This value seems to be reasonable when compared to the non-intentional doped $In_xGa_{1-x}N$ SQW samples with similar InN fraction range in Ref. 22. The PL is thus seen to be degraded for the more highly doped samples, as evidenced by the decrease in PL intensity accompanied by an increase in FWHM, principally due to impurity scattering.

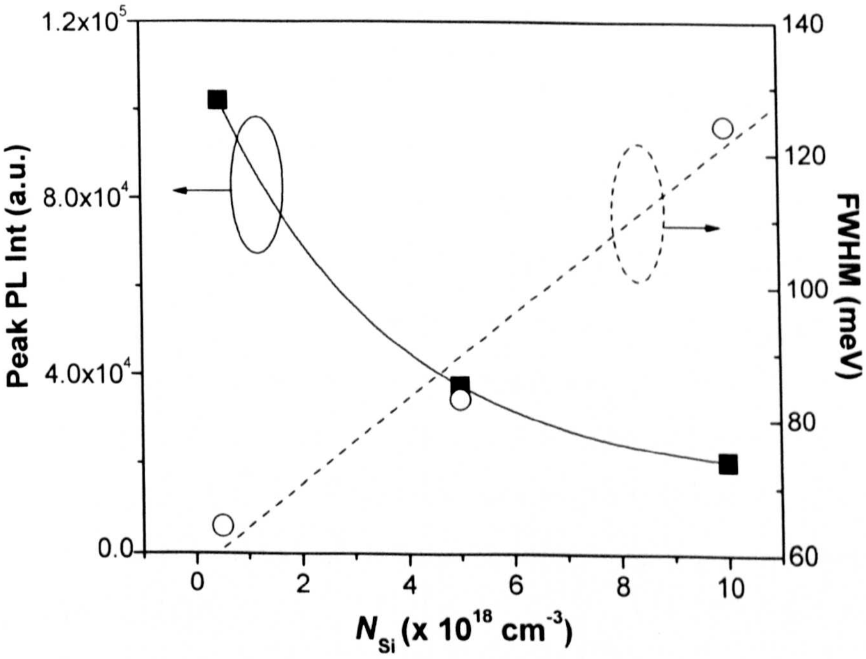

Figure 5.3 **Low temperature (≈ 16 K) peak PL intensity and linewidth of $In_{0.09}Ga_{0.91}N/GaN:Si$ SQWs as a function of dopant concentration (N_{Si}).**

Figure 5.4 plots the QW transition energy as a function of the dopant concentration. It is observed that the QW transition energy decreases nonlinearly with a reduction in energy of around 60 meV as the dopant concentration increases from 0.05 to 1 x 10^{19} cm^{-3}.

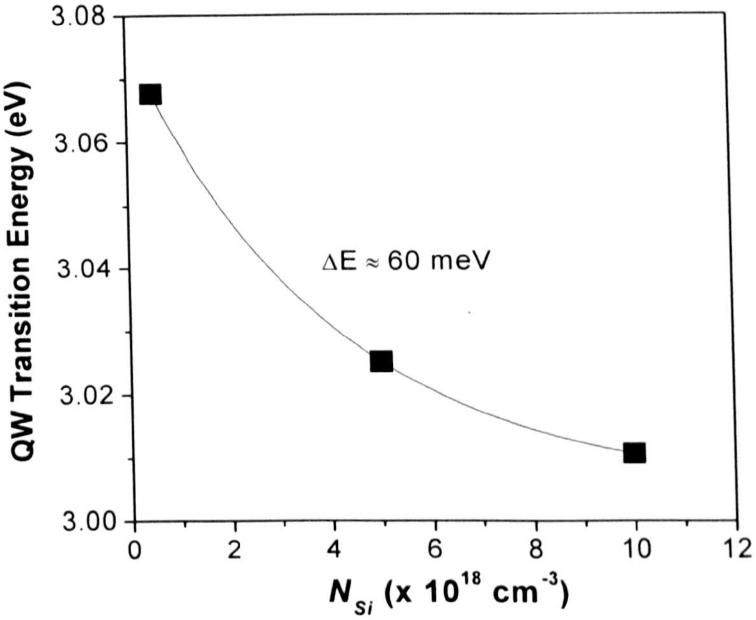

Figure 5.4 QW transition energy of $In_{0.09}Ga_{0.91}N$/GaN:Si SQWs as a function of dopant concentration (N_{Si}).

5.3.2 Power-Dependent PL Spectra

Figure 5.5 shows the power-dependent PL spectra of samples with Si-doped barriers of 0.5 and 5 x 10^{18} cm^{-3}, measured at ≈ 16 K. The power on the sample ranges from 0.05 to 0.5 mW. It is observed that there is no change in the QW peak position of any sample measured in this work as indicated by the dashed lines in the figure when the power density increases by 2 orders of magnitude. This suggests that the piezoelectric field frequently observed in strained $In_xGa_{1-x}N$/GaN QWs is suppressed in the samples studied in this work. For the heavier doped sample (in Figure 5.5(b)), a shoulder appearing at the lower energy emission of the QW (marked by the dashed arrow) at around 3 eV is observed. It becomes more visible as the power density increases towards 0.5 mW.

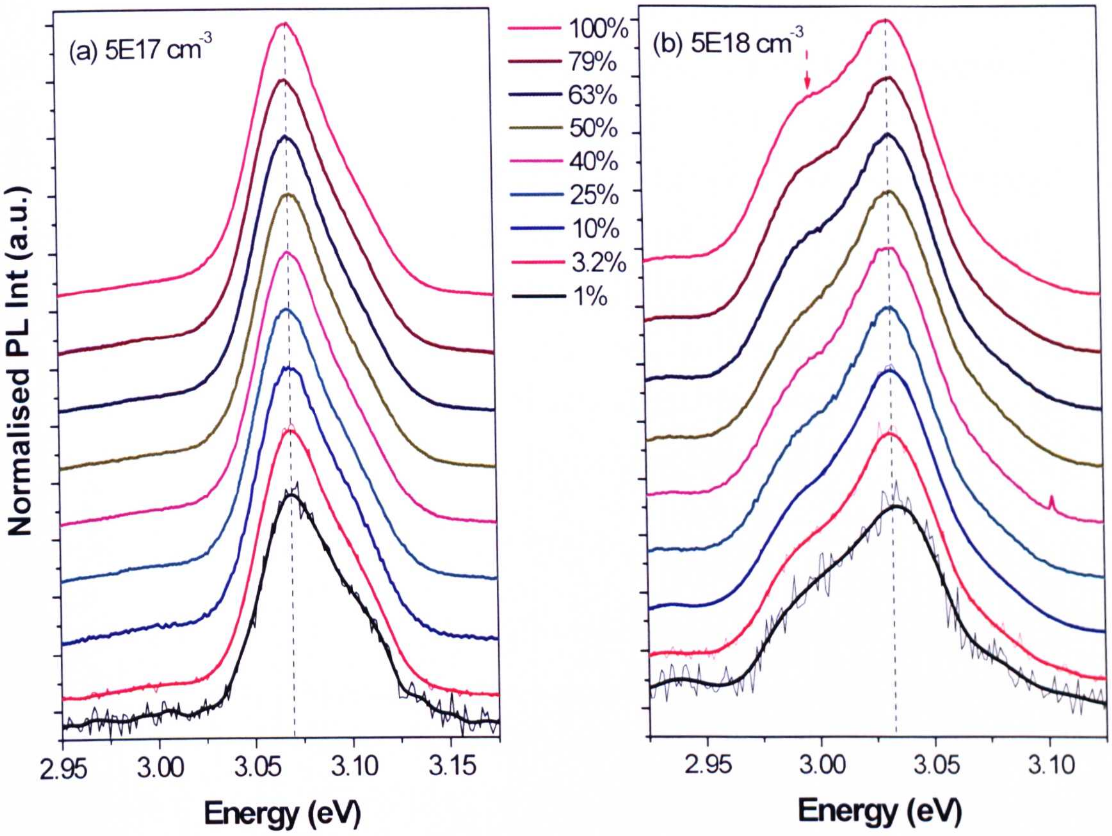

Figure 5.5 Power-dependent PL spectra at ≈ 16 K for samples with doping concentrations of (a) 5 x 10^{17} cm^{-3} and (b) 5 x 10^{18} cm^{-3}. The dashed line indicates the QW peak position and the dashed arrow points to the lower energy shoulder.

5.3.3 Analysis

Several studies have reported a blue-shift in the $In_xGa_{1-x}N$/GaN QW transition energy with increasing Si-doping concentrations and explained this in terms of band filling and/or Coulomb screening of the piezoelectric fields [10, 18-20, 23]. As shown in Figure 5.4, the QW transition energy has reduced from approximately 3.07 to 3.01 eV with an energy reduction of 60 meV as the dopant concentration increases from 0.05 to 1 x 10^{19} cm^{-3}. Given the red-shift in transition energy observed in this study and the power-dependent PL spectra (Figure 5.5), it is clear that the band filling and the field-screening are not dominant mechanisms in these samples.

At carrier concentration above the Mott transition, the band gap narrowing becomes significant through (i) merging of donor and conduction bands [24], (ii) band tailing by impurity-induced potential fluctuations [25] and (iii) electron–electron exchange and Coulomb interactions, and screened electron-ion many-body contributions to the electron and hole self-energies [4]. These optical band gap narrowing mechanisms will compete with the band filling effect as the carrier concentration (n) increases. Theoretical calculations by Allen *et. al.* [25] on the potential fluctuations by impurities predicted a linear dependence of the red-shift on n. However, it is seen from Figure 5.4 that the QW transition energy does not decrease linearly with dopant concentration. On the other hand, many-body effects due to exchange and Coulomb interactions, and screened electron-ion interactions producing BGR are expected to provide a $n^{1/3}$ dependence.

As mentioned earlier, the measured free carrier concentrations using Hall Effect technique are around 70 to 80 % of the nominal dopant concentrations as the doping increases. Thus Equation (5.2) is simplified and related to the dopant concentration, N_{Si} as follows:

$$\Delta E_g\,(BGR) \sim a.N_{Si}^{\ 1/3} \tag{5.3}$$

Figure 5.6 plots the QW transition energy as a function of the cubic root of the doping concentration. It is observed that the experimental data fits a $N_{Si}^{\ 1/3}$ power law and BGR appears to be the dominant effect causing the red-shift in energy. Using Equation 5.3, the BGR coefficient is estimated to be - 4.2 x 10^{-5} meVcm, which lies near the top of the reported range for n-GaN shown in Table 5.1.

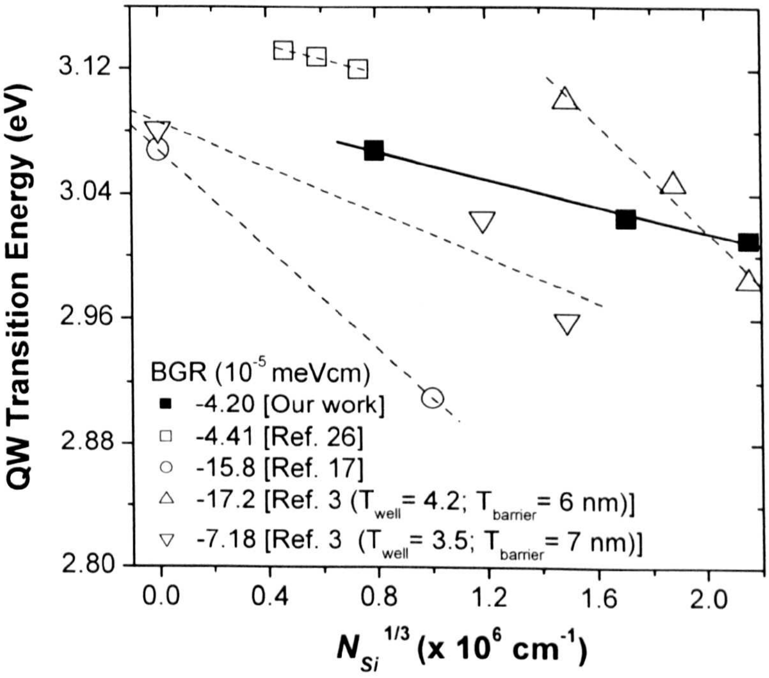

Figure 5.6 QW transition energy versus cubic root of the estimated carrier concentration with an assumption of SiH_4 flow rate being linearly proportional to carrier concentration. Filled symbols represent the current work and open symbols are extracted from the references.

Figure 5.6 also includes the experimental data extracted from the literature [3, 17, 26]. Ref. 3 described a decrease in the emission energies with increased doping for two different well/barrier thickness ratios. The flow rates are converted to doping concentration under assuming linear proportionality (30 sccm SiH_4 flow rate results in 300 K free carrier concentration n of near 1 x 10^{19} cm^{-3} [3]). The estimated BGR coefficients differ by more than a factor of 2. Ref. 17 reported a BGR coefficient of -15.8 x 10^{-5} meVcm which is almost 3 times larger than our estimate. The range of reported BGR coefficients is likely to be due to various factors including the interplay of the band filling, the Coulomb screening of the internal polarisation field, and the band gap renormalisation effect, similar to those described in Si-doped ZnO by Lu *et. al.* [16] and Si-doped $Al_yGa_{1-y}N$/GaN multiple quantum wells by Kajitani *et. al.* [27]. Another possibility is the influence of the sample structure for example the well and barrier thickness as illustrated by Grudowski *et. al.* [3].

As mentioned earlier, BGR occurs when the carrier density is above the critical Mott density (or the carrier density at which the semiconductor–metal transition occurs). Hence an estimation of the critical Mott density is necessary. F. Binet *et. al.* [28] studied the photoluminescence from GaN under intense excitation and lead to an estimate of Mott density in the range of 1.8 to 3.8 x 10^{18} cm^{-3}, dependent on carrier temperature. This lies in the middle of the range of dopant concentrations used in this work as illustrated in Figure 5.4. Moreover, the absence of a blue-shift at high concentrations appears to show that band gap renormalisation wins out over band filling in all cases.

In this study, the cap layer used is thin (8 nm). This means that the quantum well is buried near to the surface and thus the influence of surface recombination and the surface depletion field on the luminescence properties are worth to be considered. In **Chapter 4**, the thinnest cap nominal thickness is 1.5 nm and it was shown that the effect of the surface recombination is not significant. Therefore, this effect will not be an issue in this work since the cap thickness used here is much thicker. As for the surface depletion field, the surface potential of a semiconductor is determined by the position of the Fermi energy relative to the conduction band edge. For GaAs, an occupied mid-gap level determines the surface potential of 0.7 eV, which then defines the depletion layer width as a function of the doping concentration [29]. The surface potential is shown to be independent of Si doping up to a concentration of 3 x 10^{18} cm^{-3} [30]. On the other hand, experimental results on GaN [31-35] as well as a theoretical study [36] on the surface potential show a more complex situation. The experimental results vary in a wide range, from 1.75 eV [32] which would point to a mid-gap level, to 0.5 eV [34]. The origin of the variation could be the sensitive GaN surface which has a density of surface states almost a factor of 10 less than GaAs, as found in an extensive study on metal contacts to GaN. This makes it understandable that the Fermi level pinning is easily reduced by surface treatments such as NH_4OH solution and N_2 plasma [37], and nitrogen ion sputtering and annealing [38]. Another influence, which might be caused by the low density of the surface states, is the doping dependence of the surface potential [33, 39]. Köhler *et. al.* [39] investigated the surface potential of GaN:Si with Si doping in the range from 0.06 to

2.3×10^{19} cm^{-3}. It is reported that the surface potential drops with increasing doping concentration, from around 1.5 to 0.2 eV. Since no surface treatment was applied in this study therefore it is believed that doping is a crucial contribution to the Fermi level pinning.

Using the surface potential data from Ref. 40, and the depletion field and depletion width equations in **Chapter 4,** one can estimate the surface depletion field and depletion width at different doping concentrations. The maximum strength and the width of the surface depletion fields are estimated to be near 0.55, 0.72 and 1.0 MV/cm, and 63, 8 and 6 nm for 5×10^{17}, 5×10^{18} and 1×10^{19} cm^{-3}, respectively. The estimated depletion fields for 5×10^{17} and 5×10^{18} cm^{-3} samples are considerably small as compared to the internal field (>2-3 MV/cm). Also, it is noted that although the surface depletion field for the heaviest doped sample of 1×10^{19} cm^{-3} is calculated to be large (1 MV/cm), the maximum depletion width (6 nm) is within the cap layer (8 nm). This suggests that there is no impact on the quantum well. Thus the influence of surface depletion field on the optical properties is believed to be not significant.

Another factor to consider here is the strain effect due to the lattice mismatch between the GaN well and the $In_xGa_{1-x}N$ barrier, and the defects induced by Si doping. Lee *et. al* [40] reported a red-shift in the luminescence peak position in highly Si-doped GaN on sapphire. They observed the bound exciton energy decreases from around 3.483 to 3.468 eV (a change in 15 meV) as the carrier concentration increased from 0.04 to 1.6×10^{19} cm^{-3}. They ascribed the red-shift to the partial relaxation of the thermally induced mismatch strain through the formation of defects induced by the Si doping in the epilayer. On the other hand, another research group [9] reported that the values of the residual strain were scattered in their GaN:Si samples and they did not observe a clear trend of strain relaxation with Si doping range up to 1.3×10^{19} cm^{-3}. As the generation mechanism of defects due to Si incorporation is not clear yet and we lack residual strain measurements in this work, it is difficult to determine whether the strain relaxation plays a significant role or not. Nevertheless, the strain-induced band gap shift by Lee *et. al.* [40] with similar power density and carrier density is not sufficient to account for the 60 meV down shift of band gap energy observed in this work.

5.3.4 Temperature-Dependence PL Spectra

The temperature-dependent PL spectra for different doped samples are presented in Figure 5.7. The shoulder on the lower energy side of the QW peak as indicated by the dashed arrow appears in heavily doped samples and becomes more prominent as the doping increases as discussed in the earlier subsections.

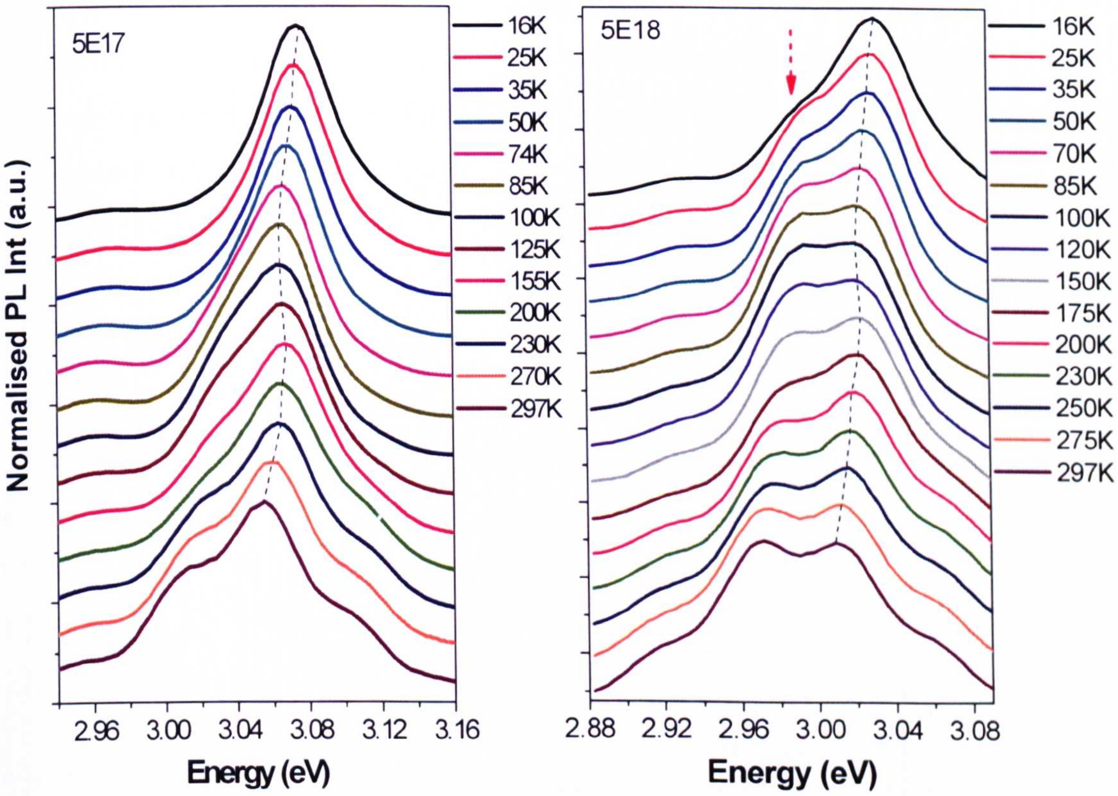

Figure 5.7 Normalised temperature-dependent PL spectra of (a) 5 x10^{17} cm^{-3} and (b) 5 x10^{18} cm^{-3} Si-doped barrier In$_x$Ga$_{1-x}$N/GaN SQW. Dashed black line indicates the QW peak position and the dashed red arrow indicates the shoulder on the lower emission energy of QW peak.

As the temperature increases from 16 K to the room temperature, the QW transition intensity becomes weaker due to thermal quenching whereas the shoulder on the lower energy emission becomes stronger. This behaviour indicates that the latter is not related to donor-bound exciton recombination. In fact, similar behaviour is observed in the most heavily doped sample (10^{19} cm^{-3}). It is believed that this shoulder on the lower energy emission could be related to Si-related defects where the carriers trapped in such defects in the quantum well may get thermally activated at high temperature, achieving sufficient energy to escape and recombine radiatively. One of the possible origins of this Si-related defect could be that the Si is introduced into the quantum well non-intentionally from the chemicals during the growth.

The temperature dependence of the QW peak positions are plotted in Figure 5.7, which shows a decrease–increase–decrease pattern or called 'S-shaped' behaviour. As explained in **Chapter 4**, this 'S-shaped' behaviour has been attributed to the effects of inhomogeneity of InN content and carrier localisation in $In_xGa_{1-x}N$ [41-42]. Figure 5.8 plots the change in the QW peak position as a function of temperature. It is observed that the blue-shift within the S-shape is smaller (1 meV) in the more heavily doped sample than for the lightly doped sample (3 meV). Pecharromán-Gallego *et. al.* [42] explained that the change in the blue-shift is related to the relative depth of localisation. This suggests that the increased doping has considerably decreased the carrier localisation, as observed in Ref. 2 but in contrast to Ref. 17. It seems most plausible that the extra free carriers will screen out localising effects within the band profile.

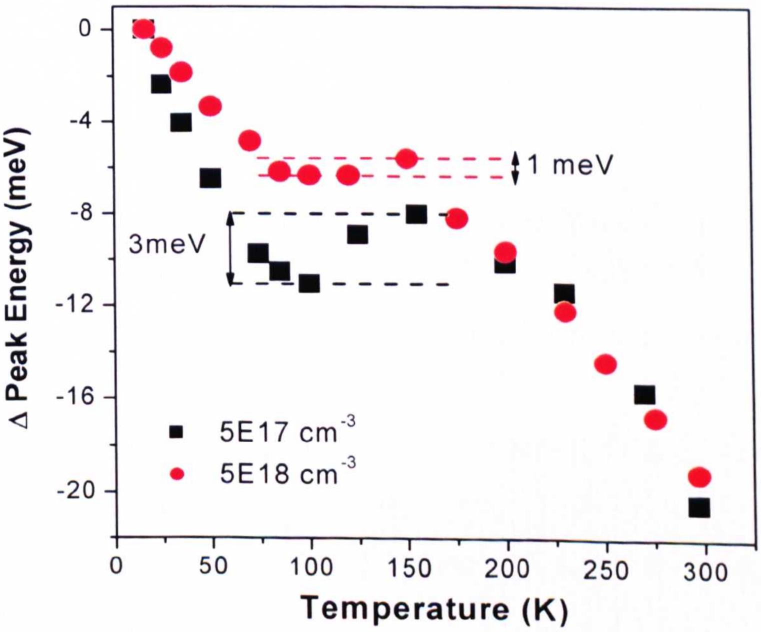

Figure 5.8 Change in peak energy as a function of temperature for different doped samples.

5.4 Summary

The influence of Si doping in the barriers of $In_xGa_{1-x}N/GaN$ SQWs on the optical properties have been studied using photoluminescence as a function of power and temperature. The QW PL peak intensity decreases by almost 5 times whereas the FWHM increases by almost two times as the Si doping concentration increases from 0.05 to 1 x 10^{19} cm^{-3}. The PL properties for more heavily doped samples are seen to be degraded principally due to impurity scattering. The QW transition energy has reduced by approximately 60 meV with increasing doping. There is no change in the QW transition peak position as the power density increases by 2 orders of magnitude. This suggests that the piezoelectric field frequently observed in strained $In_xGa_{1-x}N/GaN$ QWs is suppressed in the samples studied in this work. The red-shift in the QW transition energy is attributed to band gap renormalisation with a coefficient of - 4.2 x 10^{-5} meVcm.

For the heavier doped sample, a shoulder appearing at the lower energy emission of the QW is observed. It becomes more prominent as the doping and/or temperature increase. It is believed that the lower energy emission could be related to Si-related defects where the carriers trapped in such defects may get thermally activated at high temperature, achieving sufficient energy to escape and recombine radiatively. From the temperature-dependence PL spectra, it is shown that the heavy doping has reduced the carrier localisation in these structures.

5.5 References

[1] D. B. Li, T. Katsuno, K. Nakao, M. Aoki, H. Miyake, and K. Hiramatsu, J. Crystal Growth **290**, 374 (2006).

[2] T. Wang, H. Saeki, J. Bai, T. Shirahama, M. Lachab, S. Sakai, and P. Eliseev, Appl. Phys. Lett. **76**, 1737 (2000).

[3] P. A. Grudowski, C. J. Eiting, J. Park, B. S. Shelton, D. J. H. Lambert, and R. D. Dupuis, Appl. Phys. Lett. **71**, 1537 (1997).

[4] S. C. Jain, J. M. McGregor, and D. J. Roulston, J. Appl. Phys. **68**, 3747 (1990).

[5] V.Y. Davydov, A.A. Klochikhin, V.V. Emtsev, D.A. Kurdyukov, S.V. Ivanov, V.A. Vekshin, F. Bechstedt, J. Furthmuller, J. Aderhold, J. Graul, A.V. Mudryi, H. Harima, A. Yamamoto, and E.E. Haller, Phys. Stat. Sol. (b) **234**, 787 (2002).

[6] H. C. Casey, and F. Stern, J. Appl. Phys. 47, 631 (1976).

[7] B. K. Meyer, D. Volm, A. Graber, H.C. Alt, T. Detchprohm, H. Amano, and I. Akasaki, Solid State Commun. **95**, 597 (1995).

[8] X. Zhang, S. J. Chua, W. Liu, K. B. Chong, Appl. Phys. Lett. **72**, 1890 (1998).

[9] In-Hwan Lee, J. J. Lee, P. Kung, F. J. Sanchez and M. Razeghi, Appl. Phys. Lett. **74**, 102 (1999).

[10] M. Yoshikawa, M. Kunzer, J. Wagner, H. Obloh, P. Schlotter, R. Schmidt, N. Herres, and U. Kaufmann: J. Appl. Phys. **86**, 4400 (1999).

[11] W. Li, and A. Li, Thin Solid Films **401**, 279 (2001).

[12] K. B. Nam, M. L. Nakarmi, J. Li, J. Y. Lin, and H. X. Jiang, Appl. Phys. Lett. **83**, 2787 (2003).

[13] K. Zhu, M. L. Nakarmi, K. H. Kim, J. Y. Lin, and H. X. Jiang, Appl. Phys. Lett. **85**, 4669 (2004).

[14] B. E. Sernelius, K.-F. Berggren, Z.-C. Jin, I. Hamberg, and C. G. Granqvist, Phy. Rev. B **37**, 10244 (1988).

[15] J. D. Ye, S. L. Gu, S. M. Zhu, S. M. Liu, Y. D. Zheng, R. Zhang, and Y. Shi, Appl. Phys. Lett. **86**, 192111 (2005).

[16] J. G. Lu, S. Fujita, T. Kawaharamura, H. Nishinaka, Y. Kamada, Z. Z. Ye, Y. J. Zeng, Y. Z. Zhang, L. P. Zhu, H. P. He, and B. H. Zhao, J. Appl. Phys. **101**, 083705 (2007).

[17] Y. J. Wang, S. J. Xu, and Q. Li, D. G. Zhao and H. Yang, Appl. Phys. Lett. **88**, 041903 (2006).

[18] S. Chichibu, D. A. Cohen, M. P. Mack, A.C. Abare, P. Kozodoy, M. S. Minsky, S. Fleischer, S. Keller, J. E. Bowers, U. K. Mishra, L. A. Coldren, D. R. Clarke, and S. P. DenBaars, Appl. Phys. Lett. **73**, 496 (1998).

[19] A. D. Carlo, F. O. Sala, P. Lugli, V. Fiorentini, and F. Bernardini: Appl. Phys. Lett. **76**, 3950 (2000).

[20] Z. C. Feng, W. Liu, S. J. Chua, J. H. Chen, C. C. Yang, W. Lu, and W. E. Collins, Phys. Stat. Sol. (c) **2**, 2377 (2005).

[21] T. Paskova, B. Arnaudov, P. P. Paskov, E. M. Goldys, S. Hautakangas, K. Saarinen, U. Södervall, and B. Monema, J. Appl. Phys. **98**, 033508 (2005).

[22] L. T. Tan, R. W. Martin, I. M. Watson and K. P. O'Donnell, Appl Phys. Lett. **89**, 101910 (2006).

[23] M. Y. Ryu, P. W. Yu, E. Oh, C. Sone, O. Nam, and Y. Park, Solid State Commun. **118**, 547 (2001).

[24] A. P. Roth, J. B. Webb, and D. F. Williams, Phys. Rev. B **25**, 7836 (1982).

[25] P. B. Allen and V. Heine, J. Phys. C **9**, 2305 (1976).

[26] A. M. Fox, Private Communication.

[27] Ryo Kajitani, Misaichi Takeuchi, and Yoshinobu Aoyagi, Japanese J. Appl. Phys. **47**, 47 (2008).

[28] F. Binet, J.Y. Duboz, J. Off and F. Scholz, Phys. Rev. B **60**, 4715 (1999).

[29] A. Chandra, C. E. Wood, D. W. Woodard, and L. F. Eastman, Solid-State Electron. **2**, 645 (1979).

[30] R. F. Broom, H. P. Meier, and W. Walter, J. Appl. Phys. **60**, 1832 (1986).

[31] L. Wang, M. I. Nathan, T.-H. Lim, M. A. Khan, and Q. Chen, Appl. Phys. Lett. **68**, 1268 (1996).

[32] U. Karrer, O. Ambacher, M. Stutzmann, F. Bernardini, and F. Fiorentini, Appl. Phys. Lett. **77**, 2012 (2000).

[33] G. Koley and M. G. Spencer, J. Appl. Phys. **90**, 337 (2001).

[34] M. Kocan, A. Rizzi, H. Lüth, S. Keller, and U. K. Mishra, Phys. Stat. Sol. (b) **234**, 773 (2002).

[35] A. C. Schmitz, A. T. Ping, M. Asif Khan, Q. Chen, J. W. Yang, and I. Adesida, J. Electron. Mater. **27**, 255 (1998).

[36] D. Segev and C. G. Van de Walle, J. Cryst. Growth **300**, 199 (2007).

[37] T. Hashizume, S. Ootomo, S. Oyama, M. Konishi, and H. Hasegawa, J. Vac. Sci. Technol. B **19**, 1675 (2001).

[38] C. I. Wu and A. Khan, J. Vac. Sci. Technol. B **16**, 2218 (1998).

[39] K. Köhler, J. Wiegert, H. P. Menner, M. Maier, and L. Kirste, J. Appl. Phys. **103**, 023706 (2008).

[40] I. H. Lee, I. H. Choi, C. R. Lee, and S. K. Noh, Appl. Phys. Lett. **71**, 1359 (1997).

[41] Y. H. Cho, B. D. Little, G. H. Gainer, J. J. Song, S. Keller, U. K. Mishra, and S. P. DenBaars, MRS Internet J. Nitride Semicond. Res. **4S1**, G2.4 (1999).

[42] R Pecharromán-Gallego, R W Martin and I M Watson, J. Phys. D: Appl. Phys. **37**, 2954 (2004).

CHAPTER 6

Photoluminescence of Near-Lattice-Matched GaN/$Al_{1-x}In_xN$ Single Quantum Wells with Various Well Widths

6.1 Introduction

With a band gap extending from that of InN, 0.7 eV in the infrared, to that of AlN, 6.2 eV in the deep ultraviolet, $Al_{1-x}In_xN$ offers the widest spectral coverage of all three ternary nitride alloys. It opens up many significant III-nitride optoelectronic applications. Most importantly, $Al_{1-x}In_xN$ can be lattice-matched to GaN with an InN fraction of approximately 17 % [1-5] with a band gap estimated to be around 4.1 eV. Detailed study on the band gap of $Al_{1-x}In_xN$ will be presented and discussed in **Chapter** 7. With free-standing GaN (FS-GaN) substrates now commercially available, deployment of lattice-matched $Al_{1-x}In_xN$ offers the possibility to reduce defect densities in strain free GaN-based devices, such as laser diodes and transistors. Ref. 6 demonstrates the strain-free state and sharp excitonic transitions in the topmost GaN layers of lattice-matched GaN-$Al_{1-x}In_xN$-GaN trilayer structures grown on FS-GaN. In addition, lattice-matched GaN/$Al_{1-x}In_xN$ can be used as cladding layers for optical waveguides due to its relatively high refractive index contrast with GaN (7 % and 4 % at $\lambda = 400$ and 1500 nm, respectively) [5, 7]. This has allowed the development of lattice-matched III-N dielectric Bragg mirrors [2, 8] and insertion layers for *in situ* growth monitoring by reflectometry [3]. Another possible field of application for lattice-matched GaN/$Al_{1-x}In_xN$ structures is their use for fabricating mid-infrared intersubband (ISB) high-speed photodetectors or modulators, thanks to the large conduction band offset (CBO) offered by their heterostructures [7]. Lattice-matched GaN/$Al_{1-x}In_xN$ multi-quantum wells (MQWs) can thus be used as an alternative approach to the traditionally used GaN/$Al_xGa_{1-x}N$ system.

In order to develop efficient devices, the parameters governing the optical properties of GaN/$Al_{1-x}In_xN$ heterostructures have to be investigated. The most important are the band gap energies, the emission efficiency and the giant built-in electric field which is known to affect the optical properties of wurtzite heterostructures through the quantum confined Stark effect [7-10]. Early works performed by S. Nicolay *et. al.* [7] and R. Butté *et. al.* [10] involved growing several lattice-matched GaN/$Al_{1-x}In_xN$ single quantum wells (SQWs) with different well thicknesses to study the built-in electric field. A linear dependence of the PL emission driven by the electric field is observed from which the value varies from 3.0 to 3.6 MV/cm. Nevertheless, some properties of GaN/$Al_{1-x}In_xN$ heterostructures remain unclear owing to the challenge of finding growth conditions allowing efficient co-incorporation of Al and In into single-phase layers of high crystal quality, as discussed in **Chapter 2.** At the same time differences in growth on FS-GaN and GaN-on-sapphire substrates have not been explored.

This chapter describes the study of the optical properties of near-lattice-matched GaN/$Al_{1-x}In_xN$ single quantum wells (SQWs) as a function of GaN well width using photoluminescence (PL) and PL excitation (PLE) spectroscopy. Samples were grown on *c*-plane sapphire and on FS-GaN substrates. PL and PLE data are used to characterise the wells and provide information on the optical properties of the near-lattice-matched $Al_{1-x}In_xN$ barriers. Selectively excited PL spectra distinguish luminescence originating in the wells, barriers and the underlying GaN buffer layers. The effects of the excitation power density and sample temperature on the optical properties are also considered.

6.2 Specific Samples and Experimental Details

GaN/$Al_{1-x}In_xN$ SQW samples were grown by Dr. Ian Watson at the Institute of Photonics from University of Strathclyde using metal organic chemical vapour deposition (MOCVD) in an Aixtron 200-series reactor. Trimethylaluminium (TMAl), trimethylindium (TMIn), trimethylgallium (TMGa) and ammonia (NH_3) were used as precursors for Al, In, Ga and N respectively.

Two batches of samples were grown with different lower barrier thickness. The first batch of samples consisted of SQWs with nominal thickness 1.5, 3 and 4 nm and were grown on 1.5 μm GaN buffer layers on *c*-plane sapphire substrates. These have $Al_{1-x}In_xN$ lower barriers and caps both of 10 nm thickness. As for the second batch samples, similar GaN SQWs with nominal thicknesses 2.5 and 4 nm were grown simultaneously on FS-GaN substrates and GaN-on-sapphire templates. In these samples the thickness of the $Al_{1-x}In_xN$ barriers below the QWs is increased to 100 nm, with 10 nm $Al_{1-x}In_xN$ caps. The FS-GaN substrates had polished back-sides, while the templates had non-polished back-sides. No intentional doping was used in any layer. The GaN QW material was grown at the same temperature as the $Al_{1-x}In_xN$ (a setpoint of either 815 or 820 °C). The QW thicknesses were determined by the growth time, assuming a growth rate of 54 nm/hr, measured in a separate calibration run. The InN composition in $Al_{1-x}In_xN$ layers was targeted to the lattice-matched to GaN. A schematic structure of a GaN/$Al_{1-x}In_xN$ SQW sample is shown in Figure 6.1.

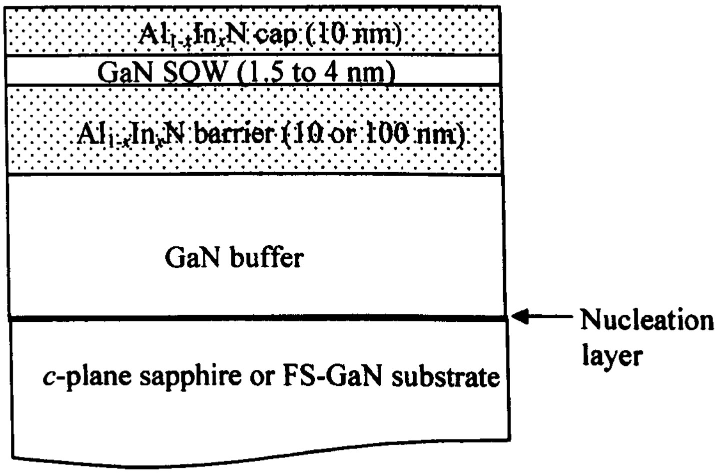

Figure 6.1 Schematic structure of a GaN/$Al_{1-x}In_xN$ SQW (not to scale).

Figure 6.2(a) and 6.2(b) present the transmission electron microscopy (TEM) images of the samples with nominal well width of 4 nm and a lower $Al_{1-x}In_xN$ barrier of 10 nm on *c*-plane sapphire and a lower $Al_{1-x}In_xN$ barrier of 100 nm on FS-GaN substrates, respectively. TEM was performed by Dr. Zhi Hao Wu and Prof. Fernando Ponce in the Department of Physics and Astronomy at Arizona State University. The images confirm an actual QW thickness of 4.1±0.2 nm close to the target value, and the coherent nature of the interfaces. It is observed that for the sample grown on sapphire substrate (in Figure 6.2(a)) that the upper interface is considerably rougher than the lower one. As for sample grown on FS-GaN substrate (in Figure 6.2(b)), both the lower and upper interfaces are considerably smoother. The growth conditions of the GaN/$Al_{1-x}In_xN$ SQW samples are summarised in Table 6.1.

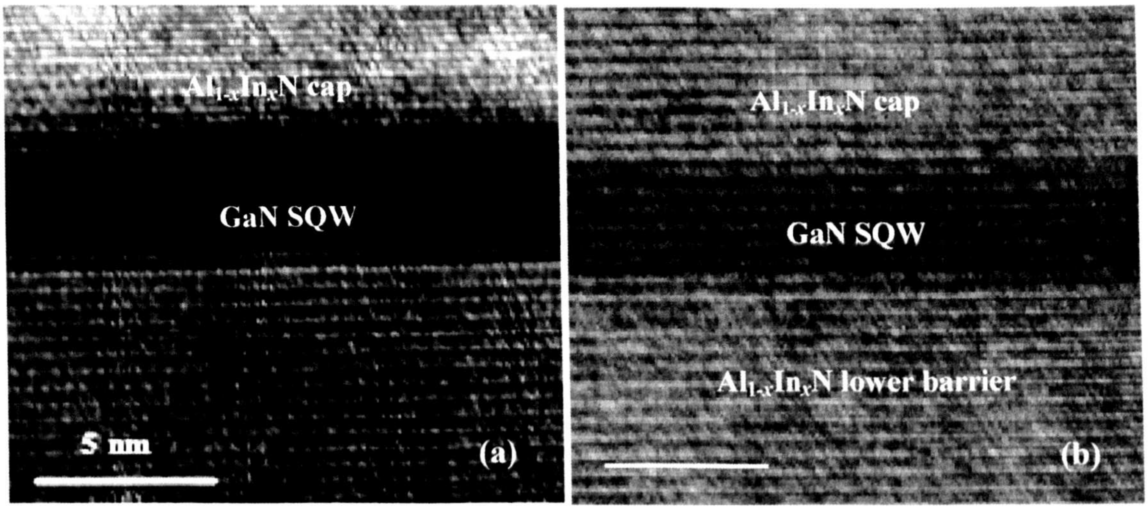

Figure 6.2 TEM images of the near-lattice-matched 4 nm GaN/$Al_{1-x}In_xN$ SQWs grown on (a) sapphire substrate and thin 10 nm $Al_{1-x}In_xN$ barrier, and (b) FS-GaN substrate and thick 100 nm $Al_{1-x}In_xN$ barrier.

Table 6.1 Growth conditions of GaN/$Al_{1-x}In_xN$ SQW samples.

Sample ID	Substrate	Growth Temp (°C)	Well Width, Twell (nm)	Cap Thickness (nm)	Lower Barrier (nm)
STR438	Sapphire	815	1.5	10	10 ("Thin")
STR440		815	3		
STR439		815	4		
STR455A	FS-GaN	820	2.5	10	100 ("Thick")
STR455 (same run as STR455A)	GaN-on-Sapphire	820	2.5		
STR447A	FS-GaN	815	4		
STR447 (same run as STR447A)	GaN-on-Sapphire	815	4		

The "thin lower barrier series" and "thick lower barrier series" each contain samples whose growth conditions differ only in the thickness of the well width. Study of each series provides information on the influence of the well width thickness on the optical properties. Comparison of the two series provides information on how the difference in the lower barrier thickness will affect such characteristics as the luminescence intensity and the peak emission wavelength. In addition, the "thick lower barrier series" contains samples whose growth conditions differ only in the choices of substrates. It is worth mentioning that these samples (STR455A and STR455; STR447A and STR447) were grown in the same run on their individual quarter-wafer substrates. Hence, studies of these samples provide accurate information on the influence of the substrates on the optical and compositional properties.

PL was excited by the monochromated emission from a 1000 W short arc xenon (Xe) lamp or by a frequency-doubled cw Ar^+ laser (244 nm). PLE spectra were also obtained using the Xe-lamp, and were corrected for the Xe-lamp output and throughput of the monochromator. The incident lamp power on the sample averages 0.3 mW on a surface area of about 2 x 5 mm^2. The laser power measured on the sample surface was either 0.06 mW in a 10 μm spot size or varied from 0.05 to 90 mW in a 200 um^2 spot area. The samples were maintained at $\approx$ 17 K in a closed-cycle helium cryostat for the lamp excitation, and $\approx$ 9 K and at room temperature (RT) for the laser excitation. For temperature dependent PL spectra, the temperature was varied from $\approx$ 10 to 300 K using a heater in combination with a temperature controller.

The compositions of the samples were primarily investigated using wavelength dispersive x-ray (WDX) measurements on a Cameca SX100 EPMA system as described in **Chapter 4**. The standards used to measure In, Ga, N and Al are given in **Table 4.1** along with the analysis crystals and x-ray lines used for all four elements. As mentioned in **Chapter 4**, the minimum practical beam energy for quantitative analysis is around 1.3 times the threshold for x-ray excitation [11]. In $Al_{1-x}In_xN$, the highest x-ray excitation energy is 3.29 keV for the In L_α line. As we are measuring In, our beam energy should be above 4.3 keV in order to obtain reasonable x-ray counts. Hence, 5 keV and 20 nA were applied on the "thick lower barrier series" SQW samples to measure the InN composition in the barrier layers. It is assumed that the thickness of the QW is very thin as compared to those of the barrier layers and thus has negligible influence on the InN composition measurement.

6.3 Experimental Results and Discussion

6.3.1 Effect of Well Width

Figure 6.3 and 6.4 show the normalised low-temperature (LT) and room temperature (RT) PL spectra of the near-lattice-matched GaN/$Al_{1-x}In_xN$ SQWs with thin (10 nm) lower $Al_{1-x}In_xN$ barriers on sapphire substrates, using 280 nm Xe-lamp and 244 nm laser excitation, respectively. The arrows indicate the QW emission peaks and the dotted line indicates the GaN emission energy.

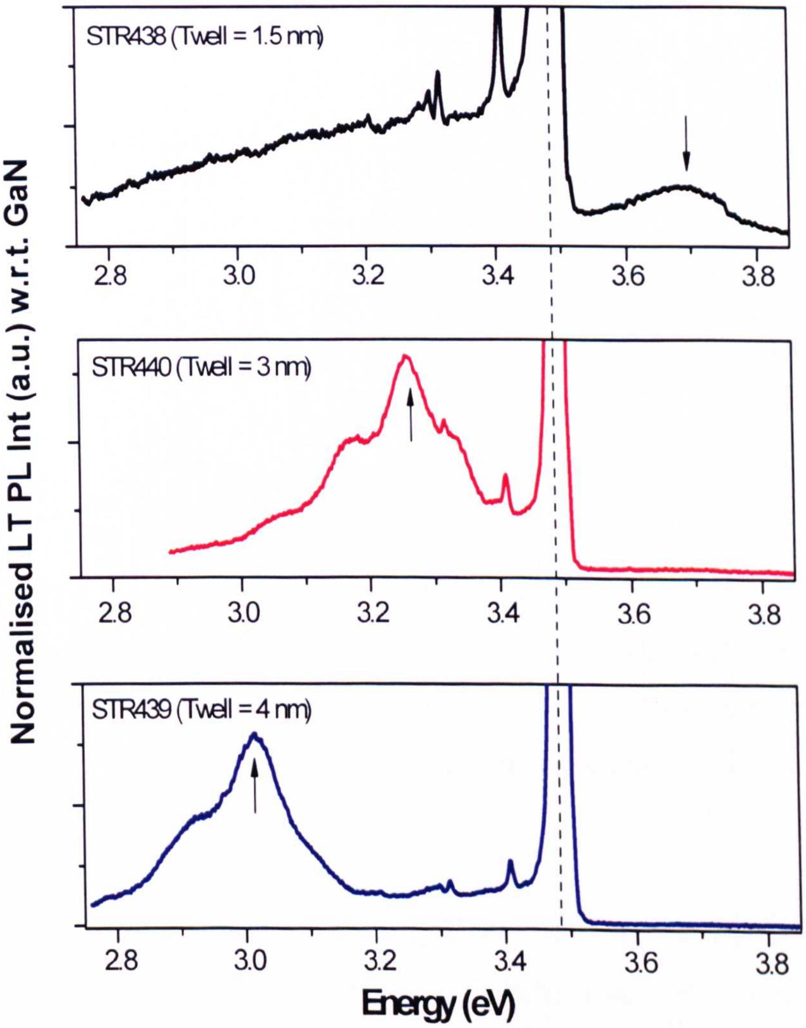

Figure 6.3 Normalised LT PL spectra of GaN/$Al_{1-x}In_xN$ SQWs with thin 10 nm lower barriers on sapphire substrates using 280 nm Xe-lamp at 17 K. The excitation power density for lamp is ≈ 0.003 W/cm^2.

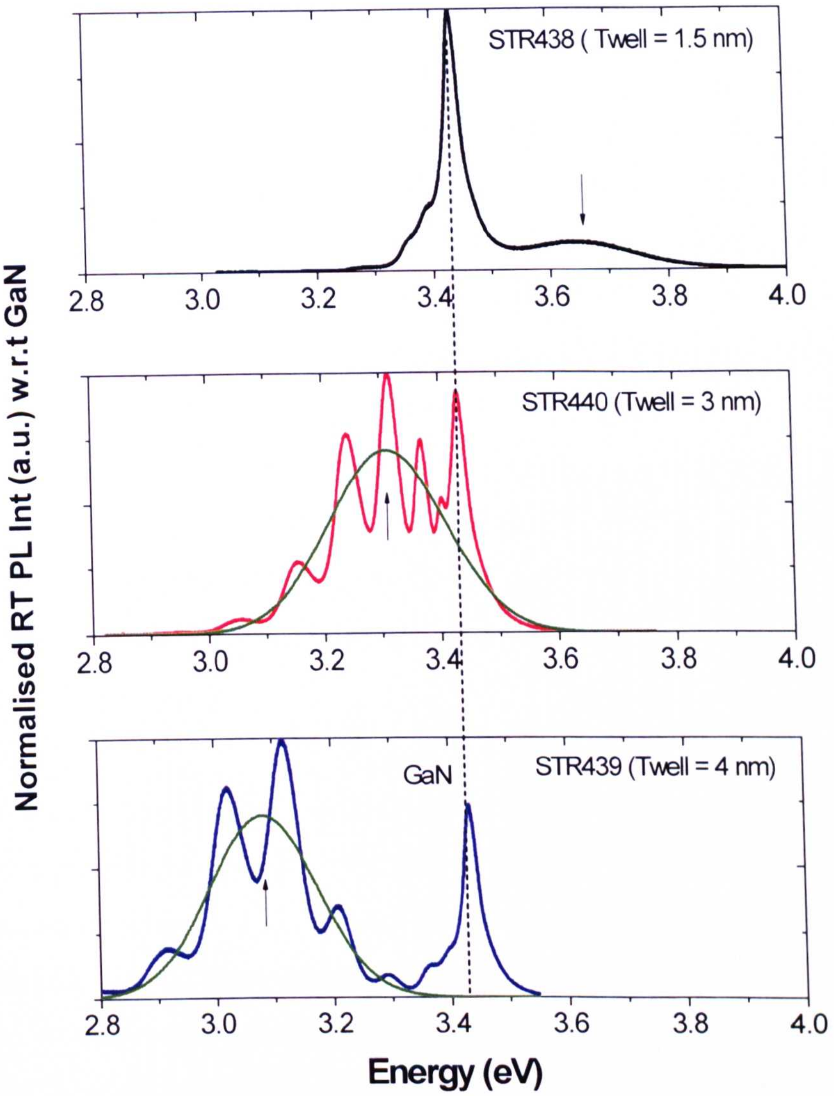

Figure 6.4 Normalised RT PL spectra of GaN/Al$_{1-x}$In$_x$N SQWs with thin 10 nm lower barriers on sapphire substrates using 244 nm laser excitation with a power density of ≈ 0.76 kW/cm^2. The green lines show Gaussians, smoothing out the interference fringes.

For the thin well of width 1.5 nm, a QW PL peak centred at an energy of near 3.65 eV is observed. This is well above the GaN band gap (at ≈ 3.48 eV), due to the quantum confinement effect. However, as the well width increases from 1.5 to 4 nm, the SQW peak energy decreases rapidly from ≈ 3.65 to 3.05 eV, moving well below the bulk GaN band gap. This is a manifestation of the quantum confined Stark effect (QCSE) resulting from the intense in-built electric field, as has been reported for GaN/Al$_{1-y}$Ga$_y$N hetero-structures [9, 12]. As explained in **Chapter 2**, the QCSE results in the separation of the wave function of the electron and hole. This is due to the fact that the electrons and holes which form the excitons are pulled in opposite directions by the internal electric field. Hence, this causes a reduction in transition energy and the red-shift of the SQW emission becomes larger as the well width increases. This electric field arises from both piezoelectric and spontaneous polarisation discontinuities between the well and barrier materials [13]. For near-lattice-matched material the piezo-component of this field approaches zero but intense spontaneous polarisation fields remain. In addition, the interference fringes are more prominent in the laser excited spectra than in Xe-lamp excited spectra. This is probably due to greater thickness uniformity of the sample within the much smaller measurement area for the laser. In addition, it is noted that the luminescence intensity of the GaN peak quenched faster than the QW peak at room temperature as presented in Figure 6.4.

A similar red-shift in the QW peak emission energy is seen in the samples on FS-GaN substrates with increasing well width as shown in Figure 6.5. The QW emission energy decreases from ≈ 3.32 to 3.08 eV as the well width increases from 2.5 to 4 nm. Gaussian fittings were employed to identify the additional features present in the figure. A broad emission band in the higher energy range at around 3.72 eV is seen. This is attributed to band-to-band emission from the $Al_{1-x}In_xN$ barrier, in agreement with an earlier $Al_{1-x}In_xN$ epilayer as shown in Figure 6.6.

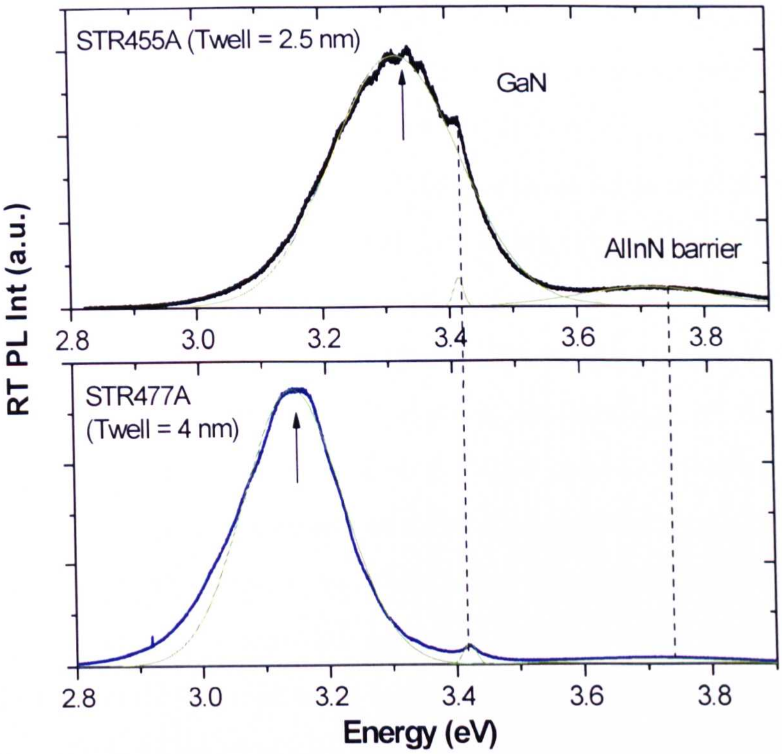

Figure 6.5 RT PL spectra of GaN/Al$_{1-x}$In$_x$N SQWs with 100 nm lower barriers on FS-GaN substrates using 244 nm laser excitation of ≈ 0.76 kW/cm^2. Arrows indicate the QW emission peaks and green lines denote Gaussian fittings.

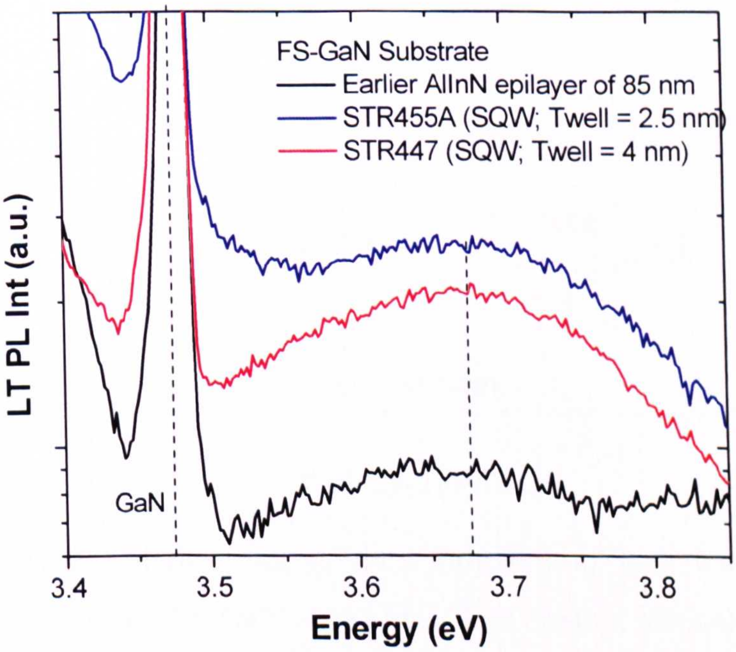

Figure 6.6 Low temperature (17 K) PL spectra of GaN/Al$_{1-x}$In$_x$N SQW samples with 100 nm lower barriers and an Al$_{1-x}$In$_x$N epilayer on FS-GaN substrate using 280 nm Xe-lamp excitation of ≈ 0.003 W/cm^2.

Figure 6.7 plots the QW peak energy as a function of well width for samples grown on sapphire and FS-GaN substrates. A linear variation of the peak PL energy with well width is observed, which is similar to that of GaN/$Al_{1-y}Ga_yN$ hetero-structures [9, 12, 14]. The two data points for FS-GaN samples suggest a slower red-shift of QW peak with increasing well width. The QW emission peak for a well width of 1.5 nm exceeds that of the GaN band gap, as a result of quantum confinement, but rapidly falls below this as the width increases due to the electric field. The electric field is estimated to be 2.6±0.5 MV/cm, using the gradient of the emission peak energy as a function of the well width and single particle calculations of confined energy levels as discussed in **subsection 6.3.1.1**. An earlier study of lattice-matched GaN/$Al_{1-x}In_xN$ quantum wells on sapphire substrate reported a red-shift of similar gradient [7]. However, the reported emission energies for a given well width are offset from those in the present work, probably due to systematic differences in the well widths or different residual strains resulting from the $Al_{1-x}In_xN$ composition.

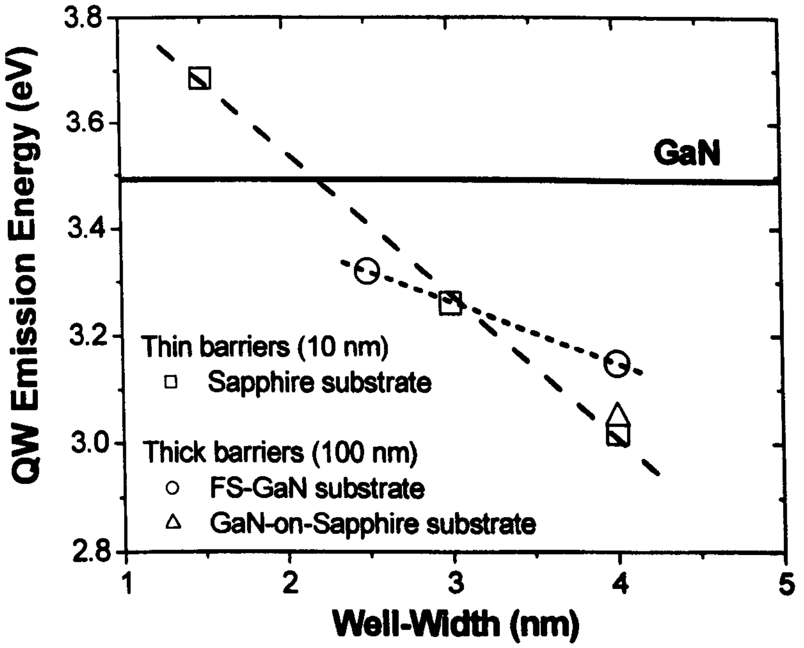

Figure 6.7 QW emission energy as a function of well width for samples grown on sapphire and FS-GaN substrates. The dashed lines are guides for the eye indicating the different gradients for the different substrates.

6.3.1.1 Electric Field Calculation

As the internal polarisation fields in nitride quantum wells lead to a pronounced QCSE, the resulting strong variation of emission energy with quantum well width can be utilised to quantitatively determine the magnitude of the internal field. In this work, the internal built-in electric field for the samples with thin barriers on sapphire substrates is estimated using the gradient of emission energy as a function of well width and a program written by Prof. Mark Fox from University of Sheffield. The program uses a tunnelling resonance model to estimate the confined levels for a single particle. By combination of these methods the internal built-in electric field is estimated to be 2.6±0.5 MV/cm.

- *Gradient of Emission Energy vs. Well Width*

A schematic diagram of the total QW transition energy for a narrow and wider well width is illustrated in Figure 6.8.

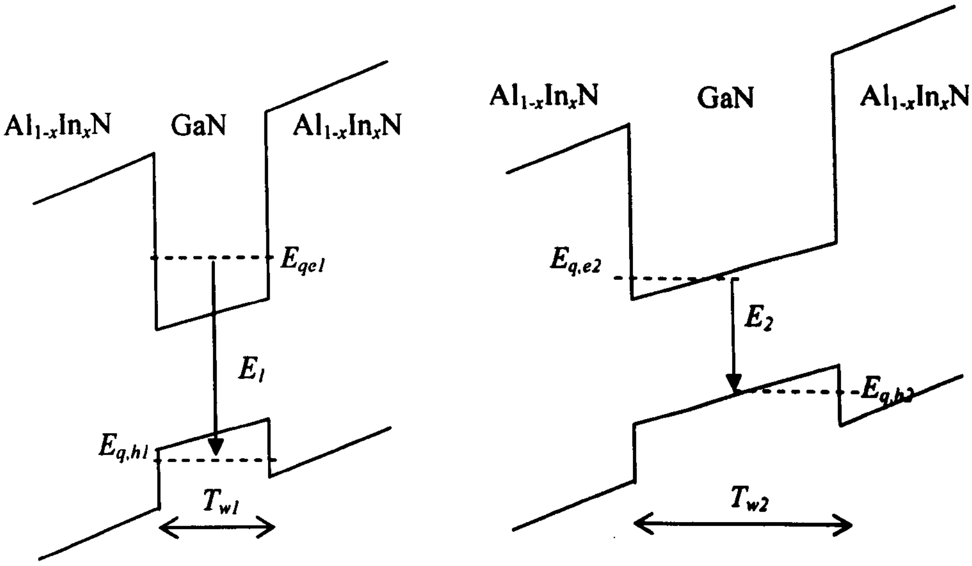

(a) (b)

Figure 6.8 Schematic diagram of total QW transition energy with (a) narrow well width and (b) wider well width. $E_{q,e}$ and $E_{q,h}$ represent the quantisation energy of electron and hole at ground state (n = 1) respectively.

The above figure shows that the total QW transition energy (E) is the summation of the quantisation energies of electron ($E_{q,e}$) and hole ($E_{q,h}$) and the energy band gap of GaN (E_{GaN}) minus the offset induced by the internal electric field (ξ):

$$E = E_{q,e} + E_{q,h} + E_{GaN} - q.(\xi.T_w) \tag{6.1}$$

Therefore, the difference in the transition energies in different well widths is as follows:

$$E_1 - E_2 = (E_{q,e1} - E_{q,e2}) + (E_{q,h1} - E_{q,h2}) - q.\xi(T_{w1} - T_{w2}) \tag{6.2}$$

If the quantisation energies of electron and hole in different well widths can be assumed to be equal, then one can estimate the internal electric field directly from the gradient of the transition energy versus well width. This would apply for triangular wells, as discussed later in **subsection 6.3.1.1.2**. Thus, Equation 6.2 is simplified as:

$$E_1 - E_2 = q.\xi(T_{w2} - T_{w1}) \tag{6.3}$$

$$\xi = \frac{(E_1 - E_2)}{q.(T_{w2} - T_{w1})} \tag{6.4}$$

The electric field estimated from the gradient of Figure 6.8 is around 2.7 MV/cm

- *Single Particle with Confined Energy Levels*

In the tunnelling resonance program, the QW structures are designed to be as similar as possible to the experimental samples with similar well width but the barrier thickness selected is 4 nm. This is because the program does not work well with wide barrier thickness where the tunnelling is observed to be very weak.

The fixed parameters used are: (i) the conduction to valence band offset ratio of 70:30 is selected in the calculation as employed in Nicolay *et. al.* [7]; (ii) concerning the band gap of the $Al_{1-x}In_xN$ barrier, a value of 4.25 eV is applied on the basis of the PLE measurements carried out on 3 and 4 nm well widths $GaN/Al_{1-x}In_xN$ SQWs (as discussed later); (iii) the energy band gap of GaN is 3.5 eV; and (iv) the effective masses of the QW ground-state electron (*e*) and heavy hole (*hh*) used in the calculation are those of GaN as 0.2 and 0.8 respectively [15]. The varied parameters are the well widths varying from 1.5 to 4 nm and the internal electric fields range from 0 to 3 MV/cm.

By applying different values to the electric field while fixing the well width, the quantised energies at respective electric fields are determined. The procedure is repeated by varying the well width while keeping the electric field constant. Using Equation 6.1, the total QW transition energy can be calculated. The calculated QW transition energies are then compared with the experimental emission energies as presented in Figure 6.9. Similar trend in the change in transition energy as a function of well widths at various electric fields is observed in Franssen *et al.* [16]. The internal electric field in these samples is estimated to be around 2.5 MV/cm. However it is important to highlight that this tunnelling resonance model is not ideal as the model is struggling to calculate the confined levels at the very high electric fields present in these structures. There are greater uncertainties when the electric field is above 1.5 MV/cm. Nevertheless, the program shows that the confined levels become independent of well thickness for electric field ≥ 1 MV/cm and well width above 2 nm as represented by the linear slopes. This is due to the electron and hole wave functions being pulled into the corner of the triangular QW at high electric field, in this case ≥ 1 MV/cm. Hence, they are not affected by increase of well width. This suggests that the above gradient model discussed earlier is applicable.

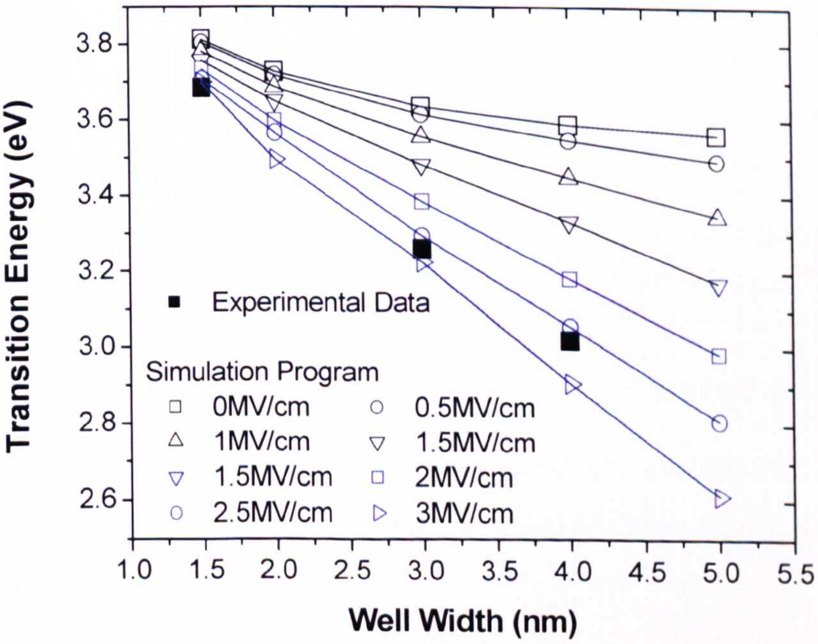

Figure 6.9 QW transition energy versus well width. The solid and open symbols are experimental data and data using tunnelling resonance program, respectively. The blue open symbols indicate the program is struggling.

Selectively excited PL and PLE spectra were measured at a low temperature of 17 K on the 3 and 4 nm well width SQW samples grown with thin barriers on sapphire substrates as shown in Figure 6.10 and Figure 6.11, respectively. For the SQW samples, there is no change in the QW peak position, i.e. 3.26 eV for 3 nm well and 3.02 eV for 4 nm well, is observed as the excitation wavelength increases from 230 to 340 nm. However, the QW PL peak intensity first increases as the excitation wavelength increases from 230 to 280 nm, before it declines with further increase in excitation wavelength.

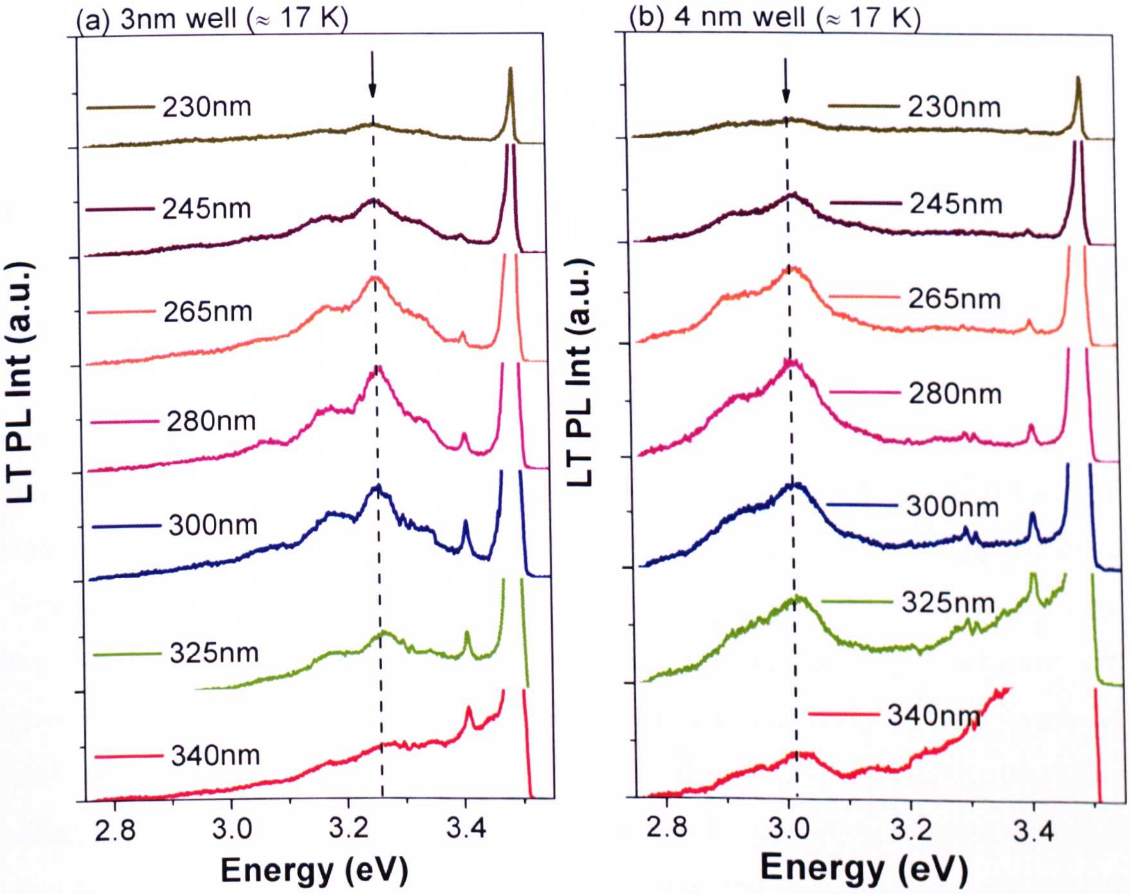

Figure 6.10 Low temperature (≈ 17 K) selectively excited PL spectra of the well width of 3 nm and 4 nm GaN/$Al_{1-x}In_xN$ SQWs with thin lower barriers on sapphire substrates.

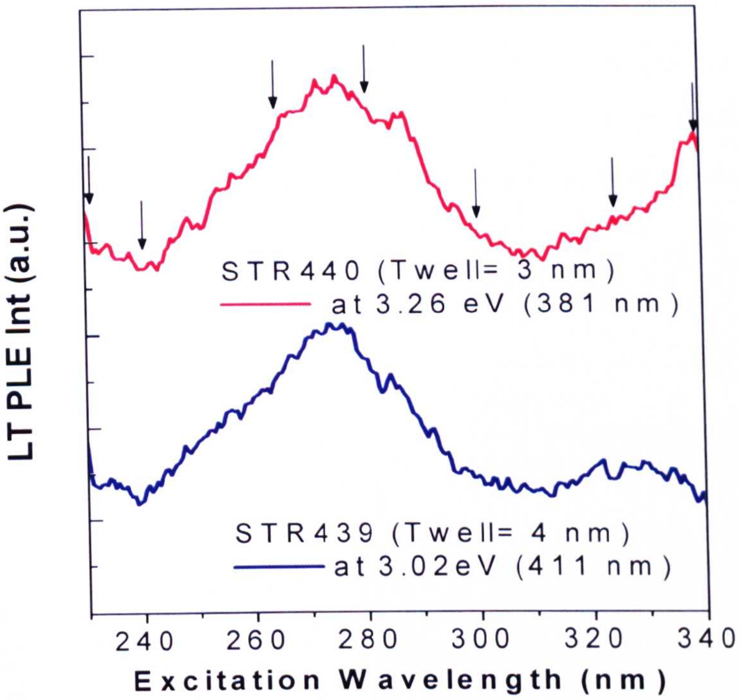

Figure 6.11 Low temperature (≈ 17 K) PLE spectra from the SQWs on sapphire substrates detected at 3.26 eV (3 nm well) and 3.02 eV (4 nm well). The arrows are the selectively excitation wavelengths as shown in Figure 6.10.

The PLE spectra provide details of the absorption in the $Al_{1-x}In_xN$ barriers, showing a peak near 275 nm in Figure 6.11. The effective band gap is estimated to be ≈ 4.25 eV using sigmoidal fitting to the PLE spectrum [17]. Hence the band gap difference between GaN and near-lattice-matched $Al_{1-x}In_xN$ is seen to be as large as almost 0.8 eV. A decrease in PLE signal at low excitation wavelength is not commonly observed in samples where the QW is placed close to the surface [18-19] as in this work with cap thickness of around 10 nm. A possible explanation is the 'hot carrier effect', consistent with the observation of a GaN peak at very short excitation wavelength (e.g. 230 nm). At high excitation energy, the photo-induced 'hot' carriers overshoot the well region, and reach the GaN buffer layer before recombining. A small bump near 327 nm (3.79 eV) is observed in the PLE spectrum of the 4 nm well width sample in Figure 6.11. This excitation could be contributed by the $Al_{1-x}In_xN$ barrier emission.

6.3.2 Effect of Substrate

In order to study the effect of the substrates on the optical properties, a direct comparison of 4 nm QW samples grown simultaneously on GaN-on-sapphire and FS-GaN substrates, both with 100 nm thick lower $Al_{1-x}In_xN$ barriers, is made using log-scale RT PL as shown in Figure 6.12.

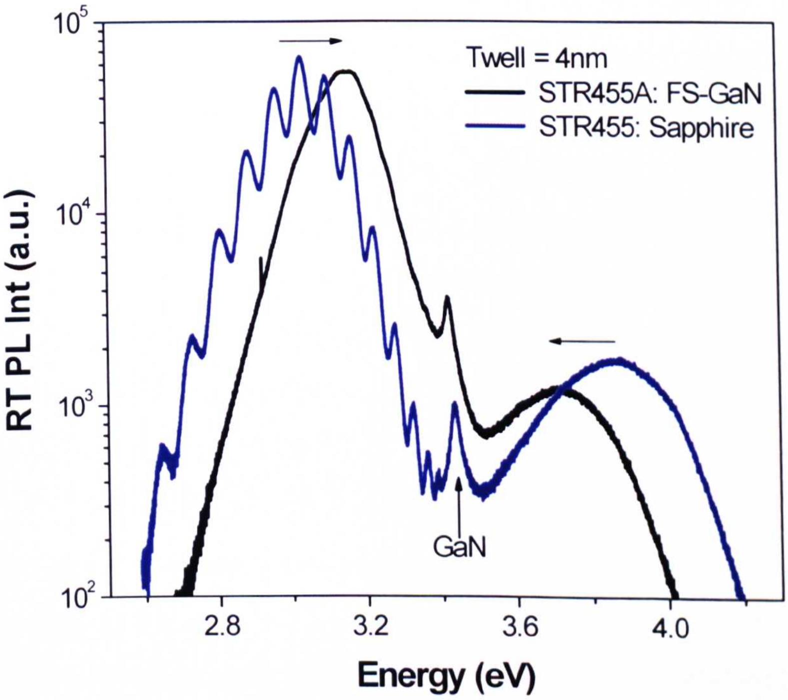

Figure 6.12 RT PL spectra of the 4 nm well width $GaN/Al_{1-x}In_xN$ SQWs grown simultaneously on GaN-on-sapphire templates and FS-GaN substrates, excited by the laser with a power density of ≈ 0.76 kW/cm^2. The thickness of the lower $Al_{1-x}In_xN$ barriers is 100 nm.

The emission from the $Al_{1-x}In_xN$ barrier is now observed near 3.86 eV (3.71 eV) for sapphire (FS-GaN) substrates, in addition to that from the QW and underlying GaN. The interference fringes are absent for FS-GaN substrates due to similar refractive index between the substrate and the layers. The peak energies have shifted in comparison to the equivalent structure on GaN-on-sapphire: the QW transition energy *blue-shifts* whilst the barrier emission *red-shifts* as indicated by arrows. The GaN peak energy at ≈ 3.42 eV is the same in both samples and very close to the value for strain-free GaN as described in Ref. 20, indicating that the strain is similar.

These spectral shifts, i.e. a *blue-shift* in QW transition energy and a *red-shift* in $Al_{1-x}In_xN$ barrier emission, are attributable to small substrate surface temperature variations resulting from the difference in the characteristics of sapphire and FS-GaN substrates. The FS-GaN evidently had a lower surface temperature than GaN-on-sapphire template, resulting in a lower QW growth rate (*blue-shift* in QW emission energy), and a higher InN incorporation in the barrier (*red-shift* in barrier emission energy). The net temperature difference arose from an interplay of the different thermal conductivities (approximately 3 times higher for FS-GaN than sapphire) [21], thickness, planarity and back-side finishes of the different substrates. In this work, the sapphire pieces had non-polished back-side as compared to the polished back-side for the FS-GaN where polishing is suggested to increase the effectiveness of radiative heating of the substrate. Similar behaviour can be observed in the $Al_{1-x}In_xN$ epilayers grown on polished and non-polished *c*-plane sapphire substrates where more studies on the effects of the substrates on $Al_{1-x}In_xN$ epilayers will be presented and discussed in **Chapter 7**.

The composition of these samples as summarised in Table 6.2 was estimated using wavelength dispersive x-ray (WDX) measurements. The WDX analysis shows all the SQW samples on FS-GaN substrates are closer to lattice match with ≈ 18 % InN in the barriers, having 3 to 4 atomic % more InN than those grown GaN-on-sapphire templates.

Table 6.2 $Al_{1-x}In_xN$ sample details and measured In composition using WDX.

Sample ID	Substrate	In Composition (%)
STR455A	FS-GaN	18.5
STR447A		18.0
STR455	GaN-on-Sapphire	15.3
STR447		14.4

Reducing the InN composition in the barriers below the lattice-match point results in a piezoelectric field that reinforces the spontaneous polarisation field. The increased field for the more highly strained samples grown on sapphire, compared to those on

FS-GaN, is illustrated by the steeper gradient in Figure 6.7. Lorenz *et al* [22] have investigated the evolution of the strain state of $Al_{1-x}In_xN$ layers close to lattice-match with GaN ($0.13 < x < 0.20$) using the combination of Rutherford Backscattering spectrometer (RBS) and x-ray diffraction (XRD) measurements. They showed that the strain state of the $Al_{1-x}In_xN$ films, about 100 nm thick, grown on GaN buffer layers changes from tensile to compressive with increasing In content with lattice-matching to GaN occurring at an indium content of 17.1 %. Another factor that could influence the electric field is the sample structure. The barrier thickness of the samples grown on sapphire (10 nm) is thinner that those grown on FS-GaN substrates and GaN-on-sapphire templates (100 nm). In this work, it is believed that the barrier thickness plays a secondary role in comparison to that of the InN composition in affecting the electric field. This is because the QW emission energies of the 4 nm well width samples on sapphire are almost the same although their barrier thicknesses differ by 10 times, as illustrated in Figure 6.7.

6.3.3 Effect of Power

In order to investigate the dependence of QW transition energy on the power, the laser excitation power on the sample was varied from 0.057 to 90 mW in a 200 μm^2 laser spot area.

Figure 6.13 plots the QW transition energies of the samples grown on sapphire and FS-GaN substrates as a function of the excitation power density. As shown in the figure, there is a strong dependence of the QW transition energy on the excitation intensity for some widths of SQW. Similar behaviour is seen for the wider width wells samples grown on both sapphire and FS-GaN substrates. However, there is no change in the QW transition energy for thin samples (1.5 nm) as the power density varies from 0.22 to 9.0 kW/cm^2. For wider QWs, the transition energy increases with the power, due to the screening of the internal electric fields by photo-induced free carriers. This has a larger impact in the wider wells where the wavefunctions of electrons and holes are separated further. Similar behaviour has been reported in $In_xGa_{1-x}N/GaN$ MQWs [23]. It is observed that the shift in QW transition energy increases with the well width from around 25 meV (2.5 nm) to 115 meV (4 nm).

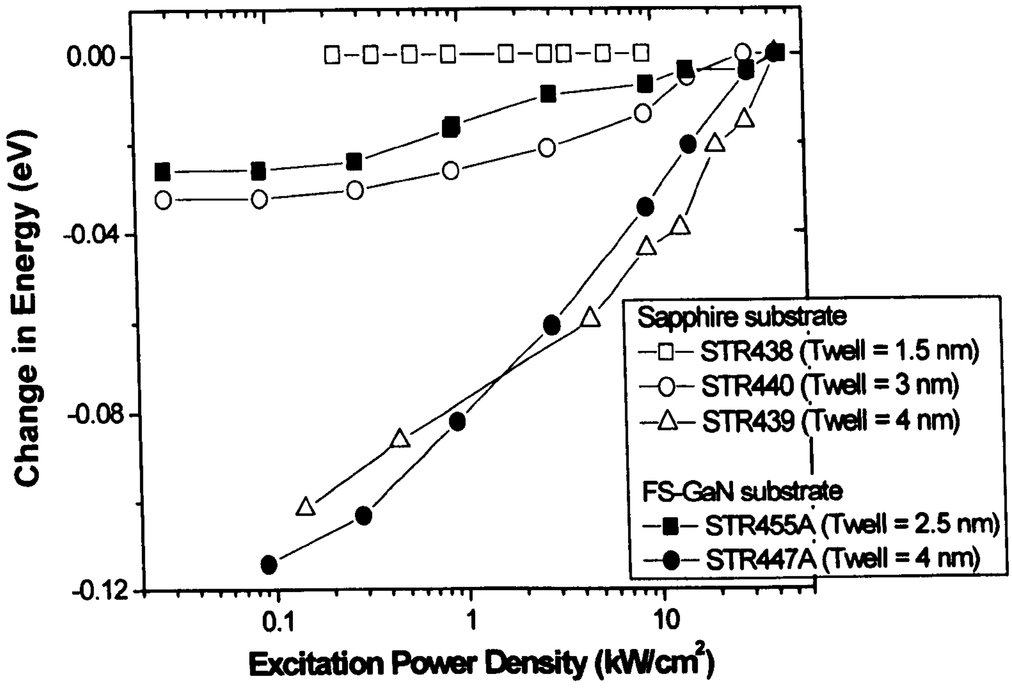

Figure 6.13 Change in QW emission energy as a function of excitation power density for GaN/Al$_{1-x}$In$_x$N SQWs on sapphire and FS-GaN substrates using laser excitation at a low temperature of ≈ 9 K.

6.3.3.1 Carrier Density Calculation

In order to estimate the photo-induced carrier density, the generation rate equation due to light in Ref. 24 and electron density equation in Ref. 25 were employed as presented in the following subsections.

- *Generation Rate Equation*

When a semiconductor is illuminated with light, carriers can be generated. The energy of incoming photons is used to bring an electron from a lower energy level to a higher energy level. In the case where an electron is removed from the valence band and added to the conduction band, an electron-hole pair is generated. A necessary condition is that the energy of the photon, E_{ph}, is larger than the band gap energy, E_g.

If each absorbed photon creates one electron-hole pair, the electron and hole generation rates are given by [24]:

$$G_{electron,light} = G_{hole,light} = \alpha.\frac{P_{opt}(x)}{E_{ph}.A} \tag{6.5}$$

where α is the absorption coefficient of the material at the energy of the incoming photon and $P_{opt}(x)$ is the optical power (W) as a function of distance x. The absorption of light in a semiconductor causes the optical power to decrease with distance by a factor of $exp(-\alpha.x)$.

In this work, the parameters and assumptions used are:

- $E_{ph} = hc/\lambda$ where λ is the excitation wavelength (244 nm), h is the Planck constant and c is the speed of light;
- $\alpha_{AlN} = 15 \times 10^4$ cm^{-1} [26] is chosen as the In content in the samples used in this work is low and the GaN well is thin ;
- Assume the absorbed power density per area ($P_{opt}(x)/A$) is 100 %;
- The quantum well structure is considered as 3 individual epilayers as illustrated in Figure 6.14.

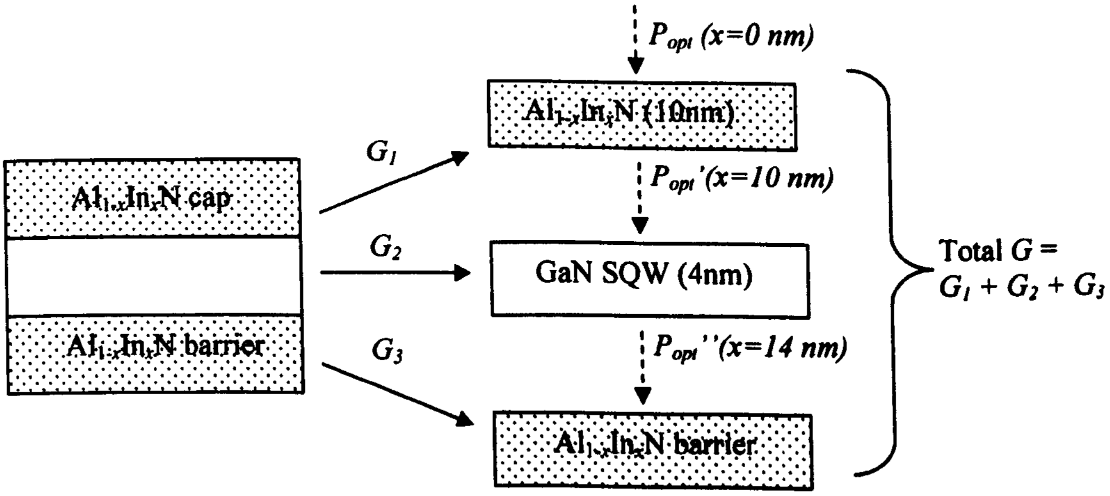

Figure 6.14 Quantum well structure as three individual epilayers.

- *Electron Density Equation*

The electron density n is expressed as [25]:

$$\frac{dn}{dt} = -A.n - B.n^2 - C.n^3 + G \tag{6.6}$$

where A is Shockley-Read-Hall non-radiative recombination, B is radiative recombination, C is Auger non-radiative recombination, and G is generation rate. The values of A, B and C coefficients are obtained from Ref. 25. At steady state, *dn/dt* is equal to zero. Hence, Equation 6.6 is simplified to:

$$A.n + B.n^2 + C.n^3 = G \tag{6.7}$$

In order to achieve steady state, a long laser pulse is required. In this work, a continuous-wave 244 nm laser was used. Using the combination of Equation 6.5 and Equation 6.7, the electron density n can be calculated. In this work, the photo-induced free carrier density is calculated to increase from 0.02 to 4.8×10^{19} cm^{-3} as the power density increases from 0.02 to 43.5 kW/cm^2.

6.3.4 Effect of Temperature

Temperature-dependent PL measurements were carried out as described in **Chapter 4**. Figure 6.15(a) to 6.15(c) show the temperature evolution of the PL spectra for samples with various well width, barrier thickness and substrates. There is clearly a decrease in the intensity as the temperature increases for each of the sample. This is due to the increase in non-radiative recombination with increasing temperature and hence a decrease in intensity.

(a) STR438 (Twell = 1.5 nm; Tbarrier = 10 nm; Sapphire substrate)

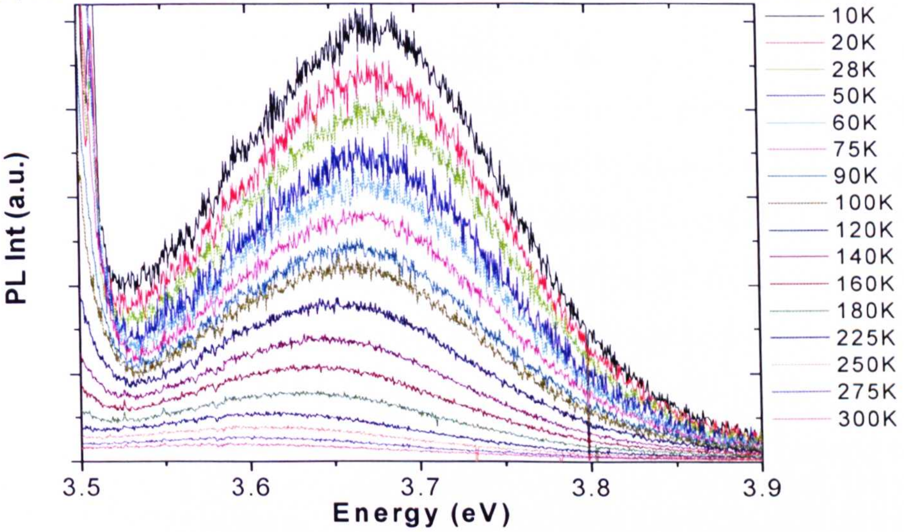

(b) STR455A (Twell = 2.5 nm; Tbarrier = 100 nm; FS-GaN substrate)

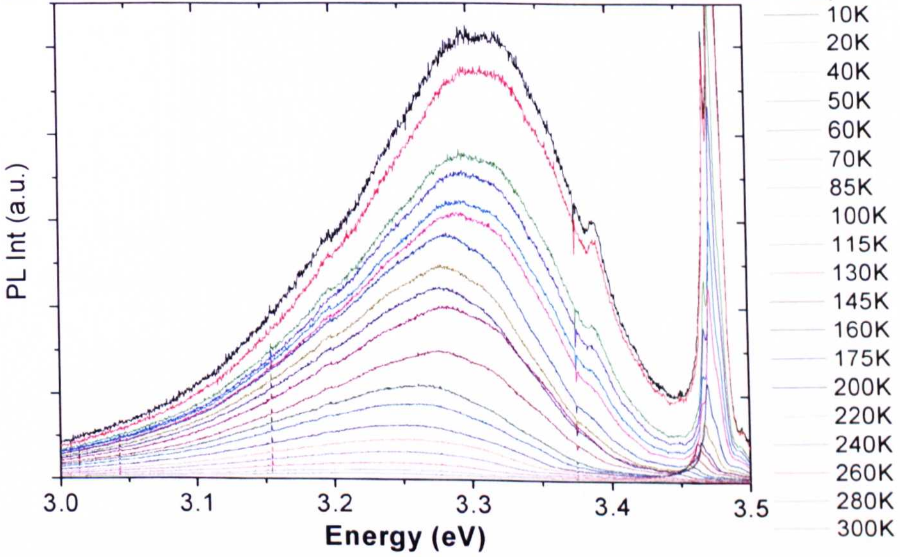

(c) STR447A (Twell = 4 nm; Tbarrier = 100 nm; FS-GaN substrate)

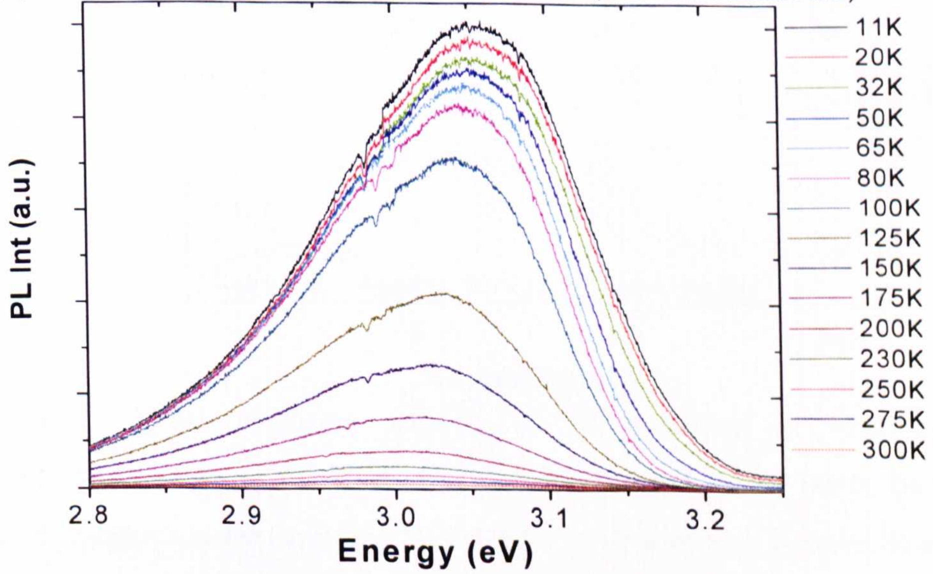

Figure 6.15 Temperature PL spectra of (a) STR438, (b) STR455A and (c) STR447A.

The position of the peak emission energy as a function of temperature for these samples is plotted in Figure 6.16. Decreasing in the QW transition energy with increasing temperature is clearly visible in all cases. No clear S-shaped behaviour is observed in contrast to the S-shaped pattern observed in $In_yGa_{1-y}N$/GaN QW samples presented in **Chapter 4**. In fact, the QW transition energies for all samples, regardless of the types of substrates, well and barrier thickness, decrease smoothly with increasing temperature and follow the temperature-induced shrinkage of the band gap. The lack of S-shaped pattern observed in this work suggests that the quantum confined stark effect is very strong and it could have overlapped the carrier localisation effect.

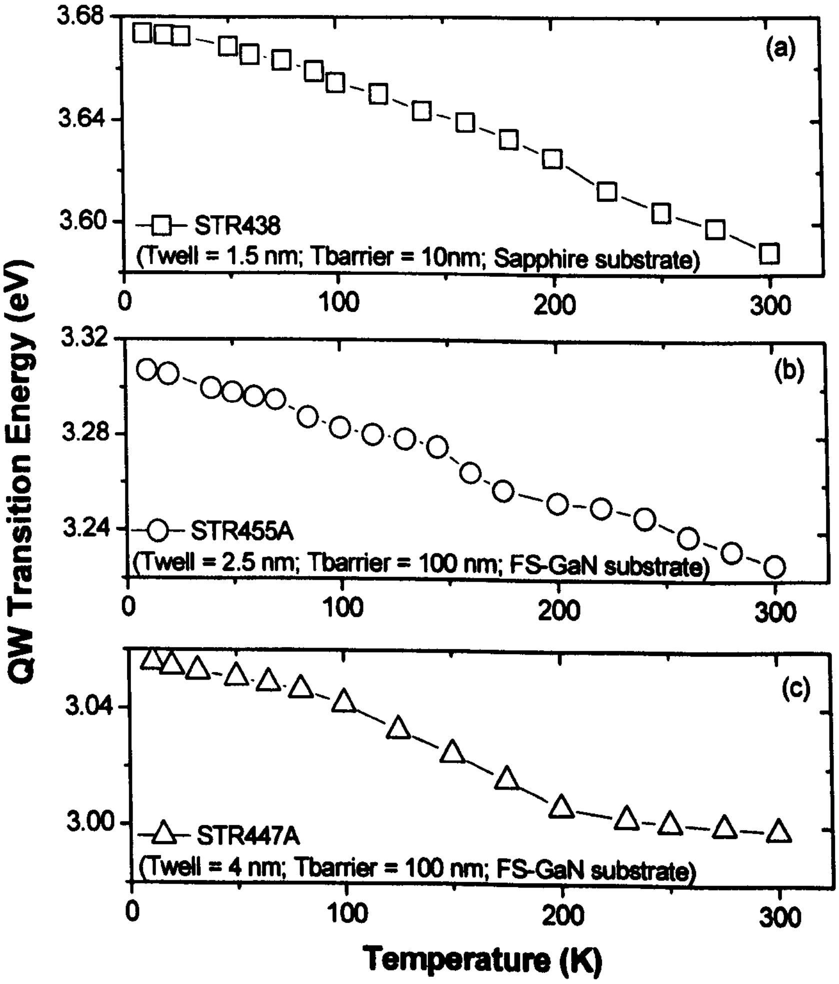

Figure 6.16 QW transition energy as a function of temperature for GaN/$Al_{1-x}In_xN$ samples (a) STR438 (well width of 1.5 nm, lower barrier of 10 nm and sapphire substrate), (b) STR455A (well width of 2.5 nm, lower barrier of 100 nm and FS-GaN substrate)and (c) STR447A (well width of 4 nm, lower barrier of 100 nm and FS-GaN substrate).

6.4 Summary

Low temperature and room temperature photoluminescence spectra of near-lattice-matched GaN/$Al_{1-x}In_xN$ single quantum well structures grown on sapphire and FS-GaN substrates have been studied as a function of GaN well width (ranging from 1.5 to 4 nm), and excitation power density and excitation wavelength. The QW peak energy decreases as the well width increases. This is a manifestation of QCSE resulting mainly from intense spontaneous polarization fields, which persist even in the absence of strain in the QW layer. The in-built electric field is estimated to be 2.6±0.5 MV/cm using the gradient of emission energy as a function of well width and single particle calculations of the confined energy levels. Also, the dependencies of the QW energy on the excitation power reveal the effects of carrier screening of the built-in electric fields in thicker wells.

The peak energies observed in the samples grown in FS-GaN substrates have shifted in comparison to the equivalent structure on GaN-on-sapphire: the QW transition energy blue-shifts whilst the barrier emission red-shifts. These spectral shifts are attributable to small substrate surface temperature variations resulting from the difference in the characteristics of sapphire and FS-GaN substrates. The net temperature difference arose from an interplay of the different thermal conductivities, thickness, planarity and back-side finishes of the different substrates. In this work, the sapphire pieces had non-polished back-side as compared to the polished back-side for the FS-GaN where polishing is suggested to increase the effectiveness of radiative heating of the substrate. In addition, the samples on FS-GaN substrates have 3 to 4 atomic % more InN than those grown on sapphire.

Temperature-dependent PL spectra show no 'S-shaped' behaviour for GaN/$Al_{1-x}In_xN$ SQW materials regardless of the types of substrates, well width and lower barrier thickness. The QW emission energy decreases as the temperature increases due to band gap shrinkage.

6.5 References

[1] J-F. Carlin, C. Zellweger, J. Dorsaz, S. Nicolay, G. Christmann, E. Feltin, R. Butté, and N. Grandjean, Phys. Stat. Solidi (B) **242**, 2326 (2005).

[2] K. Lorenz, N. Franco, E. Alves, I. M. Watson, R. W. Martin and K.P. O'Donnell, Phys. Rev Lett. **97**, 085501 (2006).

[3] I. M. Watson, C. Liu, E. Gu, M. D. Dawson, P. R. Edwards, R. W. Martin, Appl. Phys. Lett. **87**, 151901 (2005).

[4] L. T. Tan, R. W. Martin, K. P. O'Donnell, I. M. Watson, Z. H. Wu and F. A. Ponce, Appl. Phys. Lett. **92**, 031907 (2008).

[5] H. P. D. Schenk, M. Nemoz, M. Korytov, P. Vennéguès, A. D. Dräger, and A. Hangleiter, Appl. Phys. Lett. **93**, 081116 (2008).

[6] K. Bejtka, R.W. Martin, I. M. Watson, S. Ndiaye and M. Leroux, Appl. Phys. Lett. **89**, 191912 (2006).

[7] S. Nicolay, J.-F. Carlin, E. Feltin, R. Butté, M. Mosca, N. Grandjean, M. Ilegems M. Tchernycheva, L. Nevou, and F. H. Julien, Appl. Phys. Lett **87**, 111106 (2005).

[8] J.-F Carlin and M. Ilegems, Appl. Phys. Lett. **83**, 668-670 (2003).

[9] 10] N. Grandjean, B. Damilano, S. Dalmasso, M. Leroux, M. Laügt, and J. Massies, Phys. Stat. Sol. (A) **176**, 219 (1999).

[10] R Butté, J-F Carlin, E Feltin, M Gonschorek, S Nicolay, G Christmann, D Simeonov, A Castiglia, J Dorsaz, H J Buehlmann, S Christopoulos, G Baldassarri Höger von Högersthal, A J D Grundy, M Mosca, C Pinquier, F Demangeot, J Frandon, P G Lagoudakis, J J Baumberg and N Grandjean, J. Phys. D: Appl. Phys. **40**, 6328 (2007).

[11] D. E. Newbury, Nanotechnology **1**, 103 (1990).

[12] M. D. Craven, P. Waltereit, J. S. Speck, and S. P. DenBaars, Appl. Phys. Lett. **84**, 496 (2004).

[13] F. Bernardini, V. Foirentini, and D. Vanderbilt, Phys. Rev. B **56**, R10024 (1997).

[14] N. Grandjean, B. Damilano, S. Dalmasso, M. Leroux, M. Laügt, and J. Massies, J. Appl. Phys. **86**, 3714 (1999).

[15] Effective masses of electron and heavy hole website: http://www.ioffe.rssi.ru/SVA/NSM/Semicond/GaN/index.html

[16] G. Franssen, T. Suski, M. Kryśko, A. Khachapuridze, R. Kudrawiec, J. Misiewicz, Kamińska, E. Feltin, and N. Grandjean, Appl. Phys. Lett. **92**, 201901 (2008).

[17] R. W. Martin, P. G. Middleton, and K. P. O'Donnell, W. Van der Stricht, Appl. Phys. Lett. **74**, 263 (1999).

[18] W. H. Fan, S. M. Olaizola, J. -P. R. Wells, A. M. Fox, T. Wang, P. J. Parbrook, D. J. Mowbray, and M. S. Skolnick, Appl. Phys. Lett. **84**, 3052 (2004).

[19] S. F. Chichibu, A. C. Abare, M. S. Minsky, S. Keller, S. B. Fleischer, J. E. Bowers, E. Hu, U. K. Mishra, L. A. Coldren, and S. P. DenBaars, Appl. Phys. Lett. **73**, 496 (1998).

[20] S. J. Chua, S. Tripathy, P. Chen, E. Takasuka, and M. Ueno, Phys. E **25**, 356 (2005).

[21] M. Seyboth S.-S. Schad, M. Scherer, F. Habel, C. Eichler, M. Kamp, and V. Schwegler, J. Mat. Science: Materials in Electronics **13**, 659 (2002).

[22] K. Lorenz, N. Franco, E. Alves, I. M. Watson, R. W. Martin, and K. P. O'Donnell, Phys. Rev. Lett. **97**, 085501 (2006).

[23] K. Kazlauskas, G. Tamulaitis, J. Mickevicius, E. Kuokstis, A. Zukauskas, Y. C. Cheng, H. C. Wang, C. F. Huang, C. C. Yang, J. Appl. Phys. **97**, 013525 (2005).

[24] B. Van Zeghbroeck, *Principles of Semiconductor Devices* (http://ece-www.colorado.edu/~bart/book/, 2004)

[25] Y. C. Shen, G. O. Muller, S. Watanabe, N. F. Gardner, A. Munkholm, and M. R. Krames, Appl. Phys. Lett. **91**, 141101 (2007).

[26] J. F. Muth, J. D. Brown, M. A. L. Johnson, Z. H. YU, R. M. Kolbas, J. W. Cook Jr., and J. F. Schetzina, MRS Internet J. Nitride Semicond. **Res. 4S1**, G5.2 (1999).

CHAPTER 7

Optical Properties and Surface Morphology of $Al_{1-x}In_xN$ Epilayers with Various InN Compositions, Epilayer Thickness and Substrates

7.1 Introduction

The $Al_{1-x}In_xN$ alloys have the ability to cover a wide range of energy gaps from 0.7 to 6.2 eV by varying the InN fraction. In recent years there has been increased interest in $Al_{1-x}In_xN$ mainly due to the fact that at InN fraction of around 17 % it can be lattice-matched to GaN [1-2] and alloy compositions in this range provide a significantly large energy band gap, for example to act as the barriers in GaN/$Al_{1-x}In_xN$ heterostructures presented in **Chapter 6**. There is also the possibility of using $Al_{1-x}In_xN$ in lattice matched layers in ultraviolet light emitters, where the absence of strain should lead to improved crystalline quality and hence improved luminescence properties. This is especially pertinent with the increasing availability of bulk GaN substrates. However, $Al_{1-x}In_xN$ is much less studied than the other III-nitride compounds. This can be essentially ascribed to growth related issues leading to poor material quality. Indeed, the growth of $Al_{1-x}In_xN$ material is made difficult due to the large mismatch existing between InN and AlN covalent bonds, which leads to phase separation and composition inhomogeneities. In addition, the large difference in the growth temperature between AlN (1100 °C) and InN (600 °C) for layers grown by metal-organic chemical vapour deposition makes it difficult to incorporate In atoms in the alloy and crystal quality worsens as the InN fraction increases.

Accurate values of the band gap for a wide composition range of $Al_{1-x}In_xN$ alloys are desirable in order to attain a better understanding of their optical properties and their suitability for inclusion in devices. Experimental values of the band gap of $Al_{1-x}In_xN$ lattice-matched to GaN, reported in the literature, are spread from 2.5 to 4.4 eV [1, 3-7]. Early reports measured extremely low band gaps, even lower than that of GaN at the lattice-matched concentration [8-9]. It is important to note that these samples were polycrystalline and at least those of Yamaguchi *et. al.* [9] had a high electron concentration which they believed to have modified the band gap [6]. More recent results give higher band gap values but there still remained a considerable spread of values and no consensus on the bowing parameter. Recent experimental works performed on $Al_{1-x}In_xN$ samples having a wide range of InN content, and using the updated band gap value of 0.7 eV for InN, led to bowing parameter values typically between 3.0 to 6.2 eV [3, 10-13]. These uncertainties could be attributed to large differences in the sample structure and the influence of strain, defects and fluctuations in InN content [13]. It is most often assumed that the bowing parameter is independent of alloy composition. However Iliopoulos *et. al.* [14] recently suggested that the $Al_{1-x}In_xN$ bowing parameter is strongly dependent on composition.

There are even fewer reports on the luminescence of $Al_{1-x}In_xN$ than on the band gap values. Broad PL was observed from 1.6 to 2.8 eV with InN fraction (x) varies from 0.6 to 0.14 by Yamaguchi *et. al.* [6]; 2 to 3.7 eV with x from 0.47 to 0.07 by Onuma *et. al.* [3]; and 3.5 to 4.2 eV with x from 0.19 to 0.11 by Carlin *et. al.* [1]. The emission energies from Carlin *et. al.* are higher than the GaN band gap but scatter is observed even for samples with nominally same InN fraction. Such scattering may possibly be due to the fact that these data are from the early work, or from uncertainty in the InN measurement and/or different epilayer thicknesses. For thick samples (> 0.5 μm), they observed another intense broad PL emission at around 2.6 to 3 eV. This broad PL peak could be attributed to the defects that develop with increasing $Al_{1-x}In_xN$ thickness. Carlin *et. al.* demonstrated that the full-width-half maximum (FWHM) x-ray diffraction (XRD) peak increases with layer thickness, indicating the $Al_{1-x}In_xN$ quality degrades as the thickness increases. It seems that there is an onset of the degradation of the crystal quality at a certain thickness.

This chapter presents the composition and optical study of $Al_{1-x}In_xN$ epilayers with a range of InN molar fractions between 0.08 and 0.191. The optical emission and absorption have been studied using photoluminescence (PL) and PL excitation (PLE) spectroscopy, and values for the band gap and the Stokes' shift have been obtained for $Al_{1-x}In_xN$ samples in this composition range. The effects of layer thickness and substrates on the optical properties and surface morphology are also considered.

7.2 Specific Samples and Experimental Details

The $Al_{1-x}In_xN$ epilayers used in this work were grown by metal-organic chemical vapour deposition (MOCVD). Sample growth was performed by a range of internal and external collaborators: (i) "Strathclyde series" by Dr. Ian Watson at the Institute of Photonics from University of Strathclyde, (ii) "Cambridge series" by Thomas Sadler, Dr. Menno Kappers and Dr. Rachel Oliver at the Department of Materials Science and Metallurgy from University of Cambridge, and (iii) "CRHEA series" by Dr. David Schenk at CRHEA-CNRS, Valbonne, France. Trimethylaluminium (TMAl), trimethylindium (TMIn), trimethylgallium (TMGa) and ammonia (NH_3) were used as precursors for Al, In, Ga and N respectively. The substrates used were either *c*-plane sapphire or commercial $Al_yGa_{1-y}N$ templates with AlN fraction (y) ranging up to 23.4 %.

Each run began with the growth of a low temperature GaN nucleation layer followed by the growth of a few μm thick (1 to 1.5 μm for "Strathclyde series"; 6 μm for "Cambridge series"; 2.3 to 4.3 μm for "CRHEA series") GaN buffer layer except for the samples grown on $Al_yGa_{1-y}N$ templates. Figure 7.1 shows the schematic structure of the $Al_{1-x}In_xN$ epilayers on *c*-plane sapphire substrate.

Figure 7.1 Schematic diagram of $Al_{1-x}In_xN$ epilayer sample on *c*-plane sapphire substrate (not to scale). 'n-i-d' stands for non-intentional doped.

For samples on $Al_yGa_{1-y}N$ templates, the $Al_{1-x}In_xN$ layers were grown directly onto the template. The motivations are to shift the lattice match point in achieving higher bandgap as well as to see how the lattice parameters of different templates will affect the composition and quality of the $Al_{1-x}In_xN$. A pre-growth heating step in an ammonia/hydrogen ambient was followed by a cool down to the $Al_{1-x}In_xN$ growth temperature, and this exact sequence of steps is specific to the growths with $Al_yGa_{1-y}N$ templates. The purpose of this step is to remove surface oxides from the $Al_yGa_{1-y}N$, but using too high a temperature would degrade the semiconductor surface. The setpoint temperatures in the recent runs studied in this work were 1000 and 1070 °C. Table 7.1 summarises the growth temperature, nominal thickness and substrates for all series of $Al_{1-x}In_xN$ epilayer samples studied in this work.

Table 7.1 Growth temperature, nominal thickness and substrate for $Al_{1-x}In_xN$ epilayers. $^+$ and * indicate the AlN fraction of the $Al_yGa_{1-y}N$ templates obtained by RBS and given by the manufacturer [15] respectively.

Sample ID	**Growth Temperature (°C)**	**Nominal Thickness (nm)**	**Pre-heating Temperature (°C)**	**Substrate**
A) “Strathclyde series”				
STR508	830	150	nil	Polished sapphire
STR514	810	70		
STR503	800	120		Non-polished sapphire
STR504	830	120		
STR517	780	35		
STR513	780	70		
STR516	780	140		
STR518	780	200		
STR520B	790	100	1000	$Al_{0.23}Ga_{0.77}N^+$
STR520D	790	100	1000	GaN
STR523B	790	100	1070	GaN
STR523D	790	100	1070	$Al_{0.21}Ga_{0.79}N^+$
STR528A	790	100	1070	GaN
STR528B	790	100	1070	$Al_{0.15}Ga_{0.85}N^*$
STR528C	790	100	1070	$Al_{0.04}Ga_{0.96}N^*$
STR528D	790	100	1070	$Al_{0.23}Ga_{0.77}N^*$
B) “Cambridge series”				
C3044	820	100	nil	Non-polished sapphire
C3047	810	100		
C3041	800	100		
C3051	790	100		
C) “CRHEA series”				
T1353	790	60	nil	Non-polished sapphire
T1363	810	60		
T1364	810	60		
T1365	810	60		

In combination, the "Strathclyde series", "Cambridge series" and "CRHEA series" allow study of a wide composition range of $Al_{1-x}In_xN$ alloys. In addition, the "Strathclyde" series contains samples whose growth conditions differ only either in the epilayer thickness, or in the choices of substrates. It is worth mentioning that STR528(A,B,C,D) were grown in the same run on their individual quarter-wafer $Al_yGa_{1-y}N$ templates. A similar method was also applied to STR520 and STR523 runs. Hence, studies of these samples provide accurate information on the influence of the substrates on the optical, structural, compositional and surface properties.

PL and PLE measurements were performed at a low temperature in a closed-cycle helium cryostat. A 1000 W short arc xenon lamp combined with a 0.25 m focal length monochromator, as described in **Chapter 4,** was used as the excitation source. In all of the PL and PLE measurements using the Xe-lamp, the excitation area on the sample was about 2 x 5 mm^2. The sample surface quality was checked by SEM at a beam energy of 5 keV, whereas the crystal quality and compositions were assayed by RBS. In this work, RBS was chosen over WDX for the composition measurement. This is because the epilayer thicknesses of some samples are very much less than the probing depth of the electron beam at a beam energy of 5 keV which has been estimated to be ≈ 120 nm using Monte Carlo simulation as mentioned in **Chapter 4.** This will result in a large penetration into the underlying GaN buffer layer and give high inaccuracies in the ratio of In/Al content if using WDX technique.

7.3 Experimental Results and Discussion

7.3.1 Composition and Crystalline Quality

The RBS measurements were conducted by Dr. Katharina Lorenz together with her PhD student Sérgio Magalhães at the Instituto Tecnologico e Nuclea (ITN), Sacavém, Portugal. The measurements were performed with a 1 mm diameter beam of 2 MeV He$^+$ ions using silicon surface barrier detectors. The composition and layer thickness values from an RBS spectrum are obtained through fitting using a simulation program. In contrast, the χ_{min} parameter is measured from the data as the ratio of the backscattered yield in an aligned (or channelled) spectrum to that in a random spectrum. It is used as a measure of the crystalline quality. Low values of

χ_{min} correspond to good crystalline quality and high values correspond to relatively bad crystalline quality. A value of 100 % corresponds to complete amorphisation. State of the art values of χ_{min} for GaN are around 2 % [16]. Figure 7.2(a) and 7.2(b) show the random and <0001>-aligned RBS/C spectra measured from "Strathclyde series" samples STR504 and STR513 respectively. It is observed from these figures that the channelled spectrum shows much lower backscattering yield than that of the random spectrum. The channelled spectrum of STR504 has a higher backscattering yield than that of STR513. This indicates that the former has poorer crystalline quality as compared to the latter.

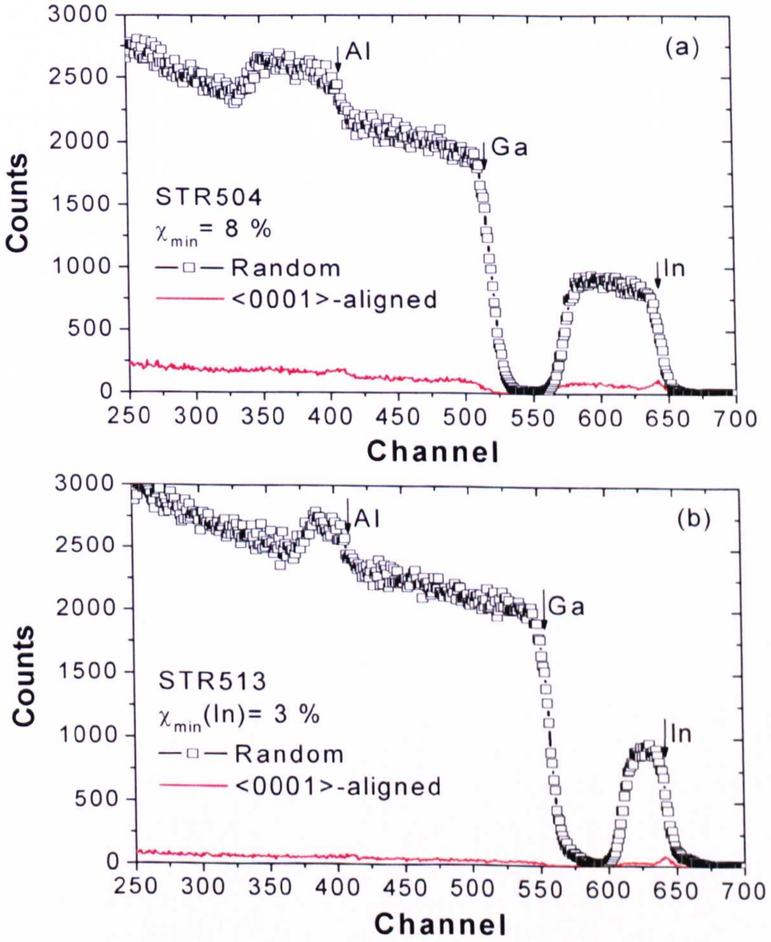

Figure 7.2 RBS/C random and <0001>-aligned spectra taken with a 2 MeV He^+ beam for (a) STR504 and (b) STR513 respectively. The *x*-axis 'Channel' is directly proportional to the energy of the backscattered ions.

The InN molar fractions, layer thickness and χ_{min} parameters derived from the RBS/C spectra are summarised in Table 7.2. The fractional errors for InN molar fraction, epilayer thickness and χ_{min} parameters are ± 5 %, ± 5 % and ± 10 %, respectively. The error for InN molar fraction and thickness are based on the information given in Dr. Lorenz's paper [2] and for χ_{min} is from the RBS/C graphs. It is important to mention that these errors are based on the worst situation.

Table 7.2 InN molar fraction, χ_{min} and thickness of $Al_{1-x}In_xN$ epilayers determined by RBS at ITN, Portugal.

Sample ID	InN Molar Fraction	Thickness (nm)	χ_{min} (%)
A) "Strathclyde series"			
STR503	0.161	164	3.0
STR504	0.108	152	8.0
STR508	0.133	162	5.0
STR514	0.116	72	3.0
STR517	0.136	37	3.4
STR513	0.158	73	3.0
STR516	0.141	139	3.7
STR518	0.143	211	4.9
STR520B	0.086	93	16.4
STR520D	0.141	93	3.9
STR523B	0.120	98	2.6
STR523D	0.093	98	13.7
STR528A	0.191	114	6.2
STR528B	0.132	102	39.3
STR528C	0.156	104	11.1
STR528D	0.136	101	7.5
B) "Cambridge series"			
C3044	0.082	85	4.0
C3047	0.099	86	4.2
C3041	0.115	91	6.2
C3051	0.145	93	3.3
C) "CRHEA series"			
T1353	0.134	50	4.9
T1363	0.132	48	3.8
T1364	0.167	65	4.0
T1365	0.170	70	4.1

Low chi-min (χ_{min}) values of 3 to 4 % (see above table) for In reveal relatively good single crystalline quality, although they are slightly higher than for the GaN buffer layer (2 %). Minimum χ_{min} values of 3 % are obtained in samples STR503, STR513 and C3051. This is because the compositions of the $Al_{1-x}In_xN$ in these samples are closest to that lattice-matched with GaN buffer layer. However, it is noted that

STR514 has equally low χ_{min} although its InN molar fraction differs significantly from the lattice-matched molar fraction of 0.17. There are other samples with relatively high χ_{min} values from 5 %, indicating the qualities of these samples are poorer. This is especially true for those grown on $Al_yGa_{1-y}N$ templates.

7.3.2 Luminescence and Surface Morphology

The PL and PLE spectroscopic study of the series of $Al_{1-x}In_xN$ epilayers listed in Table 7.1 will be discussed in this section. SEM images will also be presented along the way together with the χ_{min} values in order to give a fuller picture of these materials under investigation. Several factors affecting the luminescence and surface quality are studied. They are the effects of InN compositions, $Al_{1-x}In_xN$ layer thickness and different substrates.

7.3.2.1 Effect of InN Composition

- *Low Temperature PL Spectra*

The low temperature (≈ 20 K) PL spectra of the $Al_{1-x}In_xN$ epilayers from the "Strathclyde series", "Cambridge series" and "CRHEA series", excited by the Xe-lamp are shown in Figure 7.3 to 7.5, respectively. It is observed that there are two important PL features in each spectrum: a sharp and strong peak at 356 nm, which is attributed to the band-edge emission from the GaN buffer layer; and a broad emission band on the higher energy side. Although high absorption of exciting light in $Al_{1-x}In_xN$ epilayers at high excitation energy is expected, the GaN buffer layers have also been excited either by the light penetrating the ternary or by the diffused excess carriers. The broad emission bands at higher energy are observed to show a red-shift from ≈ 297.5 nm (4.17 eV) to 341.4 nm (3.63 eV) as the InN molar fraction increases from 0.082 to 0.170. They are attributed to intrinsic emission from the $Al_{1-x}In_xN$ epilayers.

It is also noted that the high energy emission bands of samples STR508, STR516, STR517 and C3041 display double structures with maxima at: ≈ 315 and 330 nm; 318 and 333 nm; 320 and 335 nm; 315 and 330 nm, respectively. The presence of the double structures suggests the existence of regions with different alloy composition [17]. In addition, a shoulder at around 345 nm is observed clearly on samples STR504 and C3044 only. These samples have low InN molar fraction of 0.082 and 0.099 respectively. Also, there are multiple PL features appearing at the lower energy side of GaN. There are broad emission bands as the background on which the sharp emission lines at around 365 nm (3.40 eV), 380 nm (3.26 eV), 391 nm (3.17 eV), and 402 nm (3.08 eV) are superimposed. These sharp lines do not shift as the InN fraction varies. The PLE spectra detected at these sharp lines confirm they are due to GaN. These lines are attributed to the GaN-related defect (3.40 eV), donor-acceptor-pair (DAP) transition (3.26 eV) and its LO-DAP replicas (3.17 and 3.08 eV) with an energy separation of 90 meV.

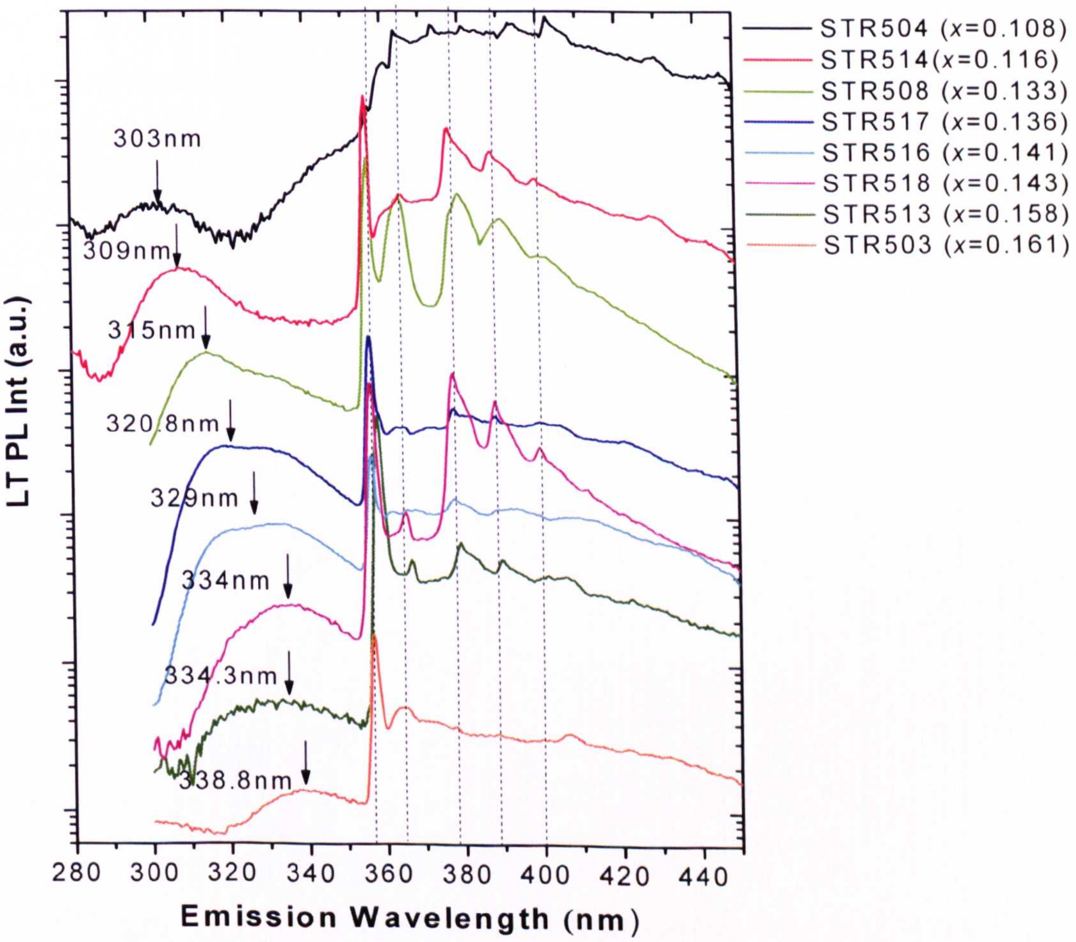

Figure 7.3 Low temperature PL spectra of "Strathclyde series" $Al_{1-x}In_xN$ epilayers with InN molar fraction (x) from 0.108 to 0.161 excited by the Xe-lamp at 280 nm except STR504 and STR514 at 265 nm. The arrows indicate the $Al_{1-x}In_xN$ emission peak positions.

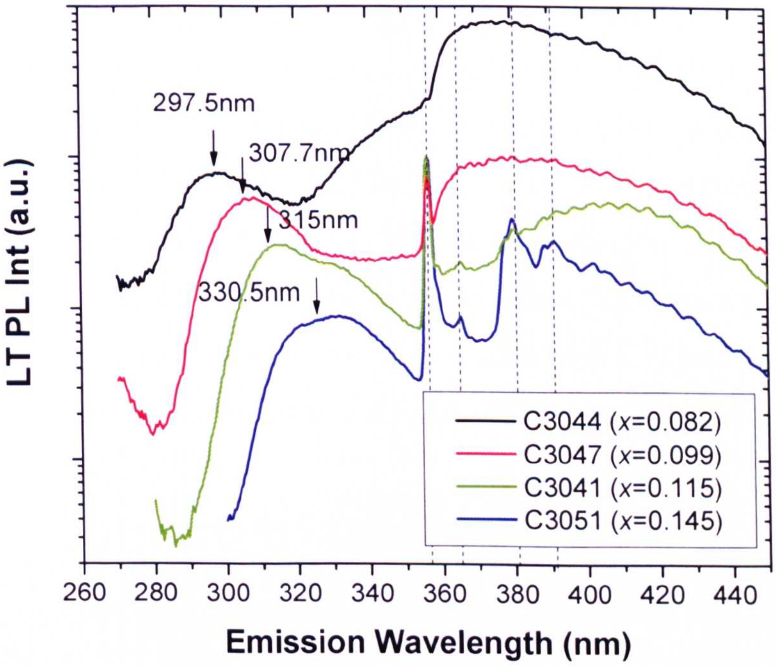

Figure 7.4 Low temperature PL spectra of "Cambridge series" $Al_{1-x}In_xN$ epilayers with InN molar fraction (x) from 0.082 to 0.145 excited by the Xe-lamp at 250 nm (C3044, C3047), 265 nm (C3041) and 280 nm (C3051). The arrows indicate the $Al_{1-x}In_xN$ emission peak positions.

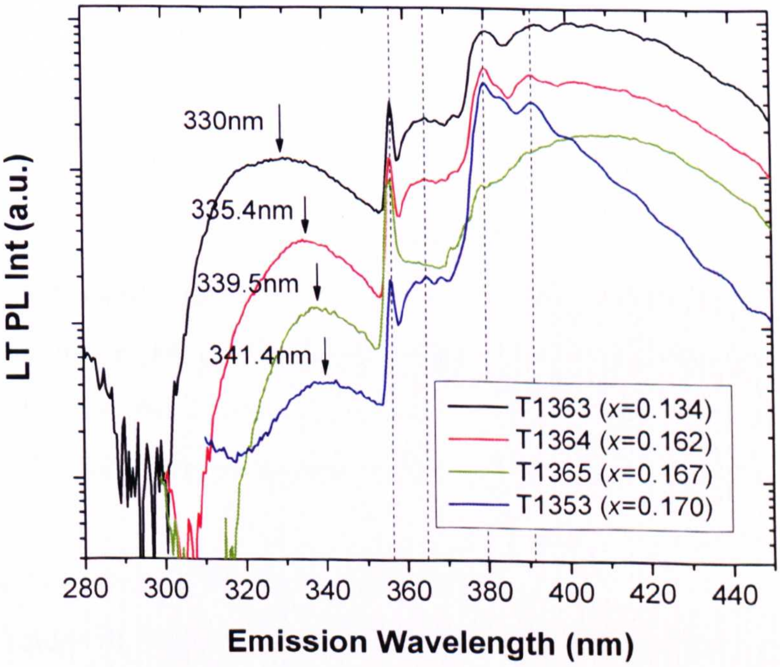

Figure 7.5 Low temperature PL spectra of "CRHEA series" $Al_{1-x}In_xN$ epilayers with InN molar fraction (x) from 0.15 to 0.187 excited by the Xe-lamp at 280 nm except T1363 at 265nm. The arrows indicate the $Al_{1-x}In_xN$ emission peak positions.

Figure 7.6 plots the energies of the $Al_{1-x}In_xN$ luminescence peak in the PL spectra from the epilayers studied in this work as a function of InN fraction. The emission energy displays a linear dependence on the InN fraction in the studied composition range. The emission energy decreases linearly from ≈ 4.2 to 3.6 eV as InN fraction increases from 0.082 to 0.170. Figure 7.6 also compares the current work with the previous work by Dr. Michael K. Wang, a colleague from my research group [12] and literature data from Carlin *et. al.* [1]. Similar linear behaviour is observed in Wang's work whereas the data from Carlin *et. al.* shows a greater degree of scatter.

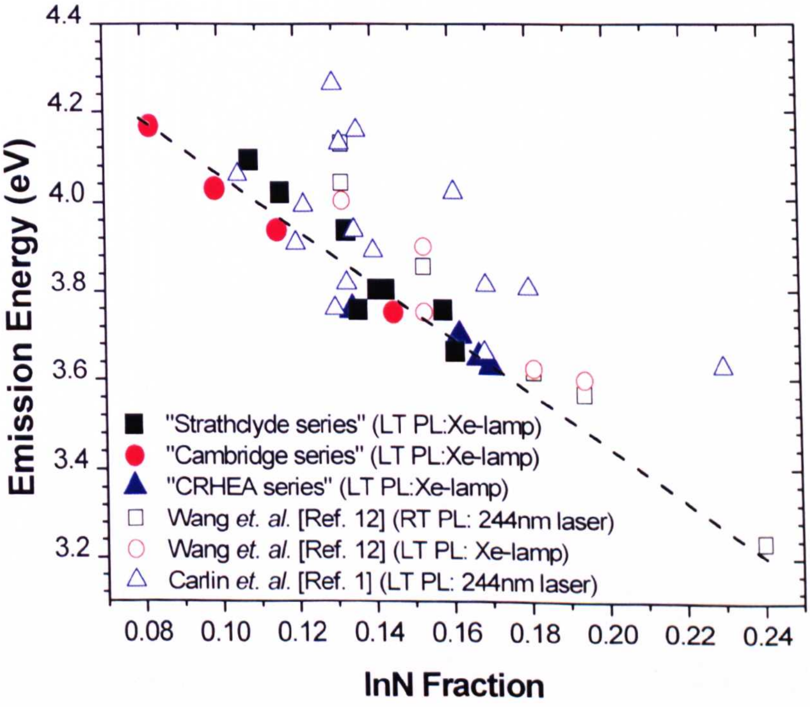

Figure 7.6 Luminescence emissions of $Al_{1-x}In_xN$ epilayers as a function of InN molar fraction using PL spectroscopy. Filled symbols are current work. Open symbols are literature data from Wang *et. al.* [12] and Carlin *et. al.* [1]. 'LT' and 'RT' stand for low temperature and room temperature respectively.

- *Low Temperature PL Excitation (PLE)*

Low temperature PLE spectra excited by the Xe-lamp and detected at the $Al_{1-x}In_xN$ emission peak from each of the series of samples are shown in Figure 7.7 to 7.9. The PLE spectra were acquired by fixing the detection wavelength at the maximum of the respective PL emission bands. As for those samples with double structures and a shoulder in the high energy band as mentioned earlier in PL section, PLE was also performed at different positions of their emission bands. All PLE spectra have been corrected for the combined throughput of the Xe-lamp and the detection monochromator. A clear absorption edge can be seen in each of the PLE spectra and is attributed to the band gap absorption in the $Al_{1-x}In_xN$ layer. The absorption edge revealed by PLE also displays a red-shift as the InN fraction increases. Each of the PLE spectra has been cut off on the low energy side at the point where the PLE intensity rises again towards the detection emission energy.

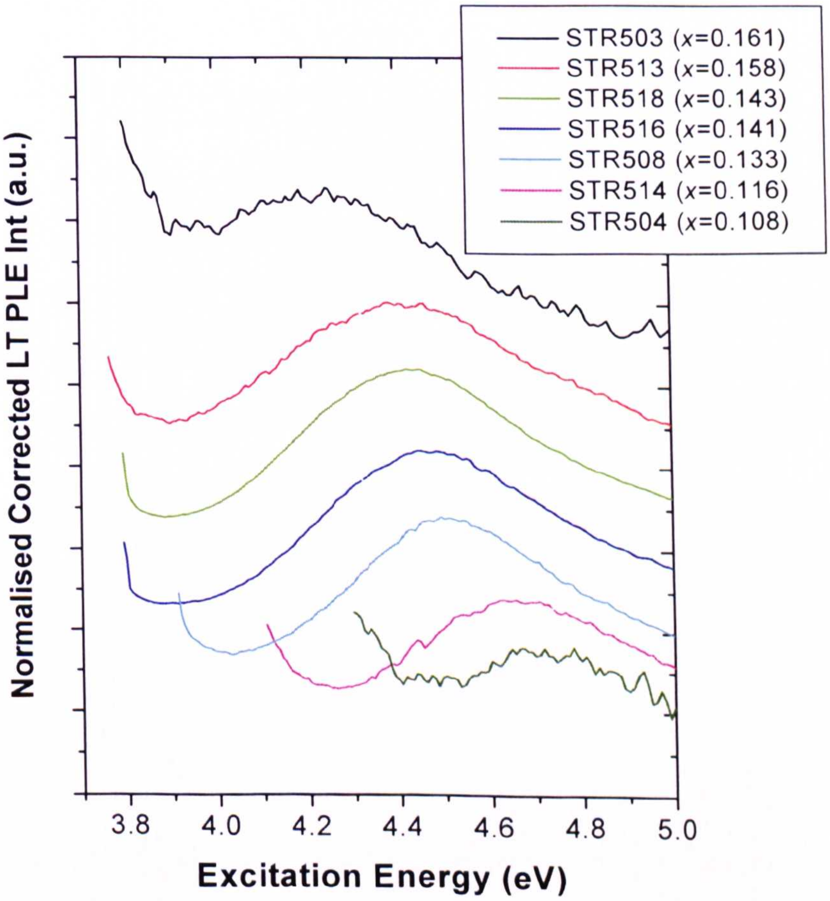

Figure 7.7 Normalised corrected PLE spectra of "Strathclyde series" $Al_{1-x}In_xN$ epilayers with InN molar fraction (x) varying from 0.108 to 0.161, measured using the Xe-lamp.

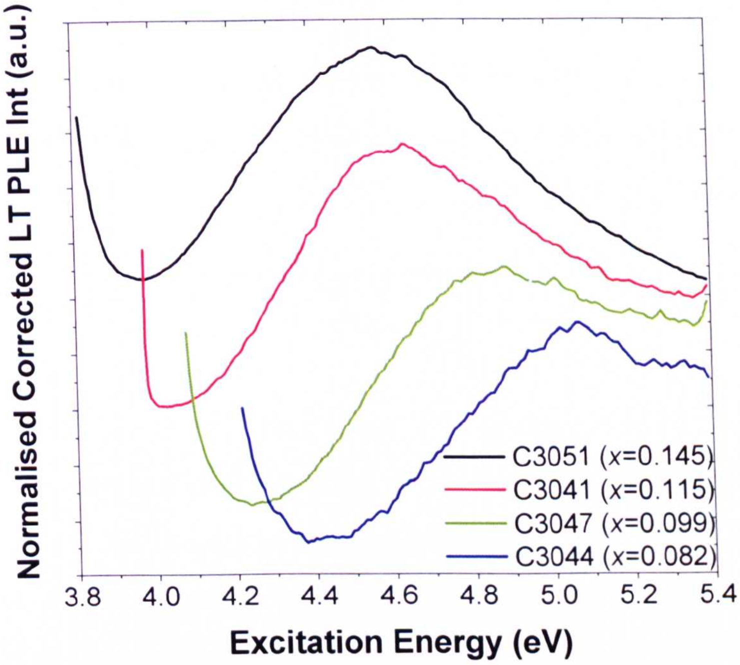

Figure 7.8 Normalised corrected PLE spectra of "Cambridge series" $Al_{1-x}In_xN$ epilayers with InN fraction (x) varying from 0.082 to 0.145, measured using the Xe-lamp.

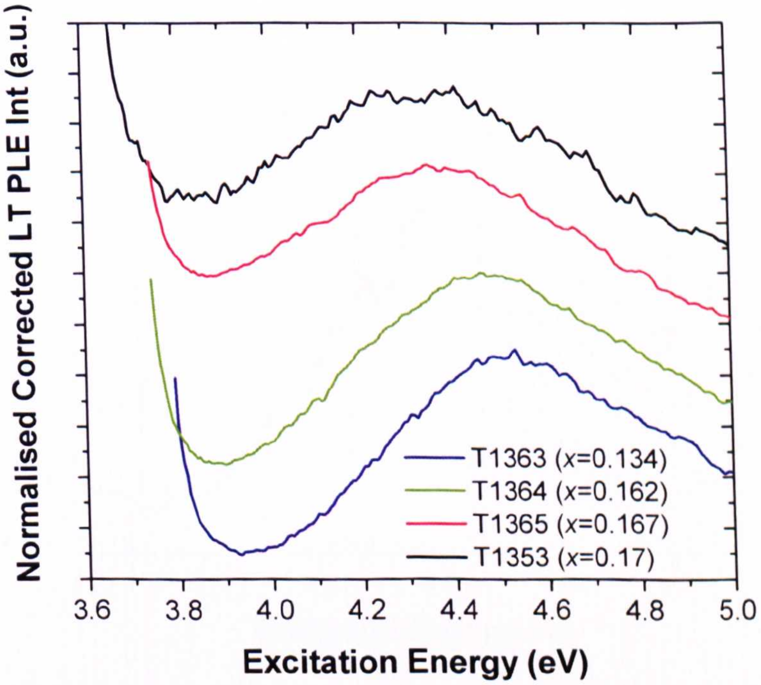

Figure 7.9 Normalised corrected PLE spectra of "CRHEA series" $Al_{1-x}In_xN$ epilayers with InN fraction (x) varying from 0.134 to 0.170, measured using the Xe-lamp.

The positions of the absorption peaks give an estimate of the band gap of the samples. An effective energy gap can be evaluated by fitting the low energy side of the PLE spectrum to a sigmoidal function as performed earlier for $In_xGa_{1-x}N$ epilayers [18]:

$$\alpha = \frac{\alpha_0}{1 + \exp(\frac{E_g - E}{\Delta E})} \tag{7.1}$$

where E_g is defined as an effective band gap energy, ΔE(eV) is a broadening parameter, α_0 is a constant and E(eV) is the excitation energy at which the intensity α is recorded. Figure 7.10 illustrates the sigmoidal fitting to a PLE spectrum from STR514. Table 7.3 summarises the effective band gap energies, broadening parameters and the emission energies of $Al_{1-x}In_xN$ epilayers in this work. The double structures and the shoulder of the high energy band in the samples are a reflection of inhomogeneity of the $Al_{1-x}In_xN$ layers, as evidenced by the slight variations in the effective band gap.

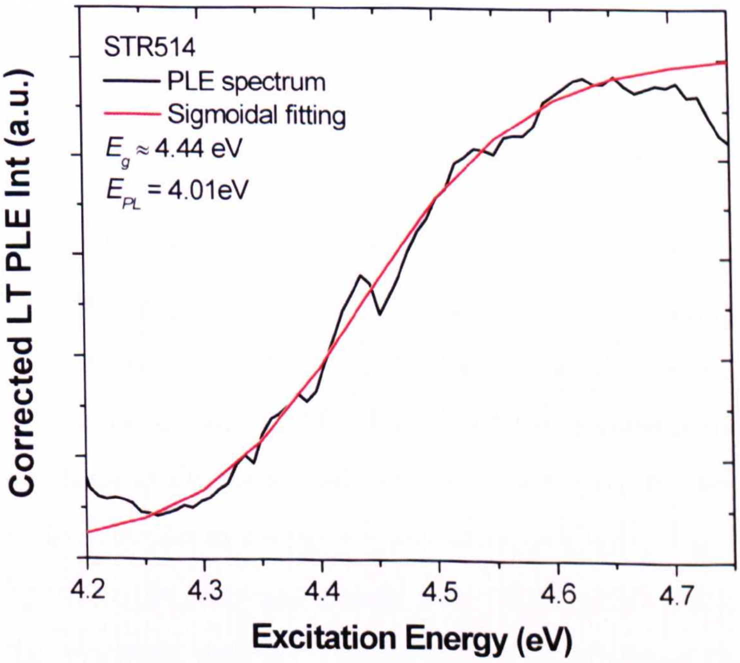

Figure 7.10 Typical representation of sigmoidal fitting to a PLE spectrum. E_g is the effective band gap and E_{PL} is the emission energy obtained by PL spectroscopy.

Table 7.3 Effective band gap energies E_g, broadening parameters ΔE and emission energies of the set of $Al_{1-x}In_xN$ layers. The typical error for E_g is ± 0.02 eV and ΔE is ± 12 meV but for the two samples marked * the uncertainties are much greater (± 0.05 eV (E_g) and ± 17 meV (ΔE)).

Sample ID	InN Molar fraction	Effective Bandgap E_g (eV)	Broadening Parameter ΔE (meV)	Emission Energy (eV)
A) "Strathclyde series"				
STR504*	0.108	4.51	70	4.09
STR514	0.116	4.44	70	4.01
STR508	0.133	4.29	81	3.94
STR517	0.136	4.25	55	3.87
STR516	0.141	4.20	86	3.79
STR518	0.143	4.17	82	3.71
STR513	0.158	4.15	80	3.71
STR503*	0.161	4.09	75	3.67
B) "Cambridge series"				
C3051	0.145	4.27	88	3.75
C3042	0.115	4.33	90	3.94
C3047	0.099	4.55	100	4.03
C3044	0.082	4.75	122	4.17
C) "CRHEA series"				
T1363	0.134	4.22	91	3.76
T1364	0.162	4.14	100	3.70
T1365	0.167	4.11	110	3.65
T1353	0.170	4.07	100	3.63

Figure 7.11 presents the experimental dependence of the estimated band gap of the $Al_{1-x}In_xN$ epilayers studied in this work determined by the sigmoidal fitting of the PLE spectra as a function of InN fraction. The band gap energy is observed to display a linear dependence on the InN fraction in the restricted composition range studied. This behaviour is similar to that observed for $In_xGa_{1-x}N$ epilayers and diodes [18] and the $Al_{1-x}In_xN$ emission energy shown earlier in Figure 7.6. In the case of the lattice-matched system, the band gap energy to $x = 0.17$ yields ≈ 4.1 eV. Figure 7.11 also includes the literature data for comparison. It is observed that the band gap energies agree reasonably well with Iliopoulos *et. al.* [14], Wang *et. al.* [12] and Carlin *et. al.* [1] in the similar InN fraction range. However, it is noted that the data from Carlin obtained by optical reflectance (OR) measurements appear with higher band gap energy values. This may be related to the fact that Carlin *et al.*'s samples

were around 500 nm thick and hence fully relaxed, whereas our samples are probably under tensile strain. Also, an issue with OR measurements is that the band gap energy of $Al_{1-x}In_xN$ is deduced from the high-energy edge of the interference fringes related to the $Al_{1-x}In_xN$ layer [3]. Although some reflectance anomalies at the higher-energy fringes can be observed in binary materials, this is not the case of alloy materials due to broad band edge. Hence, there is a tendency of overestimating the band gap values for $Al_{1-x}In_xN$ using OR spectrum. The inset shows the complete energy band gap data of Iliopoulos *et. al.* from $0.1 < x < 0.8$.

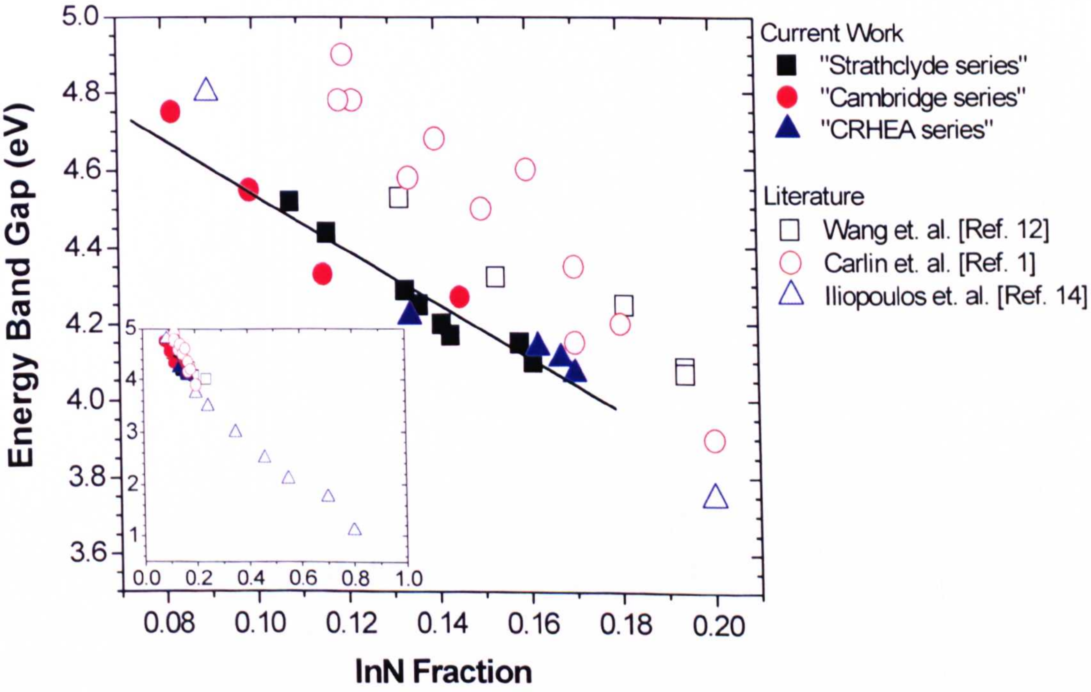

Figure 7.11 Dependence of $Al_{1-x}In_xN$ band gap energy on InN molar fraction. Filled symbols are from the current work whereas open symbols are from the literature [1, 12, 14].

The literature values of the band gap energies for AlN and InN are 6.28 eV [19] and 0.68 eV [20] at low temperature, respectively. Therefore, the band gap (E_g) of $Al_{1-x}In_xN$ alloys can be predicted using the following equation:

$$E_g(x) = 6.28.(1-x) + 0.68.x - b.x.(1-x) \tag{7.2}$$

where b denotes the bowing parameter. It is most often assumed that the bowing parameter is independent of alloy composition. Figure 7.12 plots the effective energy band gap as a function of InN fraction with different values of *b*. It is interesting to note that the range of alloy compositions studied experimentally does not allow a direct determination of the bowing of the band gap. In fact, a strong deviation from the quadratic approximation is observed. This suggests that the *b* might vary with the InN composition.

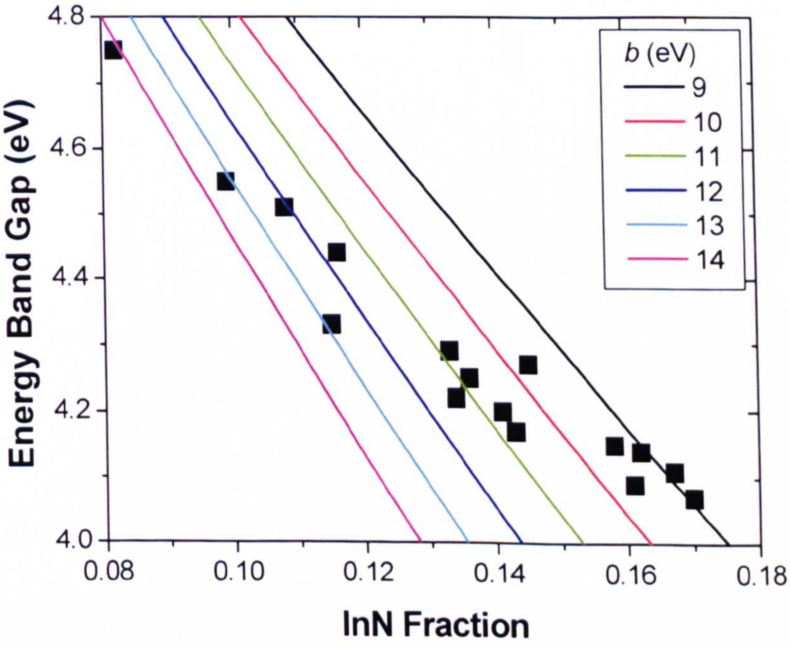

Figure 7.12 Band gap energy of $Al_{1-x}In_xN$ versus InN molar fraction (x). The solid lines are the parabolic fit to $E_g(x)$ line using Equation 7.2 with different bowing parameters b of 9, 10, 11, 12, 13 and 14.

To further analyse this problem, the bowing parameter was evaluated at each measured InN fraction x using Equation 7.2 and is presented in Figure 7.13. It is observed that the bowing parameter is strongly composition dependent. It decreases linearly from around 14 to 9 as the InN fraction increases from 0.08 to 0.17 in the restricted composition studied range. In fact, the independent-to-composition assumption for the bowing parameter of $Al_{1-x}In_xN$ has been questioned by several research groups [5, 14, 21-22]. Earlier work by Peng *et. al.* [5] gave a cubic expression for the energy gap that fitted results spanning the entire range of compositions. In later years, Vurgaftman *et. al.* [21] suggested that the bowing parameter *b* should be expressed as $16 - 9.1x$ (blue line as shown in the inset) but at this point the InN band gap value was accepted as 1.9 eV. Recently Iliopoulos *et. al.*

[14] suggested that b is behaving in a rapidly decaying manner, in this case $b = A_1/(1+A_2x)$ where A_1 and A_2 are constants (red line as shown in the inset). A strong composition dependence of the bowing parameter behaviour has also been claimed for $In_xGa_{1-x}N$ [22-23].

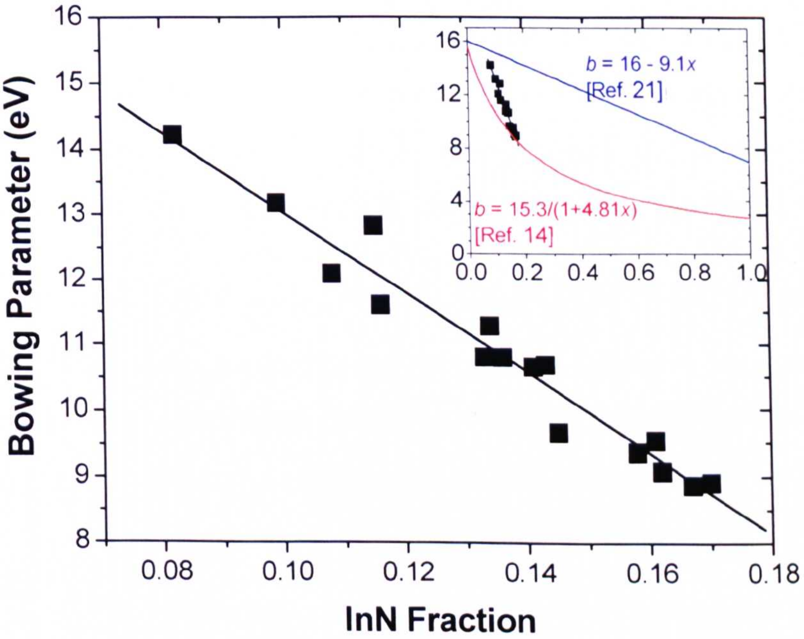

Figure 7.13 Bowing parameter *b* as a function of InN fraction. The solid lines in the inset are from Ref. [21] (blue) and Ref. [14] (red).

In order to better understand the physical origins of the large and composition-dependent bowing in $Al_{1-x}In_xN$ and $In_xGa_{1-x}N$ alloys, M. Ferhat and F. Bechstedt [22] have decomposed the total bowing parameter b into physically distinct contributions as follows:

$$b = b_{VD} + b_{CE} + b_{SR} \tag{7.3}$$

where b_{VD}, b_{CE} and b_{SR} account for the volume deformation, different atomic electronegativities, and structural relaxation, respectively. They observed that: (i) the volume-deformation term b_{VD} of $In_xGa_{1-x}N$ and $Al_{1-x}In_xN$ alloys is large, particularly for $Al_{1-x}In_xN$. The importance of b_{VD} can be correlated to the large mismatch of the lattice constants of the corresponding binary compounds (≈ 10 % between GaN and InN and ≈ 14 % between AlN and InN). Thus, the b_{VD} term, i.e., the composition-induced disorder in the bond lengths, appears to control the large gap bowing in $In_xGa_{1-x}N$ and $Al_{1-x}In_xN$ alloys; (ii) the charge-transfer contribution b_{CE} due to the different electronegativities of the In and A (A = Al or Ga) atoms is considerable for $Al_{1-x}In_xN$ alloys but small for $In_xGa_{1-x}N$ alloys. Indeed, b_{CE} scales with the electronegativity mismatch [≈ 2 % (≈ 13 %), between In and Ga (In and Al)]; and (iii) the structural relaxation b_{SR} contribution measures the changes in passing from the unrelaxed to the relaxed alloy. Considering these contributions, the bowing for the samples assessed here should be dependent on the microscopic structure including the defects. This may be the reason why the reported values of bowing parameters for $Al_{1-x}In_xN$ scatter [3, 10-13]. Nevertheless, the discussion of bowing parameter is still at an early stage and the range of InN fraction studied in this work is limited.

A plot of the broadening parameter ΔE versus the emission energy of $Al_{1-x}In_xN$ layers studied in this work together with the $In_xGa_{1-x}N$ epilayers and diodes from Martin *et. al.* [18] for comparison is shown in Figure 7.14.

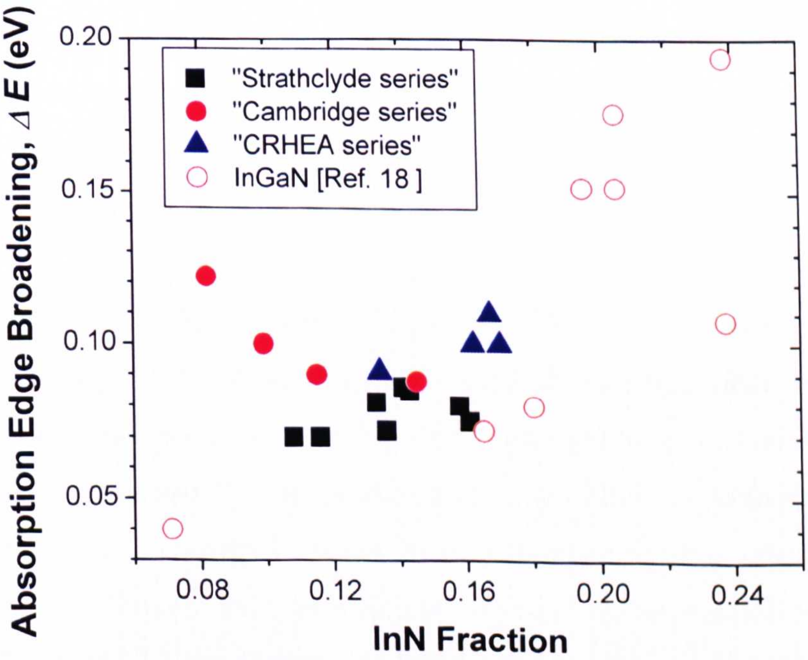

Figure 7.14 Broadening parameter (ΔE) of $Al_{1-x}In_xN$ epilayers from current work (filled symbols) and $In_xGa_{1-x}N$ epilayers and diodes from Martin *et. al.* [18] (open symbols) as a function of InN molar fraction.

It is observed that the broadening of $Al_{1-x}In_xN$ decreases from ≈ 120 to 70 meV with decreasing InN fraction from 0.17 to 0.13. It seems to fit reasonably well with the

$In_xGa_{1-x}N$ trend where a rough linear relationship is noted. However, the broadening data are scatter at low InN range (<0.12). Hence, no distinct trend can be concluded in this restricted composition range. The broadening parameter is related to the Urbach tail [18, 24]. The Urbach tail has been previously identified for a large number of semiconductors and can have a number of originating mechanisms including the presence of point defects; of extended states at the valence or conduction bands; disordered structure; excitonic transitions or the presence of inhomogeneous strain in the semiconductor [25].

7.3.2.1.3 Stokes' Shift

The energy difference between the luminescence and the absorption in a solid state system is known as the Stokes' shift. It can be regarded as a result of the luminescence from localised states. The excess carriers generated by the exciting radiation relax non-radiatively to local potential minima through interaction with the crystal lattice and then form localised excitons. Luminescence occurs when the dwell time of an exciton in a localised site exceeds its radiative decay time [26]. The recombination in these localised states results in the luminescence peak energy being red-shifted from the absorption energy. Thus, a quantitative measure of exciton localisation can be extracted from the Stokes' shift [18].

In order to analyse the Stokes' shift, it is essential to have an accurate description of the absorption edge that includes the effects of broadening. This is provided by fitting the rising edge and plateau of the absorption spectra to the sigmoidal formula as described in Equation 7.1. In practice, then, the Stokes' shift is estimated by taking the difference in energy between the effective band gap and the emission peak energy. A plot of Stokes' shift as a function of InN molar fraction is presented in Figure 7.15 for $Al_{1-x}In_xN$ epilayers studied in this work, and InGaN epilayers and diodes from Martin *et. al.* [18] for comparison.

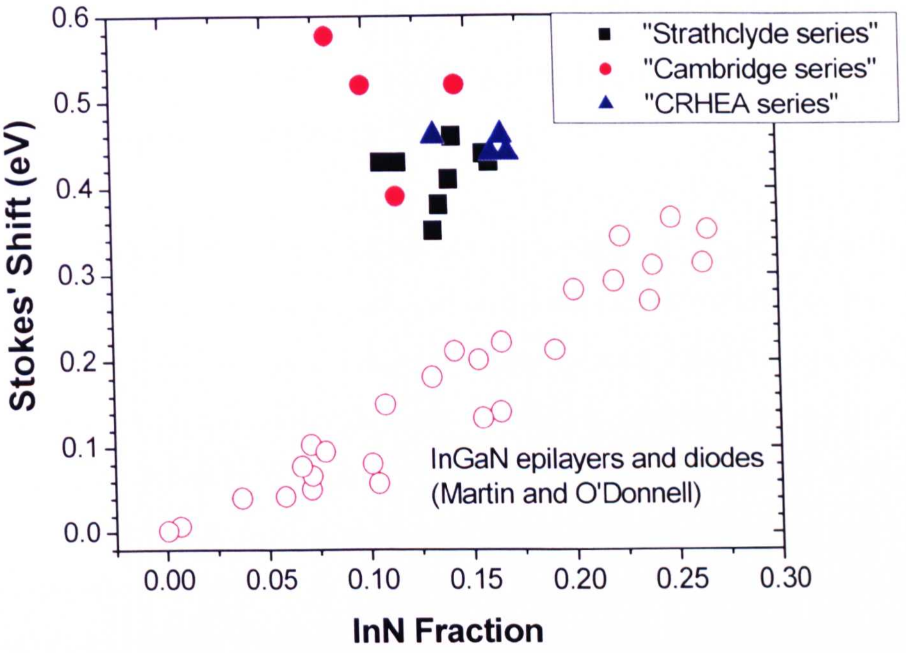

Figure 7.15 Stokes' shift of $Al_{1-x}In_xN$ epilayers (filled symbols) and InGaN epilayers and diodes (open circles) from Martin *et. al.* [18].

It is observed that the Stokes' shift of $Al_{1-x}In_xN$ varies between ≈ 350 to 600 meV in the InN studied range. The $Al_{1-x}In_xN$ Stokes' shifts are seen to be almost two times larger than those for $In_xGa_{1-x}N$ with the same InN fraction as illustrated in the figure. Onuma *et al.* [3] reported optical reflectance and PL data over the range $0.07 < x < 0.5$ indicating extremely large Stokes' shifts of ≈ 1 to 2 eV and a lattice-matched band gap of approximately 5 eV. Carlin *et al.* [1] reported high quality $Al_{1-x}In_xN$ on GaN layers, with compositions near the lattice-match point, with somewhat smaller Stokes' shifts and a lattice-matched band gap of ≈ 4.3 eV. Such a large energy difference between band edge and luminescence could be possibly ascribed to In composition fluctuations or to the presence of deep defects or impurities acting as preferential recombination centres. All of these lead to a high degree of exciton localisation. However, the supporting structural evidence and temperature-resolved PL measurements in MOCVD-grown $Al_{1-x}In_xN$ in this work are so far lacking. In addition, there is no definite trend in the Stokes' shift as a function of InN content observed in $Al_{1-x}In_xN$ epilayers as shown in Figure 7.15. Such scattering of data can also be seen in the Carlin *et al.*'s results. On the other hand, a clear linear-dependence relationship is observed for $In_xGa_{1-x}N$ materials as shown in the figure. It is attributed to an increase in localisation due to increased disorder. An increase in the Stokes' shift between emission and absorption has also been observed in $Al_yGa_{1-y}N$ structures [27-28].

A significant consideration is the dependence of in-built electric field strength on InN content and strain. Lorenz *et. al.* have obtained an accurate determination of the strain state of the same set of GaN/$Al_{1-x}In_xN$ layers by analysing their RBS data [2]. It is reported that the strain changes from tensile to compressive when the InN content of the layer increases through the matching value ($x = 0.171$). Consequently, strain induced piezoelectric field goes to zero at the lattice-match point and changes its sign from positive to zero and to negative, or vice versa, although the field due to spontaneous polarisation in GaN/$Al_{1-x}In_xN$ remains large [1, 29]. However the strain state for $In_xGa_{1-x}N$ layers is another story. The compressive strain in InGaN layers increases with increasing InN content linearly [30-32]. There is no change in the sign of the strain, and the sign of the piezoelectric field induced by the strain. This indicates that both the piezoelectric and spontaneous polarisation fields increase with InN content. As explained in **Chapter 2**, in the presence of a polarisation-induced electric field, the shape of the rectangular well has to be replaced by a triangular QW in which the recombination of the photogenerated electron–hole pairs is red shifted in energy due to the quantum confined stark effect (QCSE). The increase in the electric field play a role in explaining why the Stokes' shift for $In_xGa_{1-x}N$ increases with increasing InN content whereas the different Stokes' shifts as a function of InN content for $Al_{1-x}In_xN$ layers close to lattice-matched to GaN could be due to possibility of removing the piezoelectric fields induced by the strain.

- *Surface Morphology*

In order to have an accurate analysis of the impact of InN composition on the surface quality of $Al_{1-x}In_xN$ samples epilayers of the highly strained "Cambridge series" with similar layer thickness range of around 90 nm were chosen and studied using SEM. Figure 7.16 presents the SEM images of "Cambridge series" $Al_{1-x}In_xN$ samples in which the InN composition varies from 8.2 to 14.3 % under magnifications of 10,000 (left) and 35,000 (right).

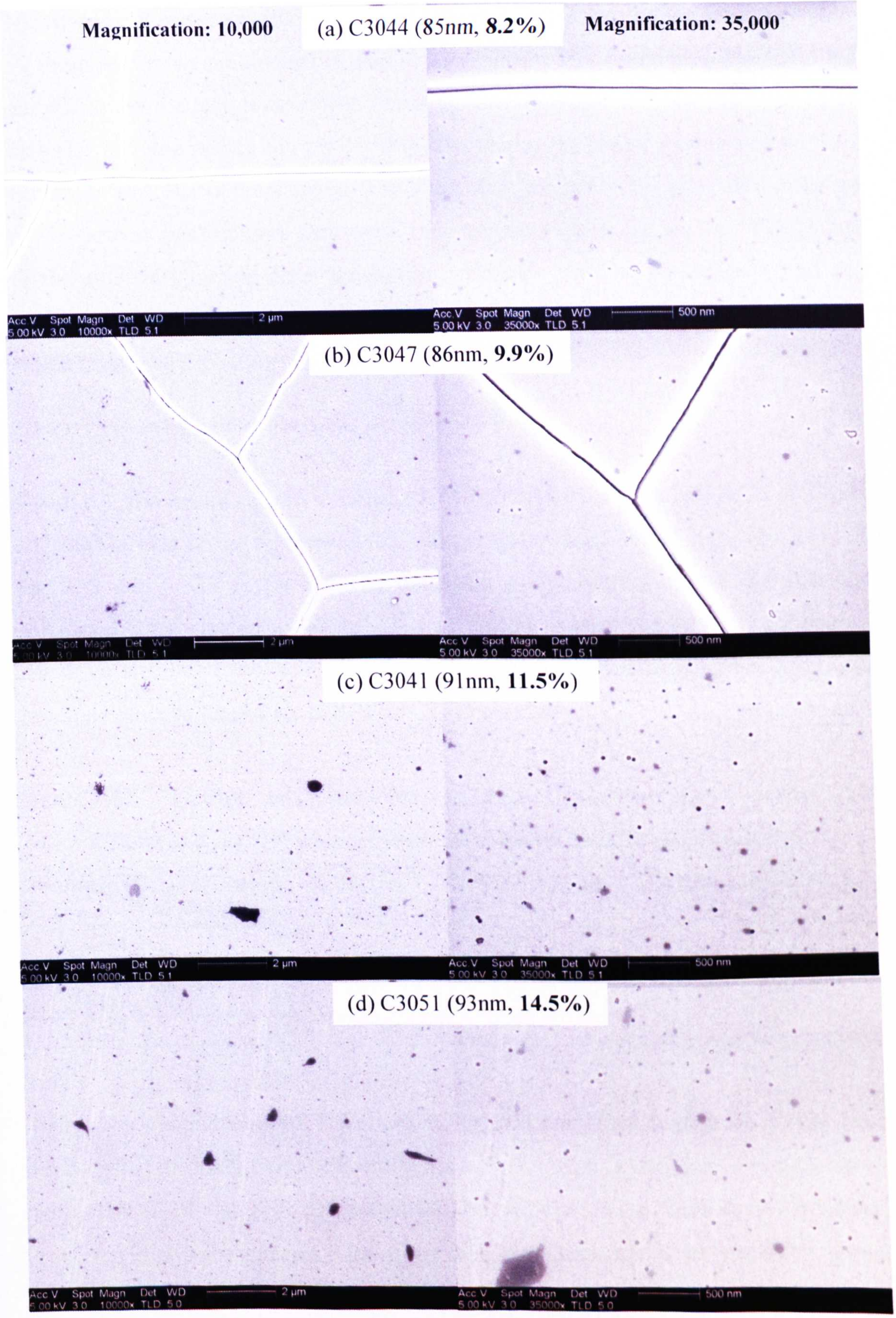

Figure 7.16 SEM images of "Cambridge series" $Al_{1-x}In_xN$ epilayers for InN compositions from 8.2 to 14 % with almost same layer thickness of ≈ 90 nm.

Nearly smooth surfaces with small pits distributed across the surface are observed in all samples. Cracks are present in samples with lower InN contents, in this case 8.2 and 9.9 %. As the InN composition increases from 8.2 to 11.5 %, the pit density and diameter increase before the pit density decreases with further increase of the InN content to 14.5 %, but there are no cracks on these samples as the pits could intercept newly-formed cracks before they could run very far towards the surface. This is due to the strain originating from the lattice mismatch between the epilayer and the bottom layer. The lattice mismatch can be measured by the misfit parameter, f_m, which is defined as:

$$f_m = \frac{a_{epi} - a_{bottom}}{a_{bottom}} \tag{7.3}$$

where a_{epi} and a_{bottom} are the in-plane lattice parameters a of the $Al_{1-x}In_xN$ epilayers and the GaN buffer layer, respectively. The a values used in this study are 3.111 Å for AlN and 3.538 Å for InN, as presented in **Chapter 2**. Table 7.4 lists the calculated lattice mismatch for the $Al_{1-x}In_xN$ samples using Vegard's law although it has to be noted that the validity of Vegard's law in the case of $Al_{1-x}In_xN$ alloy, has been recently challenged [2, 33].

Table 7.4 Lattice mismatch for $Al_{1-x}In_xN$ epilayers with various InN compositions and layer thickness were determined by RBS measurement.

Sample ID	InN composition (%)	Thickness (nm)	Lattice mismatch, f_m (%)
C3044	8.2	85	-1.3
C3047	9.9	86	-1.1
C3041	11.5	91	-0.9
C3051	14.5	93	-0.5

Using the combination of RBS and XRD measurements Lorenz *et al* [2] have investigated the evolution of the strain state of $Al_{1-x}In_xN$ layers close to lattice-match with GaN ($0.13 < x < 0.20$) grown by Dr. Ian Watson in Strathclyde University. They reported that the strain state of the $Al_{1-x}In_xN$ films, about 100 nm thick, grown on GaN buffer layers changes from tensile to compressive with increasing In content with lattice-matching to GaN occurring at an indium content of 17.1 %. This indicates that the strain present in the samples C3044, C3047, C3041 and C3051 is tensile. The tensile strength becomes smaller as the InN content increases towards the lattice-matching value as illustrated by the calculated lattice mismatch f_m in Table 7.4. The absolute f_m value becomes smaller from 1.3 to 0.5 % as the InN content increases from 8.2 to 14.5 %. Misfit strain begins to relax by the introduction of dislocations, in this case cracks for the highly tensile-strained samples C3044 and C3047 and increase in the pit diameter for less tensile-strained samples C3041 and C3051. Also the lower pit density in C3051 as compared to C3041 is because the lattice mismatch in the former case is smaller.

7.3.2.2 Effect of $Al_{1-x}In_xN$ Epilayer Thickness

This section investigates the influence of the layer thickness on the surface quality and luminescence of $Al_{1-x}In_xN$ epilayers. The "Strathclyde series" samples STR513, STR516, STR517 and STR518 were examined to see the effect of layer thickness varying by almost 6 times from 37 to 211 nm whilst they have similar InN compositions of around 14.7 ± 1.1 %. The SEM images of STR513, STR516, STR517 and STR518 are displayed in Figure 7.17.

It is observed that all the samples are crack-free. The sample with the thinnest layer thickness of 37 nm in Figure 7.17(a) presents a nearly flat surface with small pits distributed across the surface. As the thickness increases, the surface quality worsens. As can be seen in the figure, the sample with a thickness of 139 nm presents a higher pit density. In addition, some features can be observed around the pits and the pit diameter becomes bigger. When the thickness is increased to 211 nm, the pit diameter increases further and the 'dot' shape becomes 'hexagonal-shaped' with the structures around the pits becoming more prominent as shown in the inset in Figure 7.17(d).

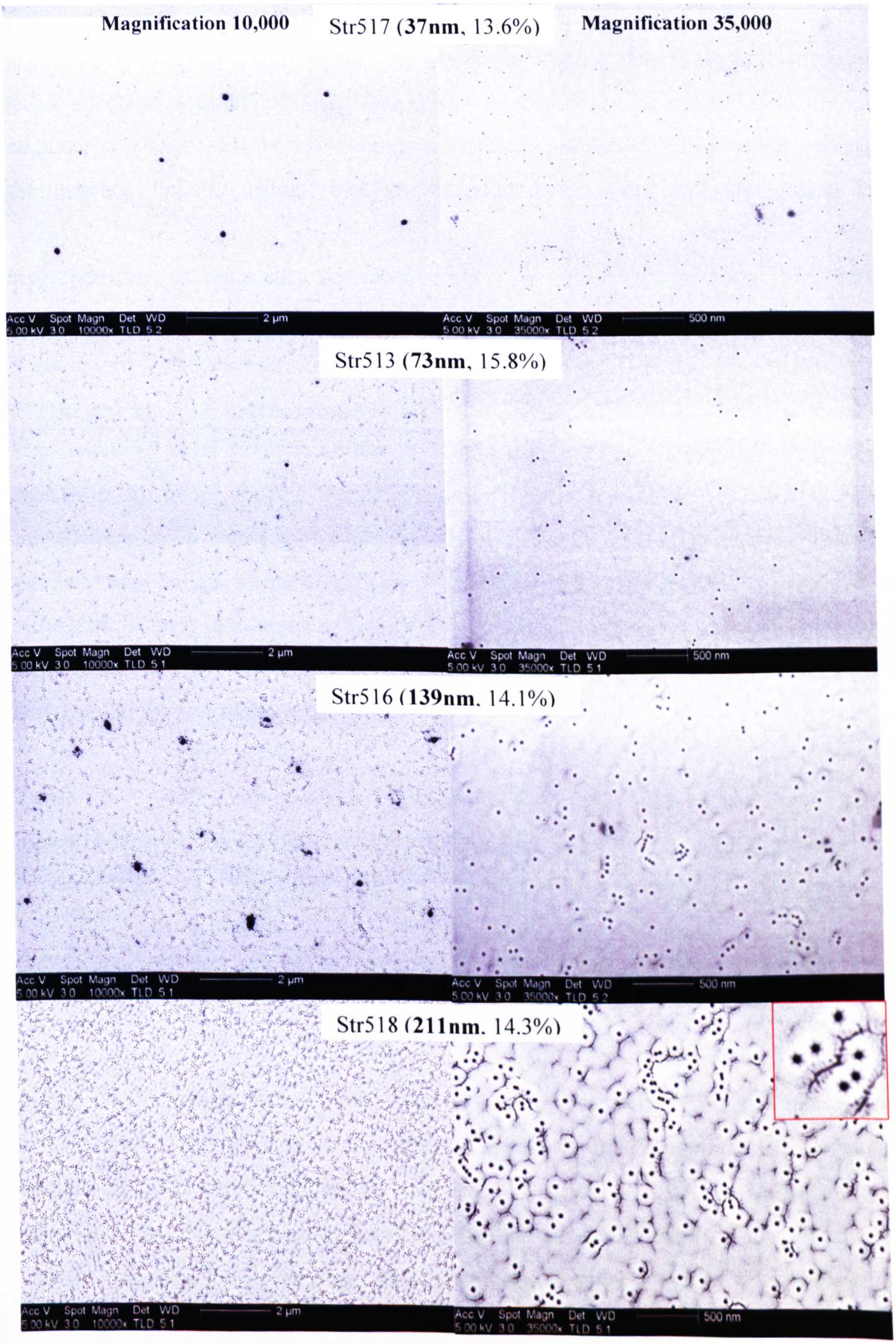

Figure 7.17 SEM images of "Strathclyde series" $Al_{1-x}In_xN$ epilayers for layer thicknesses from 37 to 211 nm with similar InN fraction of 14.7 ± 1.1%.

The degradation in the surface quality with increasing layer thickness can be explained as follows: When an alloy is grown on another one of slightly different lattice constant, a pseudomorphic layer can be formed if the thickness is thin. In that case, the misfit between the two crystals is accommodated by a biaxial strain, so that the in-plane lattice constant remains unchanged; no structural degradation is observed. If the thickness increases further, the elastic energy accumulated in the layer becomes so large that the crystal relaxes to its unstrained form. It occurs through the generation of pits and/or dislocations, resulting in a structural degradation. The structural degradation can be also seen by the χ_{min} parameters determined by RBS measurement as shown in Table 7.5. The χ_{min} value increases from 3.4 to 4.9 % as the layer thickness increases from 37 to 211 nm. It is noted that there is a dip in the χ_{min} at 73 nm thickness. This is more likely due to the InN composition being closer to the lattice-matched to GaN. It is worth mentioning that the increment in χ_{min} is not significant even though the thickness has increased by more than 6 times in contrast to that of InN fraction. A comparison of the influence of thickness and InN fraction on the quality of $Al_{1-x}In_xN$ layers will be presented and discussed in the following subsection.

Table 7.5 InN composition, thickness and χ_{min} determined by RBS measurement for STR517, STR513, STR516 and STR518 $Al_{1-x}In_xN$ epilayers.

Sample ID	Thickness (nm)	InN composition (%)	χ_{min} (%)
STR517	37	13.6	3.4
STR513	73	15.8	3.0
STR516	139	14.1	3.7
STR518	211	14.3	4.9

Figure 7.18 compares the low temperature PL spectra of STR517, STR513, STR516 and STR518 which were excited by 280 nm Xe-lamp and measured under the same conditions. It is observed that the $Al_{1-x}In_xN$ emission intensity is higher in the samples with thicker layers. In addition, thicker samples display double structures. The increase in the emission intensity arises because more carriers are generated in the thicker layer as illustrated in the inset using the absorption coefficient of 15×10^4 cm^{-1} estimated for AlN [34]. As for the double structure, it might be related

to the degradation in the surface quality with increasing layer thickness. Based on the surface quality obtained from SEM, χ_{min} parameters from RBS and emission intensity from PL spectra, it seems that there is a competition between the structural quality and the luminescence intensity when deciding on the optimum thickness.

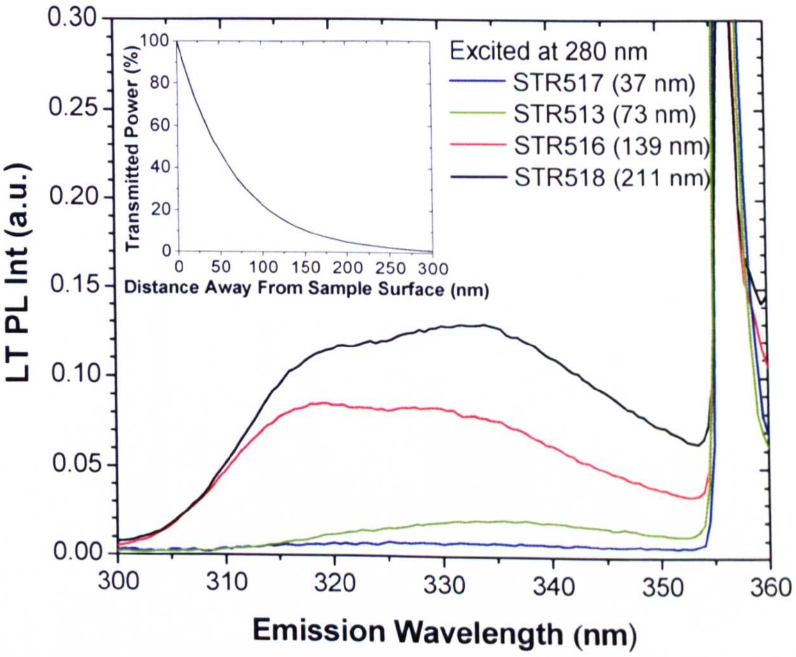

Figure 7.18 Low temperature (20 K) PL spectra of STR517, STR513, STR516 and STR518 with layer thickness ranges from 37 to 211 nm, excited by 280 nm lamp and measured under the same setup conditions. The layer thickness was determined by RBS measurement. The inset shows the transmitted power as a function of distance away from the sample surface.

- *Analysis*

As discussed in the previous sections, it has found out that the quality of $Al_{1-x}In_xN$ layers depend on InN fraction and layer thickness. In order to determine which of these factors has the dominant effect over the quality, χ_{min} is used as the indicator. Figure 7.19 plots the χ_{min} of the $Al_{1-x}In_xN$ samples grown on sapphire substrates studied in this work as a function of InN fraction and layer thickness. It is observed that the χ_{min} decreases significantly from around 16 to 3 % as the InN fraction increases towards the lattice-matched value before it starts to increase with further increase in InN fraction. However, it is not the case for various layer thicknesses where only a slight increase in the χ_{min} is observed as the thickness increases from 37 to 211 nm. The sharp black lines with high χ_{min} as indicated by * are the samples with low InN contents. Consequently, the InN fraction appears to play a more important role in affecting the $Al_{1-x}In_xN$ quality than the layer thickness.

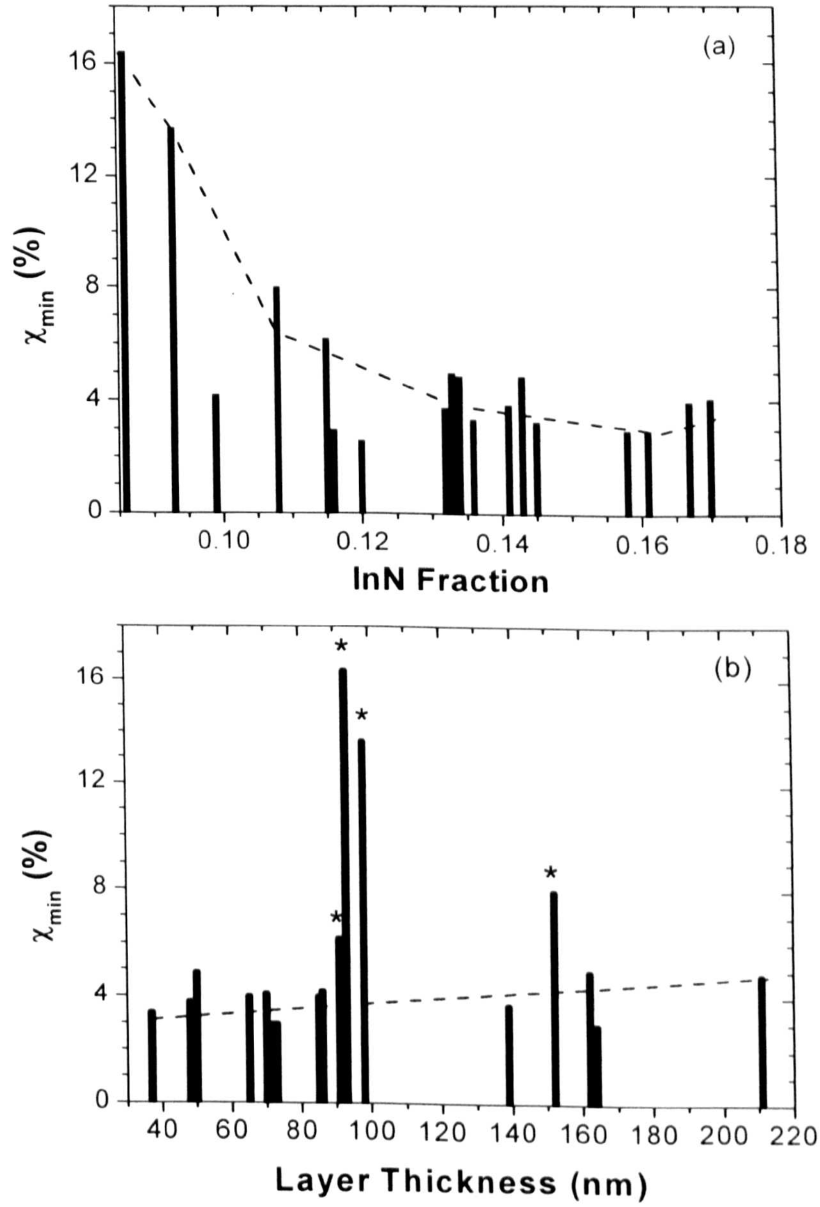

Figure 7.19 χ_{min} **as a function of (a) InN fraction and (b) layer thickness. * indicates the samples with low InN content. The dashed lines are guides for the eye indicating the influences of InN fraction and thickness on the quality of** $Al_{1-x}In_xN$**.**

7.3.2.3 Effect of Substrates

The effects of the substrates, in this case polished versus non-polished *c*-plane sapphire and $Al_yGa_{1-y}N$ templates with various Al contents, on the composition and structural properties and surface morphology of $Al_{1-x}In_xN$ epilayers will be discussed and presented.

- *Polished vs. non-polished c-plane sapphire substrates*

Samples STR504 and STR508 were chosen as they were grown under the same conditions except for different backside finishes on the sapphire substrates. Table 7.6 summarises their InN molar fraction and χ_{min} parameters determined by RBS measurement. It is noted that STR508 with polished sapphire has a higher InN molar fraction (0.133) than STR504 (0.108) with non-polished sapphire substrate. This indicates that the polished sapphire substrate had a lower surface temperature than the non-polished sapphire template, resulting in higher InN incorporation in the epilayer. The nature of the substrate backside (polished versus non-polished) can affect the surface temperature by influencing the radiative component of heat flow from the graphite susceptor underneath the substrate. If all other factors are equivalent, a non-polished substrate will have a slightly higher surface temperature, owing to better radiative coupling. However, in practice such effects are difficult to distinguish from deformation of substrates at the growth temperature (for example substrate bowing), which affects the nature of the contact with the graphite susceptor. Nevertheless, the polished substrate sample STR508 also displays better crystalline quality as evidenced by the lower χ_{min} value in Table 7.6 and crack-free surface from SEM images presented in Figure 7.20. STR504 has cracks due to the large lattice mismatch as explained earlier.

Table 7.6 Polished and non-polished sapphire samples and their InN molar fractions and χ_{min} determined by RBS technique.

Sample ID	Growth Temperature (°C)	InN molar fraction	χ_{min} (%)	Substrate
STR508	830	0.133	5.0	Polished sapphire
STR504	830	0.108	8.0	Non-polished sapphire

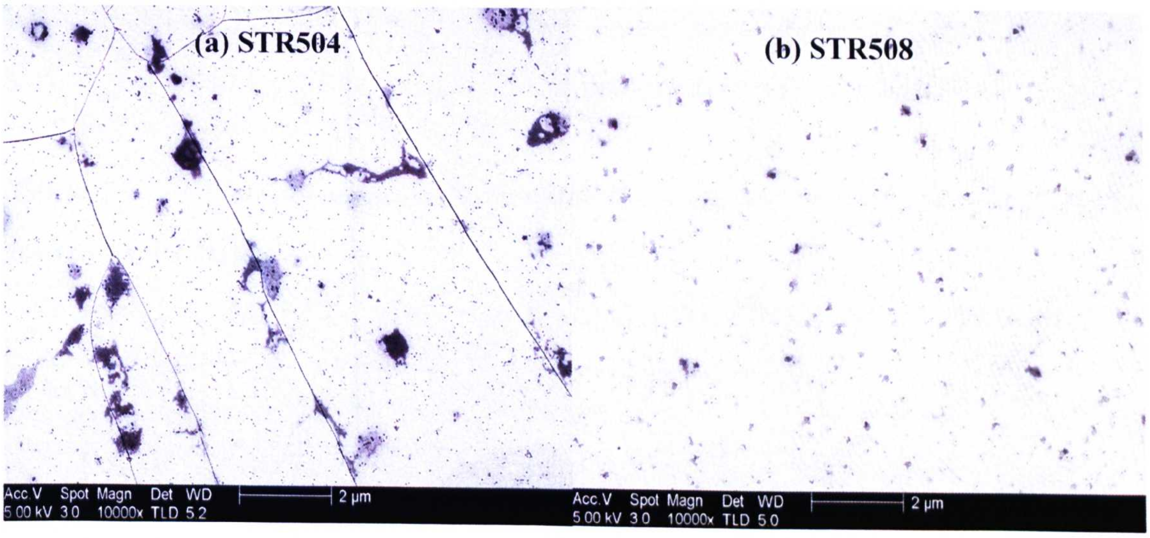

Figure 7.20 SEM images of (a) STR504 with non-polished sapphire and (b) STR508 with polished sapphire substrate taken under magnification of 10,000.

- $Al_yGa_{1-y}N$ *templates*

In this part, two factors will be considered: (i) to determine the suitable pre-growth heating temperature (T_{pre}) and (ii) to study how different template lattice parameters of $Al_yGa_{1-y}N$ ($0 \leq y \leq 0.234$) will affect the composition of the $Al_{1-x}In_xN$. The motivation of this work is to shift the lattice-matching point in achieving higher bandgap. This work is at a preliminary stage and early results are described.

(i) Pre-growth Heating Temperature

As explained in **Section 7.2**, a pre-growth heating step is needed before growth of the $Al_{1-x}In_xN$ layer on the $Al_yGa_{1-y}N$ templates. Table 7.7 compares the compositional and structural properties of STR520 (T_{pre} = 1000 °C) and STR523 (T_{pre} = 1070 °C) samples as measured by RBS technique. It is observed that in each growth run, the $Al_{1-x}In_xN$ grown on $Al_yGa_{1-y}N$ is significantly less InN-rich than that grown on GaN. χ_{min} values are also almost 6 times higher for the $Al_{1-x}In_xN$ layers grown on $Al_yGa_{1-y}N$ than those on GaN. There is a modest improvement in χ_{min} values with the different pre-growth heating condition used in STR523 as compared to STR520. The $Al_{1-x}In_xN$ thickness values are all close to the nominal 100 nm. Comparison of the RBS minimum channelling yields for STR520 versus STR523 suggests that the higher temperature, in this case 1070 °C, results in slightly better quality $Al_{1-x}In_xN$. Hence, 1070 °C was selected in the next growth run (STR528) when studying the influence of different lattice parameters of $Al_yGa_{1-y}N$ on the surface, composition, structural and optical properties of the $Al_{1-x}In_xN$.

Table 7.7 Compositional and structural properties of STR520 and STR523 measured by RBS.

Sample ID	T_{pre} (°C)	InN molar fraction	χ_{min} (%)	Thickness (nm)	Substrate
STR520B	1000	0.086	16.4	93	$Al_{0.23}Ga_{0.77}N$
STR520D	1000	0.141	3.9	93	GaN
STR523B	1070	0.120	2.6	98	GaN
STR523D	1070	0.093	13.7	98	$Al_{0.21}Ga_{0.79}N$

(ii) $Al_yGa_{1-y}N$ templates as a function of Al compositions

A direct comparison of the SEM images from STR528 samples is presented in Figure 7.21.

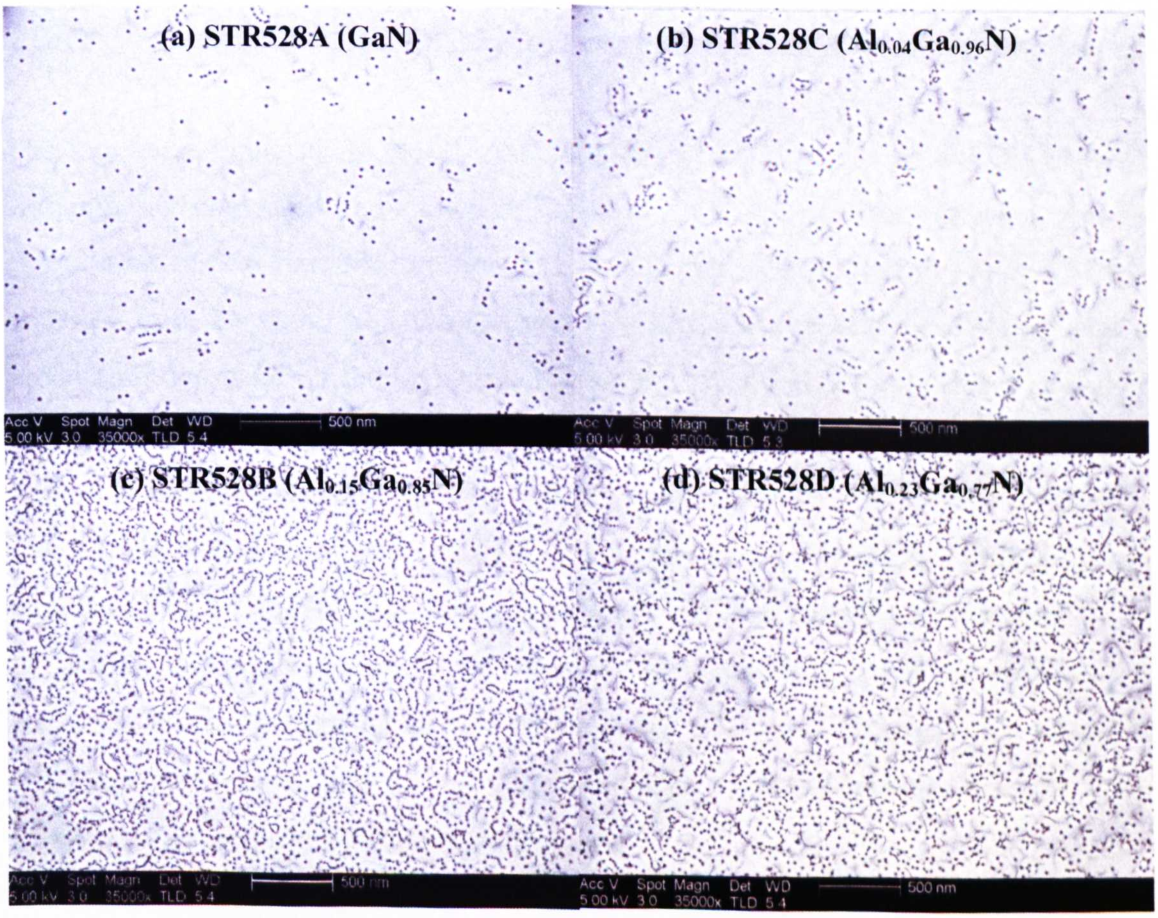

Figure 7.21 SEM images of STR528 samples on $Al_yGa_{1-y}N$ templates with AlN molar fraction y ranges 0 to 0.23 under magnification of 35,000.

From the SEM images, it is observed that the surface quality degrades (as monitored by an increasing pit density), as the Al molar fraction increases. However it is noted that the pit diameter remains unchanged and all samples are crack-free. In order to have a clearer idea of the degradation of the $Al_{1-x}In_xN$, the crystalline quality of the $Al_{1-x}In_xN$ is examined using RBS technique as summarised in Table 7.8. It is observed that in each growth run, the $Al_{1-x}In_xN$ grown on $Al_yGa_{1-y}N$ is significantly less InN-rich than that grown on GaN. χ_{min} values are higher for the $Al_{1-x}In_xN$ layers grown on $Al_yGa_{1-y}N$ than those on GaN except for sample STR528D.

Table 7.8 InN molar fraction and χ_{min} parameters of STR528 samples on $Al_yGa_{1-y}N$ templates measured by RBS technique.

Sample ID	T_{pre} (°C)	InN molar fraction	χ_{min} (%)	Thickness (nm)	Substrate
STR528A	1070	0.191	6.2	114	GaN
STR528C	1070	0.156	11.1	104	$Al_{0.04}Ga_{0.96}N$
STR528B	1070	0.132	39.3	102	$Al_{0.15}Ga_{0.85}N$
STR528D	1070	0.136	7.5	101	$Al_{0.23}Ga_{0.77}N$

The low temperature (≈ 34 K) PL spectra of STR528 samples, excited by 265 nm Xe-lamp, are compared and shown in Figure 7.22. It is observed that there are: a strong peak at 356 nm, 345 nm and 331 nm, which is attributed to the band-edge emission from the GaN, $Al_{0.04}Ga_{0.96}N$ and $Al_{0.15}Ga_{0.85}N$ template respectively; and a broad emission band on the higher energy side. This broad emission band at higher energy is attributed to intrinsic emission from the $Al_{1-x}In_xN$ epilayers. A clear $Al_{1-x}In_xN$ emission band for STR528A (GaN template) is seen at 331 nm (3.75 eV). The $Al_{1-x}In_xN$ emission band can only be partially seen in STR528C ($Al_{0.04}Ga_{0.96}N$ template) and STR528B ($Al_{0.15}Ga_{0.85}N$ template) as it is partially overshadowed by the strong $Al_yGa_{1-y}N$ emission. However there is difficulty in distinguishing the $Al_{1-x}In_xN$ emission from $Al_yGa_{1-y}N$ emission for STR523D ($Al_{0.23}Ga_{0.77}N$ template with calculated band gap of 3.9 eV (318 nm)). This is possibly due to being completely overlapped by $Al_yGa_{1-y}N$ emission.

In addition, there are several PL features appearing at the lower energy side of GaN. It seems that there are broad emission bands as background. The sharp emission lines at around 367 nm (3.38 eV), 380 nm (3.26 eV) and 391 nm (3.17 eV) are added to this background. The PLE spectra detected at these sharp lines confirm they are due to GaN. These lines are attributed to the GaN-related-defect (3.38 eV), and donor-acceptor-pair (DAP) transition (3.26 eV) and its LO-DAP replicas (3.17 eV).

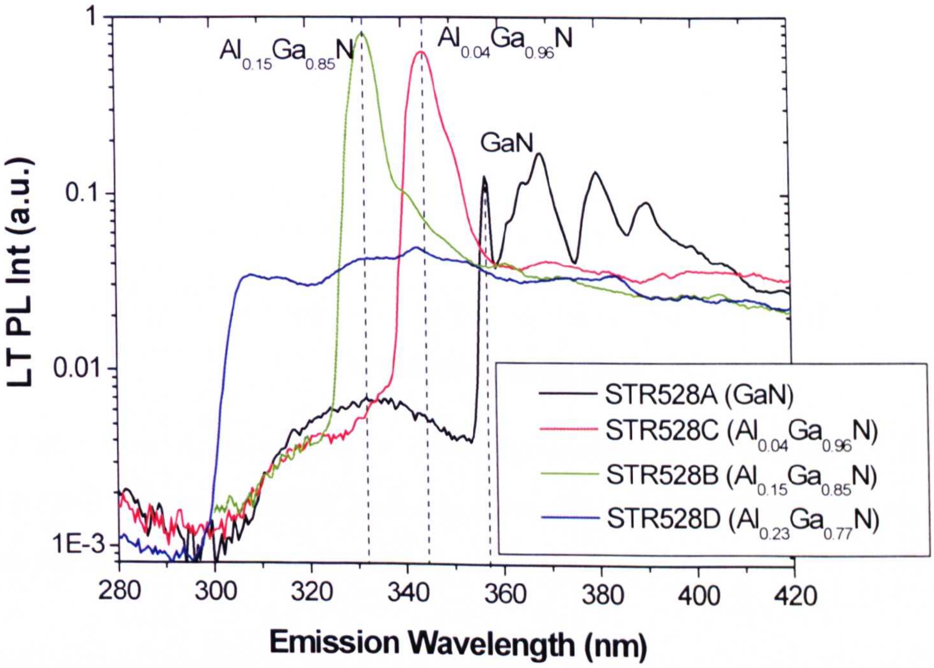

Figure 7.22 Low temperature (≈ 34 K) PL spectra of STR528 samples excited by 265 nm Xe-lamp.

In order to estimate the band gap of $Al_{1-x}In_xN$, PLE measurements were performed. Figure 7.23 presents the low temperature corrected PLE spectra of STR528A (GaN template) and STR528B ($Al_{0.15}Ga_{0.85}N$ template) samples measured at ≈ 34 K. The effective band gap of STR528A is approximately 4.15 eV. The PLE intensity is higher in STR528A than in STR528B, suggesting that the quality of the latter is poorer.

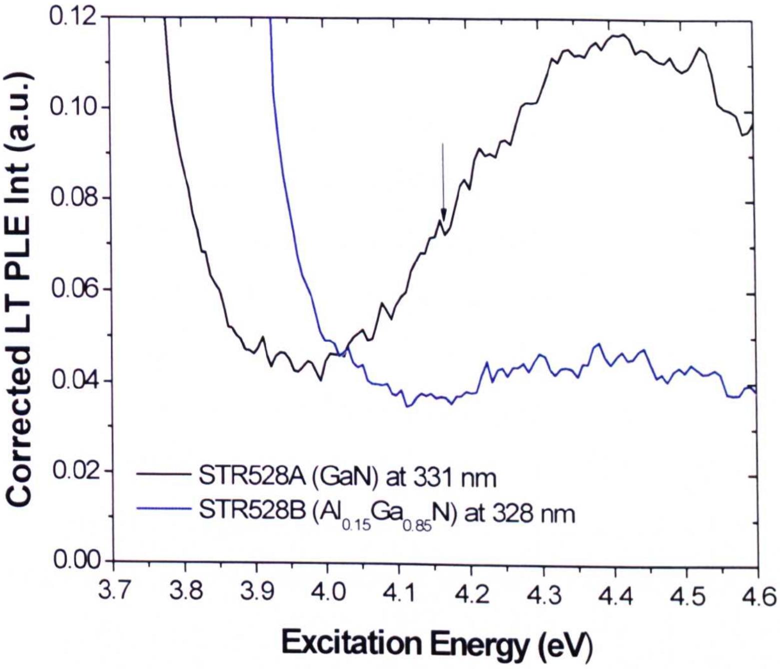

Figure 7.23 Low temperature (≈ 34 K) corrected PLE spectra of STR528A and STR528B grown on GaN and $Al_{0.15}Ga_{0.85}N$ templates respectively. Arrow indicates the effective energy band gap.

7.4 Summary

In this chapter composition, luminescence and surface morphology of a series of $Al_{1-x}In_xN$ epilayers with a range of InN composition, layer thickness and substrates have been presented and discussed.

The InN composition and the crystalline quality of the samples were determined using the RBS technique performed at ITN in Portugal. The data show that the InN molar fraction varies from 0.082 to 0.191, and the χ_{min} parameter ranges from 3 to as high as 39 %, revealing relatively good single crystalline quality for some samples and poorer for others especially those samples grown on $Al_yGa_{1-y}N$ templates.

The luminescence of the $Al_{1-x}In_xN$ epilayers was studied using PL technique excited by Xe-lamp at low temperature. Samples were observed to emit $Al_{1-x}In_xN$ peak on the higher energy side of the GaN band gap. It is observed that the PL peak energies from $Al_{1-x}In_xN$ epilayers were found to red-shift with increasing InN content. The emission energy decreases linearly from ≈ 4.2 to 3.6 eV as InN fraction increases from 0.082 to 0.170. PLE was carried out to determine the band gap energies of the $Al_{1-x}In_xN$ alloys. By fitting the PLE spectra with the sigmoidal function, one could obtain the effective band gap energy, E_g. It is observed that the E_g decreases with InN fraction. It decreases linearly in the restricted composition studied in this work. Using the band gap equation, the bowing parameter of $Al_{1-x}In_xN$ alloy is observed to depend on the InN composition. It decreases linearly as InN fraction increases in the restricted studied composition range. By taking the difference between the PL emission energy and the effective band gap determined from the PLE spectra, one could obtain the Stokes' shift. It is observed that the Stokes' shift varies between 350 to 650 meV, which is higher than the literature data of InGaN and $Al_yGa_{1-y}N$ structures. There is no clear dependence of the Stokes' shift and InN fraction seen in this work.

The surface morphology of the $Al_{1-x}In_xN$ epilayers as a function of InN composition and the layer thickness was investigated using SEM technique. It is observed that cracks are present in samples with low InN content (≤ 10 %) whereas the pit density and diameter increase with increasing InN content. As for the case of increasing layer thickness, the surface quality and crystal quality worsens with increasing thickness. However, it is noted that the emission intensity is higher in thicker samples. This could be because more carriers are generated in thicker layers. Hence, it seems that there is a competition between the surface quality and emission intensity when deciding on the optimum thickness. In addition, it is found out that the InN fraction affects the quality of $Al_{1-x}In_xN$ more significantly than that of the layer thickness.

Finally, the effects of the substrates, in this case polished versus non-polished sapphire, and $Al_yGa_{1-y}N$ with various Al contents, on the composition, crystalline quality and optical properties were studied. It is noted that the polished sapphire has lower InN content and displays better crystalline quality than the sample with non-polished sapphire substrate. There is a modest improvement in χ_{min} values with the higher pre-growth heating condition (1070 °C) than 1000 °C, suggesting slightly better quality. Surface quality degrades and lower PLE intensity is observed as the Al content in the $Al_yGa_{1-y}N$ template increases.

7.5 References

[1] J. F. Carlin, C. Zellweger, J. Dorsaz, S. Nicolay, G. Christmann, E. Feltin, R. Butté, and N. Grandjean, Phys. Status Solidi B **242**, 2326 (2005).

[2] K. Lorenz, N. Franco, E. Alves, I. M. Watson, R. W. Martin, and K. P. O'Donnell, Phys. Rev. Lett. **97**, 085501 (2006).

[3] T. Onuma, S. F. Chichibu, Y. Uchinuma, T. Sota, S. Yamaguchi, S. Kamiyama, H. Amano, and I. Akasaki, J. Appl. Phys. **94**, 2449 (2003).

[4] T. Fujimori, H. Imani, A. Wakahara, H. Okada, A. Yoshida, T. Shibata, and M. Tanaka, J. Cry. Growth **272**, 381 (2004).

[5] T. Peng, J. Piprek, G. Qiu, J. O. Olowoiafe, K. M. Unruh, C. P. Swann, and E. F. Shubert, Appl. Phys. Lett. **71**, 2439 (1997).

[6] S. Yamaguchi, M. Kariya, S. Nitta, T. Takeuchi, C. Wetzel, H. Amano, and I. Akasaki, Appl. Phys. Lett. **76**, 876 (2000).

[7] M. J. Lukitsch, Y. V. Danylyuk, V. M. Naik, C. Huang, G. W. Auner, L. Rimai, and R. Naik, Appl. Phys. Lett. **79**, 30 (2001).

[8] K. Kobuta, Y. Kobayashi, and K. Fujimoto, J. Appl. Phys. **66**, 2984 (1989).

[9] S. Yamaguchi, M. Kariya, S. Nitta, T. Takeuchi, C. Wetzel, H. Amano, and I. Akasaki, Appl. Phys. Lett. **73**, 830 (1998).

[10] J. Wu, W. Walukiewicz, K. M. Yu, J. W. Ager, S. X. Li, E. E. Haller, H. Lu, and W. J. Schaff, Solid State Commun. **127**, 411 (2003).

[11] W. Terashima, S. B. Che, Y. Ishitani, and A. Yoshikawa, Jpn. J. Appl. Phys., Part 2 **45**, L539 (2006).

[12] K. Wang, R. W. Martin, D. Amabile, P. R. Edwards, S. Hernandez, E. Nogales, K. P. O'Donnell, K. Lorenz, E. Alves, V. Matias, A. Vantomme, D. Wolverson, and I. M. Watson, J. Appl. Phys. **103**, 073510 (2008).

[13] M. J. Lukitsch, Y. V. Danylyluk, V. M. Naik, C. Huang, G. W. Auner, L. Rimai, and R. Naik, Appl. Phys. Lett. **79**, 632 (2001).

[14] E. Iliopoulos, A. Adikimenakis, C. Giesen, M. Heuken, and A. Georgakilas, Appl. Phys. Lett. **92**, 191907 (2008).

[15] $Al_yGa_{1-y}N$ Template Website: http://www.tdii.com/products/AlGaN_sap.html

[16] K. Lorenz to R. W. Martin, Private Communication.

[17] S. Hernández, K. Wang, D. Amabile, E. Nogales, D. Pastor, R. Cuscó, L. Artús, R. W. Martin, I. M. Watson, K. P. O'Donnell and the RENiBEl Network. Mater. Res. Soc. Symp. Proc. **892**, 0892-FF23-04.1 (2006).

[18] R. W. Martin, P. G. Middleton, and K. P. O'Donnell, W. Van der Stricht, Appl. Phys. Lett. **74**, 263 (1999).

[19] P. B. Perry and R. F. Rutz, Appl. Phys. Lett. 33, 319 (1978).

[20] M. Feneberg, J. Däubler, K. Thonke, R. Sauer, P. Schley and R. Goldhahn, Phys. Rev. **77**, 245207 (2008).

[21] Vurgaftman, Meyer, and Ram-Mohan, J. Appl. Phys., **89**, 5815 (2001).

[22] M. Ferhat, and F. Bechstedt, Phys. Rev. B **65**, 075213 (2002).

[23] M. D. McCluskey, C. G. Van de Walle, C. P. Master, L. T. Romano, and N. M. Johnson, Appl. Phys. Lett. **72**, 2725 (1998).

[24] Urbach F, Phys. Rev. **92** ,1324 (1953).

[25] A. Cremades, L. Gorgens, O. Ambacher, M. Stutzmann and F. Scholz, Phys. Rev. B **61**, 2812 (2000).

[26] F. Yang, M. Wilkinson, E. J. Austin, K. P. O'Donnell, Phys. Rev. Lett. **70**, 323 (1993).

[27] T. Onuma, S. F. Chichibu, A. Uedono, T. Sota, P. Cantu, T. M. Katona, J. F. Keading, S. Keller, U. K. Mishra, S. Nakamura, S. P. DenBaars, J. Appl. Phys. **95**, 2495 (2004).

[28] Y. –H. Cho, G. H. Gainer, J. B. Lam, J. J. Song, W. Yang, W. Jhe, Phys. Rev. B **61**, 7203 (2003).

[29] L. T. Tan, R. W. Martin, K. P. O'Donnell, I. M. Watson, Z. H. Wu, and F. A. Ponce, Appl. Phys. Lett. **92**, 031907 (2008).

[30] F. Bernardini, V. Fiorentini, and D. Vanderbilt, Phys. Rev. B **56**, R10024 (1997).

[31] A. D. Bykhovski, V. V. Kaminski, M. S. Shur, Q. C. Chen, M. A. Khan, Appl. Phys. Lett. **68**, 818 (1996).

[32] S. Chichibu, T. Sota, K. Wada, O. Brandt, K. H. Ploog, S. P. Denbaars, S. Nakamura, Phys. Stat. Sol. (A) **183**, 91 (2001).

[33] V. Darakchieva, M. Beckers, M.-Y. Xie, L. Hultman, B. Monemar, J.-F. Carlin, E. Feltin, M. Gonschorek, and N. Grandjean, J. Appl. Phys. **103**, 103513 (2008).

[34] J. F. Muth, J. D. Brown, M. A. L. Johnson, Z. H. YU, R. M. Kolbas, J. W. Cook Jr., and J. F. Schetzina, MRS Internet J. Nitride Semicond. **Res. 4S1**, G5.2 (1999).

CHAPTER 8

Conclusions

8.1 Conclusions

This thesis has presented results on the optical, surface and composition properties of the III-nitride ternary alloys $In_xGa_{1-x}N$ and $Al_{1-x}In_xN$. The aim of these experiments is to gain a better understanding of the workings of the nitride system by studying the effects of different cap thicknesses, well widths, Si doping concentrations in the barriers, InN compositions, layer thicknesses and substrates.

An introduction to III-nitrides was given in **Chapter 1**, starting with a brief history of their development and current applications. **Chapter 2** summarised the growth technique used in the production of nitrides in this work, along with some of the challenges associated with their growth. The structure of the samples, including their crystal and energy band structure, together with optical properties including the carrier localisation, the spontaneous and piezoelectric polarisation fields and the band-gap tailoring due to heavy doping effects are also outlined. **Chapter 3** described the experimental techniques used to obtain the results presented in this thesis. The main techniques used are photoluminescence (PL) and PL excitation (PLE) spectroscopy for investigating the optical properties; secondary electron microscopy (SEM) and atomic force microscopy (AFM) for visualisation of the surface morphology; and electron probe micro-analysis (EPMA) and Rutherford backscattering spectroscopy (RBS) to study the compositional properties. The experimental results and their analyses are presented in chapters 4, 5, 6 and 7.

Chapter 4 studied the optical properties and surface morphology of two series of $In_xGa_{1-x}N$/GaN single quantum wells (SQWs) with peak emission wavelengths near 390 and 415 nm as a function of the thickness of GaN cap thickness (ranging from 2.5 to 15 nm). In addition, similar structures with the same cap thickness of 2.5 nm but different doping are compared to evaluate the effect of surface depletion fields. Similar trends are seen for both series of samples. Low temperature PL intensity is observed to decrease by almost 2 times as the cap thickness decreases from 15 to 2.5

nm. Larger values of PL linewidth are seen for the thinner cap samples compared to those with a thick cap of 15 nm. The relative strength of the LO-phonon satellites, manifested by Huang-Rhys parameters S_0 and S_1, is found to have a clear dependence on the cap thickness. S_0 decreases as the cap thickness increases from 2.5 to 15 nm. At the same time S_1 gives an insignificant change and remains at all times larger than S_0. In order to explain the optical dependence on the cap thickness, several factors are considered here: (i) change in density of excess carriers excited within the wells; (ii) surface depletion field; (iii) intense built-in electric field; and (iv) additional localisation of the excitons. The latter is believed to be the dominant factor. SEM and AFM techniques are performed to study the surface roughness of these samples. Pits on the sample surfaces are revealed and the pit density is estimated to increase from 2.4 to 3.3 x 10^9 cm^{-2} as the cap thickness decreases from 15 to 2.5 nm. The root-mean-square (RMS) surface roughness is found to increase from 0.96 to 1.58 nm as the cap thickness decreases. In addition, temperature-dependent PL spectra are carried out and 'S-shaped' peak emission is observed, indicating the presence of carrier localisation. By analysing the Huang-Rhys parameters, peak energies, surface morphology and temperature-dependent PL spectra, it is suggested that the amount of localisation excitons increases as the cap thickness reduced is related to the increase in the surface roughness, which would go some way to explain the overall degradation of PL described earlier.

Chapter 5 studied the influence of Si doping in the barriers of $In_xGa_{1-x}N/GaN$ SQWs on the optical properties using photoluminescence as a function of power and temperature. The QW PL peak intensity decreases by almost 5 times whereas the FWHM increases by almost two times as the Si doping concentration increases from 0.05 to 1 x 10^{19} cm^{-3}. The PL properties for more heavily doped samples are seen to be degraded principally due to impurity scattering. The QW transition energy has reduced by approximately 60 meV with increasing doping. There is no change in the QW transition peak position as the power density increases by 2 orders of magnitude. This suggests that the piezoelectric field frequently observed in strained $In_xGa_{1-x}N/GaN$ QWs is suppressed in the samples studied in this work. The red-shift in the QW transition energy is attributed to band gap renormalisation with a coefficient of - 4.2 x 10^{-5} meVcm. For the heavier doped sample, a shoulder appearing at the lower energy emission of the QW is observed. It becomes more prominent as the doping and/or temperature increases. It is believed that the lower energy emission could be related to Si-related defects where the carriers trapped in such defects may get thermally activated at high temperature, achieving sufficient energy to escape and recombine radiatively. From the temperature-dependence PL spectra, it is shown that the heavy doping has reduced the carrier localisation in these structures.

Chapter 6 presented the low temperature and room temperature photoluminescence spectra of near-lattice-matched GaN/$Al_{1-x}In_xN$ single quantum well structures grown on sapphire and FS-GaN substrates as a function of GaN well width (ranging from 1.5 to 4 nm), excitation power density and excitation wavelength. The QW peak energy decreases as the well width increases. This is a manifestation of QCSE resulting mainly from intense spontaneous polarization fields, which persists even in the absence of strain in the QW layer. The in-built electric field is estimated to be 2.6±0.5 MV/cm using the gradient of emission energy as a function of well width and single particle calculations of the confined energy levels. Also, the dependencies of the QW energy on the excitation power reveal the effects of carrier screening of the built-in electric fields in thicker wells.

The peak energies observed in the samples grown in FS-GaN substrates have shifted in comparison to the equivalent structure on GaN-on-sapphire: the QW transition energy blue-shifts whilst the barrier emission red-shifts. These spectral shifts are attributable to small substrate surface temperature variations resulting from the difference in the characteristics of sapphire and FS-GaN substrates. The net temperature difference arises from interplay of the different thermal conductivities, thickness, planarity and backside finishes of the different substrates. In this work, the sapphire pieces had non-polished backside as compared to the polished backside for the FS-GaN where polishing is suggested to increase the effectiveness of radiative heating of the substrate. In addition, the samples on FS-GaN substrates have 3 to 4 atomic % more InN than those grown on sapphire. Temperature-dependent PL spectra show no 'S-shaped' behaviour for GaN/$Al_{1-x}In_xN$ SQW materials regardless of the types of substrates, well width and lower barrier thickness. The QW emission energy decreases as the temperature increases due to band gap shrinkage.

Chapter 7 investigated the composition, luminescence and surface morphology of a series of $Al_{1-x}In_xN$ epilayers with a range of InN compositions, layer thicknesses and substrates. The InN composition and the crystalline quality of the samples are determined using RBS technique where the InN molar fraction ranges from 0.082 to 0.191, and the χ_{min} parameter ranges from around 3 to 39 %. The luminescence of the $Al_{1-x}In_xN$ epilayers is studied using PL technique excited by Xe-lamp at low temperature. Samples are observed to emit $Al_{1-x}In_xN$ peak on the higher energy side of the GaN band gap. It is observed that the PL peak energies from $Al_{1-x}In_xN$ epilayers are found to red-shift with increasing InN content. The emission energy decreases linearly from $\approx$ 4.2 to 3.6 eV as InN fraction increases from 0.08 to 0.17. PLE is carried out to determine the band gap energies E_g of the $Al_{1-x}In_xN$ alloys by fitting the spectra with the sigmoidal function. It is observed that the E_g decreased with InN fraction and decreases linearly in the restricted composition studied in this work. The bowing parameter of $Al_{1-x}In_xN$ alloy is linearly dependent on the InN composition studied in this restricted range. By taking the difference between the PL emission energy and the effective band gap determined from the PLE spectra, one could obtain the Stokes' shift. It is observed that the Stokes' shift varies between 350 to 650 meV, which is higher than in the literature data for $In_xGa_{1-x}N$ and $Al_yGa_{1-y}N$ structures. There is no clear dependence of the Stokes' shift on the InN fraction seen in this work.

Surface morphology of the $Al_{1-x}In_xN$ epilayers as a function of InN composition and the layer thickness are investigated using SEM technique. It is observed that cracks are present in samples with low InN content ($\leq$ 10 %) whereas the pit density and diameter increase with increasing InN content. As for the layer thickness case, the surface quality and crystal quality worsens with increasing thickness. However, it is noted that the emission intensity is higher in thicker samples. This could be because more carriers are generated in thicker layers. Hence, it seems that there is a competition between the surface quality and emission intensity when deciding on the optimum thickness. In addition, it is found out that the InN fraction affects the quality of $Al_{1-x}In_xN$ more significantly than that of the layer thickness.

Finally, the effects of the substrates, in this case polished versus non-polished sapphire, and $Al_yGa_{1-y}N$ with various Al contents, on the composition, crystalline quality and optical properties were studied. It is noted that samples with the polished sapphire substrates results in layers with lower InN content and displaying better crystalline quality than the samples on non-polished sapphire substrates. There is a modest improvement in χ_{min} values with the higher pre-growth heating condition (1070 °C) than 1000 °C, suggesting slightly better quality. Surface quality degradation, decrease in InN content and lower PLE intensity are observed as the Al content in the $Al_yGa_{1-y}N$ template increases.

8.2 Suggestions for Future Work

In the device engineering field on $In_xGa_{1-x}N$ devices, more research is needed in order to improve the power of LEDs. Ideas like doping the GaN in the barrier layers in $In_xGa_{1-x}N$/GaN QWs with the hope of improving the luminescence has been tested in the thesis. However the number of $In_xGa_{1-x}N$/GaN QWs samples doped with Si was limited. Thus, this could restrict the detailed study of the Si impact on the optical properties. Hence more samples with various doping concentrations could be a possible future investigation line. Also, it is also worth studying their electrical properties.

As for $Al_{1-x}In_xN$, the quality of $Al_{1-x}In_xN$ epilayers is still the main obstacle for their wide applications. Although the quality of $Al_{1-x}In_xN$ epilayers studied in this thesis are improved with some samples with chi-min values of 3 to 4 %, it is still very difficult to achieve good quality for high AlN content samples. An interesting point could be the fabrication of $Al_{1-x}In_xN$ epilayers with a reasonable quality with high AlN contents as well as high InN contents in order to test the linearity of some physical parameters such as bowing parameter measured in this thesis. Also, more works on the influences of various templates to shift the lattice-match point and structures such as multi-quantum wells could be a possible future investigation line.

Appendix A
List of Publications

i. L.T. Tan, R.W. Martin, I. M. Watson, Z. H. Wu, F. A. Ponce, and K. P. O'Donnell and, 'Photoluminescence of near-lattice-matched GaN/AlInN quantum wells grown on free-standing GaN and on sapphire substrates', Appl. Phys. Lett., **92**, 031907 (2008).

ii. L.T. Tan, R.W. Martin, I. M. Watson, and K. P. O'Donnell, 'Photoluminescence and phonon satellites of single InGaN/GaN quantum wells with varying GaN cap thickness', Appl. Phys. Lett., 89, 101910 (2006).

iii. L.T. Tan *et. al.*, 'Carrier concentration induced band-gap shift in InGaN/GaN single quantum wells with Si-doped barriers', to be submitted to Journal of Applied Physics.

iv. L.T. Tan *et. al.*, 'Anomalous observations of photoluminescence and surface morphology of AlInN epilayers with various InN compositions', to be submitted to Appl. Phys. Lett.

v. L.T. Tan *et. al.*, 'Characterization of AlInN films on various layer thicknesses and substrates', to be submitted to Appl. Phys. Lett.

Appendix B
List of Conferences

i. L.T. Tan, R.W. Martin, and K.P. O'Donnell, *United Kingdom Nitrides Consortium Meeting*, 1st July 2008, University of Sheffield (Oral presentation).

ii. L.T. Tan, R.W. Martin, I.M. Watson, and K.P. O'Donnell, *The Rank Prize Funds: Mini-Symposium on Physics and Applications of InN and InGaN Semiconductor Materials*, 16th-19th June 2008, Grasmere, U.K (Oral presentation).

iii. L.T. Tan, R.W. Martin and K.P. O'Donnell, *Europe-Material Research Society (E-MRS) Spring Meeting*, 26th- 30th May 2008, Strasbourg, France (Oral presentation).

iv. L.T. Tan, R.W. Martin, I.M. Watson, and K.P. O'Donnell, *Material Research Society (MRS) Fall Meeting*, 27th November-1st December 2006, Boston, USA (1 Oral and 1 Poster presentations).

v. L.T. Tan, R.W. Martin, I.M. Watson, and K.P. O'Donnell, *United Kingdom Nitrides Consortium Meeting*, 4th July 2006, University of Sheffield, U.K. (Poster presentation).

vi. L.T. Tan, R.W. Martin, I.M. Watson and K.P. O'Donnell, *United Kingdom Nitrides Consortium Meeting*, 11th-12th January 2006, University of Strathclyde, U.K. (Oral presentation).